Arc magma sources : contribution of primitive olivine-hosted melt inclusions from Ecuadorian volcanoes

Diego Narvaez

UNIVERSITÉ CLERMONT AUVERGNE

Collegium des Sciences Fondamentales

Laboratoire Magmas et Volcans

ÉCOLE DOCTORALE DES SCIENCES FONDAMENTALES

N° 178

THÈSE DE DOCTORAT

Présentée pour obtenir le grade de

DOCTEUR D'UNIVERSITÉ

Spécialité : *Structure et évolution de la Terre et des autres planètes*

Par

Diego Fernando NARVÁEZ RIVADENEIRA

Titulaire du Master Recherche Magmas et Volcans

Arc magma sources: Contribution of primitive olivine-hosted melt inclusions from Ecuadorian volcanoes

Soutenue publiquement le 15 avril 2021 devant le jury:

Susanne M. Straub	Columbia University	Rapporteur
Nicole Métrich	Institut de Physique du Globe de Paris	Rapporteur
Pierre Schiano	Université Clermont-Auvergne	Président du jury
Silvana Hidalgo	Escuela Politécnica Nacional	Examinatrice
Gaëlle Prouteau	Université d'Orléans	Examinatrice
Estelle Rose-Koga	Université Clermont-Auvergne	Directrice de thèse
Pablo Samaniego	Université Clermont-Auvergne	Directeur de thèse
Kenneth Koga	Université Clermont-Auvergne	Directeur de thèse

Acknowledgments

I thank you both, mom and dad, for your unconditional support that encouraged me to continue my studies until this point. I thank my sister and brothers for their support from distance and at home the last 6 months. I also thank my cousins for all the weekends we spent together, it was always a great stress reliever for me.

I am grateful to you Estelle, Pablo and Ken, for all the time you invested in this project. I thank you Estelle for your kindness and positivity that always motivated me to continue this work, especially during moments of frustration. Ken, I am grateful for all the knowledge you shared with me through long discussions, not only about this project but also politics and metamorphic petrology. Thank you Pablo for the daily discussion we had when I was in Ecuador. I definitely made great progress because you were always available when I needed any clarifications. I was very lucky to have you three as my advisors, because it was very easy to work with you all. Many thanks to all the LMV staff for their support during my PhD because you made my stay in France more pleasant. I thank Antoine, Frank and Nicolas C. for their support with the 1-atm furnace and the homogenization stage. I thank you for your kindness and patience in helping me when I had problems with the instruments. I thank Claire and Jean-Luc DeVidal for your help with olivine separation and melt inclusion analysis. I thank all the people with whom I discussed aspects of my project, especially to Marion G., Taya, Muriel, Yves, Swetha, Etienne, Federica and many others.

I thank the Institut de Recherche pour le Développement (IRD) for their financial support through its ARTS program. It was my dream to earn a PhD and you made it possible. Pablo, thank you for all the paperwork you had to go through to get this scholarship. Also I thank the geology department of the Escuela Politécnica Nacional for their financial support when I was in Ecuador. In particular, I thank Pedro Reyes and Ana Cabero for allowing me to work in your department because, in doing so, I discovered my love for teaching. I thank all the people from the volcanology group of Instituto Geofísico for their friendship and the work space you provided to me. I especially thank Silvana Hidalgo for your support to this project and all the helpful advice you offered to me about my thesis and my future career.

I thank all the people with whom I spent some time during the last 3 years both in France and in Ecuador. My friends in France Anne, Alessandro, Celine L., Taya, Julia, Swetha, Yves, Ines, Sara, Federica, Masa, Guillaume, Antonio, Freddy, Lu, Susi and Yoshi. I especially thank Anne and Alessandro for all the lunches and beers we had together. I thank my friends in Ecuador: Francisco, Camilo, Marco, Dario, Nicole, Jorge, Mike, Maria Paula, Valeria, Joselyn, Pame S., Daniel N., Marivi and everybody else that have shared some time with me. I want to thank you Alina for all the time we spent together (from distance) during my PhD.

Part of this work has been carried out during the coronavirus (COVID-19) global health crisis, when unprecedented changes occurred in all our lives. Mine was no exception, and I am very thankful for the people that supported me during this period.

Abstract

Arc magmas inherit its composition from three reservoirs: the mantle wedge, the arc crust and the subducted slab. The contribution of the mantle and slab components is constrained from the study of primitive magmas, which is the magma yet to interact extensively with the crust. Determining the slab component signature is particularly important, because the nature of the petrological and geochemical signature is an indicator of the thermal state occurring along subduction zones. For instance, primitive volcanic rocks that are enriched in fluid-mobile elements (e.g. Ba, Pb, B) are related to cold subduction zones where the slab component is expected to be an aqueous fluid. Hotter subduction zones favors the occurrence of higher-temperature fluids or hydrous siliceous melts which are characterized by a geochemical signature that is enriched in fluid-immobile elements (e.g. La, Th). The geochemical signature of the slab component (either fluid, melt or something between this dichotomy) is ultimately transferred to arc magmas through mantle metasomatism and subsequent partial melting. Some high fluid-immobile element signatures of arc magmas can also be acquired in the crust by assimilation, although, in general this is a feature observed in evolved rocks. In Ecuador, some lavas are enriched in fluid-immobile elements and the origin of this geochemical signature is discussed between whether it is imparted by the slab or acquired in the continental crust. Both scenarios have good basis. On one hand, the subduction of a young oceanic crust in the Northern Ecuador (<20 Ma) could account for the addition of high-temperature fluids or melts to the mantle wedge. On the other hand, arc magmas have to traverse the thick continental crust (>50 km) where they could acquire such geochemical signature.

The aim of my work was to analyze the composition of melt inclusions hosted in rare high-forsterite ($Fo_{>80}$) olivines from high magnesium basaltic andesite and andesite lavas and tephras to assure the study of the most primitive magmas from the Ecuadorian volcanic arc. All melt inclusions were crystalized, therefore, I experimentally heated them to reverse post-entrapment crystallization. After homogenization, I analyzed major, trace and volatile elements in glassy melt inclusions and their compositions were corrected for post-entrapment modifications. At the beginning, I studied olivine-hosted melt inclusions from Puñalica and Sangay volcanoes located in the southern termination of the Andean Northern Volcanic Zone. Sangay and Puñalica melt inclusions were silica-poor and resulted from partial melting of silica-poor lithologies (i.e. amphibole-bearing clinopyroxenes). Also, Puñalica melt inclusions showed high chlorine content (or high Cl/F), a feature linked with the presence under Puñalica volcano of the highly altered oceanic crust associated with Grijalva fracture zone (GFZ). GFZ is an oceanic fracture that separates a young oceanic crust (<25 Ma) to the north from an older oceanic crust to the south (>31 Ma).

In the second part, I enlarged the study of olivine-hosted melt inclusion from volcanoes located in Northern Ecuador in order to cover the Ecuadorian volcanic arc from north to south. The analysis of this unique melt inclusions dataset showed an along-arc compositional variation of melt inclusions that could not be explained by crustal assimilation. However, the observed variation indicated the presence of a compositional change of the slab component. The cause of this change was explained by a change of the thermal regime along the subduction zone due to the different age of the slab. Despite the limited occurrence of high-forsterite olivine at the surface, this study shows that the trace element content of the most primitive melts from Ecuador vary considerably and that such variations depend mainly on the composition of the slab component

Résumé

Les magmas d'arcs héritent leur composition de trois réservoirs: la péridotite du coin mantellique, la croûte et la plaque plongeante. La contribution du manteau et de la plaque plongeante est déterminée par l'étude des magmas primitifs avant qu'ils interagissent fortement avec la croûte. La détermination de la signature de la plaque plongeante est importante car d'une part elle apporte les principales caractéristiques géochimiques des magmas d'arc, et d'autre part, elle peut apporter des contraintes sur le régime thermique présent le long des zones de subduction. Par exemple, les roches volcaniques primitives qui sont enrichies en éléments les plus facilement mobilisés par des fluides (par exemple Ba, Pb, B) sont liées à des zones de subduction « froides » où le composant de la plaque plongeante est censé être un fluide aqueux. Les zones de subduction plus « chaudes » favorisent l'apparition de fluides à température plus élevée ou des liquides silicatés qui sont caractérisés par une signature géochimique enrichie en éléments fluides-immobiles (par exemple La, Th). La signature géochimique du composant de la plaque plongeante (soit un fluide aqueux, soit un liquide silicaté ou plutôt quelque chose entre les deux) est finalement transférée aux magmas d'arcs par le métasomatisme du manteau et la fusion partielle qui s'ensuit. Une partie de la signature des éléments fluides-immobiles des magmas d'arcs peut également être acquise dans la croûte par assimilation de cette dernière, cependant cette caractéristique est généralement observée dans les roches plus évoluées. En Équateur, certaines laves sont enrichies en éléments fluides-immobiles et l'origine de cette signature géochimique demeure discutée. Est-ce qu'elle est transmise par le composant de la plaque plongeante ou acquise dans la croûte continentale ? Les deux scénarios reposent sur les arguments suivants : d'une part, la subduction d'une croûte océanique jeune dans le nord de l'Équateur (<20 Ma) pourrait expliquer l'ajout de fluides à haute température ou coin de manteau. D'autre part, les magmas d'arc doivent traverser l'épaisse croûte continentale (>50 km) où ils pourraient acquérir une telle signature géochimique.

L'objectif de mon travail était d'analyser la composition des inclusions vitreuses piègées dans des olivines à haute teneur en forstérite (Fo>80) provenant des laves et téphras de compositions andésite-basaltiques et andesitiques à haute teneur en magnésium. Ce choix permettrait d'assurer l'étude des magmas les plus primitifs de l'arc volcanique équatorien. Toutes les inclusions vitreuses étaient cristallisées, c'est pourquoi je les ai re-homogénéisées expérimentalement pour inverser la cristallisation post-piégeage. Après l'homogénéisation, j'ai analysé les éléments majeurs, traces et volatils dans les inclusions vitreuses et leurs compositions ont été corrigées pour tenir compte des modifications post-piégeage. J'ai tout d'abord étudié les inclusions vitreuses piégées dans des olivines des volcans Puñalica et Sangay, situés dans la terminaison sud de la zone volcanique des Andes du Nord. Les inclusions vitreuses du Sangay et du Puñalica étaient pauvres en silice et résultaient de la fusion partielle de lithologies tels que des clinopyroxènes contenant des amphiboles. De plus, les inclusions de Puñalica présentaient une teneur élevée en chlore (ou Cl/F), une caractéristique liée à la présence sous le volcan Puñalica de la croûte océanique très altérée associée à la zone de fracture de Grijalva (GFZ). La GFZ est une structure océanique qui sépare une croûte océanique jeune (<25 Ma) au nord d'une croûte océanique plus ancienne au sud (>31 Ma).

Ensuite, j'ai élargi l'étude des inclusions vitreuses piégées dans des olivines provenant des volcans situés au Nord de l'Équateur afin de couvrir l'arc volcanique équatorien du Nord au Sud. L'analyse de cet ensemble unique a montré une variation de la composition des inclusions le long de l'arc qui n'a pas pu être reproduite par une simple assimilation crustale, en revanche, ces variations géochimiques indiquent plutôt un changement de la composition du matériel provenant de la plaque plongeante. J'ai associé cette variation à un changement du régime thermique le long de la zone de subduction en raison de l'âge différent de la plaque plongeante. Malgré la présence limitée des olivines à haute teneur en forstérite à la surface, cette étude montre que la teneur en éléments traces des magmas les plus primitives de l'Équateur varie considérablement et que cette variation dépend principalement de la composition du composant de la plaque plongeante.

Table of content

Acknowledgments I

Abstract II

Résumé III

Preface 1

Background 1

Organization of the thesis 2

Chapter I: Overview of the Ecuadorian subduction zone 4

1.1 The subducting slab: age and structures 4

1.2 Thermal regime along subduction zones 6

1.2.1 Can the oceanic crust melt under Ecuador? 8

1.2.2 Dehydration and melting of sediments 10

1.3 Compositional characteristics of the slab metasomatic agent 12

1.4 Primitive melts in continental arcs 13

1.5 Review of the geochemistry of the Ecuadorian volcanic rocks 14

1.5.1 Across- and along-arc variation of trace elements in Ecuador 17

1.5.2 Across- and along-arc isotopic variations in Ecuador 17

1.6 Magma genesis under Ecuador: two scenarios 19

1.6.1 Scenario 1: slab melting and subsequent metasomatism of the mantle wedge 20

1.6.2 Scenario 2: the continental crust control magma composition 22

1.7 Scientific problem and approach 24

Chapter II: Olivine-hosted melt inclusions 26

2.1 An introduction to the study of olivine-hosted melt inclusions 26

2.2 Post-entrapment composition modifications 26

2.2.1 Magnesium and iron exchange 26

2.2.2 H_2O, CO_2, S, F, Cl modifications 29

2.2.3 Silica modification 31

2.2.4 REE and other trace element modifications 32

2.3 Corrections of post-entrapment modifications 33

2.3.1 Major element composition of melt inclusions 33

2.3.2 Water and CO_2 contained in bubbles 35

Chapter III: Analytical methods **37**
3.1 Melt inclusion preparation 37
3.2 Re-homogenization procedure 40
3.3 Electron probe microanalysis 42
3.3.1 Functioning principle 42
3.3.2 Analytical conditions 43
3.4 Laser Ablation-Inductively Coupled Plasma-Mass Spectrometer 44
3.4.1 Functioning principle 44
3.4.2 Analytical conditions 45
3.5 Secondary Ion Mass Spectrometer 47
3.5.1 Functioning principle 47
3.5.2 Analytical conditions 48

Chapter IV: Compositions of melt inclusions from Puñalica and Sangay volcanoes **50**
4.1 Background 50
4.2 Constraining magma sources using primitive olivine-hosted melt inclusions from Puñalica and Sangay volcanoes (Ecuador). Article published on the journal *Contribution to Mineralogy and Petrology*, 2018 51

Chapter V: Extended melt inclusion analysis from Ecuadorian volcanoes 77
5.1 Background 77
5.2 Two types of slab components under Ecuadorian volcanoes supported by primitive olivine-hosted melt inclusion study. Article under revision on the journal *Geochemistry, Geophysics, Geosystems*... 78
1 Introduction 81
2 General information on the Ecuadorian arc and sample descriptions 84
2.1 The Ecuadorian arc: geodynamic setting and geochemical summary 84
2.2 Sample locations 85
3 Methods 90
3.1 Olivine-hosted melt inclusion preparation 90
3.2 Analytical methods 90
4 Results 92
4.1 Major and trace elements 92
4.2 Volatile elements 102

5 Discussion 103
5.1 Assessment of post-entrapment modifications and entrapment pressure ...103
5.2 Composition of Ecuadorian primitive magmas 105
5.2.1 Melt inclusions represent the most primitive magmas beneath Ecuador 105
5.2.2 Clues for CLV melt inclusion source given by alkali and volatile elements 107
5.3 Mantle and slab contributions, the constraints from trace elements systematics 109
5.3.1 Mantle end-members and continental sediment contribution 109
5.3.2 Two types of slab components 111
5.3.3 Geochemical modelling of primitive melt inclusions 115
5.4 Geochemical signatures of melt inclusions in the geodynamic context of Ecuadorian continental arc 120
6 Conclusions.....123
Chapter VI: General conclusions and perspectives 125
6.1 General conclusions 125
6.2 Perspectives 126

References.....**128**
Annexes.....**156**

Preface

Background

The standard model of arc magma genesis considers that primitive magmas are produced by partial melting of the subarc peridotite due to volatile-rich material addition from the subducting slab (e.g. Ringwood, 1974; Pearce, 1982; Grove et al., 2002). The volatile-rich material, that results from dehydration and (or) melting reactions occurring in the sedimentary, basaltic and (or) mantellic layers of the subducting slab (e.g. Schmidt and Poli, 1998, 2014; Klimm et al, 2008, Walowski et al., 2015), carries the incompatible trace element arc signature to arc magmas (i.e. Ulmer, 2001; Kelemen et al., 2014; and many other before and after). From the subarc mantle to the surface, magmas change in their composition by crustal assimilation, mixing and (or) fractional crystallization (Hildreth and Moorbath, 1988; Sisson and Grove, 1993; Nandedkar et al., 2014) deriving wide range of magma composition observed around arc volcanoes.

In Ecuador, the role of the slab component in the arc magma composition is debated between, whether or not, the addition of hydrous siliceous melts from the slab is responsible of some geochemical indices such as: high La/Yb, Sr/Y or low Ba/Th. Some studies (e.g. Samaniego et al. 2010; Ancellin et al., 2017) consider that the subduction of the young oceanic crust (<25 Ma) north of Grijalva fracture zone (GFZ), which contains the even younger Carnegie ridge (<20 Ma), is warm enough for the subducting slab to melt and produce the observed geochemical features. However, other studies (e.g. Chiaradia et al. 2009; 2020) reproduce such geochemical characteristics of magmas with crustal processes (i.e. fractional crystallization, assimilation) which implies the addition of more common aqueous fluids from the slab due to dehydration reactions. This discussion has persisted during the last two decades because of a lack of primitive rocks, which has prevented geochemists from studying magmas that are little affected by crustal contamination.

The purpose of this work is to put a term to the controversy between slab melting and crustal assimilation in the source of Ecuadorian volcanoes. I analyzed the composition of the most primitive Ecuadorian melts, found in melt inclusions hosted in primitive olivines (Fo_{80-89}). This eliminated to some extent the crustal contribution and

allowed me to estimate the significance of the slab component to magma composition. The study of Ecuadorian primitive melt inclusions was previously initiated by Le Voyer et al. (2008) who selected two volcanoes from the Northern Ecuador (Rucu Pichincha and Pan de Azúcar). Here, I extended the study of primitive melt inclusions to other volcanoes from Northern and Central region, thus covering most of Ecuador's volcanic arc.

Organization of the thesis

I organized this thesis in 6 chapters. ***Chapter I*** is a synthesis of the literature data on the Ecuadorian arc. It presents the geodynamic setting of Ecuador and briefly describe the calculation of the thermal model for the Colombia-Ecuador subduction zone. In this chapter, I also cover the main mineral transformations that occur in the basaltic/sediment layer of the subducting slab, especially those with the potential to produce melts. Finally, I describe the geochemical variation along and across the volcanic arc in Ecuador and summarize the petrogenetic models for magma generation proposed for this arc.

Chapter II is about melt inclusions. It briefly covers examples of geological problems resolved by studying melt inclusions and describes the physical and chemical modifications experienced by the melt after being trapped inside olivine crystals. Also, at the end of the chapter, I discuss the different approaches to correct geochemical data of melt inclusions resulted from olivine-melt interactions, bubble formation and melt crystallization.

Chapter III describes the procedure for melt inclusion preparation and description of analytical methods. I mention the full procedure for melt inclusion selection and describe the laboratory heating procedure to re-melt crystalized melt inclusions (homogenization). Moreover, I described the analytical techniques used for major, trace and volatiles analysis of melt inclusions.

Chapter IV and ***V*** shows the main results obtained from this melt inclusion study in the form of two different papers. ***Chapter IV*** describes the composition of melt inclusions from Sangay and Puñalica volcanoes located in the southern termination of the Northern Andean volcanic zone. This chapter is a published paper in the journal *Contribution to Mineralogy and Petrology* (Narváez et al., 2018) and shows that the trace

and volatile element signatures of primitive melt inclusions depend on the composition of the material added from the slab and that their source lithologies are metasomatised-peridotites or cumulative amphibole-bearing clinopyroxenites.

Chapter V presents the compositions of primitive melt inclusions from three volcanoes located in the Northern Ecuador (Cotacachi, Cucilche, Cono de la Virgen) and two volcanoes from Central Ecuador (Conos de Licto, Sangay). This chapter is a form of a paper submitted to the journal *Geochemistry, Geophysics, Geosystems*. These results enlarged the melt inclusion data and used published data to show that the slab component varies north-south in Ecuador and respond to a change in the thermal regime along the subduction zone due to the presence of a younger oceanic crust north of Grijalva Fracture Zone.

Chapter VI summarizes the main conclusions of this work and addresses some perspective on this topic.

Chapter I

Overview of the Ecuadorian subduction zone

1.1 The subducting slab: age and structures

The Andean Northern Volcanic Zone (NVZ) results from the subduction of Nazca plate under the South-American plate. The limits of the Nazca plate are to the west the East Pacific Rise (EPR), to the north the Cocos-Nazca spreading center (CNSC) and to the south the Chile rise spreading center. The age of the Nazca plate varies from north to south and west to east due to the presence of EPR and CNSC. CNSC, that is oriented west-east, initiated its activity after the split of Farallon plate into Nazca and Cocos (23 Ma ago; Lonsdale, 2005). The evidence of the Farallon splitting is the Grijalva fracture zone (GFZ, Fig. 1.1) which enters in subduction in front of the Guayaquil gulf (central Ecuador). GFZ consists of a 500 m-high escarpment that separates the older oceanic crust created along the EPR to the south, from the younger oceanic crust created along the CNSC to the north. The age difference between these two crusts is at least ~9 Ma near the trench (22 Ma in the north compared to 31 Ma in the south, Fig. 1.1) and the age difference is certainly greater along the subducted part where the oceanic crust south of GFZ must be even older. A contrasting density and buoyancy (mostly related to the age difference) of the subducting slab north and south of GFZ is, according to Yepes et al. (2016), responsible for a slab flexure around of GFZ.

The slab flexure model for Ecuador is a new concept that differ from a previous idea which supposed that the slab was torn along GFZ with the northern slab slice plunging at a shallower angle compared to the southern part (Gutscher et al., 1999). However, the principal geochemical evidence against the slab tear model is, accordingly to Yepes et al. (2016), the absence of adakitic magmas along the projected edge on the surface of the slab tear. The generation of adakites in the slab tear model occur when deeper and hotter mantle is in contact with the oceanic lithosphere along the slab tear (or slab window) allowing the lithosphere to melt (i.e. Johnston and Thorkelson, 1997). The

slab tear model along GFZ was recently called up by Rosenbaum et al. (2018) to explain the geochemical composition of Sumaco volcano that is the easternmost volcano of Ecuador.

In addition to the contrasting age of the subducted slab on both sides of GFZ, the even younger Carnegie ridge that is located north of GFZ also subducts in front of the Ecuadorian arc (Fig. 1.1). Carnegie ridge is an aseismic ridge that resulted from the eruptive activity of the Galápagos hotspot (Sallarès and Charvis, 2003). This ridge is located between 0.5°N and 1.5°S and reach 2000 m elevation from the seafloor. From Fig. 1.1, the oceanic crust over which the Carnegie ridge is built is younger than 20 Ma old (magnetic lineation number 6) and, therefore, the ridge must be younger than this age. The subduction of Carnegie ridge for at least the last 6-8 Ma (Gutscher et al., 1999; Michaud et al., 2009; Collot et al., 2019), is probably responsible for the lack of intermediate seismicity (>50 km; Guillier et al., 2001; Yepes et al., 2016) along the subduction interface. This mostly aseismic subduction of Carnegie ridge makes it difficult to assess the subduction angle under Ecuador, which could vary from almost 0° (flat subduction, Gutscher et al., 1999) to 20-35° (Guillier et al., 2001; Yepes et al., 2016).

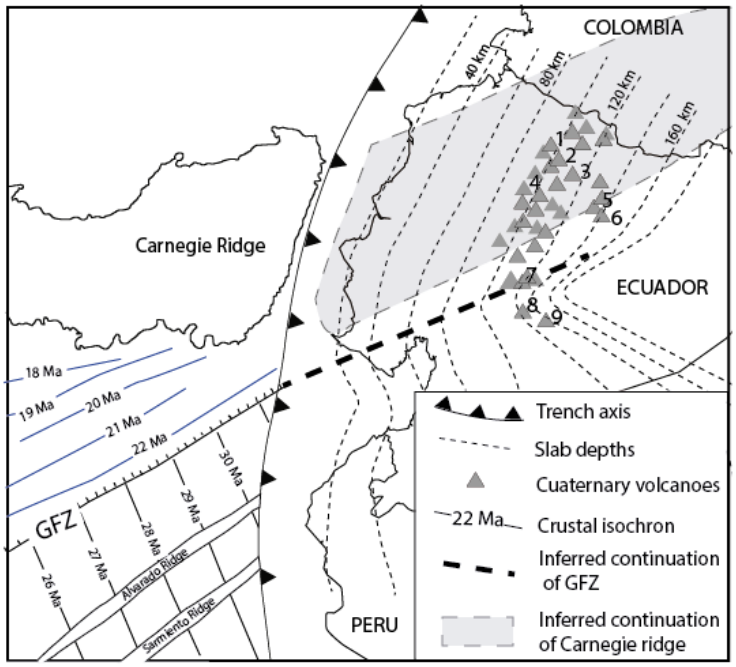

Fig. 1.1 Schematic map showing slab depths and quaternary volcanoes in Ecuador after Yepes et al. (2016). Also shown magnetic lineation and age interpretations of the oceanic crust below water (crustal isochron) after Lonsdale (2005). The oceanic crust gets older toward the south when it was formed from CNSC (blue crustal isochron) and toward the east when it was created in the EPR (black crustal isochron).GFZ stands for Grijalva fracture zone. Inferred continuation of Carnegie ridge from Gutscher et al. (1999). Labelled volcanoes are: 1. Cotacachi; 2. Cubilche; 3. Cono de la Virgen; 4. Rucu Pichincha; 5. Pan de Azúcar; 6. Sumaco; 7. Puñalica; 8. Conos de Licto; 9. Sangay.

1.2. Thermal regime along subduction zones

The thermal regime along subduction zones is defined as the pressure and temperature conditions at which the slab (measured along the plate interface) subducts. The exact values of the thermal regime are difficult to define but some approaches to calculate them are proposed in the literature and discussed by van Keken et al. (2019). In general, the thermal regime depends on known parameters such as: subduction rate, dip angle and age of the subducting slab. Furthermore, many of these thermal models are solved in 2-D grid and their boundary conditions and the consideration of the third dimension have strong influence to the final solution (Honda et al., 2010; Wada et al., 2015). Other parameters that are unknown induce the main disparities between models, such as for example, the rheology and its temperature dependence of the metasomatised mantle wedge or the shear heating along the plate interface. Syracuse et al. (2010) modeled 56 sections of subduction zones around the world including that of Colombia-Ecuador, which allow us to compare it among other subduction zones. This 2D model resolves heat advection-diffusion equations assuming that the flow in the mantle wedge is only driven by the kinetic velocity of the slab. The thermal regime calculated with this model is time-dependent, therefore, the results observed in Fig. 1.2 (taken from Syracuse et al., 2010) represent a period of 20 Ma when the model reaches a near steady state thermal structure. For mantle viscosity, they used the temperature- and stress-dependent model of Karato and Wu (1993) for dry peridotite. This, compared to iso-viscous models (i.e. Peacock and Wang, 1999), gives higher temperatures along the slab surface. The movement between the subducting slab and the mantle are considered to move independently before reaching 80 km depth and to move together after this depth (the so-called model D80). The full coupling between slab-wedge interface after 80 km is the main reason for a steep temperature increase at this depth (see flattening gradient at ~2 GPa in Fig. 1.2). For Colombia-Ecuador segment in this study, the slab geometry is defined as: slab dip, 28°; subduction rate, 60 km/Ma and sediment thickness, 1.8 km. The results show that the thermal regime in Colombia-Ecuador is among the hottest of the world with only three profiles hotter (i.e. Central, North Cascadia and Mexico). It should be noted that this model represents the thermal regime in the Northern Ecuador where the young oceanic crust north of GFZ subducts and that the subduction of the old oceanic crust south of GFZ (>30Ma, Lonsdale, 2005) should render lower temperatures.

It is worth to say that Syracuse et al. (2010) proposed other models to calculate the thermal regime of subduction zones which yield completely different results for Colombia-Ecuador subduction zone. For example, their W1300 model, which sets the maximum mantle wedge temperature beneath the volcanic front as 1300°C, results in much lower temperature for the range 2.5-5 GPa (Fig. 1.2). The model W1300, as well as the X25 model (where the boundary between the partial and full coupling occurs 25 km trenchwards of the arc) are not representative of the Ecuador segment. While their results are constrained on the location of the arc, the placement for the Colombia-Ecuador segment is based on the location of volcanoes in Colombia. The study defines the depth to the top of the slab (*H*) under the arc at 155 km (or 305 km away from the trench). This, in reality, corresponds to the location of volcanoes at 50 km east of the actual volcanic front on the Eastern cordillera in Ecuador.

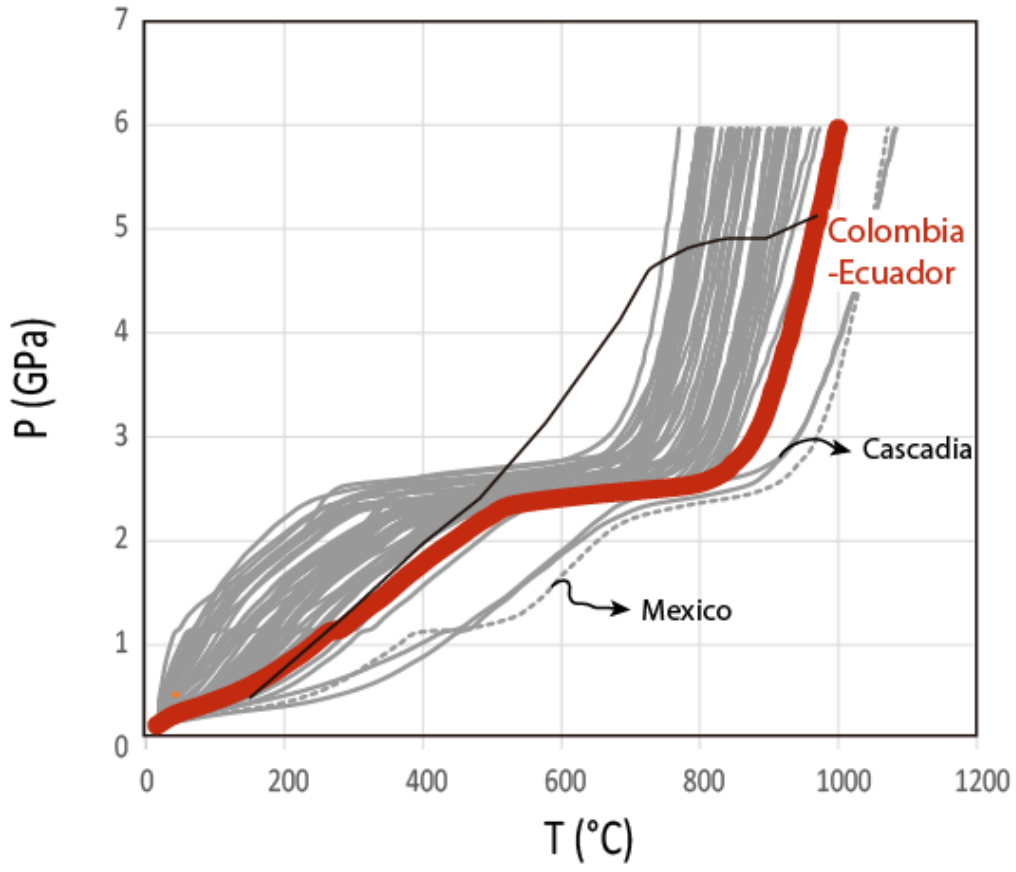

Fig. 1.2. Pressure-temperature paths of the slab surface taken from Syracuse et al. (2010) corresponding to the model D80. Thick red line is the P-T path along the Benioff plane calculated for Colombia-Ecuador subduction zone. Continuous black line corresponds to results of W1300 model for Colombia-Ecuador subduction zone.

1.2.1. Can the oceanic crust melt under Ecuador?

The oceanic lithosphere increases its temperature as it enters in subduction promoting dehydration reactions in the sedimentary, basaltic and (or) mantle layers (e.g. Schmidt and Poli, 1998, 2014; van Keken et al., 2011; Walowski et al., 2015). The fluid addition from the slab to the mantle wedge allow the peridotite to melt in a process that is known as volatile-rich flux melting (Grove et al., 2002). The addition of water to the mantle wedge is a continuous process that occurs due to several continuous and discontinuous reactions that destabilize the hydrated minerals present at the slab, such as: lawsonite, epidote/zoisite, chloritoid, talc, amphibole and muscovite/phengite (Schmidt and Poli, 1998). For example, in hot subduction zones (high temperature end of gray zone in Fig. 1.3a), MORB is dominated by greenschist-facies assemblage (with hydrous minerals such as: chlorite, zoisite and amphibole) at the beginning of the subduction and evolves toward blueschist (chlorite, amphibole, phengite, lawsonite), amphibole-eclogite (glaucophane) and dry eclogite facies. The breakdowns of these hydrous minerals at higher P-T are responsible of water release in subduction zones. On the contrary, in cold subduction zones (the lower temperature end of gray field in Fig. 1.3a), lawsonite, chloritoid (Ctd) and phengite are the principal hydrous minerals that cloud be destabilized at depth producing water-rich fluids and MORB is dominated by blueschist- and eclogite-facies assemblage. Some of the hydrous minerals mentioned above are more or less abundant depending on the MORB composition, for example, the higher K content in MORB could readily stabilize phengite (Schmidt et al., 2004).

If the temperature along the subduction zone is high enough for the slab to melt, a hydrous siliceous melt is added to the mantle wedge. It should also be noted that the temperature at which MORB melts depends on its composition and pressure it reaches. The principal factor is water content, thus, when the rock is fluid-saturated the temperature of melting is minimum (red line Fig. 1.3b) while it is maximum for dry conditions (solidus increase by ~250°C). Schmidt and Poli (2014) argued that the continuous dehydration of mineral could move the system towards saturated conditions if the fluid does not escape, therefore, the melting could start at low temperature boundary. The solidus also increases with pressure, thus, at fluid saturation conditions and 2.5 GPa, the solidus is at 750°C (Poli and Schmidt, 1998) while at 5 GPa it is at 1000°C (Kessel et al., 2005b). Under fluid-absent conditions and pressure relevant for

subduction zones (1-2.5 GPa), the two hydrous phases that generate the first melts are amphibole and epidote/zoisite through the reaction amp + zo + qz = grt + melt (±cpz) until zoisite disappears, then only amphibole reacts through the reaction amp + qz = grt + cpx + melt (Vielzeuf and Schmidt, 2001). Fig. 1.4 show the P-T path along Colombia-Ecuador subduction zone and MORB solidus obtained from experimental petrology. This figure shows that the temperature along the subduction zone in Colombia-Ecuador (in red) is high enough to allow MORB to melt.

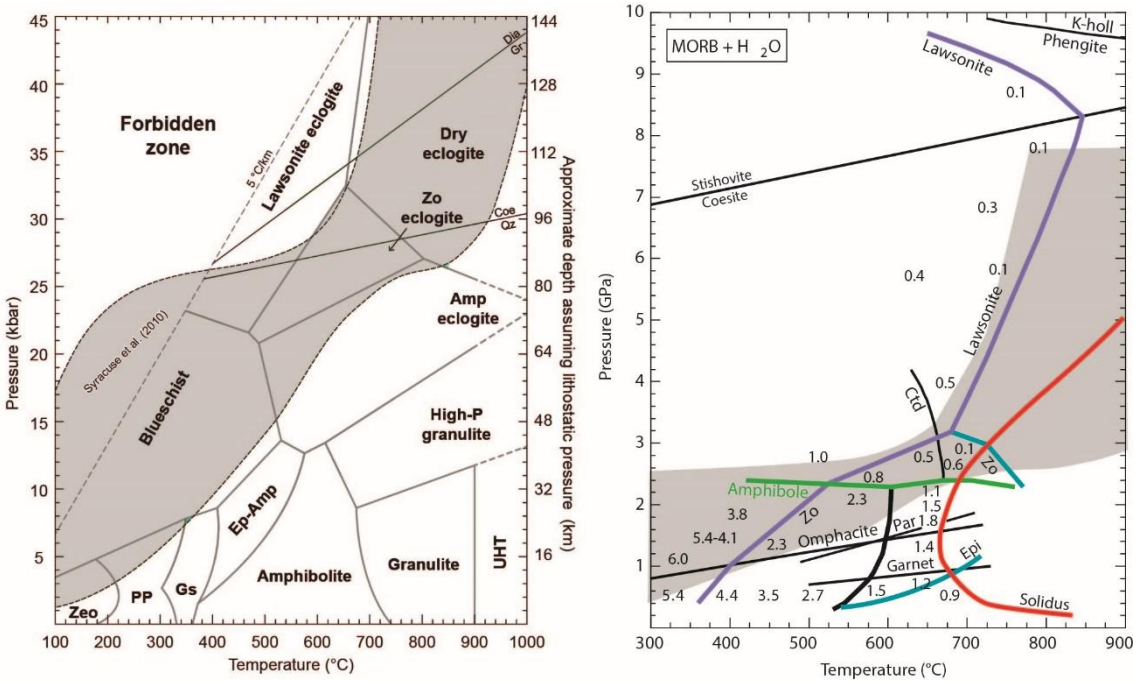

Fig. 1.3. **(a)** Pressure-temperature diagram showing metamorphic facies modified from Hernández-Uribe and Palin (2019). Gray field is the P-T paths along subduction zones from Syracuse et al. (2010). **(b)** Major phase stability boundaries in H_2O-saturated MORB and water content (numbers besides colored lines in wt.%) stored in hydrous phases. Modified from Schmidt and Poli (1998, 2014).

More recently, Hernández-Uribe et al. (2019) argued that melting of MORB is not common along subduction zones after defining the solidus of MORB to be at higher temperatures than previously calculated by experimental petrology (Fig. 1.4). In Hernández-Uribe et al. (2019) work, the authors used Theriak-Domino thermodynamic software (de Capitani and Brown, 1987) updated with more recently published activity–composition models for common minerals in metabasic rock types and water saturated conditions. The higher solidus temperatures obtained by Hernández-Uribe et al. (2019) are problematic because thermodynamic models should reproduce experimental results or being calibrated to reproduce them. In fact, experimental petrology has shown that the solidus could move to higher temperature, for example, when the initial material has

lower wt.% K_2O (Kessel et al., 2005b; Carter et al., 2015) or when the oxygen fugacity is higher during the experiments (Martin and Hermann, 2018). However, none of those experiments (results shown in Fig. 1.4) have rendered temperatures as high as those calculated by Hernández-Uribe et al. (2019).

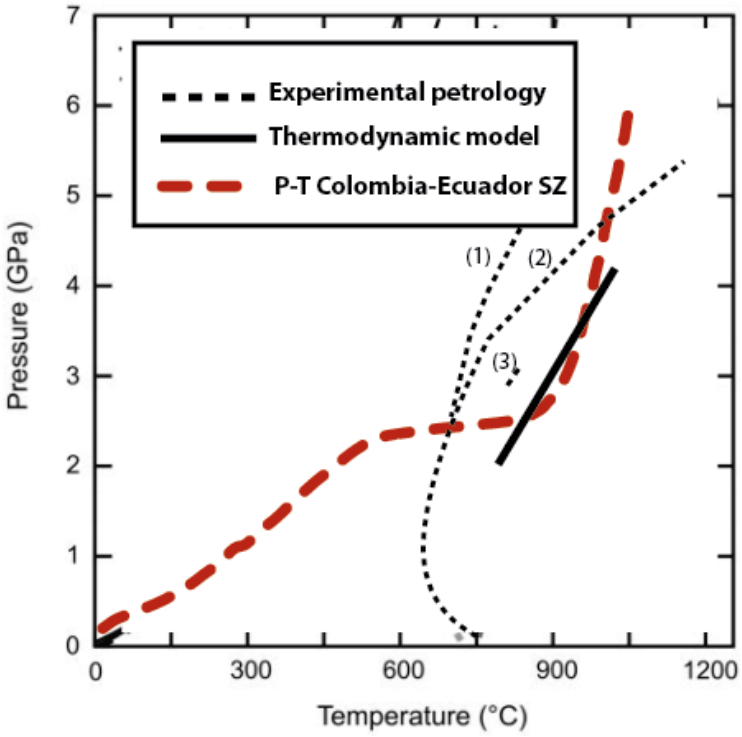

Fig. 1.4. Comparison between solidus determined by experimental petrology and thermodynamic model for MORB at fluid-saturated conditions. Experimental petrology solidus are from (1) Klimm et al. (2008) based on Poli and Schmidt (1998) and Kessel et al. (2005b); (2) Martin and Hermann (2018) and (3) Carter et al. (2015). The thermodynamic model solidus is from Hernández-Uribe et al. (2019). P-T paths along Colombia-Ecuador subduction zone from Syracuse et al. (2010).

1.2.2. Dehydration and melting of sediments

The nature and composition of sediments that enter in subduction around the globe is variable (*cf.* Plank and Langmuir, 1998; Dutkiewicz et al., 2015). For instance, sediments on the oceanic floor are divided in siliciclastic (e.g. sand, clay), volcanoclastic and biogenetic (e.g. calcareous-, radiolarian-ooze). The metamorphism along subduction zones of most common siliciclastic clay sediments (also known as pelites) stabilize some hydrous minerals as for example chlorite, chloritoid, talc, phengite and biotite and their disappearance outside their stability field release water that is added to the mantle wedge. The contribution of sediments to the total amount of water released by the slab is low, for

instance, Schmidt and Poli (2014) calculated that during subduction from 20-80 km, a 300 m-thick mica-schist contribute only with 2-6% of the total mass of water released from 2 km of underlying, fully-hydrated MORB. However, pelites play an important role in the addition of K and some minor and trace elements (i.e. Zr, Nb, Ta, La, Th) to the mantle wedge, because some accessory phases (rutile, allanite, monazite, zircon) enriched in these elements are present in pelites (e.g. Klimm et al., 2008; Hermann and Rubatto, 2009; Skora and Blundy, 2010).

The melting of subducted sediments is probably more common compared to MORB, because sediments are exposed to the highest temperatures along the subduction zone (temperature decrease from the slab-mantle interface toward the inner part of the slab), because melting likely occur under fluid-saturated conditions due to the water addition from underlying basaltic and peridotitic lithologies (Hermann and Rubatto, 2009) and because at fixed pressure, solidus sediment temperature is lower (Fig. 1.5). The melting temperature of wet pelites is 720°C at 2.5 GPa and increase to 800°C at 4.5 GPa (Fig. 1.5). Additionally, pelites melt proportion above the solidus increase sharply with temperature, for instance at 2.5 GPa, 35% of melt is produced 50°C above solidus (Hermann and Spandler, 2008). The first melts in pelites at pressure <2.5 GPa is produced through muscovite (phengite) and biotite breakdown until muscovite is exhausted, then biotite is the main hydrous phase that control melting (Vielzeuf and Schmidt, 2001; Schmidt et al., 2004). At higher pressure, biotite is no longer stable and melt is produced through phengite (Schmidt et al., 2004).

The metamorphism of graywackes and volcanoclastic sediments along subduction zones can be seen as intermediate between pelites and MORB, that is stabilizing similar mineral assemblages but in different proportions. The similar mineral assemblage would allow the rock to dehydrate or melt at comparable temperatures between that of pelites and MORB (Schmidt and Poli, 2014).

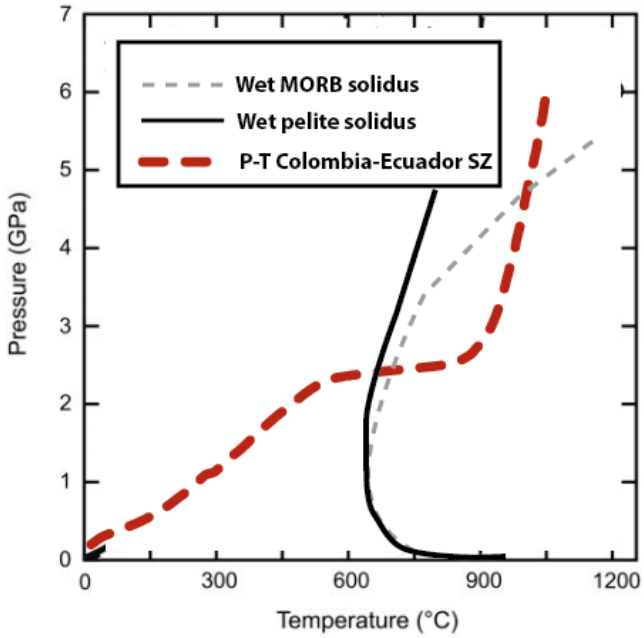

Fig. 1.5. Position of the wet pelite solidus (Nichols et al., 1994; Hermann and Spandler, 2008) compared to that of wet MORB (Klimm et al., 2008). Geotherm of Colombia-Ecuador subduction zone from Syracuse et al. (2010).

1.3. Compositional characteristics of the slab metasomatic agent

Metamorphic dehydration reactions produce water-rich, low-density fluid (i.e. aqueous fluids) at low pressure and low temperature (below the wet solidus) and change to high-density, hydrous silicate melt (or hydrous siliceous melt) when the temperature exceed the wet solidus. Aqueous fluids and hydrous siliceous melts produced in subduction zones have different physical (e.g. viscosity, compressibility) and chemical properties (e.g. composition). For instance, aqueous fluids are characterized by an enrichment in large-ion fluid-mobile lithophile elements (LILE, e.g., Rb, Ba, Sr), while hydrous siliceous melts are relatively enriched in so-called fluid immobile elements than aqueous fluid, such as light rare earth elements (e.g., La, Ce, Nd), high-field-strength elements (HFSE, e.g., Nb, Zr), as well as Th (Kessel et al., 2005a). In general, the concentration of trace elements in melts is higher than in aqueous fluids showing that hydrous siliceous melts are more efficient to move trace elements from the slab to the mantle wedge (Hermann and Rubatto, 2009). Such enrichment is related to a change of the bulk partition coefficient $D^{fluid/solid}$ (Fig. 1.6) with temperature and pressure. For example, the mobility of LREE ($D_{LREE}^{fluid/solid}$) in aqueous fluids is <1 at 700-800°C but

greater than 1 in melts at 1000°C (Fig. 1.6a). Thus, aqueous fluids would have lower concentration of LREE than hydrous siliceous melts. This characteristic is exploited in the literature to discriminate materials added from the subducted slab. Thus, volcanic rocks with high values of fluid-mobile over fluid-immobile elements (e.g. Ba/Th, Pb/Ce) are linked to aqueous fluids while the contrary is attributed to melts (e.g. Elliot et al., 1997; Elliot, 2003; Kelemen et al., 2004; Labanieh et al., 2012).

At high pressure, above the second critical end point, the distinction between fluids and melts no longer exist because the solubilities of H_2O in melts and silicate in fluids both increase and a chemical continuum between fluids and melt is possible (Schmidt and Poli, 2014). This single phase field above second critical point is called supercritical fluids, and occurs over a limited range of temperature. The second critical end point is located between 3.4-6 GPa in MORB, graywackes and pelites (Schmidt et al, 2004; Mibe et al., 2011).

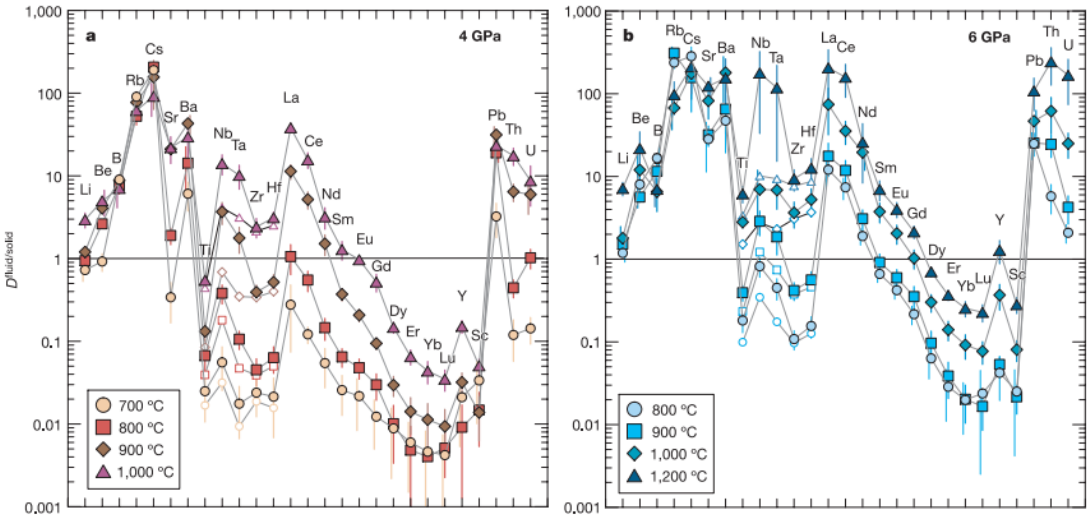

Fig. 1.6. Experimental fluid-solid partition coefficient for average MORB. (a) Aqueous fluid (700-900°C) and hydrous siliceous melt (1000°C) at 4 GPa. (b) Aqueous-fluid or hydrous siliceous melt at 6 GPa. Taken from Kessel et al. (2005a).

1.4. Primitive melts in continental arcs

Schmidt and Jagoutz (2017) have defined 5 types of primitive compositions in continental arcs: (1) tholeiitic arc basalts, (2) calc-alkaline basalts, (3) calc-alkaline andesites, (4) primitive shoshonites and (5) low-silica basalts. This work used an extensive database of rocks with Mg# of 65-75 (Mg# defined as 100*molar

(MgO/(MgO+FeO_T) in equilibrium with Fo_{86-91} olivines (calculated from the rock composition) and included Ecuadorian samples from Puyo cones and Calpi volcano. Tholeiitic arc basalts are formed by decompression melting driven by corner flow in the mantle wedge while the addition of the water rich component produce calc-alkaline basalts and andesites through porous flow flux melting (Grove et al., 2002). Primitive K-rich rocks (shoshonites) are likely formed from phlogopite-bearing lithologies (pyroxenites, harzburgite or lherzolite) located in the mantle (Foley, 1992; Luhr, 1997; Condamine and Médard, 2014, Condamine et al., 2016). Finally, low-silica basalts mostly recognized in olivine-hosted melt inclusions result from the melting of amphibole-bearing clinopyroxenites (Médard et al., 2006; Sorbadère et al., 2013a). All primitive arc melts are variably enriched in LILE, LREE and depleted in HFSE, HREE compared to MORB. As a whole, this signature is known as the incompatible trace element arc signature which is imparted by the slab component to the mantle wedge.

1.5. Review of the geochemistry of the Ecuadorian volcanic rocks

The geometry of the volcanic arc and the density of volcanoes in the Andean Northern Volcanic Zone varies from North to South. In Colombia the volcanic arc is 40-50 km width while in Ecuador the arc is broader (~120 km) and shows more than 80 Quaternary volcanic centers in this country (Hall et al., 2008). The widening of the arc occurs in front of the Carnegie ridge that subducts under Ecuador (Fig. 1.1). It is, therefore, probably that the change of subducting parameters, especially the lower angle of subduction and the higher thermal regime, are the responsible for the widening of the arc and higher number of volcanoes in Ecuador (i.e. Gutscher et al. 2000; Bourdon et al., 2003).

In Ecuador, volcanoes are distributed along four groups/alignments based on their location with respect to the two principal mountain ranges (Fig. 1.7b). The frontal and the main arc groups roughly correspond to volcanoes located above the Western and Eastern Cordilleras, respectively. Volcanoes from the frontal arc lie upon Meso-Cenozoic volcanic and sedimentary rocks of oceanic affinity (Jaillard et al., 2008; Vallejo et al., 2009), while those from the main arc are built over a continental-like crust that consists of felsic and intermediate igneous and metamorphic rocks (Aspden and Litherland, 1992;

Pratt et al., 2005). The third group corresponds to the volcanoes of the Inter-Andean valley, which are constructed above Miocene and Pliocene volcanic and sedimentary rocks (Winkler et al., 2005). Finally, a few scarce volcanoes that are further east constitute the Sub-Andean zone group, and are located in the upper Amazon basin.

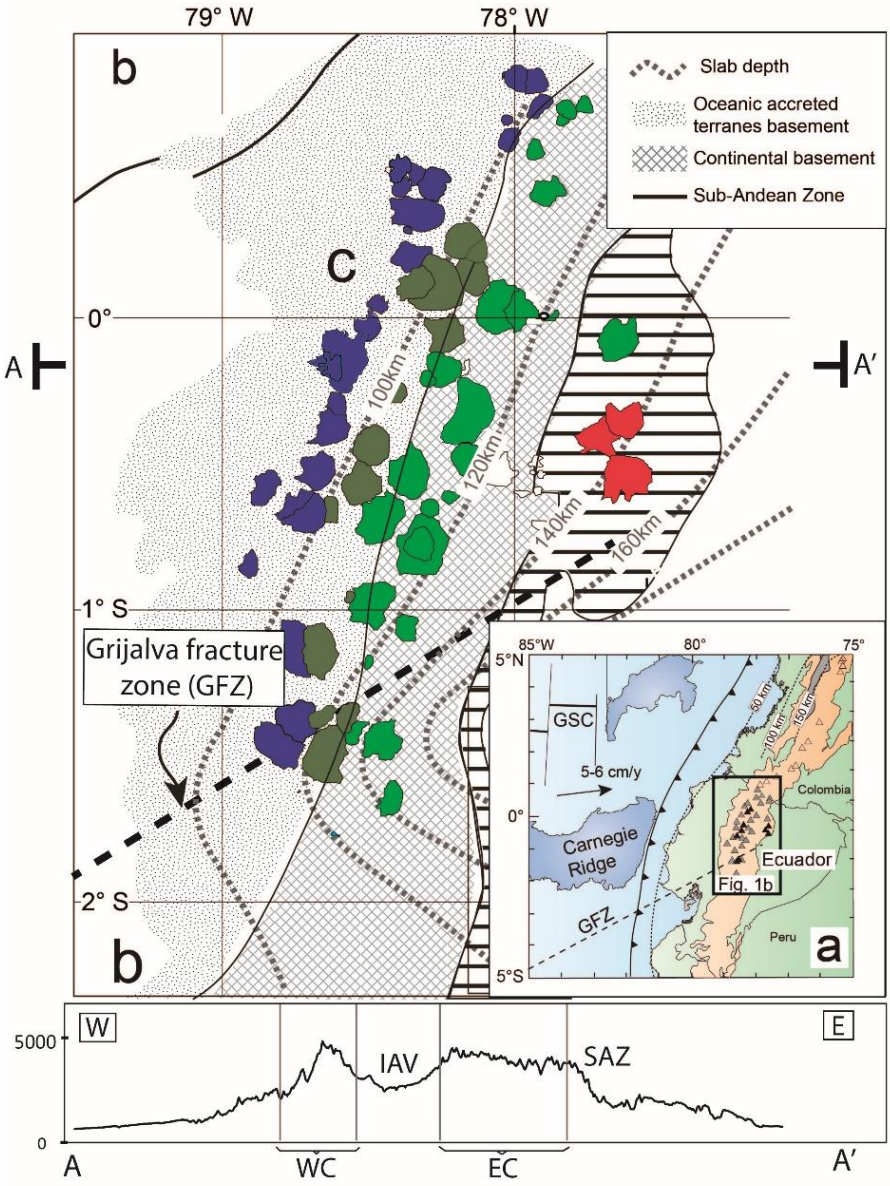

Fig. 1.7 (a) Geodynamic setting of Ecuadorian arc. **(b)** Schematic map of the main geological units in Ecuador [modified from Jaillard et al., (2008)] showing quaternary volcano locations. Volcanoes are divided in four groups: (1) volcanoes from Western Cordillera (blue), (2) from the Inter-Andean valley (dark green), (3) from the Eastern Cordillera (green) and (4) from the Sub-Andean zone (red). The dashed black line is the surface projection of the Grijalva fracture zone (GFZ). Slab depth contours are from Yepes et al. (2016). A-A' is a topographic profile across Fig. 1.7b. WC: Western Cordillera. IAV: Inter-Andean valley. EC: Eastern Cordillera. SAZ: Sub-Andean zone.

In general, volcanic rocks from Ecuador show silica content between 52-76 wt.% and belong to the calc-alkaline series. The most common phenocrysts are plagioclase, orthopyroxene, clinopyroxene, and amphibole, with biotite and some rare quartz present in more evolved rocks and olivine in the mafic end-members (Hall et al., 2008). Few volcanoes (e.g. Sumaco, Pan de Azucar,. Puyo) from the Sub-Andean zone group have emitted shoshonitic lavas that are, in general, silica-poor (42-50 wt.%) and composed of Na-pyroxene, plagioclases and less commonly olivine, haüyne and phlogopite (Bourdon, et al., 2003; Garrison et al., 2018; Hoffer et al., 2008). High-forsterite olivines ($Fo_{>80}$), which are the target of this study, are scarce and their occurrence is restricted to also rare basaltic and andesitic primitive rocks (Mg#>55). The lack of primitive rocks at the surface is probably due to the thick crust over with Ecuadorian volcanoes are constructed (>50 km, i.e. Vaca et al., 2019) which acts as barrier for the primitive magmas reaching to the surface. Once formed, mantle magmas move upwards due to their higher buoyancy and lower density than surrounding rocks. Such magmas stagnate somewhere between the upper mantle and the middle crust where they reach a level of neutral buoyancy with continental rocks (e.g. Lister and Kerr, 1991; Putirka et al., 2017). At this level, magma can evolve toward silica rich compositions trough assimilation, fractional crystallization and mixing (e.g. Hildreth and Moorbath, 1988; Annen et al., 2006) and lose its primitive signatures. Only few batches of primitive magma which are probably richer in volatiles and less crystalized find the way to the surface.

Except for lavas from the back arc, only one primitive calc-alkaline basalt (Fig. 1.9; SAN20B) is reported in Ecuador. Monzier et al. (1999) concluded that SAN20B (SiO_2 = 50 wt.% and Mg# = 69.0) came from a mantle metasomatised by aqueous fluids. This sample contains olivines of high forsterite content (Fo_{87-89}; defined as molar 100*Mg/(Mg+Fe)) and CaO (0.13 wt.% ±0.04) close to that of mantle olivines (Fo>91 and CaO<0.17; Putirka et al., 2007). Most common calc-alkaline basaltic andesites and andesites with Mg#>65 (10 samples from Puñalica, Calpi and Almas Santas volcanoes in Ancellin et al., 2017 dataset) have not been studied in detail and their detailed origin is not constrained.

1.5.1. Across- and along-arc variation of trace elements in Ecuador

One of the most important geochemical characteristic of this arc is an increase in incompatible trace elements (e.g. Ba, Nb, Rb, Th) further from the trench accompanied by a decrease in LILE over HFSE ratios (i.e. B/Nb, B/Be). This scatter is conventionally interpreted as resulting from a decrease in the amount of fluids added into the sub-arc mantle from the subducting slab and consequently, a decrease of mantle melting (Barragan et al., 1998; Bryant et al., 2006; Hidalgo et al., 2012). Another geochemical feature of this arc is the north-south (along-arc) variation described in volcanoes from the volcanic front, principally the increase of Th, Nd, Sm, Nb and the decrease of Ba/Th away from 0° latitude. These geochemical characteristics have been associated with a change in the slab component composition (Ancellin et al., 2017), or with a distinctive depth of magma-crust interactions (Chiaradia et al., 2020).

More localized, yet important, geochemical signature in some volcanic edifices is the high Sr/Y and La/Yb that is referred to as the adakitic-signature. Some volcanoes with reported adakitic signatures are: Antisana (Bourdon et al., 2002), Mojanda-Fuya-Fuya (Robin et al., 2009), Cayambe volcanic complex (Samaniego et al., 2005), Atacazo-Ninahuilca (Hidalgo, 2006), Imbabura (Bryant et al., 2006), Illiniza volcanic complex (Hidalgo et al., 2007), Yanaurcu (Béguelin et al., 2015), and Chachimbiro (Bellver-Baca et al, 2019) located on Northern Ecuador. This characteristic has been explained by either the addition of hydrous siliceous melts from the slab or by fractional crystallization or/and magma assimilation outside the stability field of plagioclase and within that of garnet.

1.5.2. Across- and along-arc isotopic variations in Ecuador

Similarly to trace elements, Sr-Nd and Pb isotopes studies show E-W (across-arc) geochemical variations, especially when comparing volcanoes from the Western and Eastern Cordilleras. Volcanoes from the Eastern Cordillera show the highest Sr isotopic compositions and the lowest $^{143}Nd/^{144}Nd$ values (Bourdon et al., 2003; Bryant et al., 2006; Hidalgo et al., 2012; Ancellin et al., 2017). The contrary is true for volcanoes located above the Western Cordillera that show the highest Nd isotopic compositions and the lowest $^{87}Sr/^{86}Sr$ (Fig. 1.8). Lavas from the Inter-Andean valley and back-arc have Sr and

Nd isotopic signatures more similar to those of the volcanic front (or Western Cordillera), although they are built over the bed rocks of a distinctive composition, which suggest that the upper crust is not a major contribution to the magma composition. Lead-isotopes distribution in the arc are more complex because they show not only an across-arc, but also an along arc (N-S) variation. For example, southern volcanoes of the volcanic front have similar $^{206}Pb/^{204}Pb$ and $^{207}Pb/^{204}Pb$ to volcanoes from the Eastern Cordillera.

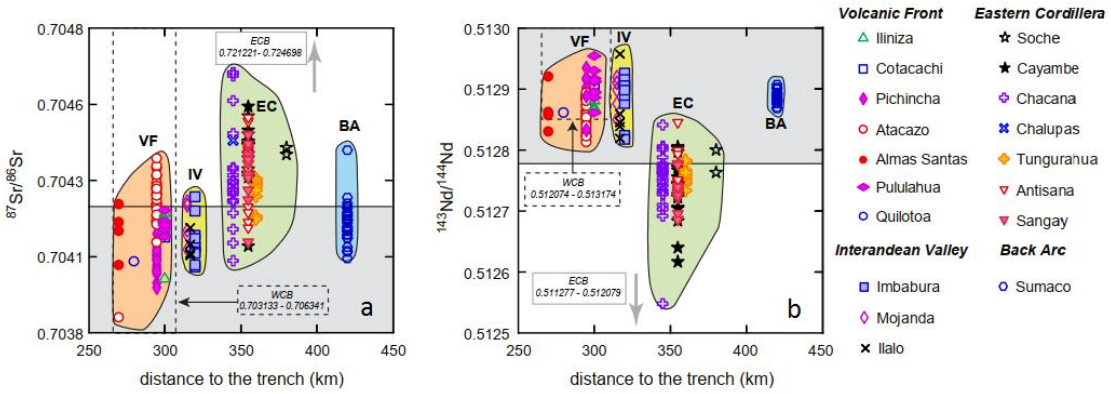

Fig. 1.8. $^{87}Sr/^{86}Sr$ and $^{143}Nd/^{144}Nd$ versus the distance to the trench of quaternary Ecuadorian lavas. Volcanic front are volcanoes located over the Western Cordillera. Taken from Hidalgo et al. (2012).

The crustal assimilation of Ecuadorian lavas has been evaluated by means of O and Pb isotopes. Hidalgo et al. (2012) used O isotopes and concluded that the crustal assimilation in lavas from Western and Eastern Cordilleras were similar (6-13 vol.% and 7-14 vol.% for lavas above Western and Eastern Cordilleras, respectively). Using lead isotopes, Ancellin et al. (2017) obtained similar values than Hidalgo et al. (2012) for lavas from the Western Cordillera (3-14 vol.%) and higher values for those from Eastern Cordillera (up to 27 vol.%) and proposed that the main assimilating material was the lower crust. Ancellin et al. (2017) also recognize a N-S variation of $^{206}Pb/^{204}Pb$, $^{207}Pb/^{204}Pb$ and Ba/Th in volcanoes front the frontal arc. Ancellin et al. (2017) concluded that an increase of $^{207}Pb/^{204}Pb$ toward the south was correlated with an increase in lower crustal assimilation, whereas an increase in $^{206}Pb/^{204}Pb$ accompanied by low Ba/Th observed further from 0.5S latitude was due to a change in the slab component (fluids close to 0.5ºS and melts away from it).

1.6. Magma genesis under Ecuador: two scenarios

In the literature, there are two models to explain the geochemical signatures described above. Both models agree that the decrease of slab component further from the trench, and subsequent lower degree of mantle melting, is the responsible for W-E geochemical zonation. However, some key trace elements indices (low Ba/Th, high La/Yb, Sr/Y) have been interpreted as either related to deep slab and mantle processes or conversely to shallower crustal processes. The two petrogenetic models are fully described in the following two sections. In simple words, one of them considers that hydrous siliceous melts from the slab can be added to the mantle wedge imparting the mentioned geochemical features while the other considers that such geochemical characteristics are acquired in the crust through fractional crystallization, magma assimilation and mixing. This controversy has lasted for the last two decades and the lack of primitive magmas is to blame. In fact, only one primitive basaltic rock (Mg#=70, defined as molar $100*Mg/(Mg+Fe^{T})$) from Sangay volcano (SAN20B) has been reported. Most of the Quaternary rocks, except for those from volcanoes of the back-arc, typically display silica contents higher than 52 wt.% and Mg# <65 (Fig. 1.9). Therefore and because geochemists do not have access to primitive magma composition, they would assume its composition conveniently in order to satisfy their preferred petrogenetic model. For instance, Chiaradia et al. (2009, 2020) assumed that the sub-arc mantle-derived melt composition is that of an island arc basalt (e.g. Kelemen et al., 2004) produced from the melting of a mantle metasomatised with aqueous fluids. Therefore, any trace element enrichment of Ecuadorian lavas with respect to the preferred composition is assumed to be acquired in the crust. However, primitive rocks in arcs have variable trace element composition that indicate their source is metasomatised not only by aqueous fluid but also by hydrous siliceous melts and/or supercritical fluids (e.g. Kelemen et al., 2004; Plank, 2005; Schmidt and Jagoutz, 2017), therefore entangling their origin.

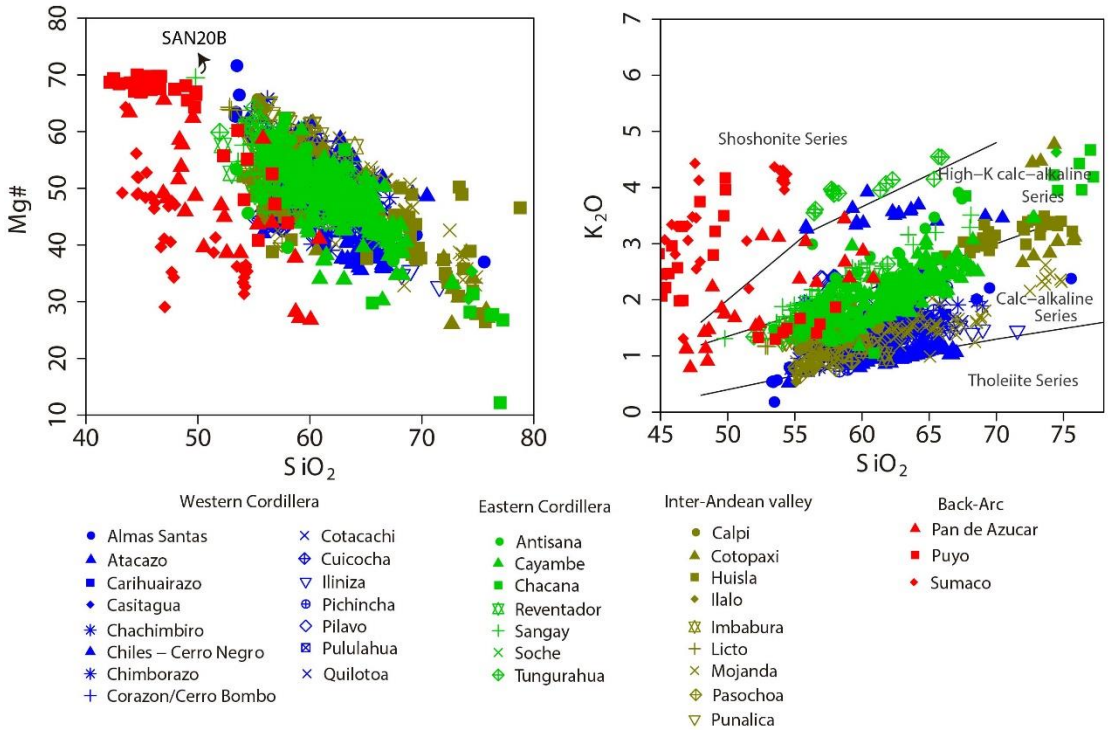

Fig. 1.9. (a) SiO_2 versus Mg# of Ecuadorian volcanic rocks (database from Ancellin et al., 2017 and Hidalgo et al., 2012). **(b)** SiO_2 versus K_2O diagram of Peccerillo and Taylor (1976) for arc rock classification.

1.6.1. Scenario 1: slab melting and subsequent metasomatism of the mantle wedge

Since the work of Bourdon et al. (1999), the adakitic signature of Ecuadorian magmas was used as an evidence for melting of the subducting oceanic crust. For clarification, the term "adakite" is defined as intermediate to felsic volcanic rocks that range from andesite to rhyolite in composition with high Sr (>300 ppm), low Y (<18 ppm) and low HREE (Yb<2 ppm) giving steep REE patterns (Defant and Drummond, 1990; Martin, 1999). The petrogenetic origin of adakites is controversial because their geochemical indices (specially their high Sr/Y and La/Yb) reflect a mineral ensemble of garnet + hornblende, and this mineral assemblage can be obtained by different process such as: (1) melting of subducted crust (Defant and Drummond, 1990; Sen and Dunn, 1994); (2) melting of underplated basalt of lower continental crust (Atherton and Petford, 1993; Jagoutz, 2010) and (3) by fractionation of garnet and amphibole within calc-alkaline series magmas (Müntener and Ulmer, 2006; Alonso-Perez et al., 2004).

Due to the ambiguity of the process at the origin of the adakitic signature, other geochemical indices (different from Sr/Y and La/Yb) are now used to discuss the role of the slab melts in the genesis of magmas. Samaniego et al. (2010) reported a temporal change of fluid-mobile over fluid-immobile ratios (i.e. Ba/Th, B/Th decrease with time) in rocks from Pichincha volcanic complex. Such geochemical variation was linked to a change in the slab component from an aqueous fluid to a hydrous siliceous melt probably because of an increase of the thermal gradient along the slab due to the presence of the Carnegie ridge in the subduction system. As I discussed in section 1.3, the hydrous siliceous melts have more capacity to transport HFSE and Th than aqueous fluids (i.e. Kelemen et al., 2005; Hermann and Rubatto, 2009), therefore, magmas coming from a source metasomatised by melts would have, for example, low Ba/Th, B/Th values. Later, Ancellin et al. (2017) combined the trace element signature with lead isotopic data and found that northern volcanoes of the volcanic front showed low Ba/Th, low $^{207}Pb/^{204}Pb$ and high $^{206}Pb/^{204}Pb$. According to the authors, such composition and isotopic signature is better explained by addition of hydrous siliceous melts from the oceanic crust to the mantle wedge.

In Ecuador, the melting of the subducting slab seems possible (see sections 1.2.1 and 1.2.2 that discuss the temperatures along the subduction zone are similar or close to those calculated by Syracuse et al., 2010). The composition of rocks for solidus calculation in Fig. 1.4 and 1.5 are suitable for the composition of the slab under Ecuador. The solidus in Fig. 1.4 is calculated for MORB and Fig. 1.5 for pelites. Pelites, together with carbonaceous sediments, subduct under Ecuador (Michaud et al., 2005; Ratzov et al., 2010). The solidus of carbonaceous sediments is not shown in Fig. 1.5 and it is expected to plot at higher temperatures because the addition of CO_2 to the fluid of mineral assemblage similar to pelitic rocks increase the temperature of melting.

If the hydrous siliceous melt addition model is governing the magma generation under Ecuador, mantle-derived magmas (primitive magmas) would have low Ba/Th, Sr/Th and high Th/La, Th/Nb typical of mantle metasomatised with melts (Elliot et al, 1997; Plank, 2005; Labanieh et al., 2012). Inversely, primitive magmas that come from a source metasomatised with aqueous fluid would have high Ba/Th, B/Th, Sr/Th. In other words, primitive magmas change their compositions depending of the type of slab metasomatic agent interacting with mantle peridotite.

The addition of hydrous siliceous melt from the slab to the overlying peridotite change the mineralogy of the peridotite. This modification has been described by Kelemen et al. (1995), and more recently by Straub et al. (2008). The addition of such slab component, which is water- (54-88 wt.% H_2O) and silica-rich (9.0-32 wt.% SiO_2) with concentration of Al_2O_3 (0.9-6.5 wt.%), CaO (1.0-4.5 wt.%) and Na_2O (0.5-4.0 wt.%, Kessel et al., 2004), would consume olivine and produce orthopyroxene in the peridotite. This is possible through the reaction SiO_2 + $(Mg, Fe)_2SiO_4$ = $(Mg, Fe)_2Si_2O_6$ (Kelemen, 1995; Sobolev et al., 2007). The formation of orthopyroxene would occur along the ascent paths and would be embedded into surrounding peridotite that contains the mantle clinopyroxene and orthopyroxene. Other studies, as for example Rapp et al. (1999), have also reported the formation of sodic-amphibole in this context. So far in Ecuador, to my knowledge, no studies have aimed to search for geochemical evidences of orthopyroxenes in the mantle (e.g. high Ni abundances in olivines similar to Straub et al., 2013).

1.6.2. Scenario 2: the continental crust control magma composition

Twenty years ago, while some authors explained the adakitic-like signatures of some Ecuadorian volcanoes (high Sr/Y and low Y) through slab melting (e.g. Gutscher et al., 2000; Bourdon et al., 2003), others pointed to the crust as the main cause for such geochemical characteristic through assimilation of garnet-bearing rocks or fractionation of garnet + hornblende at depth (e.g. Garrison and Davidson, 2003; Garrison et al., 2006). This model has been strengthened by combination of other trace elements and isotopic studies. For example, Bryant et al. (2006) reported lava compositions where La/Yb, Ba/La and Ba/Nb increased with crustal contamination indices (i.e. $^{207}Pb/^{204}Pb$). Also, Chiaradia et al. (2009) noted that La/Yb and Sr/Y from lavas of Pichincha, Pululahua, Chacana and Ilaló volcanoes correlate positively with fractionation indices (e.g. SiO_2). It is worth to say that the correlations reported by Bryant et al. (2006) and Chiaradia et al. (2009) is not a feature of other volcanoes (such as Tungurahua, Sumaco, Cotopaxi *cf.* Ancellin et al., 2017 database). Chiaradia et al. (2009) proposed a model of MASH (mixing, assimilation, storage and homogenization) for the origin of intermediate and silicic lavas of the Ecuadorian arc. This model includes the (1) fractional crystallization of mantle-derived melts outside the stability field of plagioclase and within that of clinopyroxene, amphibole and ± garnet, accompanied with crustal assimilation. (2) Magma mixing with

crustal melts formed in the clinopyroxene, amphibole and ± garnet field, and (or) (3) mixing of mantle derived melts that have assimilated crustal rocks and fractionated at depth or have already mixed with crustal melts. The assimilation of precursor mantle-derived solidified magmas allows to reproduce the trace element signature variation (e.g. variable La/Yb) while keeping the lead isotopic signatures different from crustal values. The self–assimilation model of precursor mantle derived magmas has also been used to explain the composition observed in other volcanoes, for instance, Sangay (Monzier et al., 1999). In summary, authors who favors the crust contribution model would assume that the slab component that metasomatises the mantle is an aqueous fluid and therefore, the high Th/La, La/Y, Sr/Y and low Ba/Th (elsewhere mentioned as evidence of hydrous siliceous melts), are suspected to be acquired in the crust (Bryant et al., 2006; Chiaradia et al., 2009, 2020; Beguelin et al., 2015; Beller-Vaca et al., 2019).

The participation of the crust in magma composition from Ecuador seems obvious because the crust is >50 km thick (Vaca et al., 2019 and references therein) and in fact, some volcanoes from the Eastern Cordillera show up to 27 vol.% of lower crustal assimilation (Ancellin et al., 2017). This model has been supported by geochemical analysis of single minerals. Ancellin et al. (2019) studied the isotopic composition of high-Al amphibole, orthopyroxenes and plagioclases of two rocks from Guagua Pichincha volcano and showed that individual minerals recorded lead isotopic compositions very different from those of the whole-rock. Ancellin et al. (2019) concluded that the observed isotopic variability was due to assimilation of radiogenetic crustal compositions. However, crustal interaction of Ecuadorian magmas does not explain some geochemical indices, such as $\delta^{18}O$ and $\delta^{37}Cl$ that need the addition of sediment melts into the mantle wedge (Hidalgo et al., 2012; Chiaradia et al., 2014). Besides crustal assimilation, garnet is also required as a key fractionating phase in this petrogenetic model to control the HREE depletion, however garnet has not been yet reported in Ecuadorian quaternary lavas.

I consider that these two simplified models about the origin of adakitic signatures do not fully describe the complexity of magmatism in Ecuador. Reality lies probably in a more complex model where the composition of mantle-derived melts would have variable composition of trace elements denoting the addition of aqueous fluids and/or hydrous siliceous melts to the mantle wedge and it is this magma that would later be affected by

intracrustal processes. In this sense, we cannot just rule out the addition of hydrous siliceous melts from the slab to the mantle wedge, nor assume a production of single type of primitive magma in the arc mantle. Instead, we need to find more alternative ways (i.e. the study of primitive olivine-hosted melt inclusions) to define the composition of the melts before they are extensively modified by processes occurring in the crust. In this more complex model, I imagine that the composition of some rocks (i.e. high Mg# andesites) are mantle-related while for other rocks (i.e. more evolved andesites) their compositions mostly indicate crustal processes. Also, in order to fully describe the petrogenetic model of magmas in Ecuador, it is needed to analyze the composition of rocks that compose the oceanic lithosphere that enter in subduction because their composition would largely influence the mantle composition and ultimately gives the geochemical flavor to primitive arc magmas (i.e. Plank, 2005).

1.7. Scientific problem and approach

The origin of some geochemical indices (low Ba/Th, high La/Yb, Sr/Y) reported in Ecuadorian magmas is controversial as to whether it is imparted by hydrous siliceous melts from the slab or they are acquired in the crust. What is the magma source of Ecuadorian volcanoes? What is the transport agent from the slab to the mantle wedge? Is the chemical variability of the lavas of the entire arc due to crustal contamination?

This problem is grounded in the lack of primitive rocks which petrologic traces are masked by the interaction with thick continental crust. In order to sample primitive magmas, we focused on the study of melt inclusions hosted in primitive olivines (Fo_{82-90}) from Ecuadorian lavas and tephra with high Mg#. Melt inclusions are droplets of melt trapped in growing crystals (Anderson and Wright, 1972; Roedder, 1979; Sobolev, 1996, Schiano, 2003). Once the melt inclusion is trapped, they are less affected by compositional changes than external bulk magma surrounding olivine, thus preserving some insight of the pre-eruptive material.

High forsterite content olivines represents the beginning of crystal fractionation from primitive magmas. For example, experiments that reproduce early fractional crystallization conditions (Nandedkar et al., 2014; Ulmer et al., 2018) showed that Fo_{88-91} olivine is the first mineral that precipitate from a tholeiitic or calc-alkaline basalt at 0.7 to 1 GPa under oxygen fugacities relevant for arcs. They also showed that clinopyroxene

is the only crystalizing phase together with olivine in such experiments. Additionally, olivines composition changed from Fo_{88-91} to Fo_{81-83} during crystallization.

In Ecuador, Le Voyer et al. (2008) was the first to analyze major, trace and volatile element compositions, as well as B isotopes, in olivine (Fo_{74-89})-hosted melt inclusions from Ecuador. They studied melt inclusions from Pan de Azucar and Rucu Pichincha volcanoes that were silica-poor (<48 wt.% SiO_2). The authors demonstrated that the $\delta^{11}B$ signature of melt inclusions was not acquired in the crust but, instead it represented a compositional variation of the magma source (variable degree of mantle metasomatism or change in the composition of the slab component). Le Voyer et al. (2008) study was crucial to prove the feasibility to study deep magmatic processes using melt inclusions hosted in high-forsterite olivines in Ecuador. Finally, having in mind that Le Voyer et al. (2008) melt inclusions were silica-poor and considering that whole-rock dataset (Ancellin et al. 2017) shows that the crustal assimilation is minimum in more basaltic compositions, we considered that melt inclusions were the best candidates to study the composition of primitive magmas that are rarely accessible as whole-rocks in Ecuador.

Chapter II

Olivine-hosted melt inclusions

2.1 An introduction to the study of olivine-hosted melt inclusions

Melt inclusions are droplets of melt trapped as defects in growing crystals (Anderson and Wright, 1972; Roeder, 1979, Sobolev, 1996; Schiano, 2003). Once the melt inclusion is trapped, they are less affected by compositional changes than external bulk magma surrounding olivine, thus preserving some insights of the pre-eruptive magma. In general, melt inclusion are used to constraint, among other parameters, the pre-eruptive volatile content of magmas (e.g. Wallace et al., 2005; Moore et al., 2018), the imprint of the slab derived fluid (e.g. Le Voyer et al., 2010; Walowski et al., 2016), and the oxidation state of magmas (e.g. Cottrell et al., 2009; Moussallam et al., 2014, 2016). The composition of some melt inclusions (especially those with low cooling rates) can be modified trough post entrapment processes such as: crystallization of the host mineral on the walls of the inclusion; crystallization of mineral phases inside the inclusions (the so-called "daughter minerals" different from the host) inside the inclusion; diffusion of major elements and H^+ (through the host's wall), and formation of a fluid phase (or bubble). Some of these modifications can be reversed via laboratory experiments or thermodynamic models and these calculations are discussed in the following section.

2.2 Post-entrapment composition modifications

2.2.1 Magnesium and iron exchange

Mg and Fe modifications of olivine-hosted melt inclusions were extensively discussed by Danyushevsky et al. (2000, 2002). It starts with the crystallization of olivine in the walls of the inclusion. The composition of new crystallized olivine depends on the concentration of Mg and Fe of the melt inside the inclusion. According to Roeder and Emslie (1970), the olivine composition follows the thermodynamic expression for the

exchange coefficient: $K_{D\ Ol-Liq}^{Mg-Fe} = \frac{X_{liq}^{Mg}/X_{liq}^{Fe^{+2}}}{X_{Ol}^{Mg}/X_{Ol}^{Fe^{+2}}} \approx 0.3$. In this expression, X_{liq}^{Mg} or $X_{liq}^{Fe^{+2}}$ are the molar concentration of Mg and Fe in the melt inclusion while X_{Ol}^{Mg} or $X_{Ol}^{Fe^{+2}}$ are the molar fraction of Mg and Fe in the hosting olivine. During instantaneous olivine crystallization, the residual melt loses more Mg than Fe decreasing the numerator of the $K_{D\ Ol-Liq}^{Mg-Fe}$ expression. Therefore, the denominator also has to decrease to keep $K_{D\ Ol-Liq}^{Mg-Fe}$ constant. It follows the same reasoning, even when we consider other models proposed for $K_{D\ Ol-Liq}^{Mg-Fe}$, for instance that of Toplis (2005) that calibrated $K_{D\ Ol-Liq}^{Mg-Fe}$ for temperature, pressure, water and alkalis composition of the system.

In general, olivine crystallization on the walls of the inclusion continues until the inclusion is quenched or olivine is not the liquidus phase anymore. The result is a zoned interface boundary where the Mg decrease and Fe increase toward the residual melt (Fig. 2.1, panel B). If one melt inclusion is at this step, a laboratory heating procedure can reverse wall crystallization by melting it. On the contrary, if the host mineral is kept at high temperatures the zonation along the interface boundary tend to disappear by diffusion. The residual melt and interface boundary will equilibrate with the host-olivine composition and remelting procedure can no longer reverse the initial composition of the initial trapped melt. At this step, the residual melt has less Mg and Fe than the initial trapped melt (Fig. 2.1, panel B2) and the melt inclusion is considered to be re-equilibrated.

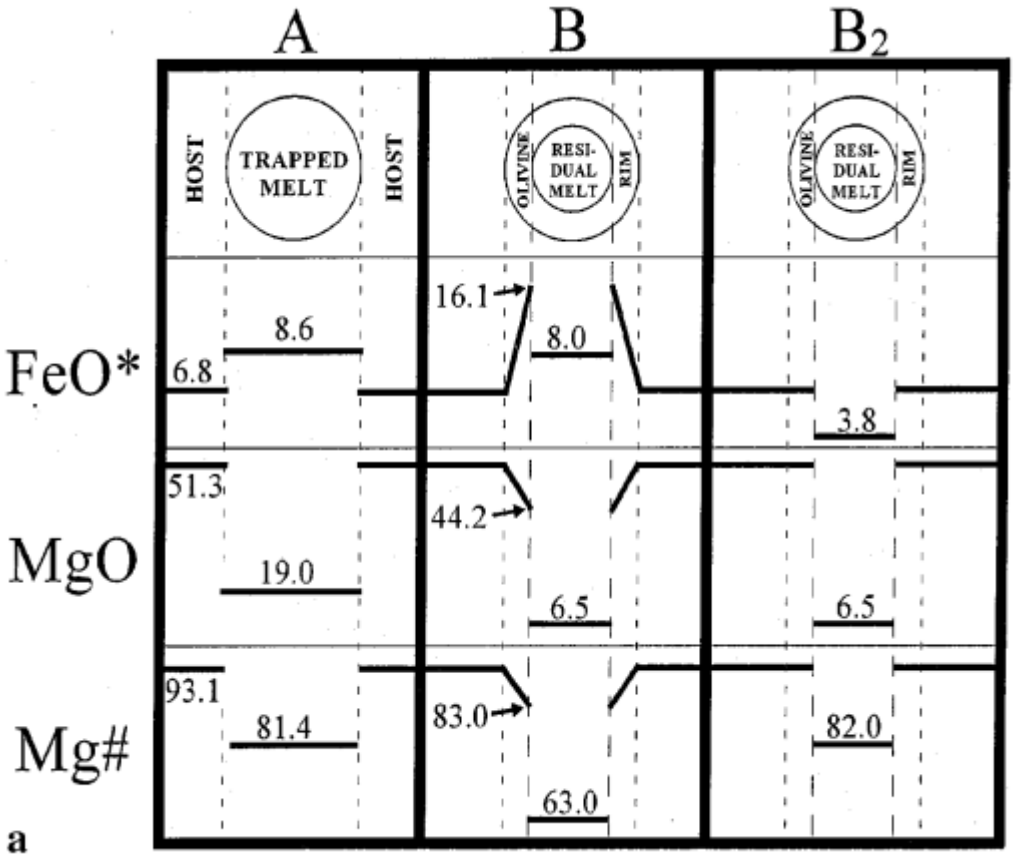

Fig. 2.1. Schematic FeO, MgO and Mg# composition of host olivine and melt inclusion during crystallization of olivine in the walls of the inclusion. Fe and Mg composition of the trapped melt were calculated using the temperature/compositional dependence of de $K_{D\ Ol-Liq}^{Mg-Fe}$ built in the model of Ford et al. (1983). (**A)** Represent the compositions observed at the time of entrapment when the olivine rim is absent. (**B)** Composition of the olivine rim and the residual melt after crystallization of olivine on the walls. FeO* increase and MgO decrease towards the residual melt. (**B2)** Composition of the olivine rim and the residual melt after crystallization of olivine in the walls and total re-equilibration by diffusion. FeO* and MgO zonation of the olivine rim disappeared by diffusion. Composition of the residual melt is the one expected after total re-equilibration with the host olivine. Taken from Danyushevsky et al. (2000).

Contrary to Danyushevsky et al. (2000) that reported olivine-hosted melt inclusions poor in Fe, Rowe et al. (2006) reported anomalous Fe-enrichment in experimentally heated olivine-hosted melt inclusions. This work shows that olivines from an alkaline basaltic lava contain melt inclusions with composition of iron up to 21 wt.%. They concluded that the excessive iron content was due to magnetite melting during experimentally heating procedure. In this case, magnetite had to be in equilibrium with high forsterite olivine prior to melt inclusion entrapment which is only possible in high oxidized magmas from volcanic arcs (Sisson and Grove, 1993).

2.2.2 H_2O, CO_2, S, F, Cl modifications

Melt inclusions also lose water due to H^+ diffusion. H^+ diffusion is an effective process that can decrease the initial content of water in few hours and therefore they rarely preserve water content of the melt at the time of entrapment (e.g. Chen et al. 2011; Gaetani et al. 2012). The exchange protons between the inclusion and the host olivine occurs through the mechanism of Fe reduction in an octahedral lattice site and the creation of 2 OH^- defects associated with an octahedral site metal vacancy (Gaetani et al. 2012)

$$\underbrace{2H_{melt} + 2Fe_{Me}^{\cdot} + 2O_O^{\times} + V_{Me}^{''}}_{\text{Olivine structure}} = \underbrace{\left\{\left\{(OH)_O^{\cdot} - V_{Me}^{''} - (OH)_O^{\cdot}\right\}\right\}^{\times} + 2Fe_{Me}^{\times}}_{\text{Olivine structure}} \quad \text{eq. (1)}$$

$Fe_{Me}^{\cdot} = Fe^{+3}$ on the octahedral site

$Fe_{Me}^{\times} = Fe^{+2}$ on the octahedral site

$V_{Me}^{''}$ = octahedral site metal vacancy with a net double negative charge

$O_O^{\times} = O^{-2}$ on the oxygen site

The H^+ diffusion is accompanied by O exchange through the oxidation of Fe on the octahedral site and creation of an octahedral site metal vacancy.

$$O_{melt} + \frac{1}{2}[SiO_2]_{melt} + \underbrace{3Fe_{Me}^{\times}}_{\text{Olivine structure}} = \underbrace{V_{Me}^{''} + 2Fe_{Me}^{\cdot} + \frac{1}{2}Fe_2SiO_4}_{\text{Olivine structure}} \quad \text{eq. (2)}$$

These two reactions lead the melt inclusions to exchange water with the host olivine. Those same reactions occur between the olivine phenocryst and the surrounding magma that could allow the melt inclusions to equilibrate their oxygen fugacities (f_{O_2}) and water content with that of the surrounding magma. This implies that the oxygen fugacity obtained from the melt inclusion is that of the last magma in equilibrium with the olivine phenocryst and not necessarily that of the initial trapped melt.

Melt inclusions can also lose water by another process different from that of point defect diffusion in the olivine structure (Gaetani et al., 2012; Portnyagin et al., 2019). H_2O content in melt inclusions can decrease by formation of the fluid phase (or bubble) inside melt inclusions. The bubble formation occurs by decreasing the internal pressure inside the melt inclusion that leads to exsolution of volatiles (e.g. CO_2 and H_2O). The volatiles become less soluble in the silicate melt with decreasing pressure. This could happen by decompression of the entraining magma that result in the expansion of the host olivine (Zhang, 1998), or H^+ diffusion out of the melt inclusion, or both. Two other processes also lead to bubble formation inside melt inclusions. First, during quenching when the silicate melt contracts more that the host olivine producing a free space that is filled by volatiles (Lowenstern, 1995). The second, when the olivine crystallization on the walls of the melt inclusion reduce the volume and pressure of the residual melt allowing the volatiles to be exsolved. The molar volume of the olivine is less than the partial volume of olivine component in the melt.

With H_2O being prone to significant modification, the interpretation of H_2O concentrations in melt inclusions, especially those in primitive magmas from volcanic arcs, has been discussed by many researchers. Plank et al. (2013) compiled melt inclusion data (hosted in ol, cpx and plg) from volcanic arcs and showed that their water content can reach up to 7.1 wt.% with a global average of 3.9±0.4 wt.%. However, the water concentration in melt inclusion could even be higher than those values reported by Plank et al. (2013) because, for example in olivine-hosted melt inclusions, H^+ can totally re-equilibrate with melt surrounding olivine within few days (e.g. Portnyagin et al., 2008; Gaetani et al., 2012). Thus, if melt were at water saturation conditions once formed in the peridotite, it would lose water due to pressure decreasing during ascent. In this case, water of olivine-hosted melt inclusions would re-equilibrate towards lower water-content. Additionally, Gavrilenko et al. (2019) discussed that the lack of melt inclusions with H_2O concentration higher than ~6 wt.% could be due to the difficulty to quench wet magmas. The authors showed that mafic melts with water concentration between 6-9 wt.% are difficult to quench and those with concentration >9 wt.% do not quench at all. Therefore, primitive magmas from volcanic arc could have water content >4 wt.% and up to 16 wt.% accordingly to Gavrilenko et al.'s work.

My opinion is that water in olivine-hosted melt inclusions do not represent that of primitive magmas, unless it can be demonstrated that studied melt inclusions have ascended from the mantle to the surface very rapidly (less than few days). In this context, I assume that most melt inclusions have been re-equilibrated at crustal depth. Because the water content of primitive magmas is dependent on, among other parameters: the degree of mantle melting, the bulk partition coefficient of water, and the mechanism of extraction of the melt from the peridotite; I consider that water can largely vary in primitive magmas and is not uniform in arc magmas as proposed by Plank et al. (2013).

Similarly to H_2O and CO_2, S can also be partitioned in the bubble phase of melt inclusions. Bucholz et al. (2013) showed S in the melt phase decreased with progressive diffusive H_2O-loss, which in other words means that S moved to the bubble with decreasing pressure. This was also shown by Lesne et al. (2011) who reported a strong partition of S in the fluid when internal pressure is lower than 100 Pa. S can also be contained as solid phases in natural quenched or experimentally re-heated melt inclusions. For example, Moore et al. (2018) reported native sulfur (as well as carbonates) in bubbles present in natural quenched melt inclusions. In some extreme cases, gypsum, Fe-sulfides in re-heated melt inclusions can contain up to 84% of S according to calculations (e.g. Schiavi et al., 2020; Venugopal et al., 2020).

Contrarily to S, Cl is not strongly partitioned into the fluid phase at low pressure and, therefore, experimental melts show constant Cl content at variable pressure (Lesne et al., 2011). Finally, Spilliaert et al. (2006) have shown that F exsolved at lower pressure than S in basaltic magmas. Therefore, the composition of Cl and F measured in the melt inclusion is likely less affected (conclusion shared by Bucholz et al., 2013) by post-entrapment modification than H_2O, CO_2 and S.

2.2.3 Silica modification

Silica is another major element potentially modified in olivine-hosted melt inclusions after their entrapment. Portnyagin et al. (2019) showed that experimentally re-hydration of olivine-hosted melt inclusion increased their H_2O and SiO_2 concentration. On the contrary, experimental dehydration of previously hydrated melt inclusions lost H_2O and SiO_2. They explained this phenomenon by release/incorporation of silica and

water in the olivine structure through dissolution/crystallization of metal-defect olivine (eq. 2). Melt inclusions during experiments changed in some cases from almost 0 to nearly 6 wt.% H_2O and vice versa. For silica, the total change went up to 10 wt.% (major elements expressed in a volatile-free basis). Such variation of SiO_2 would be enough to move melt inclusion from SiO_2-undersaturated to hypersthene-saturated (*c.f.* Sorbadere et al., 2013a, c) compositions when melt inclusions are rich in water as those from volcanic arcs.

It is difficult to argue against the results presented by Portnyagin et al. (2019) because the data shows clearly that diffusion of H^+ out or into olivine-hosted melt inclusions produce a decrease or enrichment of silica content. During olivine crystallization, some silica as well as Mg and Fe enter in the olivine structure, however, the amount of silica lost during Portnyagin et al.'s experiments are much higher than that accounted for stoichiometric olivine crystallization. Instead, it requires the crystallization of olivine with a great number of metal defects that would be occupied by H^+. This olivine must be metal (i.e. Mg, Fe) deficient, or in other words, the structural sites M1 and M2 of olivine would be occupied partially and totally by H^+. Such mechanism imply that the newly created olivine would contain great quantities of water (few wt%) which is contradictory with naturally occurring mantle olivine data that show water content up to 250 ppm (Bell et al., 2003; Hirschmann et al., 2005). H_2O in olivine can increase up to 1500 ppm with pressure in the lower upper mantle (Férot and Bolfan-Casanova, 2012). The diffusion of silica neither cannot be the responsible for silica lost because this process is very slow (6-7 orders of magnitude slower than Fe and Mg; e.g. Dohmen et al., 2002; Chakraborty, 1997).

2.2.4 REE and other trace element modifications

Diffusion of REE out of the olivine-hosted melt inclusion are expected to be minimal because timescales for preservation of REE signatures are relatively long (10^4-10^5 years, Cherniak, 2010). Although, Spandler et al. (2007) had reported high diffusivities of REE that suggested short time for these elements to re-equilibrate (few years to some decades), it was contradicted by Cherniak (2015) and Burgess and Cooper (2013) who argued that the high diffusivities of Spandler et al. (2007) work was due to

creation of extended defects under high TiO_2 potential gradient which is only present in experiments. Also, the expected high diffusivities of HREE due to their smaller ionic radii (e.g. Cottrell et al., 2002) was challenged by Cherniak (2010) that found similar diffusivities for REE (i.e. La, Dy and Yb). The diffusivities of Nd, Sr and Hf in olivines are similar to those of La, Dy and Yb (Remmert et al., 2008) and therefore, commonly analyzed trace elements may not be modified after melt inclusion entrapment.

During olivine crystallization (or melting) on the walls of melt inclusions, REE can be enriched (or diluted) in the residual melt due to their high incompatibility in olivine structure (e.g. Rollinson, 1993). The same would occur for every incompatible element in olivine and the best way to circumvent this problem is to use the ratio of these elements to develop geochemical models of melt inclusion compositions.

2.3 Corrections of post-entrapment modifications

2.3.1 Major element composition of melt inclusions

As discussed previously, major elements in melt inclusions change after entrapment, and several strategies exist to retrieve the pre-entrapment melt composition. The Mg-Fe modification due to crystallization/melting of olivine on the walls of the melt inclusions or Mg-Fe inter-diffusion of the melt inclusions with their hosts can be tested by assessing the $K_{D\ Ol-Liq}^{Mg-Fe}$ between melt inclusions and their host-olivines. If Mg or Fe inter-diffusion occurred, the $K_{D\ Ol-Liq}^{Mg-Fe}$ values would be different to that expected for equilibrated melt-olivine pairs (0.3 ± 0.03, Roeder and Emslie, 1970). Another way to test whether melt inclusions suffered Mg-Fe modification, or not, is to plot FeO_t wt.% of melt inclusions against the forsterite content of the host (Danyushevsky et al., 2000). In such diagram, re-equilibrated melt inclusions show lower content of FeO_T than the whole rock/glass trend (Fig. 2.2).

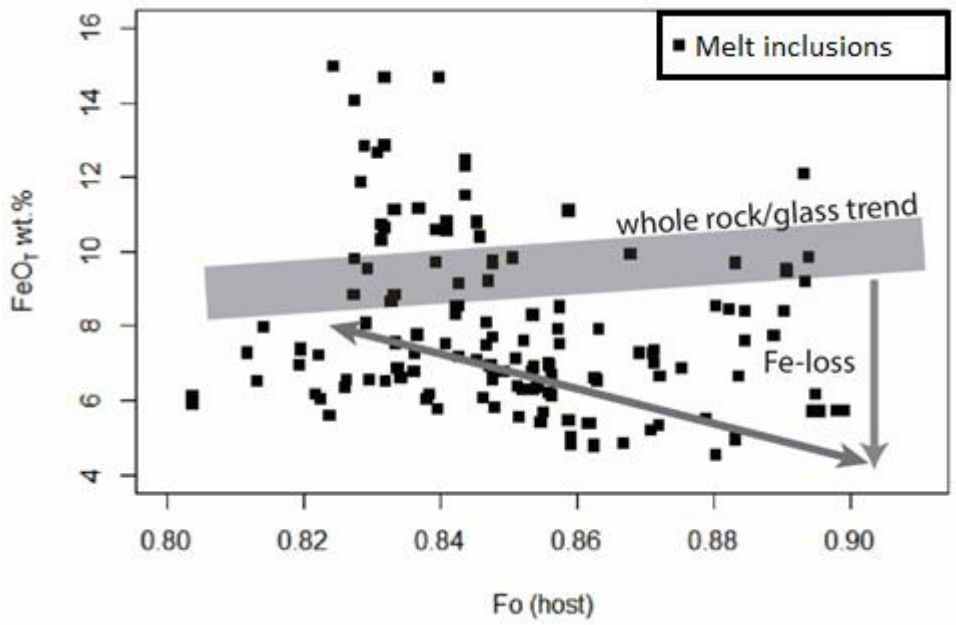

Fig. 2.2 Schematic forsterite content of host-olivine against FeO_T wt.% of melt inclusions similar to that of Danyushevsky et al. (2000).

The composition of melt inclusions affected by post-entrapment Mg-Fe modification can be numerically corrected. If we consider that melt inclusion compositions changed only due to crystallization/dissolution of olivine, we can add/remove equilibrated olivine from the melt inclusion (Laubier et al., 2007). It gets more complicated when Fe-loss is considered. In this case, we can employ Petrolog3 software (Danyushevsky and Plechov, 2011) that uses mineral-melt equilibrium models and a user-specified FeO_t content. The user-specified FeO_t is the iron content before post-entrapment modifications. This code add/remove olivine of composition similar to that of the host and allows the melt inclusion to re-equilibrate (add/remove FeO until the equilibrium $K_{D\ Ol-Liq}^{Mg-Fe}$ is attained). Once equilibrated, the code compares the calculated FeO to the user-specified value and if they do not match the addition/extraction of olivine starts again. The FeO content before post-entrapment modifications can be assessed assuming that melt inclusions and whole-rock compositions are related through a liquid-line-of-descend, although this is not always the case. Therefore, the unmodified FeO content of melt inclusions must be obtained from the linear regression model formed by whole rocks in a diagram MgO *vs.* FeO (or SiO_2 *vs.* FeO). Another parameter needed to run this code is the Fe^{+3}/Fe^{T} ratio for each melt inclusion. This ratio can be obtained directly by measuring the Fe K-edge X-ray absorption near-edge structure (XANES) using a synchrotron (Cottrell et al., 2009), or indirectly by measuring the S^{2-} and S^{6+} peak

positions of the Kα-radiation, relative to a sulfide and sulfate standards using an electron microprobe (Jugo et al., 2005). We can calculate the redox state of iron from sulfur speciation, because the sulfur speciation is a function of oxygen fugacity (Wallace and Carmichael, 1992). The precipitation of sulfides and sulfates in the bubble surroundings (e.g. Schiavi et al., 2020; Venugopal et al., 2020) would certainly modify the initial S^{2-}/S^{6+} and Fe^{+3}/Fe_T of melt inclusions that would complicate the determination of redox state from sulfur.

If Mg-Fe post-entrapment modification of melt inclusions are difficult to reverse numerically (because unknown parameters are needed), it becomes even more complicated when we consider that melt inclusions lose SiO_2 as proposed by Portnyagin et al. (2019). This can be done using Portnyagin et al. (2019) spreadsheet file that allow us to correct melt inclusion compositions for Mg, Fe and Si if we consider that the FeO and SiO_2 of melt inclusions is similar to that of their hosted whole-rocks . This assumption could lead the user to lose potential insights given by melt inclusions about the genesis of magmas. For example, it has been proved that some silica-poor melt inclusions with $CaO/Al_2O_3>1$ that are formed by partial melting of an amphibole-bearing clinopyroxenite are hosted in olivine-bearing mafic magmas issued from mantle peridotites. In this context, melt inclusions and host rocks cannot be related through a liquid line of descent (e.g. Médard et al., 2006; Sorbadere et al., 2013a). Thus, the major element correction for PEM potentially question the very existence of such melt. PEM corrections is reliable at least for melt inclusions that do not show Fe-loss or for those that silica modification is expected to be minimum.

2.3.2 Water and CO_2 contained in bubbles

H_2O, CO_2 and other volatiles from the melt can move to the fluid phase during decompression (*c.f.* section 2.2.2). The reconstruction of the total volatile element concentrations of the pre-eruptive magma consists in quantifying the amount of volatile elements in the bubble and add them back into the dissolved volatiles in the melt phase. Most of the studies are focused on the reconstruction of H_2O and CO_2 because they allow us to calculate the pressure of entrapment of melt inclusion if we assume that the magma was at the H_2O-CO_2 saturation (e.g. Moore et al., 2015, 2018; Wallace et al., 2015; Aster

et al., 2016; Tucker et al., 2019). For this reconstruction, it is necessary to known the size, density, H_2O and CO_2 molar fraction of the bubble and the composition of major element and volatiles of the equilibrated melt. The bubble size can be obtained optically and its volume calculation is discussed in Tucker et al. (2019). The density of the bubble can be measured by RAMAN spectrometry (e.g. Kawakami et al., 2003; Esposito et al., 2011) or calculated by equations of state (Moore et al., 2015; Wallace et al., 2015). The H_2O and CO_2 molar fraction of the bubble is obtained from H_2O-CO_2 solubility models and the composition of the equilibrated melt.

Some significant unknowns still present and exact H_2O and CO_2 bubble reconstruction remain uncertain. I will mention three of them that from my point of view can affect the interpretation of reconstructed volatile content. (1) H^+ diffusion out of the melt inclusion is not possible to reconstruct and the calculated pressure must be considered minimum. (2) The bubble could have experienced non-equilibrium expansion which means that the fluid and melt are not at equilibrium and the volatile mass obtained by reconstruction is over-estimated. This is not a problem if bubble density is measured by RAMAN, but when it is calculated by equations of state. Finally, (3) the melt was volatile-saturated at the time of entrapment resulting in heterogeneous entrapment of the fluid phase which means that calculated pressure would be over-estimated.

The volatile reconstruction can also be done experimentally by dissolving the bubble into the melt using a Vernadsky-type microscope heating stage, a piston cylinder or an internally-heated pressure vessel (e.g. Schiavi et al., 2016; Mironov et al., 2015; Rasmussen et al., 2020). By increasing the pressure and (or) temperature of olivine-hosted melt inclusions, the accompanied bubble can be reabsorbed and the melt inclusion can be quenched in a homogeneous glassy phase. This procedure does not always ensure the absorption of bubbles into the melt, and during the experiments some geochemical exchange between the melt inclusion and the surrounding olivine can occur.

Chapter III

Analytical Methods

3.1 Melt inclusion preparation

During this work I followed the subsequent steps for olivine-hosted melt inclusion selection (Fig. 3.1). First, we selected 19 volcanic rocks with Mg# higher than 55 from the sample collection (including more than 1300 samples) that resulted from a joint scientific program between the IG-EPN and the IRD. These samples correspond to 17 lavas and 2 tephra from Cotacachi, Cubilche, Cono de la Virgen, Puñalica, Conos de Licto and Sangay (location shown in Fig. 3.2). Three samples from Cubilche and one from Cotacachi were discarded because olivines were scarce or because olivines showed Fo<80. Secondly, I crushed samples with visible olivines and separated the fraction 0.4-1.5 mm. I picked about 100 olivines crystals per sample, under a binocular microscope. Thirdly, we used Crystalbond to attach crystals on glass slides in order to polish and separate olivines in which melt inclusions were observed. I sorted about 100 crystals with melt inclusions bigger than 25 µm (Fig. 3.3) from the 15 remaining samples. All selected melt inclusions were crystalized and presented bubbles due to the slow cooling rates of parental rocks (mainly lavas) and, therefore, we experimentally heated them to reverse the crystallization process.

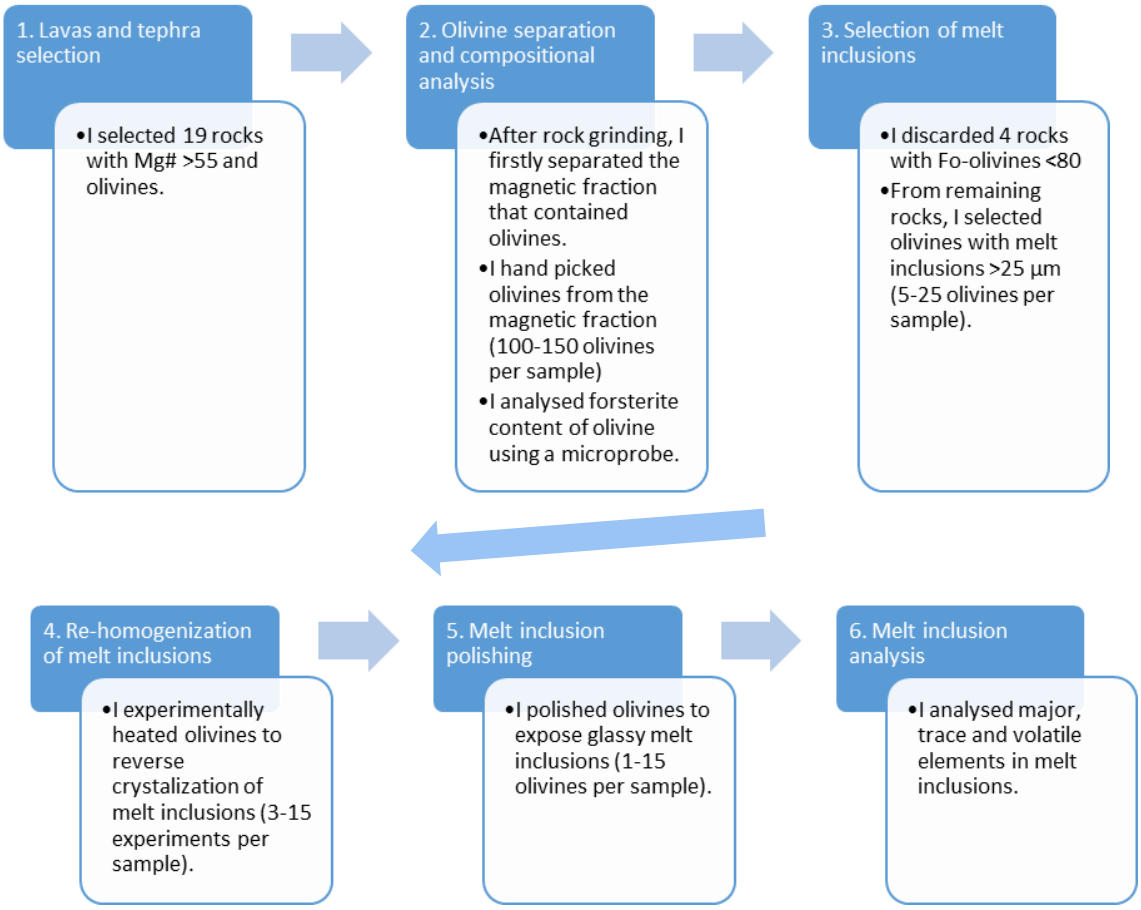

Fig. 3.1 Steps of melt inclusion preparation for geochemical analysis.

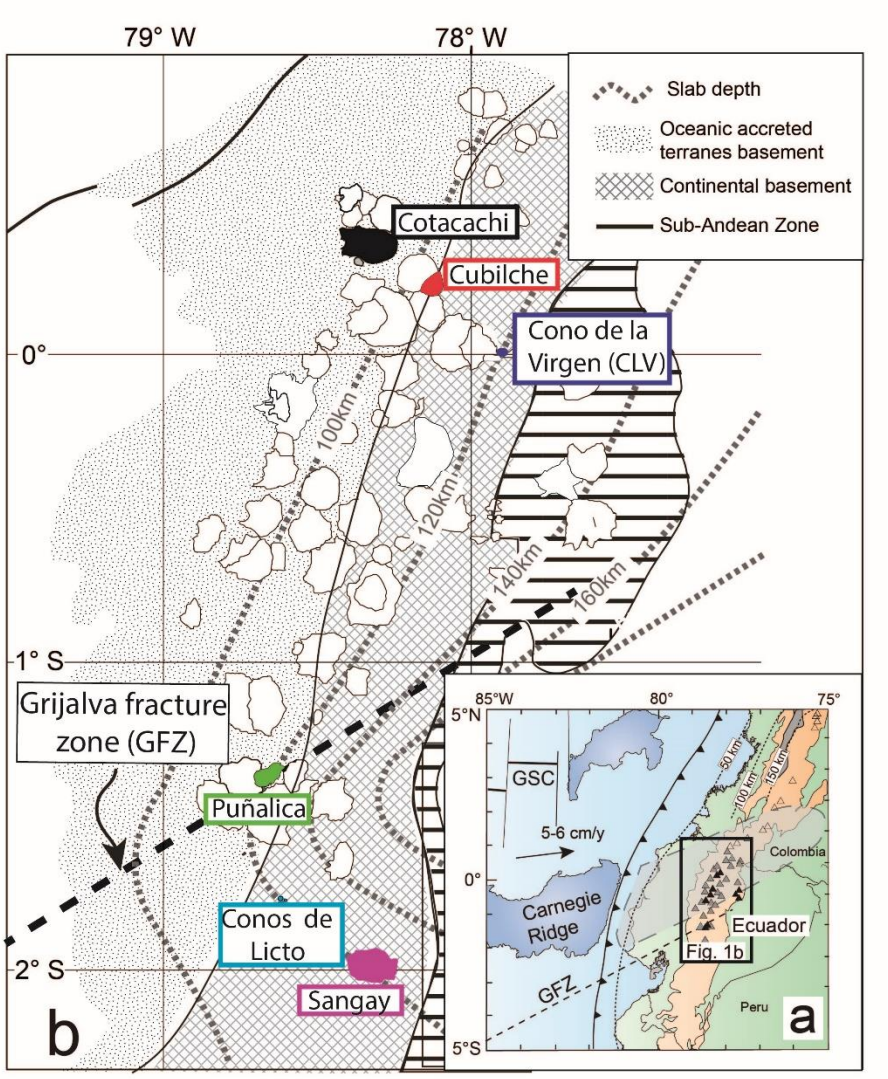

Fig. 3.2 (a) Geodynamic setting of Ecuadorian arc. Grey shaded area is the inferred continuation of Carnegie ridge from Gutscher et al. (1999). **(b)** Schematic map of the main geological units in Ecuador [modified from Jaillard et al., (2008)] showing quaternary volcano locations. Samples selected for melt inclusion analysis were performed in rock samples from Cotacachi, Cubilche, Cono de la Virgen (CLV), Puñalica, Conos de Licto and Sangay. The dashed black line is the surface projection of the Grijalva fracture zone (GFZ). Slab depth contours are from Yepes et al. (2016).

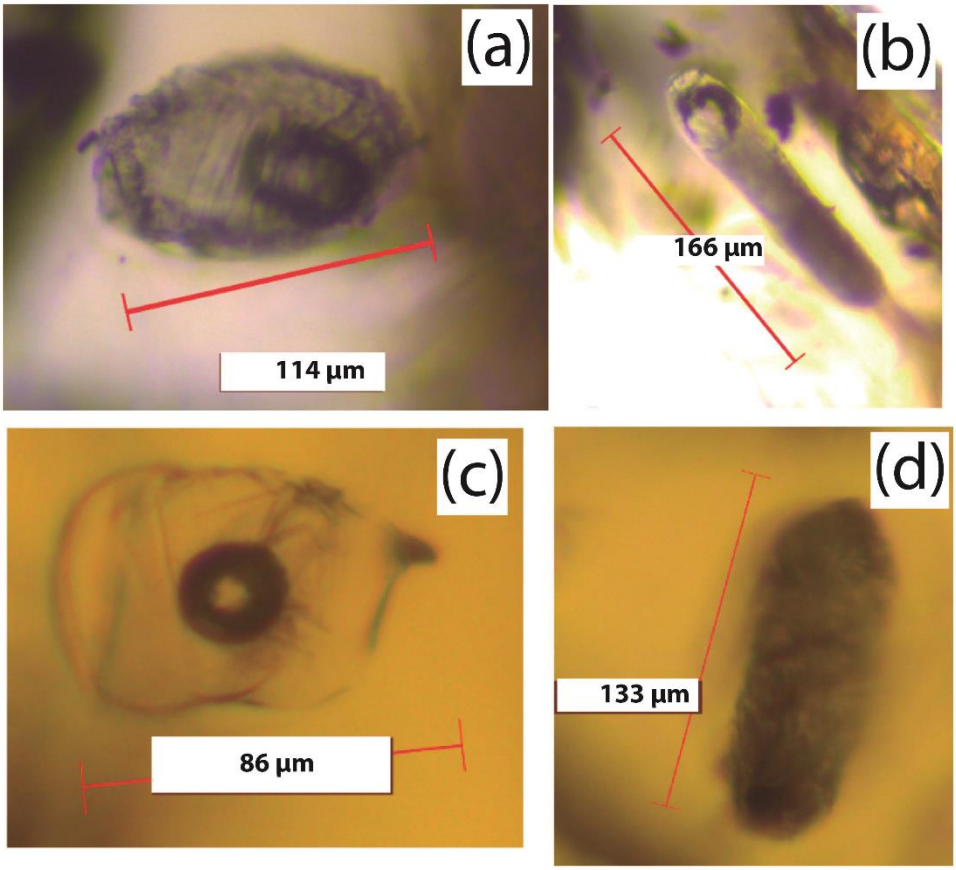

Fig. 3.3. Image of selected melt inclusions before experimentally heating procedure. **(a)** and **(b)** are melt inclusions from Cubilche volcano (17EQ95), **(c)** and **(d)** are from Conos de Licto (RIO10B) and Sangay volcanoes (SAN21B), respectively.

3.2 Re-homogenization procedure

To reverse the crystallization of olivine rim as well as the secondary minerals I heated each melt inclusion until all secondary minerals disappeared (Fig. 3.4). For this procedure, we used a Vernadsky-type microscope heating stage that allows visual observation of melt inclusions (Sobolev et al., 1980). This assemblage uses a 1 atm furnace gas-tight sealed, cooled by water (Fig. 3.5). Each experiment (>100 in total) lasted less than 30 minutes and throughout an oxygen fugacity less than 10^{-10} atm was kept so that no oxidation of olivine occurs. This highly reduced conditions are maintained by the circulation inside the furnace of purified argon. The latter is obtained by passing regular argon gas on Zirconium at 700 °C. The high thermal conductivity of He improves the cooling rate at the moment of quenching. We measured the temperature inside the furnace using a Pt-Pt_{90}-Rh_{10} thermocouple welded to the sample holder and calibrated

using Au (melting temperature equal to 1064 °C). For each experiment, the temperature was increased at a rate of 80 °C/min until the heating stage reached the Au fusion temperature (1064 °C), then at 10-30 °C/min until the last crystal inside the MI disappeared. Once we observed the disappearance of all minerals inside the MI, we kept the temperature constant for 5 min and quenched the experiment by turning off the electric current to the heater. After this procedure, melt inclusions were glassy and bubbles still present (Fig. 3.4). After experimental heating, we polished olivine crystals with silicon carbide papers and exposed the quenched melt inclusions.

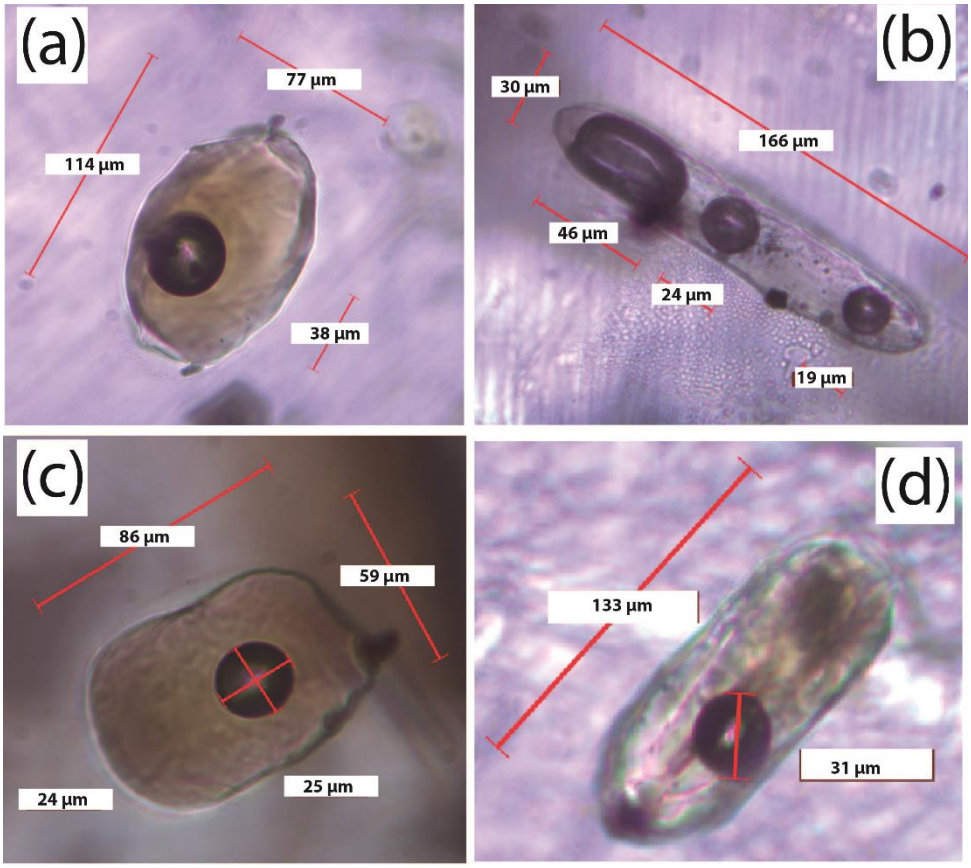

Fig. 3.4. Image of selected melt inclusions after experimentally heating procedure similar to those in Fig. 3.3. **(a)** and **(b)** are melt inclusions from Cubilche volcano, **(c)** and **(d)** are from Conos de Licto and Sangay volcanoes, respectively.

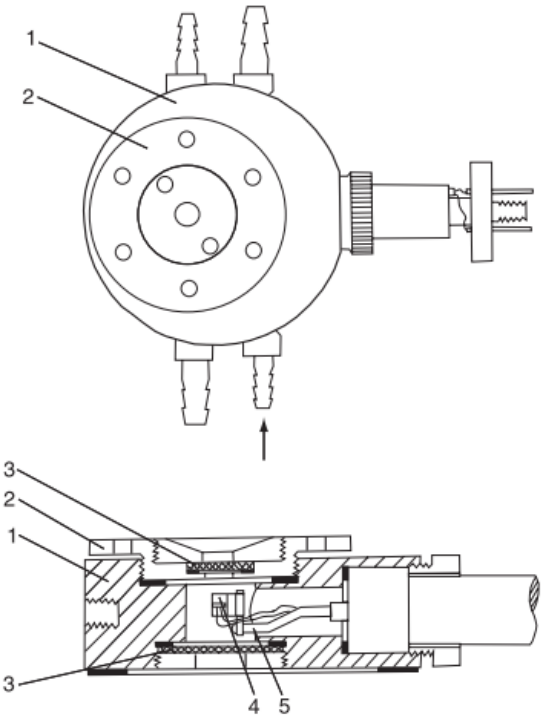

3.

Fig. 3.5. 1-atm furnace designed by Sobolev et al. (1980). (1) Gas tight sealed body cooled by water; (2) screwed lid; (3) optical quartz glass windows; (4) Pt_{90}-Rh_{10} heating element and ring-shaped metallic sample holder with Pt-Pt_{90}-Rh_{10} thermocouple; (5) electrode. Olivine crystals hosting one or more melt inclusions are placed in the sample holder and observed under a microscope through the optical quartz glass windows. Taken from Schiano (2003).

3.3 Electron probe microanalysis

3.3.1 Functioning principle

Electron probe microanalysis technique (EPMA) involves bombarding a specimen with an electron beam and analyzing the emitted x-rays. The electron beam that hits the surface of the sample removes electrons from the inners shells of the atoms creating vacancies. These vacancies are filled with higher energy electrons from the outer shells. This movement from atom's outer to inner shells releases energy that falls into the X-ray range of the electromagnetic spectrum (e.g. Reed, 2005). The emitted X-rays are analyzed with energy-dispersive (EDS) or wavelength-dispersive spectrometers (WDS). WDS are composed of analytical crystals. The crystal is placed at specific location along an arc to reflect the emitted X-rays of a specific wavelength from the sample to the detector. In the detector, the X-rays are "counted" and compared to those of standards which contain known values of the element of interest. This is a non-destructive technique that allows to analyze the composition of polished samples with high precision.

3.3.2 Analytical conditions

Major element compositions of olivine crystal and melt inclusions were determined using a CAMECA SX100 electron microprobe at the Laboratoire Magmas et Volcans. Olivine analysis were performed with a focused beam, a 15 kV accelerating voltage, a current of 15 nA and 10 s counting time. Glasses were analyzed with a focused beam of 5-20 µm in diameter (depending in the diameter of the inclusions), a low current (8 nA) for major elements, and 80 nA for Cl, S, and F. The counting time for major elements were 40 s for Fe; 30 s for Mn; 20 s for Ca, Ti, Al, K, Mg and 10 s for Na, Si. Cl and S were measured 4 times during 40 s/cycle and F for 3 times during 60s/cycle. Alkalis were measured first to avoid alkali loss. No alkali loss was detected on the natural basaltic glass VG-A99 under these beam conditions and also, alkalis of all MI plotted along expected liquid lines of descent which suggest no alkali loss. A set of CAMECA standards were used for calibration (Table 3.1). For major elements, the analytical uncertainty obtained from replicate measurement of the basaltic glass standard VG-A99 (Thornber et al., 2002) were ~5% for K_2O, 10% for P_2O_5, 30% for MnO and <3% for other major elements. Relative standard deviations (1σ) of MI are less than 1% for SiO_2 and <2% for the other major elements except for Mn that display concentrations less than detection limit (0.2 wt.%).

Table 3.1. EPMA analytical conditions for major elements analysis in olivine (olivine program) and melt inclusions (glass program), and analytical condition for volatile analysis in melt inclusions (volatile program). TAP (thallium acid phthalate), LiF (lithium fluoride) and PET (pentaerythritol) are the crystal used in WD spectrometer.

Program	Voltage	Current	Beam size	# cycles	Crystal	Element	Counting time (s)	Calibrated in
olivine	15 kV	15 nA	punctual	1	TAP	Mg	10	Forsterite
					PET	Ca	10	wollastonite
						Ti	10	titanomagnetite
						Cr	10	chromium oxide
					LiF	Fe	10	fayalite
						Mn	10	titanomagnetite
						Ni	10	olivine
					TAP	Si	10	wollastonite
glass	15 kV	8 nA	5 to 20 µm	1	TAP	Na	10	albite
						Mg	20	periclase
					LiF	Fe	40	hematite
						Mn	30	titanomagnetite
						Ti	20	titanomagnetite
						P	10	apatite
					PET	K	20	orthoclase
						Ca	20	wollastonite
					TAP	Si	10	ATHO glass
						Al	20	VG2 glass
volatiles	15 kV	80 nA	5 to 20 µm	3 to 4	TAP	F	60	CaF2
					TAP	F	60	CaF2
					PET	Cl	40	scapolite
						S	40	VG2 glass
					TAP	F	60	CaF2

3.4 Laser Ablation-Inductively Coupled Plasma-Mass Spectrometer

3.4.1 Functioning principle

Laser ablation-Inductively coupled plasma-mass spectrometer (LA-ICP-MS) is a destructive technique for trace element analysis in small samples (e.g. Longerich, 2008). Samples are placed in the LA cell and are hit by a laser that transform the sample into an aerosol of small particles. The resulted aerosol is transported by a gas flow to the ICP where a gas (Ar) is electromagnetically heated to a high temperature forming a plasma.

The plasma dissociates the molecules of the sample aerosol and remove electrons from the components forming singly charged ions which are directed into the MS. The MS separates these ions based upon their mass-to-charge ratio before they reach the detector where the intensity (ions per second or current) is measured. The intensity of a given mass-to-charge value is related to the concentration by comparing with external and internal standards of known concentrations (e.g. Jackson, 2008; Lin et al., 2016).

3.4.2 Analytical conditions

For trace elements, we used a laser ablation system (193 nm Eximer Resonetics M-50E) coupled with an inductively coupled plasma mass spectrometer (Agilent 7500 cs). We used a pulse energy of ~3 mJ, a spot diameter between 15 and 33 µm, and a laser pulse frequency of 2-3 Hz, depending on the inclusion size ensuring a fluence at sample surface of ~4 J/cm^{-2}. The background was measured for 40 s before ablation, and the analysis time was approximately 100 s. Data reduction was performed using GLITTER software. We used BCR-2G and NIST SRM 612 basaltic glasses (Gao et al., 2002) as external standard samples, and Ca as the reference element. Typical errors on the MI (1σ error of mean, $1/\sqrt{n}$ where n is the number of cycles) were less than 15% for all trace elements, except for Ta (<25%), and B (<40%).

Table 3.2 Trace elements concentration of BCR-2G and NIST-SRM-612 standards used during LA-ICP-MS analysis. Data from Gao et al. (2012).

	BCR-2G	NIST-SRM-612
Sc	32	40
Ti	13005	44
V	425	38,3
Zn	153	38
Ga	24	37
Rb	51	32
Sr	321	75
Y	31	38
Zr	167	37
Nb	10,9	36
Cs	1,17	41
Ba	641	37
La	25	37
Ce	52	38
Pr	6,3	37
Nd	27	35
Sm	6,3	37
Eu	1,91	35
Gd	6,5	36
Tb	0,95	36
Dy	6	36
Ho	1,2	38
Er	3,3	37
Tm	0,46	37
Yb	3,2	40
Lu	0,47	37
Hf	4,5	35
Ta	0,63	36
Pb	10,9	38
Th	5,5	37
U	1,7	37

3.5. Secondary Ion Mass Spectrometer

3.5.1. Functioning principle

Secondary ion mass spectrometer (SIMS) is a destructive technique that use a positive (Cs^+) or negative (O^-) primary ionized beam focused on a sample to generate ions (secondary ions) that are transferred into a mass spectrometer across a high electrostatic potential (e.g. Andersen and Hinthorne, 1972; Shimizu and Hart, 1982). The sample is placed under ultra-high vacuum to avoid secondary ions collision with interfering gases. The primary ions are focused on the sample with electrostatic lenses and deflected with electrostatic or magnetic deflectors. Primary positive ions are used to measure elements with high electronegativities (e.g. F, Cl, S) while negative ions for elements with low electronegativities (e.g. Li, B, metals). The secondary ions are accelerated, focused and transported by an electric field toward the electrostatic sector where secondary ions of a given energy would continue thought coupling lens to the magnetic sector. In the magnetic sector, the secondary ions are split by mass-to-charge ratio. This configuration (Fig. 3.6) allows to separate secondary ions of similar mass-to-charge ratio although they have different energy. After the secondary ions pass through the magnetic sector they reach the detector where they are counted. The detector can be either a faraday cup or an electron multiplier.

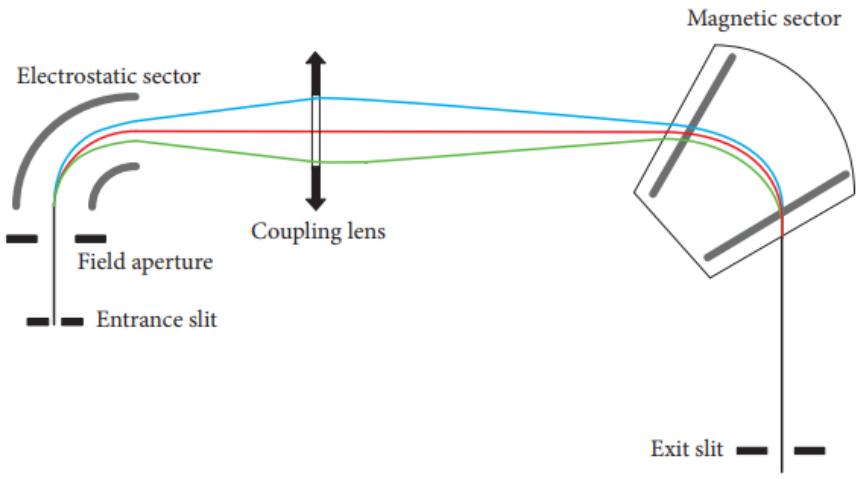

Fig. 3.6. SIMS configuration for mass-to-charge ion discrimination independently of their energy. Colored lines show paths of different energy (colors) but constant mass-to-charge ratio. Entrance and exit slit are adjusted to vary mass resolution. Taken from Kusserow (2019).

3.5.2. Analytical conditions

We use the CAMECA HR1280 that belongs to the Centre de Recherches Pétrographiques et Géochimiques (CRPG) located in Nancy. Crystal were mounted in a high purity indium substrate and then gold-coated. We use a Cs^+ primary ion beam with a current of 1 nA, a 10 kV secondary accelerating voltage, a -80 V offset and a projected beam size of 20 µm. For volatile element (H_2O, CO_2, F, Cl, S) concentration measurements, the instrument was operated with the contrast aperture at 400 µm, the energy aperture at 40 eV, the entrance slit at 52 µm and the exit slit at 173 µm, for a mass resolution power of 7007. This resolution allows the complete discrimination of mass interferences: $^{34}S^1H$ on ^{35}Cl, ^{17}O on $^{16}O^1H$, $^{29}Si^1H$ on ^{30}Si and $^{31}P^1H$ on ^{32}S. After 3 min of pre-sputtering, we collected signals for ^{12}C (8 seconds), ^{17}O (3 seconds), $^{16}O^1H$ (6 seconds), ^{18}O (3 seconds), ^{19}F (4 seconds), ^{27}Al (3 seconds), ^{30}Si (3 seconds), ^{32}S (4 seconds) and ^{35}Cl (6 seconds) (counting times in parenthesis), with 2 seconds waiting time after each switch of the magnet. This cycle was repeated 10 times during one analysis. One measurement lasted 12 min per spot. The concentrations were determined using calibration curves obtained by measuring a set of natural basaltic glasses during the same session and under the same analytical conditions (KL2G, VG2, 47963-b, M35, M40 and N72 for one session and KL2G, M40, KE12, M48, KL2Gest, T1-G, ML3B-G, alv-2746, alv-2390 during another session; see Table 3.3 for references). The maximum errors, taking into account the reproducibility over the 10 cycles of analyses and the errors on the regression of the calibration line, were less than 15% for CO_2, 3% for Cl, 4% for S, and 5% for F and H_2O (e.g. Hauri et al., 2002; Rose-Koga et al., 2020). MI with low concentrations of H_2O (<0.3 wt. % H_2O) show H_2O errors less than 30%.

Table 3.3. H_2O, CO_2, F, Cl and S content of standard used for SIMS analysis calibration

Standard	*H_2O (wt%)*	*CO_2 (ppm)*	*F (ppm)*	*S (ppm)*	*Cl (ppm)*	*Reference*
KL2-G	0,015	5,2	177	7,7	26	Jochum et al. (2006)
VG2			243	1440	325	Rose-Koga et al. (2020)
47963-b	1,49		777	776	1356	Kendrick et al., (2012), Kamenetsky et al. (2000), Kamenetsky and Maas (2002)
M35	4,23	1019				Shishkina et al. (2010)
M40	3,03	2183				Shishkina et al. (2010)
KE12			4200	210	3280	Rose-Koga et al. (2020)
M48	0,85	176				Shishkina et al. (2010)
T1-G	0,026	6,3	321	2,6	113	Jochum et al. (2006)
ML3B-G	0,015	4,7	70	1,2	7,5	Jochum et al. (2006)
Alvin-2746-15			123	1449	890	Rose-Koga et al. (2020)
Alvin-2390			300	1270	358	Rose-Koga et al. (2020)

Chapter IV

Compositions of melt inclusions from Puñalica and Sangay volcanoes

4.1. Background

In 2018, we published a paper entitled "Constraining magma sources using primitive olivine-hosted melt inclusions from Puñalica and Sangay volcanoes (Ecuador)" in the journal *Contribution to Mineralogy and Petrology*. In this work, we studied the compositions of Fo_{82-89} olivine hosted melt inclusions from other two volcanoes (Puñalica and Sangay) located in the southern termination of the NVZ. We chose to study such volcanoes because the subducting parameters drastically change with respect to Northern Ecuador (*cf.* Yepes et al., 2016). As I mentioned in Chapter I, the subduction of GFZ, that separates an old oceanic crust to the south from a younger oceanic crust to the north, was situated between Puñalica and Sangay volcano (Yepes et al., 2016) making possible to establish whether or not, the age of the subducting slab had an effect in the composition of primitive magmas. This problem has been discussed during the last two decades, especially in volcanoes from Northern Ecuador, where some geochemical indices (e.g. high Sr/Y, La/Yb, low Ba/Th) suggest the addition of hydrous siliceous melts into the mantle wedge, therefore, changing the composition of primitive magmas. This work examines the possibility that the addition of melts is not only related to the subduction of Carnegie ridge in Northern Ecuador, but also, in southern locations that are affected by the subduction of the young (<25 Ma) portion of Nazca plate north of GFZ. This work included the analysis of melt inclusions hosted in Fo_{87-89} olivines from one calc-alkaline basalt from Sangay volcano (SAN20B, Monzier et al., 1999) that corresponds to one of the most primitive rocks sampled so far in the NVZ. Additionally, this work provide insight into the source lithology at the origin of melt inclusions. Thus, we compare major element composition of melt inclusions with that of experimental melts and concluded that the source of the Ecuadorian melt inclusions were both a peridotite from the mantle wedge and an amphibole-bearing clinopyroxenite located in the lower crust.

4.2. Constraining magma sources using primitive olivine-hosted melt inclusions from Puñalica and Sangay volcanoes (Ecuador)

Contributions to Mineralogy and Petrology (2018) 173:80
https://doi.org/10.1007/s00410-018-1508-8

ORIGINAL PAPER

Constraining magma sources using primitive olivine-hosted melt inclusions from Puñalica and Sangay volcanoes (Ecuador)

Diego F. Narvaez[1,2] · Estelle F. Rose-Koga[1] · Pablo Samaniego[1] · Kenneth T. Koga[1] · Silvana Hidalgo[3]

Received: 5 April 2018 / Accepted: 31 August 2018

Abstract

Constraining arc magma sources at continental arc settings is a delicate task, because chemical signatures from crustal processes obscure the slab and mantle signatures. Here, we present major, trace, and volatile element compositions of olivine-hosted melt inclusions ($Fo_{82–89}$) selected from the most primitive lavas (Mg# > 60) from two Ecuadorian volcanoes (Puñalica and Sangay) situated at the southern termination of the Andean Northern Volcanic Zone. Melt inclusions (MI) from Puñalica are nepheline normative and have basaltic-to-basaltic-andesite compositions (45–56 wt% SiO_2) similar to peridotite-derived melts. Sangay MI is also nepheline normative, with high CaO (up to 16 wt% and $CaO/Al_2O_3 < 1$) and low silica contents (41.9–44.5 wt%) pointing out an amphibole-bearing clinopyroxenite source. Both volcanoes display volatile-rich compositions (up to 6100 ppm Cl, 2200 ppm F, and 6700 ppm S). These MI cannot be related to their host lavas by fractional crystallization, implying that they represent true primitive liquids. The source of Puñalica MI was metasomatized by slab-derived melts that imprints its low Ba/Th, Sr/Th, and high Th/La (average values of 66, 129, and 0.22, respectively). On the contrary, the slab component added to the source of Sangay MI has a higher Ba/Th, Sr/Th, and low Th/La (average values of 261, 517, and 0.11, respectively) which could suggest a relative contribution of aqueous fluids. This dichotomy is related to the presence of the Grijalva Fracture Zone that separates a younger and hotter oceanic crust to the north (below Puñalica) from a colder and older oceanic crust to the south (below Sangay).

Keywords Melt inclusions · Olivine · Primary magmas · Volatile elements · Subduction zone · Ecuador

Introduction

Theoretical and experimental studies on dehydration and melting reactions which occur during subduction have identified two different slab components (e.g., Elliott 2003; Kessel et al. 2005; Spandler and Pirard 2013). On one hand, the dehydration of the subducted slab produces a low-density aqueous phase (hereafter called "fluid"), which is characterized by enrichment in large-ion lithophile elements (LILE, e.g., B, Rb, Ba, and Pb) coupled with low concentrations of high-field strength elements (HFSE, e.g., Nb, Ta, and Zr) and heavy rare-earth elements (HREE, e.g., Yb and Y). On the other hand, the partial melting of the subducted slab (i.e., the altered oceanic crust and/or the sedimentary cover) produces a high-density hydrous siliceous phase (hereafter called "melt"), which is enriched in the so-called fluid-immobile elements, such as the light rare-earth elements (LREE, e.g., La and Ce), HFSE (e.g., Nb), as well as some LILE (e.g., Be, Th). These fluids and/or melts percolate into the hotter and shallower mantle wedge, decreasing its solidus temperature and triggering its partial melting via a porous flow process (Grove et al. 2012). Hence, the trace element signature of primitive arc magmas is typically ascribed to the nature of the subduction component (fluid or melt; e.g., Elliott et al. 1997; Class et al. 2000; Labanieh et al. 2012),

Communicated by Timothy L. Grove.

Electronic supplementary material The online version of this article (https://doi.org/10.1007/s00410-018-1508-8) contains supplementary material, which is available to authorized users.

✉ Diego F. Narvaez
diego.narvaez@etu.uca.fr

[1] Laboratoire Magmas et Volcans, Université Clermont Auvergne, CNRS, IRD, OPGC, 63000 Clermont-Ferrand, France

[2] Departamento de Geología, Escuela Politécnica Nacional, Ladrón de Guevara E11-253, Quito, Ecuador

[3] Instituto Geofísico, Escuela Politécnica Nacional, Ladrón de Guevara E11-253, Aptdo. 2759, Quito, Ecuador

whereas its major element composition is mainly controlled by the mineralogy of the mantle wedge (e.g., Grove et al. 2002).

The dichotomy between fluids and melts issued from the subducted slab was corroborated by numerical models of the thermal regime of subduction zones around the world (e.g., Syracuse et al. 2010). These models take into account the geodynamic parameters of subduction systems (age and geometry of the slab, convergence rate, etc.) as well as a temperature- and stress-dependent mantle rheology, yielding large temperature variations at the slab–mantle wedge interface. The Ecuadorian segment of the Andean Northern Volcanic Zone (NVZ) represents a unique place to test the influence of subduction parameters on the thermal regime and thus the slab component signature of primitive arc magmas. The Ecuadorian arc is characterized by an along-arc change in both the subduction parameters (Yepes et al. 2016) and the isotopic signature of the eruptive products (Ancellin et al. 2017), suggesting that the thermal regime is presumably not the same along the length of the arc from north to south. The thermal regime probably change due to the presence of Grijalva Fracture Zone (GFZ) in the subduction system which separates a younger slab (and probably hotter) to the north from an older slab (and probably colder) to the south.

In this work, we identify the nature of the mantle source that melts to produce the primitive magmas of the Ecuadorian arc and the characteristics of the slab components added to this source. To fulfill these objectives, we focused on the southern part of the Ecuadorian arc. This choice was based on two main reasons: first, this part of the Andean NVZ is developed above a young oceanic crust to the north, which is separated from an older oceanic crust located at the southern termination of the NVZ. Second, given that the differentiation processes (e.g., fractional crystallization, crustal assimilation, magma mixing, etc.) obscure the composition of the primitive magmas, the study of magma sources and slab components should be restricted to the most primitive lavas displaying a high Mg# (e.g., Kelemen et al. 2014). These kinds of primitive magmas are common in the southern part of the Ecuadorian arc, namely at Puñalica and Sangay volcanoes. We sampled and studied the most primitive rock of the Andean NVZ, which is also one of the most primitive samples of the entire Andean arc (e.g., the SAN20B basalt from Sangay volcano, Monzier et al. 1999).

Several regionally oriented whole-rock geochemical studies have investigated the Ecuadorian arc magmatism (Barragan et al. 1998; Bourdon et al. 2003; Garrison and Davidson 2003; Bryant et al. 2006; Chiaradia et al. 2009; Samaniego et al. 2010; Hidalgo et al. 2012; Ancellin et al. 2017). In this contribution, and following the melt inclusion (MI) work of Le Voyer et al. (2008) on volcanoes from the northern part of the Ecuadorian arc (Pichincha and Pan de Azúcar), we performed a similar approach by analyzing the major, trace element, and volatile contents of a group of selected MIs trapped in the Mg-rich olivines hosted in primitive lavas from the southern part of the Ecuadorian arc (Puñalica and Sangay volcanoes). This work enabled us to constrain the mantle and slab components of the most primitive magmas studied in the NVZ and to relate them to the particular geodynamical setting of this part of the Andean arc. In addition, the new Sangay MI data represent a new example of primitive, Ca-rich, Ne-normative MIs in a context of a volcanic arc constructed on a thick continental crust.

Geodynamical and geological contexts

Geodynamical setting of the Ecuadorian Andes

The Northern Volcanic Zone (NVZ) of the Andes stretches from ~6°N to ~2°S along the cordilleras of Colombia and Ecuador, and is situated at the convergent zone where the oceanic Nazca plate plunges under the continental South American plate (Fig. 1a). In Ecuador (i.e., from 1°N to 2°S), the relatively young Nazca plate (12–16 Ma; Gutscher et al. 1999; Sallarès and Charvis 2003) converges at an azimuth of N85°E, a rate of 5–6 cm/year (Kellogg et al. 1995) and a subduction angle of 25° (Guillier et al. 2001). In addition, at these latitudes, the subducting Nazca plate hosts the Carnegie ridge, a 200–250 km-wide, 2 km-high submarine mountain range issued from the activity of the Galápagos hotspot. Based on geodynamic reconstruction, Sallarès and Charvis (2003) suggest that the portion of the Carnegie ridge involved in the subduction system is younger than 10 Ma. Due to its morphology, the sedimentary blanket of the subducting Carnegie ridge is relatively thin (maximum 200–400 m, Michaud et al. 2005; Proust et al. 2016). To the south (i.e., roughly to the south of 2–3°S), the subducting slab is older (25–30 Ma; Gutscher et al. 1999). The boundary between these two contrasting domains is the Grijalva Fracture Zone (GFZ), which consists of a 500 m-high escarpment separating a "young" crust which originated in the Galápagos spreading center to the north, and a relatively "old" crust formed at the East Pacific rise to the south. The landward extrapolation of this structure was recently identified by Yepes et al. (2016) in the southern part of the Ecuadorian volcanic arc (Fig. 1b). These authors also show that the slab displays a bend around the GFZ that abruptly increases the angle of subduction from 20° to 25° to the north of the GFZ to 30°–35° towards the south (Yepes et al. 2016).

The Ecuadorian segment of the NVZ is characterized by at least 84 volcanic centers of Pleistocene and Holocene age, which are distributed along four principal alignments constructed over different terranes of contrasting ages and lithologies (Hall et al. 2008; Hidalgo et al. 2012). The crustal

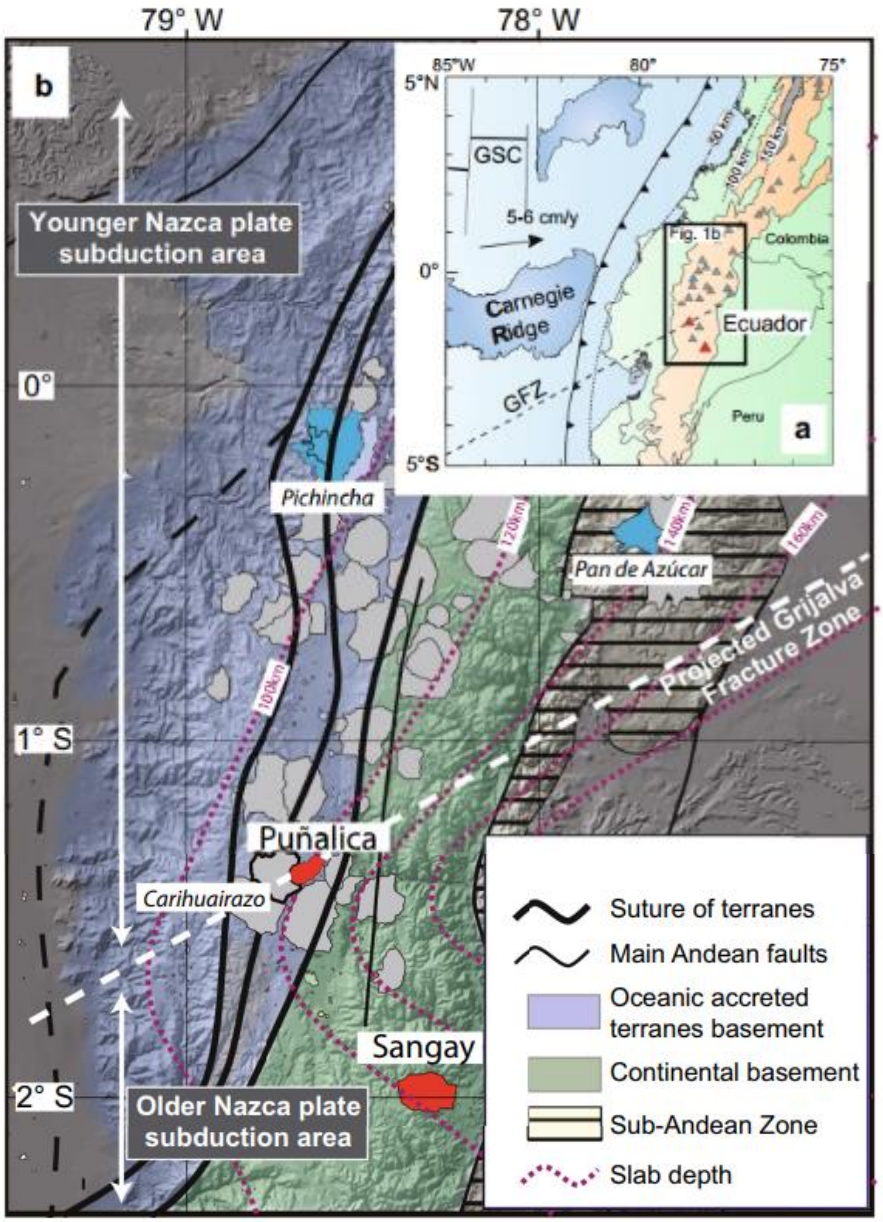

Fig. 1 **a** Geodynamical setting of Ecuadorian arc. **b** Schematic map of the main geological zones in Ecuador [modified from Jaillard et al. (2008)]. Analyses of melt inclusions were performed in rock samples from Sangay and Puñalica volcanoes (in red). Puñalica volcano is a small, young edifice associated with the older Carihuairazo volcano. Pichincha Volcanic Complex (Pichincha) and Pan de Azúcar volcanoes, which are mentioned in the text, are in cyan. White dashed line is the surface projection of the Grijalva fracture zone (GFZ) that affects subduction and separates old oceanic lithosphere to the south from young oceanic lithosphere to the north. This projection is based on the recent seismological work of Yepes et al. (2016) studying the flexure of the subducted slab along the GFZ

thickness is inferred to be > 50 km beneath the active volcanic arc (Feininger and Seguin 1983; Prevot et al. 1996; Guillier et al. 2001). Besides the primitive nature of the Puñalica and Sangay lavas, we choose these volcanoes for this study, because they are a priori constructed on slab segments with different ages and seismic characteristics (Yepes et al. 2016). Puñalica is roughly above (or immediately to the north of) the GFZ projection, while Sangay lies to the south of this boundary. We expect that the presence of the GFZ in the Ecuadorian subduction system (1) might act as a preferred fluid transport region, and (2) should allow us to identify different slab inputs from "young" and "old" slabs into the mantle wedge.

Geological context of Sangay and Puñalica volcanoes

Sangay volcano (5230 m above sea level—a.s.l.) is the southernmost active edifice of the NVZ. It was constructed over the last 500 ka by three successive edifices (Monzier et al. 1999) separated by two major sector collapses whose deposits outcrop to the east, on the upper Amazonian plain. Sangay is thought to be located ~ 120–130 km (see red-dotted line in Fig. 1b) above an old, seismogenic slab to the south of the GFZ (Monzier et al. 1999; Yepes et al. 2016) and is constructed on continental crust that consists of felsic and mafic igneous and metamorphic rocks (Aspden

and Litherland 1992; Pratt et al. 2005). In this work, we focus on the primitive basalt (SAN20B, Mg# 69, Monzier et al. 1999), from the Sangay II edifice, roughly dated at between 100 and 50 ka. *Puñalica* volcano (3988 m a.s.l.) is a 300 m-high, cone-shaped edifice slightly elongated in a north–south direction. It is constructed on the eastern flank of the Late Pleistocene Carihuairazo volcano (Ordóñez 2012). Clapperton (1990) and Ordóñez (2012) described a series of lava flows from Puñalica that overly a sequence of tephra fallout deposits from the neighboring Chimborazo volcano (Samaniego et al. 2012). Based on this stratigraphic information, we expect an age younger than 18–25 ka for this edifice. The depth of the subducted slab at this location is ~ 120 km with the inland projection of the GFZ roughly below Puñalica volcano (Yepes et al. 2016). As for Sangay, we selected the most primitive lavas and tephras from Puñalica, which correspond to scoriaceous bombs sampled on the Puñalica cone (CAR83A, CAR96A, and CAR113B), and a lava flow (RIO17A) that outcrops 4 km away from Puñalica's crater.

Methodology

Sample selection, olivine preparation, and heating experiments

The chosen rocks (CAR83A, CAR96A, CAR113B, and RIO17A from Puñalica and SAN20B from Sangay volcano) were crushed and the 0.4–1.5 mm fraction was separated. We picked about 500 olivine crystals under a binocular microscope. We used crystal-bound to attach crystals onto glass slides to polish and select olivines in which MIs were observed (about 100 crystals). We then selected about 50 crystals with MIs bigger than 30 µm. All MIs were crystallized and presented bubbles. Thus, we performed homogenization using a Vernadsky-type microscope heating stage following the method described by Le Voyer et al. (2010). A detailed description of MI homogenization procedure and analytical methods is provided in Online Resource 1.

Post-entrapment crystallization correction

The composition of a MI can be modified by crystallization of olivine from the wall of the MI after its formation, by crystallization of minerals inside the MIs during slow cooling, or by over-dissolution of the olivine wall during heating stages (e.g., Danyushevsky et al. 2000). To account for these effects, after homogenization of the MIs, the major element compositions of the MIs were corrected numerically by dissolving/adding equilibrium olivine through iterative steps, recalculating the melt composition at every step until the melt reached a Fe–Mg exchange equilibrium with the host olivine (Le Voyer et al. 2008). We used a Kd^{Fe-Mg} model to calculate the olivine composition added to the MI (Toplis 2005). For the model calculation, we adopted the average homogenization temperature (1218 ± 15 °C, min–max temperature range of 1143–1309 °C) and an oxidation state calculated following Wallace and Carmichael (1992). The speciation of sulfur was measured using the S^{2-} and S^{6+} peak positions in the MIs obtained by the electron microprobe (Jugo et al. 2005). The $Fe^{3+}/\sum Fe$ ratios for Puñalica MIs vary from 0.16 to 0.23, while, for Sangay, the ratio is 0.28 for all MIs (Table ESM1, Online Resource 1). The resulting post-entrapment olivine crystallization correction for most MIs was less than 10%, except for "BC" and "K" MIs that reach 17 and 22%, respectively. In spite of the large corrections for these two MIs, we kept them in our database, because their compositions are coherent with the others, and thus, they do not change our conclusions.

Results

The data obtained for major elements by electron microprobe (EMP), volatile element concentrations by SIMS, and trace element analysis by LA-ICPMS are provided in Table 1. We have taken specific care over the volatile element analysis in the MI (e.g., fluorine and chlorine) and post-analysis verifications of their quality such as the identification of misplaced beam-craters.

Whole-rock petrological background of Sangay and Puñalica

Sangay samples display a high-K calc-alkaline magmatic series spanning from basaltic andesites to dacites (53.6–68.1 wt% SiO_2, Fig. 2a) and include a primitive basalt (SAN20B) that plots at lower silica content than the whole Sangay series (Figs. 2b, 3). This latter is the most primitive basalt that has so far been sampled in the NVZ (Monzier et al. 1999) with 50.3 wt% SiO_2, 11.1 wt% MgO, and a Mg# of 69 (Figs. 2b, 3; Table 2). The high Ni and Cr contents (273 ppm Ni, 410 ppm Cr) and the relatively low Al_2O_3 concentration (14.8 wt%) corroborate its primitive character. The trace element abundances in SAN20B basalt show a typical arc pattern (e.g., enriched LREE and LILE, and negative HFSE anomaly) and consistently plot at the primitive end of the Sangay series (Fig. 3). It is worth noting that the Nb content in SAN20B basalt is slightly higher than that of the other NVZ basalts and basaltic andesites. Monzier et al. (1999) interpreted this feature as the result of partial melting of a relatively enriched mantle source. SAN20B mineralogy consists of phenocrysts of Mg-rich olivine (7 vol%; up to 1 mm), and euhedral clinopyroxene (3 vol%, 0.4–0.5 mm) surrounded by an intersertal groundmass consisting of

Table 1 Major, trace element, and volatile concentrations of olivine-hosted melt inclusions from Puñalica and Sangay lavas

	Sangay volcano								Puñalica volcano							
	SAN20B								CAR96A (Group 3)							
	A	B	C	D	E	El	F	G	AA	AB	AC	AE	AF	AG	AG1	AH
SiO_2	42.43	42.76	44.45	42.83	41.95	42.95	43.9	42.3	56.16	48.01	53.82	48.22	49.95	51.99	52.63	53.31
TiO_2	1.53	1.7	1.48	1.36	1.8	1.65	1.45	1.41	0.41	0.75	0.53	0.67	0.68	0.88	0.63	0.43
Al_2O_3	19.11	18.44	16.59	17.09	18.53	18.82	18.02	18.75	15.32	14.41	15.88	14.67	13.25	15.93	15.03	14.06
FeOt	8.92	9.02	10.56	10.16	8.75	7.66	8.82	8.51	8.39	15.16	9.37	14.26	12.1	8.48	11.31	10.23
MnO	0.17	0.14	0.1	0.06	0.22	0.12	0.22	0.15	0.08	0.03	0.22	0.13	0.16	0.11	0.16	0.13
MgO	8.6	8.17	8.72	9.11	7.69	6.38	7.53	8.3	5.44	9.52	6.07	9.19	8.01	5.77	7.63	6.74
CaO	13.25	14.49	13.32	14.21	15.25	16.05	14.33	14.5	7.4	6.77	7.66	7.48	10	11.64	6.14	8.67
Na_2O	4.24	3.73	3.35	3.55	4.25	4.62	4.17	4.28	4.48	3.48	4.17	3.5	3.83	3.6	3.95	4.14
K_2O	1.32	1.12	0.99	1.02	1.19	1.31	1.13	1.22	1.97	1.53	1.91	1.54	1.72	1.36	2.06	1.87
P_2O_5	0.44	0.45	0.44	0.62	0.37	0.44	0.44	0.57	0.35	0.34	0.36	0.33	0.3	0.25	0.47	0.42
Total	94.56	94.75	93.82	95.3	96.39	98.36	96.41	92.92	99.27	99.15	99.68	98.35	97.6	99.3	99.52	99.46
H_2O			3.17	2.6					0.09	0.1	0.09	0.1	0.07	0.07		0.07
CO_2 (ppm)			2776	6088					252	625	201	658	826	123		308
F (ppm)	913[b]	843[b]	720	627	963[b]	1183[b]	791[b]	873[b]	1626	1448	1492	1222	1388	1061	2187[b]	1194
Cl (ppm)	2257[b]	2052[b]	1636	1776	2193[b]	2227[b]	1941[b]	2213 [b]	5947	5813	5305	4958	5985	3928	5418 [b]	5629
S (ppm)	5417 [b]	3857 [b]	4029	3836	4519 [b]	4480 [b]	4552 [b]	5473[b]	2467	3140	2829	3109	4805	2152	2590[b]	4434
Sc	25.5	43.2	28.2	27.8	42.3		38.5		14.5	17.1	16.2	15	35.7	46.1		34.7
V	393.3	407.2	317.7	355.8	414.1		382.3		189.2	375.1	219.4	237.4	306.9	204.9		173.1
Rb	11.6	16.1	13.4	12.3	17.3		15.7		28.4	21.7	28.1	21.1	22.1	19.1		24.6
Sr	1356.4	1360.1	1123.4	1252.2	1420.3		1485		1459	1280.6	1332.7	1188.1	1351.4	1279.8		1290.5
Nb	14.2	13.2	10.3	13.4	15.5		15.1		3.9	3.3	4.2	3.4	3.5	3.1		3.6
Ta	1.1	1.4	0.4	0.8	0.8		0.8		<0.192	<0.17	0.3	0.2	0.3	0.2		0.2
Ba	758.6	688.6	549	613.8	755.4		698.4		720.9	728.8	712.7	639.6	651.8	554.2		700.5
La	23.5	24.4	19.1	22	26.4		23.3		44	47.8	48.9	46.7	40.1	41.8		50.5
Ce	58.2	54.1	44.1	48.8	61.3		57.5		85.9	102.1	97.2	93.1	85	86.7		98.9
Pb	8.2	8.3	7.1	7.8			8.3		8.5	8.4	9.8	8.1	7.5	9.1		8.6
Nd	29.3	28.8	25.6	26.6	35.9		23.7		41.4	41.8	46.3	43.3	38.2	47.5		45.4
Sm	4.7	9	4.7	7.2	9.7		10		7.3	9.7	7	7.2	7.1	8		7.4
Zr	96.3	109.9	82.3	88.3	112.5		96.8		97.4	93.9	97.8	89.8	89.6	105.6		100.1
Eu	2	1.7	1.5	1.5	1.9		2		2	1.5	2	2	1.8	2.4		1.8
Gd	3.7	3.6	4.3	5.6	4.8		2.9		4.1	3	4.9	4.6	2.6	5.4		4.5
Dy	2.7	4	3.1	3.1	5.2		3.6		3.3	3.1	2.9	2.9	3.1	4.5		3.3
Yb	1.7	2.4	1.3	1.6	1.7		1.1		1.2	0.7	1.8	1	1.2	2.1		0.8

Table 1 (continued)

	Sangay volcano								Puñalica volcano							
	SAN20B								CAR96A (Group 3)							
	A	B	C	D	E	E1	F	G	AA	AB	AC	AE	AF	AG	AG1	AH
Th	2.8	2.5	2.1	2.5	3.2		2.5		10.5	10.4	10.4	10.2	9.5	8.5		11.3
U	1	1.3	0.8	1	0.8		0.3		3.3	3.5	3.3	3.4	2.9	2.6		3.5
Pr	6.4	6.9	5.9	6.5	7.5		7.8		9.8	11.1	10.9	10.7	9	10.8		11.4
Y	15.4	19.2	14.8	15.7	20		14.2		11.3	12.9	16.6	13.4	14.6	22.6		14
Lu	< 0.19	< 0.48	0.3	0.4	< 0.32		< 0.24		< 0.174	0.3	0.3	0.2	0.4	0.4		0.2
Fo olivine	0.89	0.88	0.87	0.88	0.88	0.88	0.88	0.89		0.82	0.83	0.83	0.83	0.83	0.83	0.83
Ne	19.40	17.06	14.90	16.24	19.44	21.14	19.07	19..58		4.10		4.80	7.90	2.80		2.00
Hy									8.65		1.27				3.09	

	Puñalica volcano																
	CAR96A (Group 3)				CAR113B (Group 2)												
	AH1	AI	AJ	AK	H	H1	I	J	J1	K[a]	K2	L	M	M1	N	O	P
SiO_2	53.27	49.16	51.12	48.3	48.05	47.52	52.35	48.17	49.88	53.62	46.26	49.77	50.01	49.54	48.18	48.87	49.38
TiO_2	0.46	0.79	0.82	0.72	0.74	0.65	0.78	0.79	0.85	0.86	0.79	0.74	0.75	0.81	0.86	0.79	0.83
Al_2O_3	13.3	15.07	15.43	14.61	15.94	16.16	18.59	17.13	17.3	17.33	16.74	16.57	17.18	16.53	16	16.21	17.19
FeOt	10.85	12.82	9.46	12.81	12.72	12.92	6.91	11.01	9.71	9.36	14.38	10.63	10.45	11.12	12.01	11.16	9.78
MnO	0.06	0.18	0.18	0.13	0.04	0.16	0.11	0.17	0.11	0.21	0.08	0.07	0.22	0.24	0	0.11	0.16
MgO	7.33	8.43	6.27	8.45	9.22	9.35	4.91	8.02	7.04	6.11	8.77	7.68	7.36	7.86	8.81	8.44	7.09
CaO	8.68	8.36	10.71	9.32	8.53	8.74	9.74	9.78	9.65	6.88	7.88	9.27	9	8.77	8.88	9.74	9.74
Na_2O	3.98	3.23	4.14	3.69	3.2	3.05	4.47	3.23	3.63	3.75	3.36	3.6	3.27	3.6	3.52	3.12	4.06
K_2O	1.63	1.75	1.67	1.65	1.26	1.24	1.84	1.36	1.55	1.51	1.31	1.57	1.45	1.42	1.44	1.36	1.45
P_2O_5	0.45	0.21	0.2	0.3	0.29	0.21	0.31	0.34	0.28	0.37	0.44	0.1	0.31	0.12	0.3	0.19	0.31
Total	98.57	100.68	97.48	97.92	96.62	96.55	98.18	95.04	95.23	98.99	101.04	97.62	97.89	97.69	95.57	95.23	98.79
H_2O			0.07	0.06	1.63		0.33	2.35	3.07				1.98		2.53	2	
CO_2 (ppm)			296	512	2053		262	802	376				645		29	803	
F (ppm)	1412[b]	596	950	922	503		624	518	699		655[b]	673	483	721[b]	793	593	673[b]
Cl (ppm)	5252 [b]	3460	5458	4927	4021		5187	4598	4037		4137 [b]	5861	4318	5678 [b]	5849	4710	5430 [b]
S (ppm)	4362[b]	1151	4331	4751	3818		1959	4701	6020		1635[b]	4396	4271	4856[b]	6738	5020	3798[b]
Sc		29.6	31.9	27	21.4		20.4	23.1	19.9	16	22.1	21.6	20.5		21.3	20	
V		274.5	190.5	240.9	216.2		183.2	216.4	214.2	166.3	251.8	199.8	206.6		292.3	214.3	
Rb		23.6	23.5	22.9	21		30.8	22.6	17.8	25.3	22.9	24.6	21.3		23.9	17.2	
Sr		919.1	1298.8	1240.6	1129.3		1487.1	1228.6	1118	1021.5	935.8	1257.7	1110.7		1168	1145.5	
Nb		3.4	3.4	3.3	3.6		4.6	3.4	2.7	3	3.6	3.8	3.2		3.3	2.9	

Table 1 (continued)

	Puñalica volcano																
	CAR96A (Group 3)				CAR113B (Group 2)												
	AH1	AI	AJ	AK	H	H1	I	J	J1	K[a]	K2	L	M	M1	N	O	P
Ta		0.2	0.2	0.2	< 0.20		0.2	0.2	0.1	0.1	< 0.22	< 0.120	0.2		0.2	0.1	
Ba		558	611.1	633.2	571.9		732.4	583.9	507	3275.6	620.8	626.6	527.7		579	502.6	
La		41.8	38.9	44.7	28.9		37.4	31	31.5	26.3	44.1	30.4	26.5		28	31.9	
Ce		84.8	78	87.2	58.2		73.7	61.9	63.7	49.2	82.8	63.1	54.6		56.4	63.7	
Pb		5.5	7.9	7.7	8		10.1	8.2	6.2	6.3	7.9	9.4	7.5		8.2	6.9	
Nd		41.2	36.9	41.2	29.4		33.3	30.2	30.8	24.3	39.5	29	26.2		27.7	29.2	
Sm		7.3	6.5	7	4.1		5.8	5.1	4.8	4.3	6.1	5.9	4.9		5.2	5.2	
Zr		92.8	86.1	88.9	77		98.6	77.3	70.6	66.8	83.1	82.5	72.3		77.9	68.6	
Eu		1.8	1.5	1.8	1.6		1.4	1.4	1.5	1.2	1.4	1.4	1.2		1.3	1.4	
Gd		5.6	4	4.5	4.2		3.9	3.8	3.3	3	4	4.2	3.1		3.5	3.4	
Dy		3	3.2	2.7	2.6		2.9	2.6	2.5	2	1.8	2.6	2.4		2.6	2.5	
Yb		1.4	1.3	1.2	2.2		1.6	1.5	1.4	1.1	1.7	1.2	1.5		1.1	1.3	
Th		8.9	8.8	9.7	6		7.7	6.4	7.6	5.3	8.3	6.2	5.7		5.8	7.5	
U		3	2.8	3	1.9		2.6	1.9	2.2	1.7	3.1	1.9	1.7		1.7	2.4	
Pr		9.7	9	10	6.8		8.4	7.3	7.4	6	10.4	7.4	6		6.8	7.4	
Y		14	15.1	14	13.2		15.1	13.5	12.2	11.6	14.5	14	12.3		12.8	13.1	
Lu		0.2	0.2	0.2	< 0.182		0.2	0.2	0.2	0.2	0.3	0.2	0.2		0.2	0.2	
Fo olivine	0.83	0.83	0.83	0.83	0.84	0.84	0.85	0.84	0.84	0.83	0.83	0.85	0.84	0.84	0.84	0.85	0.85
Ne	0.5	3.59	7.23	8.55	3.69	4.28	5.56	4.97	4.67		6.13	5.21	1.22	4.28	6.18	3.84	7.23
Hy										18.03							

Puñalica volcano																	
RIO17A (Group 2)														CAR83A (Group 1)			
	Q	R	S	S1	T	U	U1	V	V2	W	X	Y1	Z	BA	BB	BC[a]	BD1
SiO_2	50.34	49.98	51.43	54.12	53.73	51.65	50.74	53.73	51.46	45.26	50.39	48.19	52.87	54.59	54.29	53.51	55.25
TiO_2	0.82	0.7	0.62	0.56	0.76	0.86	0.77	0.68	0.85	0.79	0.67	0.69	0.81	0.84	1.05	0.91	0.98
Al_2O_3	17.72	16.01	17.57	16.55	18	18.23	17.65	17.51	17.2	15.06	17.31	16.43	18.02	18.97	19.7	18.77	18.66
FeOt	9.65	11.06	8.3	7.77	6.36	7.14	8.38	7.39	9.62	15.08	9.13	13.16	6.97	6.18	5.43	7.14	5.58
MnO	0.14	0.12	0.18	0.15	0.16	0.15	0.03	0.1	0.01	0.11	0.21	0.05	0.07	0.07	0.24	0.1	0.07
MgO	6.78	7.27	5.69	5.34	4.64	5.45	6.37	5.33	6.89	10.2	6.57	8.4	5.3	4.28	3.99	4.97	3.94
CaO	8.43	9.14	9.67	9.49	9.59	10.36	9.63	9.22	8.52	8.48	9.79	7.63	9.8	8.59	9.35	8.18	8.21
Na_2O	4.25	3.81	4.37	3.97	4.54	4.07	4.3	4.19	3.76	3.34	4.02	3.68	4.32	4.85	4.27	4.67	5.26
K_2O	1.67	1.52	1.84	1.73	1.86	1.72	1.77	1.6	1.44	1.39	1.64	1.48	1.7	1.5	1.38	1.43	1.86

Table 1 (continued)

Puñalica volcano																	
RIO17A (Group 2)														CAR83A (Group 1)			
	Q	R	S	S1	T	U	U1	V	V2	W	X	Y1	Z	BA	BB	BC[a]	BD1
P_2O_5	0.21	0.39	0.33	0.31	0.35	0.38	0.36	0.25	0.26	0.29	0.27	0.29	0.15	0.14	0.3	0.32	0.18
Total	99.4	99.4	98.5	99.9	99.9	99.3	98.9	99.1	99.6	97.4	98.3	97.9	99	101.6	99.6	100.6	102.2
H_2O	0.09	0.11		0.08	0.13	0.11		0.12	0.12		0.28			0.06			0.11
CO_2 (ppm)		166	262	160	89	324		101	860		262			51			4307
F (ppm)	629	635	656	687	610	731	864[b]	700	712	923[b]	645	703[b]	1008[b]	439	558[b]	533[b]	504
Cl (ppm)	4388	5548	4563	4265	4876	5796	6112 [b]	5333	4123	5475 [b]	5839	5449 [b]	5717 [b]	1533	1625	1352 [b]	1948
S (ppm)	1457	4009	3586	2310	2970	3282	3737[b]	2540	3165	3414[b]	4335	906[b]	2829[b]	1571	609	1248[b]	1562
Sc	18.8	20.8	21.3	20.4	21.1	21.8		15.8			20.5			21.4		17.6	16.6
V	209.3	175	174.2	183.9	190.7	209.4		180			178.7			205.4		180.4	201.6
Rb	28	25.8	23.7	25.4	27.9	28.1		23.7			23			29.9		28.6	33.8
Sr	1025.9	1184.7	1208.1	1249	1216.1	1224.6		1088.3			1249.3			584.6		562.6	584.8
Nb	3.6	3.3	3.3	3.6	3.7	4		3.2			3.5			4		3.6	4.1
Ta	0.2	0.2	0.2	<0.134	0.2	0.2		0.1			0.2			<0.211		0.3	0.3
Ba	582.8	586.2	577.8	639.8	630.4	608.9		587.6			602.2			483		453.8	597.1
La	24.2	27.7	36.5	37.5	25.7	29.7		23.4			28.3			12.1		11.4	12.7
Ce	50.1	55.8	72	74.6	52.7	59.9		51.6			59.2			25.9		25.7	29.1
Pb	7.8	7.7	7.6	7.7	8.2	8.5		9.6			8.3			7.9		5.9	7.4
Nd	23.8	27	34	34.9	25.8	28.9		23.1			27.6			13.5		13.9	13.9
Sm	4.4	4.8	6	6.5	4.8	5		4.3			4.8			2.9		2.3	4.2
Zr	86	80.5	85	89.2	83.8	90.1		79.3			79.6			88.8		83	89.3
Eu	1.2	1.3	1.5	1.2	1.3	1.4		1.4			1.5			0.9		0.9	0.9
Gd	3.1	3.3	3.9	4.5	3.3	3.6		3			3			3.6		2.3	2
Dy	2.3	2.6	2.9	3.3	2.3	2.8		1.9			2.7			2.9		2.2	2.6
Yb	1.2	1.4	1.5	1	1.4	1.6		0.8			1.3			1.5		0.6	0.9
Th	5.3	5.8	8.7	9.4	5.6	6.3		5.1			6.1			2.8		2.8	3.1
U	1.7	1.8	2.7	3	1.8	2		2			1.9			1.1		1	1.2
Pr	5.9	6.5	8.4	8.9	6.3	7		6			6.9			3.6		3.2	3.4
Y	12.2	13.3	14.6	15.3	12.5	14.2		11.3			12.8			11.5		10.3	10.6
Lu	0.2	0.2	0.3	0.2	0.2	0.2		0.2			0.2			0.2		0.1	<0.19
Fo olivine	0.85	0.84	0.84	0.84	0.85	0.86	0.86	0.85	0.85	0.84	0.85	0.83	0.86	0.83	0.84	0.83	0.84
Ne	6.29	4.79	6.96		3.39	4.82	7.42	0.60	0.79	10.10	6.62	5.45	4.08	1.32		0.94	3.03
Hy				1.28											5.78		

clinopyroxene and plagioclase microlites. Olivine phenocrysts frequently include Cr-rich spinel inclusions. The Mg-rich olivines ($Fo_{86–90}$) from this sample were selected for this study.

Puñalica lavas are medium-K calc-alkaline basaltic andesites and andesites (54.6–60.1 wt% SiO_2, Figs. 2, 3; Table 2), including some primitive andesites characterized by Mg# > 60. On the basis of the MgO content, two groups are identified. A first group includes samples with low silica content (up to 57 wt% SiO_2) and variable MgO concentrations (4.3–7.8 wt%), and a second group includes more differentiated magmas (58–60 wt% SiO_2) and homogeneous MgO contents (4.8–6.2 wt%). It is worth nothing that the first group displays large incompatible elements variations, namely for LREE (e.g., 15–35 ppm La) and LILE (4–9 ppm Th). The selected Puñalica samples correspond to both groups (light-gray shaded area, Figs. 2b, 3a; Table 2). They show variable phenocrysts' abundances of olivine ($Fo_{80–86}$), orthopyroxene, clinopyroxene, and plagioclase surrounded by an interstitial groundmass that includes plagioclase and clinopyroxene microlites. Olivine (up to 7 vol%, up to 1 mm) forms euhedral and subhedral phenocrysts with homogeneous compositions.

Melt inclusion compositions

Major elements

Olivine-hosted ($Fo_{86–89}$) MIs from Sangay volcano are nepheline normative (from 14.9 to 21.1, *Ne*, Table 1) and are characterized by restricted concentrations in SiO_2 (from 41.9 to 44.5 wt%, expressed in a volatile-free basis, Fig. 3), MgO (6.4–9.1 wt%), and FeOt (7.7–10.6 wt%), as well as homogeneous Mg# values ranging from 59 to 64. Sangay MIs mostly plot in the basaltic field belonging to a shoshonitic series (Fig. 2). In most Harker diagrams, Sangay MI compositions do not form an extension of the whole-rock trend (Fig. 3), showing higher contents in Al_2O_3, CaO, and TiO_2 than their host lava. Sangay MI represent, together with Pan de Azúcar MIs studied by Le Voyer et al. (2008), the most SiO_2-poor magmas found in the Ecuadorian volcanic arc. Olivine-hosted ($Fo_{82–86}$) MIs from Puñalica display high-K calc-alkaline basaltic-to-basaltic andesitic compositions (Fig. 2), which are characterized by a variable content of SiO_2 (from 46.3 to 56.2 wt%), MgO (3.9–10.2 wt%) and FeOt (5.4–15.2 wt%) (Fig. 3). The Mg# values vary from 53 to 58. As at Sangay, Puñalica MI have lower SiO_2 contents than Puñalica whole rocks and do not form a continuous trend with them. Puñalica MI show higher contents of K_2O, Na_2O, FeOt, and lower contents of TiO_2 and CaO than the values expected from the whole-rock trend at the same SiO_2 content (Figs. 2, 3).

Table 1 (continued)

Total given are the measured values. Major elements are the corrected values after wall olivine crystallization

Ne and *Hy* are CIPW normative composition

[a]Samples with > 10% of olivine crystallization correction

[b]F, Cl, and *F* values from EMP, and the other values for these volatiles are from SIMS

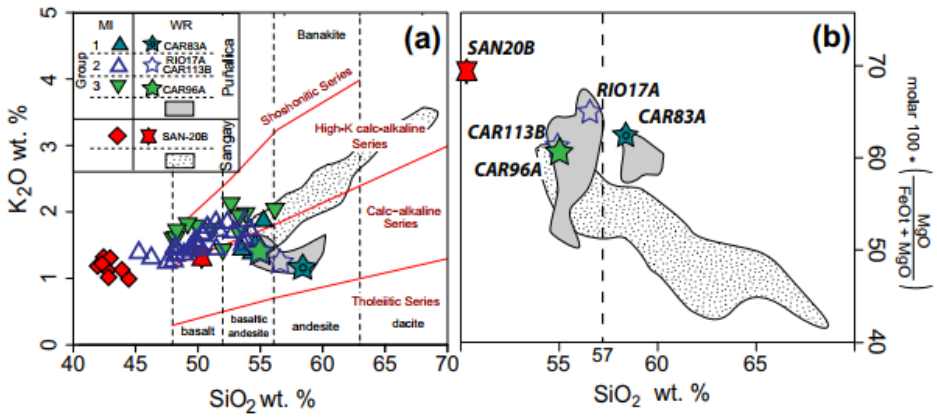

Fig. 2 **a** K_2O vs. SiO_2 classification diagram (Peccerillo and Taylor 1976) of melt inclusions (homogenization-corrected compositions; colored diamonds and triangles) and whole rocks (star symbols colored to the same as their corresponding MI and dotted/shaded areas) of Sangay and Puñalica volcanoes. 50 melt inclusion compositions are plotted; 7 belonging to SAN20B sample from Sangay volcano and the others belonging to Puñalica samples. Groups 1, 2, and 3 in the legend box correspond to the groups defined for Puñalica MI (see text for more details). **b** Molar 100*MgO/(FeOt + MgO) vs. SiO_2 wt% for melt inclusions and whole-rock lavas from Sangay and Puñalica volcanoes. Whole-rock data for Puñalica are from Schiano et al. (2010) and this work and the Sangay data are from Monzier et al. (1999)

Trace and volatile elements

Sangay MI show trace element patterns typical of arc lavas and similar to those of Puñalica MI, except for the relatively high values of Ti and HFSE (e.g., Ta and Nb), expressed as a less marked negative anomaly in Nb (Fig. 4d). MIs from Sangay have lower content of Rb, Th, K, and higher content of Ti compared to Sangay whole rocks. Sangay MI have $(La/Yb)_N$ values ranging from 7 to 15 (normalized to primitive mantle, Sun and McDonough 1989). Puñalica MI is also enriched in LILE (e.g., Ba, K, Rb, and Sr) and depleted in HREE (e.g., Yb) relative to MORB. The enrichment in LREE (e.g., La) relative to HREE is represented as $(La/Yb)_N$ and ranges from 5 to 45. These MI also display a marked negative anomaly in HFSE (e.g., Nb, Fig. 4a–c). Three different MI groups are distinguished at Puñalica volcano based on trace and volatile element concentrations (see below).

Sangay MI is volatile-rich, with H_2O between 2.6 and 3.2 wt% and CO_2 between 2776 and 6088 ppm. Puñalica MIs vary from 0.05 to 3.1 wt% H_2O and from 29 to 4307 ppm CO_2 (Table 1). H_2O concentrations measured in MIs are considered as minimum values, because MIs are leaky containers for H_2O (Chen et al. 2011; Gaetani et al. 2012). CO_2 concentrations are also considered minimum, because MIs could suffer from pre-entrapment CO_2 degassing due to degassing of CO_2 from the magma at depth (e.g., Métrich and Wallace 2008).

Sangay MI is characterized by relatively high S concentrations (3836–5473 ppm), which overlap with the S concentrations of some Puñalica MI (most of them from CAR113B, Fig. 5c; Table 1). Melt inclusions from RIO17A have less S, between 2310 and 4335 ppm, with two inclusions more degassed in S at 906 and 1457 ppm. Samples from CAR83A have the least S (between 609 and 1571 ppm, Fig. 5c). The total range of S contents in MIs from Sangay and Puñalica (609–6738 ppm) is similar to that of MIs from other continental subduction zones such as Colima, Mexico (300–4900 ppm S; Vigouroux et al. 2008) and Mt. Shasta, California (in MIs from Basaltic Andesites, BA: 512–4618 ppm S; Le Voyer et al. 2010). Sangay MI is richer in F (627–1183 ppm) than MIs from Puñalica (samples CAR113B, RIO17A, and CAR83A, 439–1008 ppm, Fig. 5a; Table 1). However, CAR96A MIs from Puñalica show the highest F concentration (Fig. 5a), and when compared to other continental arc settings, MIs are only exceeded for those from Colima, Mexico (up to 8100 ppm F; Vigouroux et al. 2008). Cl is the most contrasted volatile element. Sangay and Puñalica CAR83A MIs have low and similar Cl concentrations (1636–2257 ppm and 1352–1948 ppm, respectively), while all other Puñalica MI are Cl-rich, with concentrations between 3460 and 6112 ppm (Fig. 5b). The Cl compositions of most Puñalica MI are extremely high, only exceeded by rare MIs from Izu (up to 9400 ppm; Straub and Layne 2003), Aeolian (Métrich et al. 1993, 2004; Vaggelli et al. 1993; Clocchiatti et al. 1994; Schiano et al. 2004; Spilliaert et al. 2006; Collins et al. 2009; Rose-Koga et al. 2012; Sorbadère et al. 2013a), and Vanuatu arcs (Sorbadère et al. 2011, 2013a, b). Overall, the halogen compositions (F and Cl) of the Sangay and Puñalica MIs are high for continental arc settings, in the same range as that of the MIs from alkaline basalts of Mt. Shasta and from andesites of Izu volcanic front.

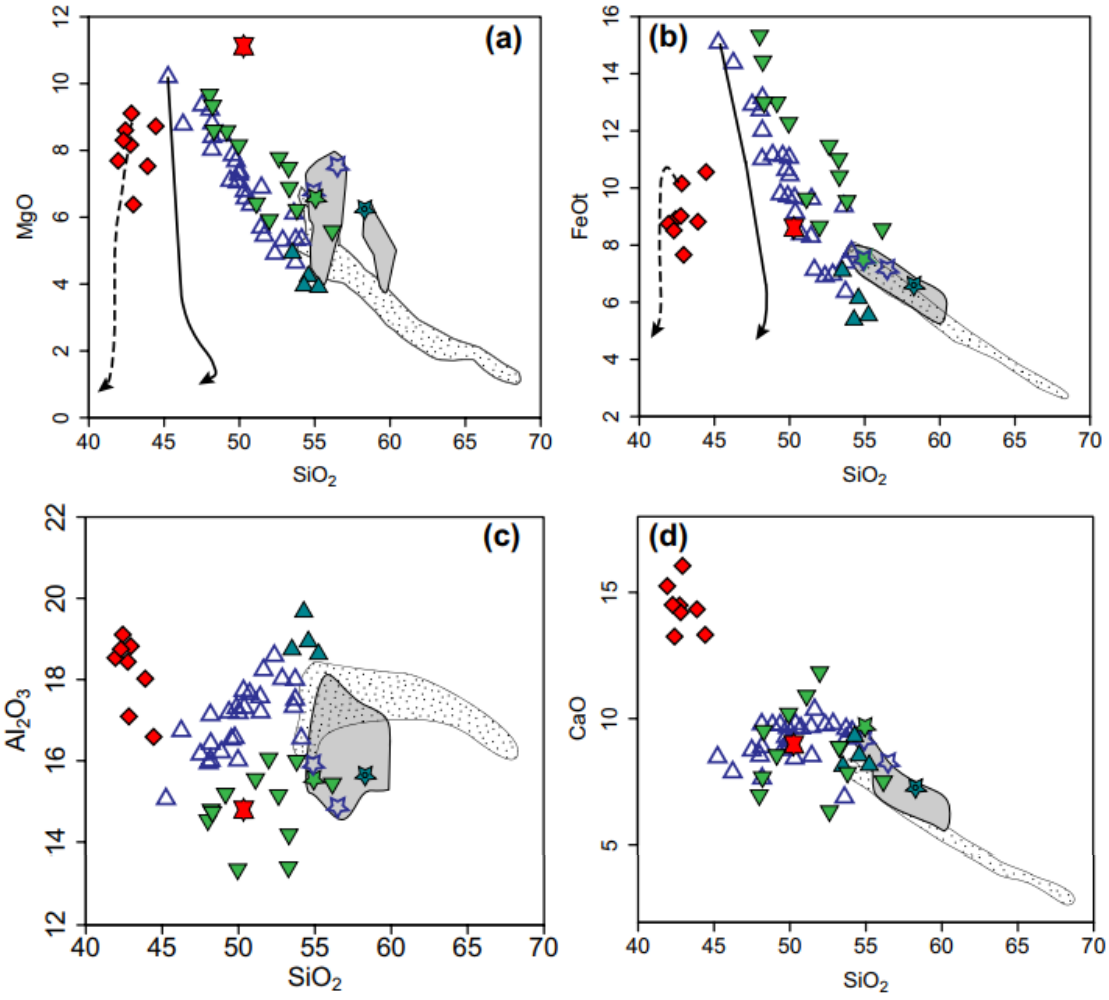

Fig. 3 Harker diagram showing the composition of MgO, FeO, Al_2O_3, and CaO vs. SiO_2 for melt inclusions (homogenization-corrected compositions) and whole-rock samples (shaded areas) of Sangay and Puñalica volcanoes. The black arrows correspond to olivine fractionation lines calculated using Rhyolite-MELTS program (Gualda et al. 2012), starting from one of the most primitive melt inclusions of each volcano, using a pressure of 4 kbar and an estimated water content of 4 wt%. For description of symbols, see Fig. 2

Classification of Puñalica melt inclusion groups

Based on the description of the chemical compositions of the Puñalica MIs, we defined three different groups. All these MIs are trapped in $Fo_{>82}$ olivines and most of them have a lower SiO_2 content than the host lavas.

Group 1 have the highest SiO_2 and the lowest MgO and FeOt contents and plot close to the trend drawn by the whole rocks in Harker and trace element diagrams (Figs. 3, 4). Group 1 consists of four MI found in sample CAR83A, which have similar trace element patterns to those of the whole rocks, and the lowest LREE (e.g., La and Ce) values normalized to primitive mantle (Fig. 4a). They are trapped in $Fo_{83–84}$ olivines. Their $(La/Yb)_N$ values vary from 5 to 14. Group 1 is also characterized by the lowest contents of Cl (1350–1950 ppm), F (439–560 ppm), and S (610–1570 ppm) compared to other groups of MI from Puñalica.

Group 2 consists of 26 MI from CAR113B and RIO17A samples. Group 2 MI are enclosed in Fo_{84} olivines. This group of MI shows high Cl (4037–6112 ppm), intermediate F (483–1008 ppm) contents, and $(La/Yb)_N$ values that vary from 9 to 25. A marked difference between CAR113B and RIO17A MI is the elevated S content, as CAR113B MI contains 1635 to 6738 ppm S and RIO17A from 906 to 4335 ppm S.

Group 3 has similar compositions to Group 2 for FeOt, MgO, and SiO_2. This group is depleted in Al_2O_3 (Fig. 3) and enriched in trace elements (e.g., Sr, Zr, Th, and REE) compared to Groups 1 and 2. Group 3 consists of 12 MI from CAR96A. The olivine crystals are Fo_{83}. Group 3 MI is characterized by high $(La/Yb)_N$ values that vary from

Table 2 New whole-rock data from Puñalica volcano. The remaining whole-rock data for Puñalica are from Schiano et al. (2010). All Sangay whole-rock data used in this paper are from Monzier et al. (1999)

Puñalica volcano																	
	RIO17A	RIO 18bis	RIO 20bis	CAR-01F	CAR-09G	CAR-09J	CAR-13F	CAR-26C	CAR-59A	CAR-59B	CAR-59B bis	CAR-59D	CAR-71	CAR 79A	CAR 80	CAR 83A	CAR-87
SiO_2	56.55	54.98	56.72	55.60	59.48	55.73	56.19	58.27	58.60	55.22	55.13	59.68	55.11	56.01	58.27	58.36	58.13
TiO_2	0.74	0.76	0.75	1.04	0.78	1.04	0.92	0.85	0.78	0.75	0.74	0.75	0.80	0.75	0.76	0.76	0.83
Al_2O_3	14.85	16.23	15.47	17.96	16.97	17.87	17.23	16.26	17.19	16.78	16.77	16.29	17.30	15.46	15.63	15.59	16.33
FeOt	7.14	7.38	7.01	7.44	5.96	7.55	7.18	6.55	6.47	7.22	7.19	6.15	7.44	7.10	6.72	6.64	6.82
MnO	0.12	0.12	0.11	0.13	0.10	0.13	0.12	0.11	0.10	0.14	0.14	0.10	0.14	0.13	0.11	0.11	0.11
MgO	7.48	6.02	6.99	4.53	3.80	4.33	5.24	5.51	4.96	5.84	5.82	4.84	4.92	7.10	6.31	6.21	5.43
CaO	8.24	9.22	7.87	7.59	6.34	7.76	8.10	6.82	6.63	8.54	8.59	6.57	8.94	8.45	7.23	7.22	6.87
Na_2O	3.41	3.58	3.68	3.89	4.44	3.77	3.77	4.03	3.86	3.69	3.75	3.99	3.79	3.49	3.69	3.77	3.90
K_2O	1.26	1.45	1.21	1.59	1.89	1.57	1.01	1.40	1.20	1.55	1.62	1.42	1.34	1.31	1.11	1.17	1.36
P_2O_5	0.21	0.25	0.20	0.24	0.24	0.26	0.24	0.21	0.21	0.26	0.25	0.20	0.22	0.20	0.18	0.17	0.22
Total	99.65	99.56	99.41	100.12	100.06	100.10	99.37	100.41	100.05	100.47	100.04	99.35	100.96	99.90	99.98	100.14	100.28
Sc	20.20	25.68	19.89	18.61	14.55	18.62	24.06	17.19	15.84	23.68	24.17	15.57	25.55	23.69	20.09	19.41	16.61
V	184.00	211.44	185.91	206.76	160.92	208.94	208.03	173.05	159.84	203.50	196.73	159.22	226.67	190.40	172.09	172.74	167.83
Rb	21.50	19.35	18.69	39.09	36.44	37.71		27.35	31.03	21.45	30.19	38.48	25.92	23.44	21.54	23.53	24.51
Sr	910.00	1140.35	857.69	617.35	636.47	599.76	718.00	629.20	671.40	1136.62	1158.32	636.99	1133.55	922.83	547.22	558.13	635.41
Nb	3.40	4.31	4.11	5.95	5.36	6.12		4.46	3.94	3.95	4.07	3.94	3.55	3.70	3.61	4.45	5.29
Ba	525.00	612.44	488.73	688.48	857.12	738.29	472.00	592.16	632.32	660.61	665.55	601.98	551.44	546.09	415.31	442.94	602.37
La	20.50	33.68	19.23	16.42	16.30	15.16		16.74	20.52	34.43	33.88	20.24	21.61	21.93	11.72	12.41	15.27
Ce	43.00	65.31	36.77	32.19	33.12	33.26		33.28	40.02	65.91	65.07	37.31	42.71	43.41	25.13	25.56	31.57
Nd	22.00	31.30	19.58	18.76	17.09	18.13		17.26	21.29	32.36	32.41	20.53	23.22	22.34	13.69	13.87	16.91
Sm	4.35	5.72	3.71	4.24	3.52	4.12		3.82	3.81	5.56	5.75	3.78	4.30	4.29	2.98	2.97	3.92
Zr	95.00	97.50	93.38	120.92	122.20	126.08	106.73	102.97	105.47	93.38	88.33	100.92	88.13	95.21	94.43	98.07	110.55
Eu	1.15	1.46	1.17	1.17	0.97	1.17		1.00	1.11	1.48	1.51	1.11	1.22	1.25	0.86	0.92	1.09
Gd	3.50	3.93	2.85	4.16	2.93	3.77		3.37	3.46	4.16	4.01	3.12	3.58	3.28	2.61	2.78	3.36
Dy	2.45	2.96	2.38	3.19	2.29	2.93		2.16	2.12	2.94	2.92	2.13	2.86	2.57	2.29	2.30	2.32
Yb	1.24	1.60	1.13	1.58	1.19	1.55		1.04	0.89	1.58	1.61	0.89	1.63	1.33	1.07	1.12	1.05
Th	4.40	7.75	4.28	4.57	3.73	3.42		4.23	6.10	7.68	7.73	5.62	4.07	5.11	3.06	3.15	4.11
Y	12.90	17.12	12.82	18.03	13.59	18.29	16.35	12.06	10.62	16.60	16.76	10.85	17.54	14.62	12.16	12.83	12.12
Ne																	
Hy	23.56	16.48	23.01	19.66	15.57	19.20	20.26	20.39	20.91	18.16	15.41	18.67	17.73	22.55	22.24	21.58	20.99

Table 2 (continued)

Puñalica volcano												Sangay volcano
	CAR-113B	CAR-88	CAR-89	CAR-96A	CAR-97	CAR-98	CAR-100	CAR-102	CAR-107	CAR-112	CAR-114A	SAN20B
SiO_2	54.91	58.38	54.64	55.03	55.20	56.65	55.02	54.79	55.26	54.55	54.85	50.28
TiO_2	0.74	0.82	0.72	0.71	0.72	0.78	0.72	0.79	0.78	0.79	0.79	1.01
Al_2O_3	15.88	16.39	15.35	15.52	15.61	16.28	15.81	17.39	17.65	17.35	17.32	14.80
FeOt	7.51	6.80	7.51	7.52	7.46	7.11	7.37	7.67	7.76	7.90	7.82	8.71
MnO	0.14	0.10	0.14	0.14	0.14	0.12	0.13	0.14	0.14	0.14	0.14	0.15
MgO	6.70	5.11	7.17	6.51	6.77	5.74	6.56	4.92	4.47	4.93	4.98	11.12
CaO	9.06	6.88	9.51	9.57	9.02	8.15	9.25	9.21	8.60	9.14	9.05	8.92
Na_2O	3.45	3.96	3.34	3.34	3.48	3.77	3.48	3.62	3.83	3.72	3.60	3.34
K_2O	1.40	1.34	1.38	1.40	1.38	1.20	1.42	1.25	1.28	1.24	1.26	1.32
P_2O_5	0.23	0.21	0.24	0.25	0.23	0.21	0.23	0.23	0.23	0.23	0.19	0.34
Total	98.71	99.92	98.69	98.19	98.61	97.55	98.64	100.30	99.14	98.08	99.85	98.78
Sc	25.27	16.27	27.30	27.45	25.27	19.52	25.42	25.72	23.53	25.49	25.73	24.00
V	197.99	173.85	211.53	214.44	202.29	182.59	208.71	219.77	213.74	221.29	221.47	220.00
Rb	18.95	24.99	17.26	16.57	19.01	17.26	19.77	13.92	15.22	14.80	14.51	25.00
Sr	1078.28	591.80	1041.79	1043.17	1061.88	801.35	1083.97	1093.99	1098.95	1066.35	1091.83	970.00
Nb	2.52	4.55	3.35	2.54	2.72	3.20	3.10	2.72	2.23	2.98	2.63	9.00
Ba	556.73	546.74	528.03	539.78	535.64	489.74	551.01	512.95	555.05	501.10	520.76	644.00
La	26.30	14.59	30.30	33.99	26.93	17.34	27.78	19.86	20.06	19.29	20.37	19.20
Ce	51.56	29.30	57.73	65.04	51.93	36.54	53.56	37.25	36.21	39.07	37.10	39.00
Nd	26.35	16.31	28.99	31.71	26.22	19.11	26.91	21.04	21.52	21.25	20.98	22.40
Sm	4.70	3.50	6.00	5.65	5.18	4.13	5.24	3.99	4.48	4.40	4.40	
Zr	93.26	115.19	104.79	100.71	98.39	95.27	98.30	104.15	98.28	97.84	101.02	91.00
Eu	1.30	0.95	1.42	1.49	1.24	1.09	1.28	1.21	1.18	1.09	1.18	1.26
Gd	3.87	3.29	3.90	4.28	3.71	3.72	3.86	3.54	3.78	3.90	3.54	3.50
Dy	2.71	2.43	3.04	3.02	2.82	2.60	2.81	3.00	3.07	2.96	3.14	2.76
Yb	1.48	1.00	1.54	1.57	1.51	1.20	1.52	1.61	1.72	1.69	1.57	1.24
Th	5.78	3.44	7.06	8.16	5.83	3.73	5.83	3.72	3.85	3.69	4.18	3.50
Y	16.09	12.01	15.96	16.70	15.63	13.53	16.05	16.66	17.97	17.20	15.97	14.90
Ne												2.08
Hy	18.40	20.08	16.40	19.05	19.51	20.17	17.49	18.43	18.56	16.46	19.02	

SAN20B whole-rock sample is shown for reference

Ne and *Hy* are CIPW normative composition

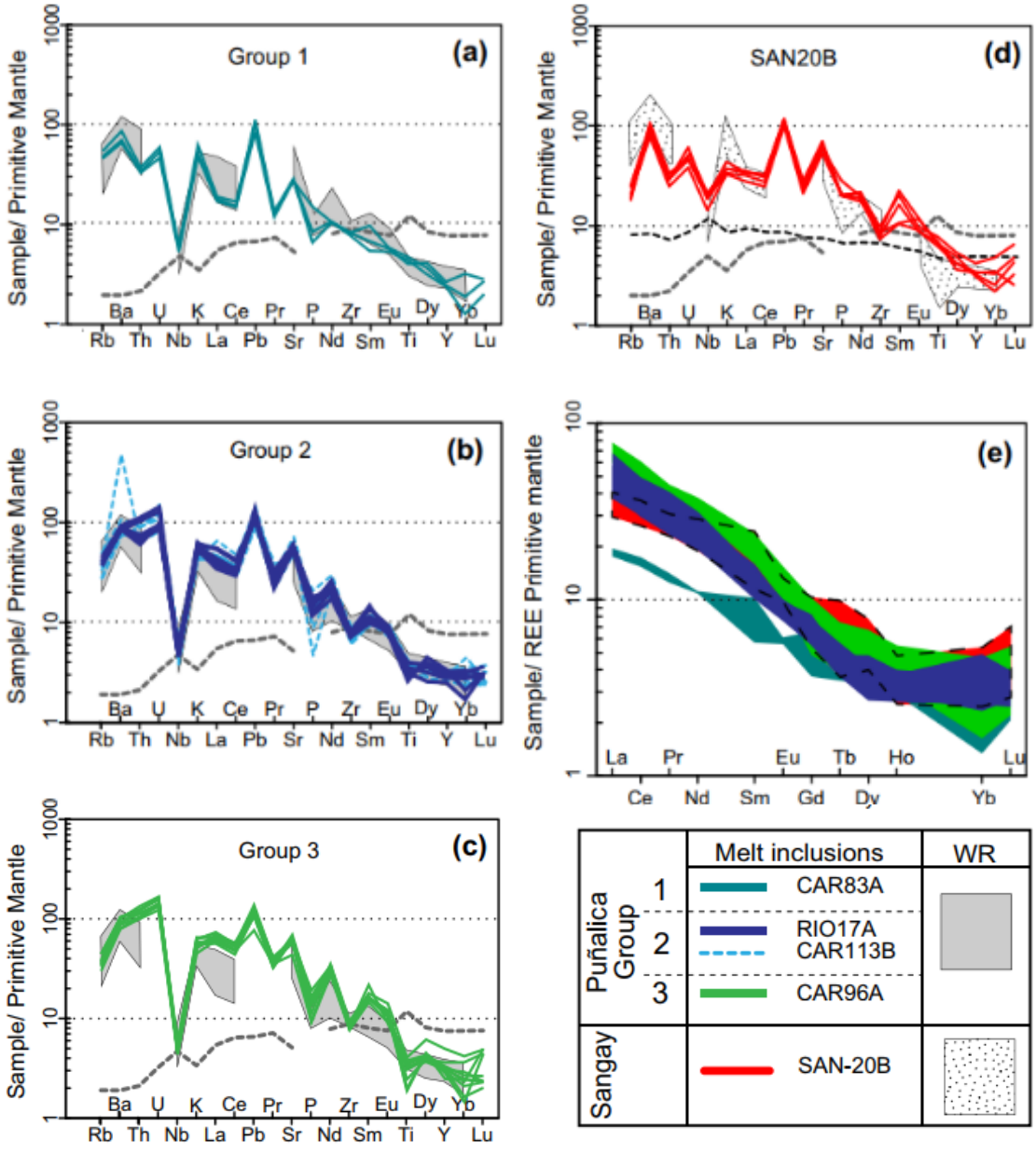

Fig. 4 Trace element compositions of Puñalica (**a–c**) and Sangay (**d**) melt inclusions and whole-rock lavas (dotted and shaded areas; Sangay from Monzier et al. 1999, Puñalica from; Schiano et al. 2010 and this work) normalized to Primitive Mantle composition (Sun and McDonough 1989). **e** REE spider diagram for Puñalica and Sangay melt inclusion. Sangay field is shown with long-dashed line border. N-MORB (dashed gray line) from Sun and McDonough (1989) and E-MORB (dashed black line) from Hofmann (1988)

13 to 45, high Sc (up to 46 ppm, Groups 1 and 2 up to 23 ppm), high F (from 596 to 2187 ppm), and similar Cl (3460–5985 ppm) contents to those of Group 2. Moreover, Group 3 MI has LREE primitive mantle-normalized values (e.g., La, Ce), higher than the Puñalica whole rocks (Fig. 4c). Group 3 has the highest F concentrations (even compared to Sangay MIs), all between 922 and 2187 ppm, except for one MI at 596 ppm (Fig. 5a).

Discussion

Magmatic processes prior to entrapment

Melt inclusions may record dissolution–reaction–mixing (DRM) processes within the magmatic plumbing system (Danyushevsky 2004). These types of inclusions

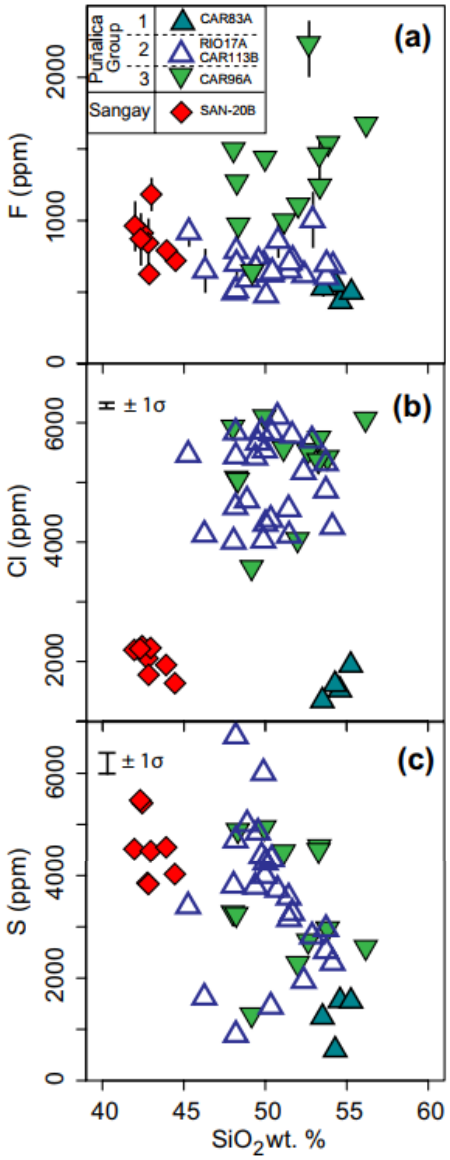

Fig. 5 F, Cl, and S vs. SiO_2 of Puñalica and Sangay melt inclusions. Standard error of the mean values ($\pm 1\sigma$) are shown as vertical lines

are commonly trapped in $Fo_{>85}$ olivines, and are numerous, often clustered in single crystals, and are due to rapid crystallization. Such characteristics differ significantly from those of our samples. Puñalica and Sangay MIs are trapped in primitive olivines, and the melt compositions are independent of the Fo content of the host crystal. Melt inclusions in our samples were scarce, and we never found groups of MIs in the same crystal as reported by Danyushevsky (2004). Based on these textural and compositional characteristics, the MIs represent a primary inclusion character that formed at the time of the first growth of olivine. Thus, the compositions of the MIs reported here have captured primitive melts that are different from host lavas. Our homogenization procedure and post-entrapment crystallization correction closely reconstitutes such primitive melt compositions at the time of capture, except for the abundance of H_2O and CO_2 (which must be considered as minimum values).

Primitive magmas determined from melt inclusions

Assessment of post-entrapment modifications

Puñalica and Sangay MIs are trapped in $Fo_{82–86}$ and $Fo_{86–89}$ olivines, respectively. Compositional corrections for post-entrapment crystallization and degassing of MIs are viable only for inclusions efficiently isolated from the influence of the external magma surrounding the host olivine. In fact, the composition of MIs in readily exchanged major elements is susceptible to irreversible, post-entrapment modifications. Specifically, the host olivine can continuously exchange Fe and Mg with the surrounding magma, potentially leading to "Fe loss" when comparing the MI composition to that of the whole rock. Therefore, the exact reconstruction of the FeO and MgO contents of the parental magma cannot be achieved (Danyushevsky et al. 2000; Gaetani and Watson 2000; Danyushevsky 2002). However, most MI extend the whole-rock trend towards low silica compositions (excepting those from Puñalica Group 1 and Z, T, and U from Group 2, Table 1), and thus, it seems reasonable to postulate that Fe–Mg exchange between the host-mineral and melt is limited. Other species, such as H^+ in MIs, can also re-equilibrate with an external melt through the host olivine crystal, and therefore, the H_2O contents of MIs represent minimum H_2O values and do not systematically represent either the initial H_2O concentrations at the time of entrapment or the primitive H_2O abundance (Chen et al. 2011; Gaetani et al. 2012, 2014). Melt inclusions from this study are, therefore, considered as representative of minimum H_2O concentrations of Puñalica and Sangay magmas, and we will not use them in the rest of the discussion. Because trace elements (e.g., the rare-earth elements) diffuse significantly more slowly than H^+, Fe, and Mg (Cherniak 2015), abundances of such elements should closely resemble those at the time of entrapment following the crystallization correction (see section on post-entrapment crystallization correction in the Online Resource 1). Thus, the ratios of incompatible trace elements remain unmodified, as they are not partitioned into olivine, and are, therefore, representative of the primitive parental magma.

Lavas and magmatic inclusions: are they related?

A petrogenetic decoupling between olivine-hosted MIs and the host eruptive products (lavas and tephra) is clearly seen

in Harker diagrams (Fig. 3). If the parental magma of the erupted products crystallized the olivines (with their inclusions), as it crossed the liquidus, the MI and lava/tephra compositions should plot along the olivine-controlled liquid line of descent. We show the liquid line of descent calculated with Rhyolite-MELTS algorithm (Gualda et al. 2012) from the more primitive MI compositions for both Puñalica (solid line, Fig. 3a, b) and Sangay (dashed line) magmatic suites, with a fixed pressure of 400 MPa, a fO_2 at NNO and 4 wt% H_2O. The liquid-line-of-descent curves, for higher pressure values (i.e., 800 MPa, not shown), would display similar results. In fact, given that the first crystallization stages of Puñalica and Sangay MI are mainly controlled by olivine fractionation, there are almost no changes with pressure. Therefore, the Puñalica and Sangay eruptive products cannot be derived from simple olivine or olivine + clinopyroxene + plagioclase fractionation, taking their respective highest MgO inclusions as their most primitive starting composition.

The projection from olivine into a Di–Ne–Q ternary plot (Fig. 6) yields additional constraints on the genesis of these MI. This projection from the olivine apex allows us to avoid any correction effect or chemical exchange between the MI and the host olivine (e.g., Sorbadère et al. 2013a, b). When plotted on the Di–Ne–Q plane, the studied Puñalica whole-rock samples are hypersthene normative, whereas most of the 42 olivine-hosted ($Fo_{82–86}$) MIs from Puñalica volcano are nepheline normative (up to 10.1 *Ne*, Table 1), only six (AA, AC, AG1, K, S1, and BB) are hypersthene normative. Sangay whole rock (SAN20B) and MIs are all nepheline normative (Fig. 6). Magma compositions of low-pressure crystallization sequence (especially at anhydrous conditions) cannot plot across the boundary separating nepheline and hypersthene normative magmas, which is defined by the Di–Pl join (Fig. 6). Typical mineral phases crystallizing from a basaltic magma (ol + cpx + plg) define an Fo–Di–Pl plane, which is projected on the Di–Ne–Q plane as a line joining Di–Pl, and magmas plotting to the left of the line can only evolve further to the left with crystallization, and vice versa for the right. Occurrence of these Ca-rich, Ne-normative primitive melts in continental arcs, like at Sangay, is scarce and so far has only been reported at Mt. Shasta, Cascades (Le Voyer et al. 2010), Vulcano, Italy (Gioncada et al. 1998; Rose-Koga et al. 2012), Ambrym and Gaua, Vanuatu (Sorbadère et al. 2013a, b), Grenada and St Vincent, Lesser Antilles (Bouvier et al. 2010), Batan, Philippines (Métrich et al. 1999),

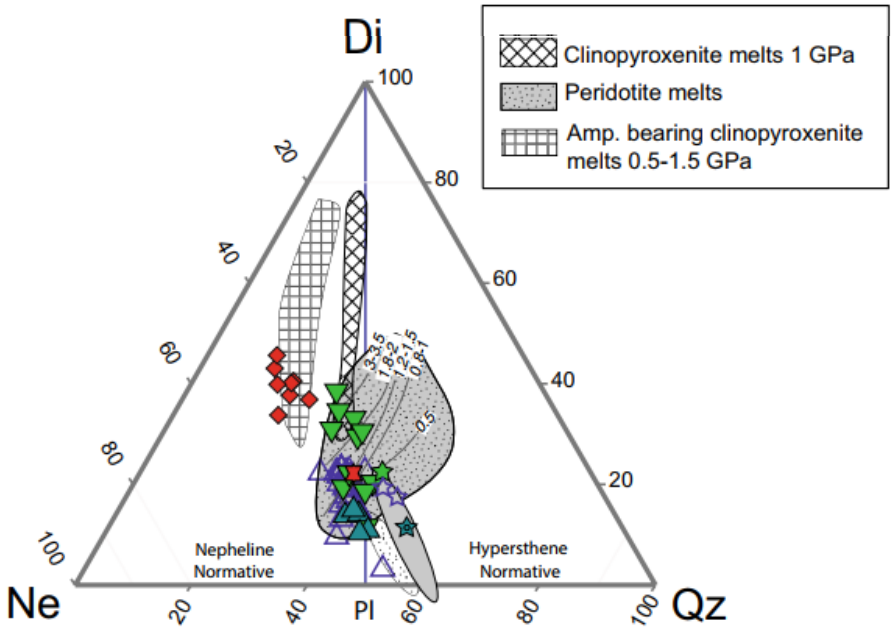

Fig. 6 Projection from olivine (M_2S) onto the Ne–Di–Qz (CMS_2–S–CA) plane for whole-rock lavas and melt inclusions from Puñalica and Sangay. Scheme using O'Hara (1976) CMAS component calculation. $C = CaO - 10/3P_2O_5 + {}_2Na_2O + 2K_2O$, $M = MgO + FeO + MnO - TiO_2$, $A = Al_2O_3 + Fe_2O_3 + TiO_2 + Na_2O + K_2O$, $S = SiO_2 - 2Na_2O - 2K_2O$. Also shown in the diagram are the fields compiled by Sorbadère et al. (2013a) of experimentally determined melts of anhydrous (Hirose and Kushiro 1993; Baker and Stolper 1994; Kushiro 1996; Falloon et al. 2001; Wasylenki et al. 2003; Laporte et al. 2004) and hydrous peridotites between 0.5 and 3.5 GPa (continuous lines are isobars with pressure given in GPa; Hirose and Kawamoto 1995; Gaetani and Grove 1998), amphibole-free (Kogiso and Hirschmann 2001), and amphibole-bearing clinopyroxenites between 0.5 and 1.5 GPa (Médard et al. 2006; Pilet et al. 2008)

Lombok, Indonesia (Elburg et al. 2007), and Pan de Azucar and Pichincha, Ecuador (Le Voyer et al. 2008).

A process to evolve magmas from the nepheline to hypersthene normative fields is fractional crystallization of silica-undersaturated minerals. For instance, amphibole crystallization can significantly increase the silica content in the residual liquid, eventually causing it to cross the nepheline-hypersthene divide (e.g., Frezzotti 2001). It is possible to examine whether or not such processes are responsible for deriving the erupted lavas from the MI compositions by investigating trace element abundances and their variations. Because amphibole preferentially incorporates Dy over Yb and La, the role of amphibole during differentiation is illustrated by a La/Yb increase and a decrease in Dy/Yb during differentiation (Davidson et al. 2007). The Dy/Yb (not shown) is highly variable in all MI and does not form a clear negative correlation with SiO_2. In addition to REE systematics, other observations argue against a role of amphibole fractionation in these inclusions. A significant amphibole fractionation is not expected in a basalt or primitive andesite at high temperature (e.g., Krawczynski et al. 2012) such as that recorded in the inclusions ($T_{homogenization}$ = 1218 °C).

In conclusion, these observations indicate that the melts trapped in olivine crystals are not the parental magmas of the erupted lavas. Puñalica and Sangay MIs represent primitive melts that are not related to host eruptive products, extending the magmatic series towards low silica contents.

Mantle sources for Puñalica and Sangay primitive magmas

Experimental studies have striven to characterize the different lithologies melting under arcs (see Fig. 6 caption for references). The experimentally determined fields for magma compositions issued from melting of different mantle lithologies (peridotite and pyroxenite) are reported in Fig. 6 for pressures between 0.5 and 3.5 GPa (see figure caption for reference). Puñalica MIs plot in the field of peridotite melts (dotted field in Fig. 6) for different pressures. Group 1 and Group 2 MIs have compositions similar to peridotite melts coming from lower pressures (up to 2 GPa; Fig. 6) than Group 3 (up to 3.5 GPa). Such a discrepancy is mainly due to lower Al_2O_3 contents of Group 3 MI (Figs. 3c, 7), which is in agreement with peridotite melting experiments (e.g., Walter 1998). These experiments have shown that garnet stability increases with pressure, reducing the Al_2O_3 content in the partial melt. The stability of garnet in Group 3 MI is also shown by an increase in La/Yb when Al_2O_3 decreases, creating a negative correlation (Fig. 7). Therefore, the chemical differences recorded by the Ne-normative Puñalica MI could be explained by variable depths of partial melting and thus the mineralogy of the mantle, with garnet probably present in Group 3 MI and spinel/plagioclase for Group 1 and 2

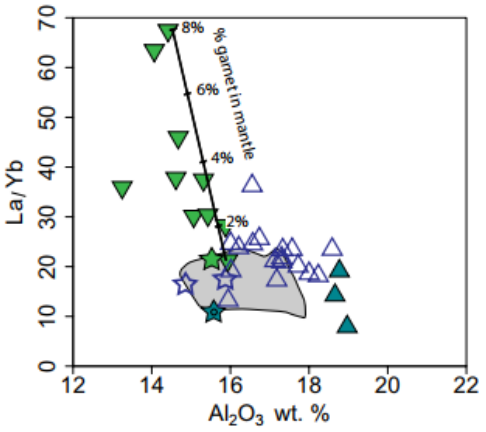

Fig. 7 La/Yb vs. wt% Al_2O_3 of melt inclusions and whole rocks. La/Yb ratio is explained by 1–8% of garnet in the mantle residue following the model proposed for Puñalica MIs (see text)

sources, implying a deeper origin for Group 3 compared to Groups 1 and 2.

The Sangay MI plot in the field of amphibole-bearing clinopyroxenite-derived melts (Fig. 6) occurring at pressures lower than 1.5 GPa and temperatures between 1200 and 1300 °C (Médard et al. 2006). The homogenization temperature of Sangay MI varies from 1189 to 1254 °C and is, therefore, in good agreement with the temperatures stipulated for amphibole-bearing clinopyroxenite-derived melts. The high CaO, relatively high FeOt, low silica contents, and high Sc contents (from 26 to 43 ppm, Table 1) of Sangay MI are also in agreement with compositions coming from the partial melting of an amphibole-bearing clinopyroxenite lithology. In fact, Sorbadère et al. (2013a) proposed that compositions similar to those of Sangay MI could be produced by mixing between partial melts of amphibole-bearing clinopyroxenite and peridotite. The compositions of the Sangay MI correspond to the amphibole-bearing clinopyroxenite-derived melt end-member. Similar Ca-rich, Ne-normative MIs from Pan de Azúcar volcano, located in the back arc of the Ecuadorian Arc, were also interpreted as the result of melting of pyroxenite-rich lithologies (Le Voyer et al. 2008).

The presence of clinopyroxenitic lithologies in arc sources has been widely discussed in the literature (e.g., Schiano et al. 2000; Médard et al. 2006; Sorbadère et al. 2013a, b). Clinopyroxenite is probably found in the lower crust, since the differentiation process of primitive basalt produces ultramafic cumulates (i.e., clinopyroxenites) allowing the magma to evolve toward andesitic compositions (e.g., Greene 2006; Blatter et al. 2013; Nandedkar et al. 2014). These ultramafic cumulates react with new ascending hydrous magmas triggering amphibole crystallization at the expense of clinopyroxene (Smith 2014), producing the amphibole-bearing clinopyroxenites. Then,

the amphibole-bearing clinopyroxenite is melted when a new hot primitive magma ($T > 1100$ °C) ascends through the clinopyroxenite. Alternatively, the amphibole-bearing clinopyroxenite delaminates and sinks into the hotter mantle wedge (Smith 2014; Jagoutz and Kelemen 2015; Schmidt and Jagoutz 2017). The lower solidus temperature and higher melt productivity of pyroxenites (Hirschmann and Stolper 1996) would promote olivine growth and enable entrapment of amphibole-bearing clinopyroxenite-derived melts.

Constraining the slab components by trace element systematics

Previous experimental studies have demonstrated the variable mobility of LILE, HFSE, REE, and other trace elements (e.g., Li and Be) during the dehydration (low temperature) or melting (high temperature) process of the basaltic oceanic crust and/or its sedimentary cap (Kessel et al. 2005; Klimm et al. 2008; Hermann and Rubatto 2009). These studies show that aqueous fluids resulting from dehydration processes are enriched in fluid-mobile elements (e.g., Ba, Rb, Cs, and Pb) and strongly depleted in fluid-immobile elements (e.g., Be, Nb, La, and Th). In contrast, hydrous siliceous melts, resulting from a melting process, are enriched in both fluid-mobile and fluid-immobile elements. Based on this dichotomy, fluid-mobile/fluid-immobile element ratios have been used to identify the nature of the slab components (e.g., Elliott et al. 1997; Elliott 2003). Figure 8a, b shows the plots of Sr/Th and Ba/Th, respectively, vs. $(La/Yb)_N$ of the MIs. Because the mobile/immobile element ratio (e.g., Ba/Th and Sr/Th) of the pre-metasomatized mantle wedge (i.e., MORB composition) is low, the addition of aqueous fluids from the slab increases this ratio. In contrast, mantle metasomatism by hydrous silicate melts does not change the ratio due to the fact that both groups of elements (fluid mobile and immobile) are transported by siliceous melts. The MIs from Puñalica plot at relatively low Ba/Th values (60–190, average 90 ± 34) compared to the range of worldwide primitive arc magmas (Fig. 8b, dotted area). There is no significant contrast in Sr/Th between groups 1, 2 and 3 of Puñalica MI (Fig. 8a). However, the three Puñalica groups have distinct and relatively constant Ba/Th ratios within each group (Fig. 8b). The combination of the low Ba/Th and $(La/Yb)_N$ (values ranging from 10 to 40) for Puñalica MIs is characteristic of magma most likely derived from the partial melting of a source metasomatized by hydrous siliceous melts. The mean values of Group 3 MI compositions for Ba/La ~ 15, Ba/Th ~ 66, Sr/Th ~ 129 and Th/La ~ 0.22 contrast with the ratios obtained for Sangay MI (Ba/La ~ 29, Ba/Th ~ 261, Sr/Th ~ 517) and Th/La ~ 0.11, and are in agreement with those reported by Brandt et al. (2017a) for the northern segment of Payenia volcanic field located in the Andean Southern Volcanic Zone (Ba/La = 16, Ba/Th = 63, Sr/Th = 103, Th/La = 0.25) whose source is also interpreted as having been enriched by siliceous melts.

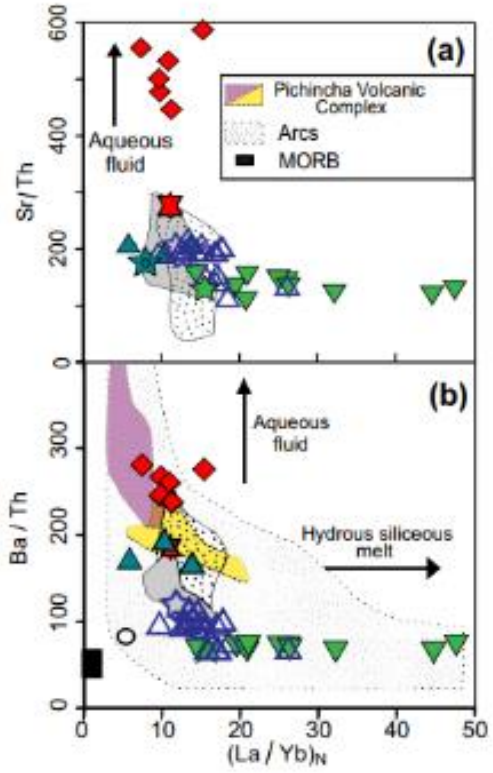

Fig. 8 Plot of $(La/Yb)_N$ normalized to primitive mantle (Sun and McDonough 1989) vs. **a** Sr/Th and **b** Ba/Th. Whole-rock data variation for Pichincha Volcanic Complex field is taken from Samaniego et al. (2010). Purple field corresponds to the older Rucu Pichincha magmatic suite, whereas yellow field corresponds the younger Guagua Pichincha suite. MORB composition represented by the small black rectangle is from Leroux et al. (2006). The primitive arc magma composition (dotted field) is taken from Elliott (2003). Symbols are those of Fig. 2

Ba/Th values from Sangay MIs are around three times higher than those of Puñalica (from 230 to 280, average 261 ± 17) and Sr/Th ratio is also high with values between 444 and 594 (Fig. 8a; Puñalica between 103 and 209). Although not exceptionally high, the higher values for both Sr/Th and Ba/Th in Sangay MIs suggest that aqueous fluids might have metasomatized the source of Sangay. This aqueous fluid would have been enriched in fluid-mobile elements such as Ba, Sr, and Pb. In a previous whole-rock study on Pichincha Volcanic Complex (north of the Ecuadorian arc), a threshold value of Ba/Th ~ 200 was used to distinguish magmas metasomatized by aqueous fluids (Ba/Th > 200) from hydrous siliceous melts (Samaniego et al. 2010). Based on this threshold value, the Ba/Th ratios of Sangay MIs can be taken as resulting from aqueous fluid metasomatism.

We would stress that, in the whole-rock studies at the southern termination of the Ecuadorian arc, this

discrimination is not evident (e.g., Ancellin et al. 2017), possibly because of the overprint by crustal contamination that has blurred the geochemical signal, whereas olivine-hosted MIs are shielded from this contamination.

Modeling the metasomatized mantle source

To test the hypothesis that two different subduction components are injected from the slab into the mantle wedge, we performed a three-step trace element modeling procedure. First, we considered the melting or dehydration of the oceanic crust for Puñalica and Sangay, respectively. Second, given that the sources for Puñalica and Sangay MI are different, we mixed the slab component with a depleted peridotite for Puñalica and with an amphibole-bearing clinopyroxenite composition for Sangay. Finally, we melted these enriched source lithologies using a batch melting equation (Shaw 1970).

1. For the basalt partial melting step, we used the high-temperature experimental Kd (1000 °C) from Kessel et al. (2005) and the average composition of the Carnegie ridge basalts (Harpp et al. 2005). This step with a melting degree set at 5% leaves an eclogitic residue. The degree of melting is imposed by the strong negative-Nb anomaly in the Puñalica MI. Such an anomaly is a characteristic only attained with > 1 vol% of rutile in the residue, and according to Gaetani et al. (2008), the rutile vol% in the residue peaks at roughly 4% of melting. Between 4 and 5% melting does not change our conclusion. For sediment melting, we used the bulk distribution coefficients given by Plank (2005), and an average composition of sediments from the Nazca plate (Plank 2014). We set the melting degree at a fairly low value (i.e., 8%). The dehydration process was modeled with the same parameters as for the melting except for Kd, which was that given by Kessel et al. (2005) at low temperature (800 °C).
2. The trace element composition of the depleted peridotite is from Workman and Hart (2005), and that of the clinopyroxenite from Smith (2014). The mixing proportion between slab fluid or melt component and the depleted source varies from 10:90 to 15:85. When the slab component is a siliceous melt, the amount of sedimentary melt relative to basaltic melt varies in a proportion of 0 to 20%.
3. For Puñalica MI, the metasomatized mantle melt is 10%, leaving a residue of ol:opx:cpx in a proportion of 68:20:12 and a variable amount of grt (1–8 vol%). We used the Kd given by Halliday et al. (1995) for basaltic melts. For Sangay, the minerals in the residue after 5% of melting are ol:cpx:hbl:sp in a proportion of 24:70:2:4. This mineral assemblage was computed by pMelts software (Ghiorso et al. 2002) at 1 GPa and 1 wt% H_2O for an amphibole-bearing clinopyroxenite composition (from Médard et al. 2006).

Results are plotted in Fig. 9 as multi-element diagrams normalized to primitive mantle values (Sun and McDonough 1989). The Puñalica-modeled composition fits very well with natural MI compositions, supporting the hypothesis that the metasomatic agent beneath Puñalica is a silicate melt (Fig. 9a). For Sangay, the modeled composition shows a reasonable agreement, although some differences (e.g., Rb and Nb) are highly source-dependent and can be explained by the scarce trace element data for amp-bearing clinopyroxenite compositions in the literature (Fig. 9b). Finally, given the primitive signature of SAN20B whole rock, we also modeled its origin as a result of a hydrous fluid-metasomatized peridotite (Fig. 9c). The parameters for dehydration were similar to those of Sangay MI modeling and the source was that of a depleted mantle (Workman and Hart 2005). The mixing proportion between the slab component and the mantle was fixed at 15:85 and the partial melting of the mantle at 5%. The relatively good fit indicates an aqueous fluid as the metasomatic agent responsible for the composition of the SAN20B olivine-hosted MIs.

Constraints provided by the volatile element compositions on the nature of the slab flux in a continental subduction zone

Sangay and Puñalica MI have high concentrations of fluorine and chlorine (Fig. 10), which is typical of volcanic arcs from continental subduction (e.g., Izu, Straub and Layne 2003; Mt. Shasta, Cascades, Le Voyer et al. 2010; Vulcano, Italy and Iwate, Japan, Rose-Koga et al. 2012, 2014). Puñalica Group 3 MIs display amongst the highest F contents in continental arc-related MI (up to 2187 ppm F). This high F content is accompanied by high Cl concentrations (Cl commonly between 4000 and 6000 ppm in Puñalica MI). For comparison, an olivine-hosted MI from Reventador volcano has 3149 ppm chlorine and 549 fluorine (Samaniego et al. 2008) and Tungurahua MIs have less than 1081 ppm chlorine (Myers et al. 2014).

High halogen contents in primitive arc magmas (the case of Puñalica) can be achieved by two processes (van den Bleeken and Koga 2015): (1) the subducted crust melts (rather than simply dehydrating), or (2) the subducted crust is enriched in halogens and eventually melts/dehydrates. Thus, one explanation is that Puñalica volcano is roughly located above the Grijalva fracture zone and the higher permeability in the fracture zone enhances interactions with seawater (compared to a normal oceanic crust), thus increasing its F and Cl contents. Furthermore and because the Puñalica slab component seems to be a siliceous melt, this

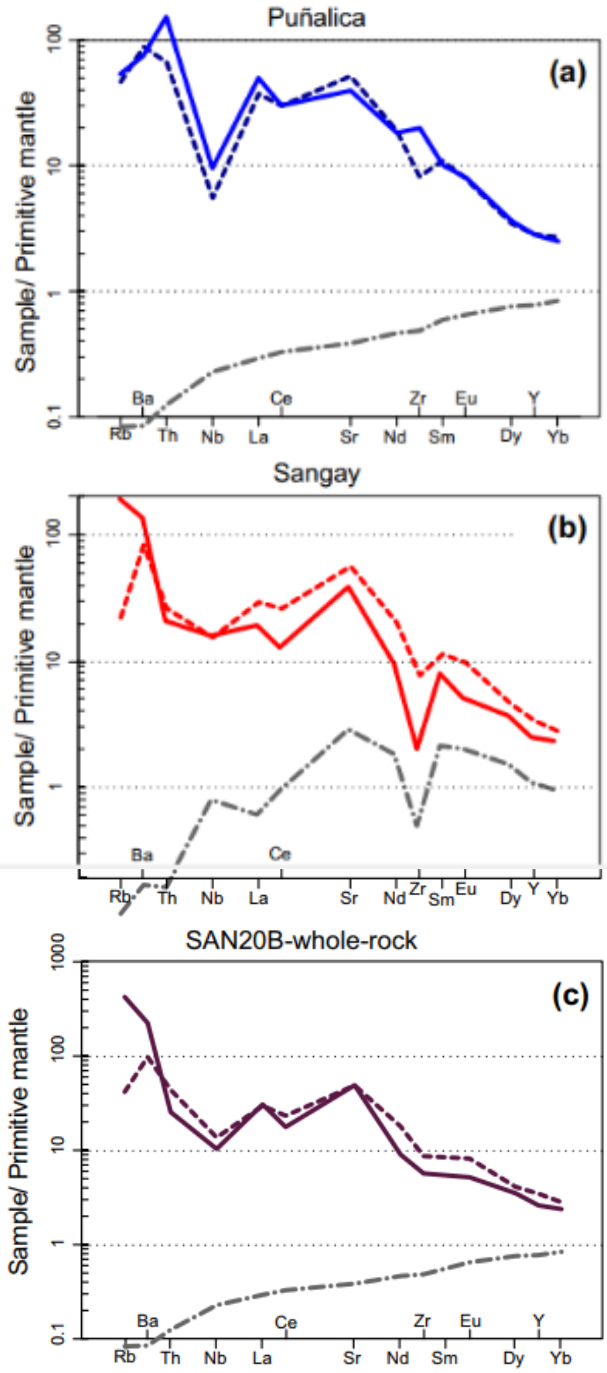

Fig. 9 Modeled composition (colored dashed lines) compared to natural melt inclusion (colored solid lines) from **a** Puñalica and **b** Sangay volcanoes. **c** Modeled composition for SAN20B whole-rock sample from Sangay volcano. Gray dot–dash lines are compositions of the non-metasomatized source lithologies: a depleted mantle (Workman and Hart 2005) for Puñalica and SAN20B, and a clinopyroxenite (Smith 2014) for Sangay. The proportion of slab component compared to peridotite/clinopyroxenite in the mixing process is 10:90 for Puñalica MI, 12:88 for Sangay MI and 15:85 for SAN20B. The amount of sedimentary-origin melt in the slab component is 20% (only for Puñalica)

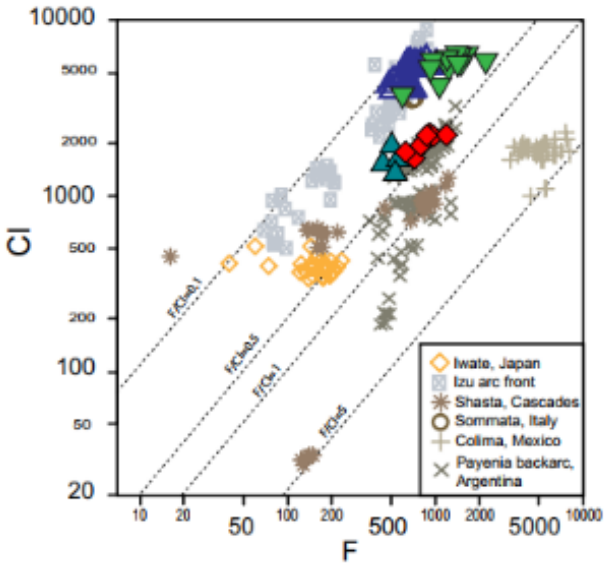

Fig. 10 F vs. Cl for Sangay and Puñalica melt inclusions. Our data are compared to other melt inclusion compositions compiled by Rose-Koga et al. (2014). Melt inclusion compositions from Payenia backarc are from Brandt et al. (2017b)

altered oceanic crust eventually melts driving F and Cl contents even higher (van den Bleeken and Koga 2015). Both fluorine and chlorine are incompatible in the typical mineral phases of a garnet-bearing peridotite (van den Bleeken and Koga 2015), and therefore, those elements would leave the mantle during partial melting.

For an amphibole-bearing source lithology, as in the case of Sangay MI, fluorine compatibility must change, because this element is compatible in amphibole, whereas chlorine is not. This preference of amphibole for fluorine would affect F/Cl ratios. Thus, Sangay F/Cl ratios (0.35–0.53) that are higher than those from Puñalica (0.11–0.39) could be explained by the interaction of ascending mantle-derived magma with an amphibole-bearing clinopyroxenite, likely enriched in F compared to Cl.

Slab components in the geodynamic context of the continental Ecuadorian arc and beyond

The origin of the metasomatic agent in the Ecuadorian arc has long been debated in the scientific literature. Some researchers consider that the metasomatic agent of the subarc mantle wedge is an aqueous fluid issued from dehydration reactions of the slab (Barragan et al. 1998; Garrison and Davidson 2003; Bryant et al. 2006; Chiaradia et al. 2009). Based on the overall adakitic signature of the Ecuadorian arc, other researchers consider that the metasomatic agent is a siliceous melt associated with slab partial melting (Bourdon et al. 2003; Hidalgo et al. 2012). In addition,

some long-lived volcanic complexes of the Ecuadorian arc are characterized by a progressive variation of the trace element signature that has been interpreted as a change of the metasomatic agent throughout its evolution. This variation in whole-rock trace elements, described at Cayambe (Samaniego et al. 2002, 2005); Illinizas (Hidalgo et al. 2007), Mojanda-Fuya Fuya (Robin et al. 2009), and Pichincha (Samaniego et al. 2010), implies that the older magmas of these volcanic complexes came from a hydrous fluid-metasomatized mantle wedge, whereas the younger magmas are related to partial melting of a siliceous melt metasomatized mantle wedge. Such a temporal evolution suggests a change from dehydration to partial melting of the slab that could be associated with an increase in the thermal regime along the slab due to the presence of the subducted Carnegie ridge (e.g., Yepes et al. 2016). In this context, the younger age and structure of the Carnegie ridge would induce an enhanced thermal gradient along the slab, which may trigger slab partial melting. This hypothesis is supported by thermal modeling studies (e.g., Syracuse et al. 2010) that estimate elevated slab-surface temperatures below the Ecuadorian arc.

In this work, we demonstrated that the subarc mantle below two of the southern Ecuadorian volcanoes is metasomatized by different slab components. The cause of such variation might be related to the geodynamical setting, where the Grijalva Fracture Zone (GFZ) sharply separates a young slab to the north from an older slab to the south. As recently pointed out by Yepes et al. (2016), this difference in age is coupled to a contrasted seismic behavior and an increase in the subduction angle: to the north of the GFZ, the slab displays low intermediary seismicity (50–150 km depth) and subducts at an angle of 20°–25°, whereas, to the south, the slab is highly seismogenic and plunges at a higher angle (30°–35°). This contrasted seismic behavior could be associated with a different thermal regime on both sides of the GFZ (Yepes et al. 2016), which, in turn, could control the dehydration, and the melting process happening at depth.

Based on whole-rock major, trace element, and Sr–Nd–Pb isotopic signature of the Ecuadorian arc lavas, Ancellin et al. (2017) describe an N–S variation of the metasomatic agent along the entire Ecuadorian volcanic arc. They interpreted these along-arc variations as an increase of the slab input northward and southward on both sides of a divide that they placed at 0.5°S (i.e., at the latitude of the Carnegie ridge subduction). They concluded that the most likely process able to explain these variations is a variable influx of slab-derived fluids or melts. In the present olivine-hosted MI study, we refine the previous findings and argue that Puñalica MI come from a mantle wedge metasomatised by a hydrous siliceous melt, whereas Sangay MI are most likely produced by partial melting of a hydrous fluid-metasomatized amphibole-bearing clinopyroxenite source.

In a more general context, the singularity of Sangay MIs is striking in Figs. 3 and 6. High-Ca, Ne-normative primitive arc melts exist in other arc systems around the world (cf. the section on "Primitive magmas determined from melt inclusions"), but are not that common in continental subduction zone settings. However, whereas the crustal thickness in the previously mentioned arc systems (Cascades, Italy, Vanuatu) is around 20–30 km thick, the Ecuadorian continental arc is characterized by a very thick arc crust (> 50 km). The influence of crustal thickness on melt compositions is not new and has already been proposed for arc lavas (e.g., Wallace and Carmichael 1992). In the case of Sangay MI, we, therefore, have to reconcile the amphibole-bearing clinopyroxenite source (Ca-rich, Ne-normative melts), the high volatile (F and Cl) contents of MIs, and the high Fo of the host olivines, with the presence of a 50 km-thick crust. One hypothesis is that melting of the amphibole-bearing clinopyroxenite happens at depth, probably at the interface between the lower crust and the upper mantle. To accommodate the deep origin of the MI and the required fast migration to the surface, the occurrence of trans-crustal major faults seems an important requirement.

Conclusions

Melts inclusions from Puñalica and Sangay volcanoes are Ca-rich and have mostly Ne-normative compositions. The magmas sampled as MIs are not the parental magmas of the whole rocks, but they constitute exceptional compositions that show the complexity of the processes occurring at subduction zones and the heterogeneity of the sources of primitive arc magmas.

All MIs from Puñalica have major element compositions similar to experimental melts derived from peridotite. Sangay MI has homogeneous compositions and their origin is attributed to mixing processes between melts derived from peridotite (represented by the whole-rock SAN20B composition) and from an amphibole clinopyroxene-rich sources.

Using a combination of trace element ratios (Ba/Th, Sr/Th, and Th/La), we decipher the metasomatic agent from the slab. The slab component that metasomatizes the mantle source of Puñalica volcano is a siliceous melt (low mobile/immobile ratios), which displays a variable enrichment in LREE. Moreover, the high content of volatiles (e.g., F and Cl) is attributed to the presence of the Grijalva Fracture Zone that separates a younger and hotter oceanic crust to the north from a colder and older oceanic crust to the south. Under Sangay volcano, the MIs are produced by partial melting of metasomatized (most likely by some relative contribution of aqueous fluids) amphibole-bearing clinopyroxenite source and the relatively higher F compared to Cl is likely due to

fluorine enrichment in the source linked to fluorine compatibility with amphibole.

Ca-rich, Ne-normative primitive melts are scarce in subduction zone settings, especially those associated with thick continental crust, and could possibly be related to the presence of major trans-crustal faults.

Acknowledgements This research was conducted as part of Diego Narvaez, Ph.D., which is financed by the Secretaría Nacional de Educación Superior, Ciencia, Tecnología e Innovación (SENESCYT, Ecuador) and the ARTS program of the French Institut de Recherche pour le Developpement (IRD). It is part of a cooperation program carried out between the Instituto Geofisico, Escuela Politécnica Nacional (IGEPN), Quito, Ecuador and the IRD, through the Laboratoire Mixte International "Séismes et Volcans dans les Andes du Nord". ER-K acknowledges funding from the French INSU scientific program SYSTER. We thank Nordine Bouden and Etienne Deloule of CRPG (France) for their precious guidance during SIMS analysis. Jean-Luc Devidal, at LMV, is deeply thank for his essential help with the LA-ICPMS measurements and tuning of the EMP. We thank Fran van Wyk des Vries for proof reading the manuscript and correcting the English. This work also benefited by the financial support from the Laboratory of Excellence ClerVolc. This is Laboratory of Excellence ClerVolc contribution no. 309.

References

Ancellin MA, Samaniego P, Vlastélic I, Nauret F, Gannoun A, Hidalgo S (2017) Across-arc versus along-arc Sr–Nd–Pb isotope variations in the Ecuadorian volcanic arc. Geochem Geophys Geosyst 18:1163–1188. https://doi.org/10.1002/2016GC006679

Aspden JA, Litherland M (1992) The geology and Mesozoic collisional history of the Cordillera Real. Ecuad Tectonophys 205:187–204. https://doi.org/10.1016/0040-1951(92)90426-7

Baker MB, Stolper EM (1994) Determining the composition of high-pressure mantle melts using diamond aggregates. Geochim Cosmochim Acta 58:2811–2827

Barragan R, Geist D, Hall M, Larson P, Kurz M (1998) Subduction controls on the compositions of lavas from the Ecuadorian Andes. Earth Planet Sci Lett 154:153–166

Blatter DL, Sisson TW, Hankins WB (2013) Crystallization of oxidized, moderately hydrous arc basalt at mid- to lower-crustal pressures: implications for andesite genesis. Contrib Mineral Petrol 166:861–886. https://doi.org/10.1007/s00410-013-0920-3

Bourdon E, Eissen JP, Gutscher MA, Monzier M, Hall ML, Cotten J (2003) Magmatic response to early aseismic ridge subduction: the Ecuadorian margin case (South America). Earth Planet Sci Lett 205:123–138

Bouvier AS, Deloule E, Métrich N (2010) Fluid inputs to magma sources of St. Vincent and Grenada (Lesser Antilles): new insights from trace elements in olivine-hosted melt inclusions. J Petrol 51:1597–1615. https://doi.org/10.1093/petrology/egq031

Brandt FE, Holm PM, Søager N (2017a) South-to-north pyroxenite–peridotite source variation correlated with an OIB-type to arc-type enrichment of magmas from the Payenia backarc of the Andean Southern Volcanic Zone (SVZ). Contrib Mineral Petrol 172:1. https://doi.org/10.1007/s00410-016-1318-9

Brandt FE, Holm PM, Hansteen TH (2017b) Volatile (Cl, F and S) and major element constraints on subduction-related mantle metasomatism along the alkaline basaltic backarc, Payenia, Argentina. Contrib Mineral Petrol 172:48. https://doi.org/10.1007/s00410-017-1359-8

Bryant JA, Yogodzinski GM, Hall ML, Lewicki JL, Bailey DG (2006) Geochemical constraints on the origin of volcanic rocks from the Andean Northern Volcanic Zone, Ecuador. J Petrol 47:1147–1175

Chen Y, Provost A, Schiano P, Cluzel N (2011) The rate of water loss from olivine-hosted melt inclusions. Contrib Mineral Petrol 162:625–636

Cherniak DJ (2015) REE diffusion in olivine. Am Miner 95:362–368

Chiaradia M, Müntener O, Beate B, Fontignie D (2009) Adakite-like volcanism of Ecuador: lower crust magmatic evolution and recycling. Contrib Mineral Petrol 158:563–588

Clapperton CM (1990) Glacial and volcanic geomorphology of the Chimborazo-Carihuairazo massif, Ecuadorian Andes. Trans R Soc Edinb Earth Sci 81:91–116

Class C, Miller DM, Goldstein SL, Langmuir CH (2000) Distinguishing melt and fluid subduction components in Umnak Volcanics, Aleutian Arc. Geochem Geophys Geosystems. https://doi.org/10.1029/1999GC000010

Clocchiatti R, Gioncada A, Mosbah M, Sbrana A (1994) Possible deep origin of sulfur output at Vulcano (Southern Italy) in the light of melt inclusion studies. Acta Vulcanol 5:49–53

Collins SJ, Pyle DM, Maclennan J (2009) Melt inclusions track pre-eruption storage and dehydration of magmas at Etna. Geology 37:571–574

Danyushevsky LV (2002) Melt inclusions in olivine phenocrysts: using diffusive re-equilibration to determine the cooling history of a crystal, with implications for the origin of olivine-phyric volcanic rocks. J Petrol 43:1651–1671

Danyushevsky LV (2004) Melt inclusions in primitive olivine phenocrysts: the role of localized reaction processes in the origin of anomalous compositions. J Petrol 45:2531–2553

Danyushevsky LV, Della-Pasqua FN, Sokolov S (2000) Re-equilibration of melt inclusions trapped by magnesian olivine phenocrysts from subduction-related magmas: petrological implications. Contrib Mineral Petrol 138:68–83

Davidson J, Turner S, Handley H, Macpherson C, Dosseto A (2007) Amphibole "sponge" in arc crust? Geology 35:787–790

Elburg MA, Kamenetsky VS, Foden JD, Sobolev A (2007) The origin of medium-K ankaramitic arc magmas from Lombok (Sunda arc, Indonesia): mineral and melt inclusion evidence. Chem Geol 240:260–279. https://doi.org/10.1016/j.chemgeo.2007.02.015

Elliott T (2003) Tracers of the slab. In: Eiler J (ed) Geophysical monograph series. American Geophysical Union, Washington, DC, pp 23–45

Elliott T, Plank T, Zindler A, White W, Bourdon B (1997) Element transport from slab to volcanic front at the Mariana arc. J Geophys Res Solid Earth 102:14991–15019

Falloon TJ, Danyushevky LV, Green DH (2001) Peridotite melting at 1 GPa: reversal experiments on partial melt compositions produced by peridotite-basalt sandwich experiments. J Petrol 42:2363–2390

Feininger T, Seguin MK (1983) Simple Bouguer gravity anomaly field and the inferred crustal structure of the continental Ecuador. Geology 11:40–44

Frezzotti ML (2001) Silicate-melt inclusions in magmatic rocks: applications to petrology. Lithos 55:273–299

Gaetani GA, Grove TL (1998) The influence of water on melting of mantle peridotite. Contrib Mineral Petrol 131:323–346

Gaetani GA, Watson EB (2000) Open system behavior of olivine-hosted melt inclusions. Earth Planet Sci Lett 183:27–41

Gaetani GA, Asimow PD, Stolper EM (2008) A model for rutile saturation in silicate melts with applications to eclogite partial melting in subduction zones and mantle plumes. Earth Planet Sci Lett 272:720–729. https://doi.org/10.1016/j.epsl.2008.06.002

Gaetani GA, O'Leary JA, Shimizu N, Bucholz CE, Newville M (2012) Rapid re-equilibration of H_2O and oxygen fugacity in olivine-hosted melt inclusions. Geology 40:915–918

Gaetani GA, O'Leary JA, Koga KT, Hauri EH, Rose-Koga EF, Monteleone BD (2014) Hydration of mantle olivine under variable water and oxygen fugacity conditions. Contrib Mineral Petrol 167:965. https://doi.org/10.1007/s00410-014-0965-y

Garrison JM, Davidson JP (2003) Dubious case for slab melting in the Northern volcanic zone of the Andes. Geology 31:565–568

Ghiorso MS, Hirschmann MM, Reiners PW, Kress VC (2002) The pMELTS: a revision of MELTS for improved calculation of phase relations and major element partitioning related to partial melting of the mantle to 3 GPa. Geochem Geophys Geosyst 3:1–35. https://doi.org/10.1029/2001gc000217

Gioncada A, Clocchiatti R, Sbrana A, Bottazzi P, Massare D, Ottolini L (1998) A study of melt inclusions at Vulcano (Aeolian Islands, Italy): insights on the primitive magmas and on the volcanic feeding system. Bull Volcanol 60:(286–306

Greene AR (2006) A Detailed Geochemical Study of Island Arc Crust: the Talkeetna Arc Section, South-Central Alaska. J Petrol 47:1051–1093

Grove T, Parman S, Bowring S, Price R, Baker M (2002) The role of an H_2O-rich fluid component in the generation of primitive basaltic andesites and andesites from the Mt. Shasta region, N California. Contrib Mineral Petrol 142:375–396

Grove TL, Till CB, Krawczynski MJ (2012) The role of H_2O in subduction zone magmatism. Annu Rev Earth Planet Sci 40:413–439

Gualda GAR, Ghiorso MS, Lemons RV, Carley TL (2012) Rhyolite-MELTS: a modified calibration of MELTS optimized for silica-rich, fluid-bearing magmatic systems. J Petrol 53:875–890

Guillier B, Chatelain JL, Jaillard E, Yepes H, Poupinet G, Fels JF (2001) Seismological evidence on the geometry of the Orogenic System in central-northern Ecuador (South America). Geophys Res Lett 28:3749–3752

Gutscher MA, Malavieille J, Lallemand S, Collot JY (1999) Tectonic segmentation of the North Andean margin: impact of the Carnegie Ridge collision. Earth Planet Sci Lett 168:255–270

Hall ML, Samaniego P, Le Pennec JL, Johnson JB (2008) Ecuadorian Andes volcanism: a review of Late Pliocene to present activity. J Volcanol Geotherm Res 176:1–6

Halliday AN, Lee DC, Tommasin S, Davies GR, Paslick CR, Fitton GJ, James DE (1995) Incompatible trace elements in OIB and MORB and source enrichments in the sub oceanic mantle. Earth Planet Sci Lett 133:379–395

Harpp KS, Wanless VD, Otto RH, Hoernle K, Werner R (2005) The Cocos and Carnegie aseismic ridges: a trace element record of long-term plume-spreading center interaction. J Petrol 46:109–133

Hermann J, Rubatto D (2009) Accessory phase control on the trace element signature of sediment melts in subduction zones. Chem Geol 265:512–526

Hidalgo S, Monzier M, Martin H, Chazot G, Eissen JP, Cotten J (2007) Adakitic magmas in the Ecuadorian Volcanic Front: Petrogenesis of the Iliniza Volcanic Complex (Ecuador). J Volcanol Geotherm Res 159:366–392

Hidalgo S, Gerbe MC, Martin H, Samaniego P, Bourdon E (2012) Role of crustal and slab components in the Northern Volcanic Zone of the Andes (Ecuador) constrained by Sr–Nd–O isotopes. Lithos 132–133:180–192

Hirose K, Kawamoto T (1995) Hydrous partial melting of lherzolite at 1GPa: the effect of H_2O on the genesis of basaltic magmas. Earth Planet Sci Lett 133:463–473

Hirose K, Kushiro I (1993) Partial melting of dry peridotite at high pressures: determination of compositions of melts segregated from peridotite using aggregates of diamond. Earth Planet Sci Lett 114:477–489

Hirschmann MM, Stolper EM (1996) A possible role for garnet pyroxenite in the origin of the "garnet signature" in MORB. Contrib Mineral Petrol 124:185–208

Hofmann AW (1988) Chemical differentiation of the Earth: the relationship between mantle, continental crust, and oceanic crust. Earth Planet Sci Lett 90:297–314

Jagoutz O, Kelemen PB (2015) Role of arc processes in the formation of continental crust. Annu Rev Earth Planet Sci 43:12.1–12.42

Jaillard E, Bengtson P, Ordoñez M, Vaca W, Dhondt A, Suárez J, Toro J (2008) Sedimentary record of terminal Cretaceous accretions in Ecuador: the Yunguilla Group in the Cuenca area. J South Am Earth Sci 25:133–144

Jugo PJ, Luth RW, Richards JP (2005) Experimental data on the speciation of sulfur as a function of oxygen fugacity in basaltic melts. Geochim Cosmochim Acta 69:497–503

Kelemen PB, Hanghøj K, Greene AR (2014) One view of the geochemistry of subduction-related magmatic arcs, with an emphasis on primitive andesite and lower crust. Treatise on geochemistry. Elsevier, Amsterdam, pp 749–806

Kellogg JN, Vega V, Stailings TC, Aiken CL (1995) Tectonic development of Panama, Costa Rica, and the Colombian Andes: constraints from global positioning system geodetic studies and gravity. Geol Soc Am Spec Pap 295:75–90

Kessel R, Schmidt MW, Ulmer P, Pettke T (2005) Trace element signature of subduction-zone fluids, melts and supercritical liquids at 120–180 km depth. Nature 437:724–727

Klimm K, Blundy JD, Green TH (2008) Trace element partitioning and accessory phase saturation during H_2O-saturated melting of basalt with implications for subduction zone chemical fluxes. J Petrol 49:523–553

Kogiso T, Hirschmann MM (2001) Experimental study of clinopyroxenite partial melting and the origin of ultra-calcic melt inclusions. Contrib Mineral Petrol 142:347–360

Krawczynski MJ, Grove TL, Behrens H (2012) Amphibole stability in primitive arc magmas: effects of temperature, H_2O content, and oxygen fugacity. Contrib Mineral Petrol 164:317–339

Kushiro I (1996) Partial melting of a fertile mantle peridotite at high pressures: an experimental study using aggregates of diamond. In: Basu A, Hart S (eds) Earth processes: reading the isotopic code. American Geophysical Union, Washington, DC, pp 109–122

Labanieh S, Chauvel C, Germa A, Quidelleur X (2012) Martinique: a clear case for sediment melting and slab dehydration as a function of distance to the trench. J Petrol 53:2441–2464

Laporte D, Toplis MJ, Seyler M, Devidal JL (2004) A new experimental technique for extracting liquids from peridotite at very low degrees of melting: application to partial melting of depleted peridotite. Contrib Mineral Petrol 146:463–484

Le Voyer M, Rose-Koga EF, Laubier M, Schiano P (2008) Petrogenesis of arc lavas from the Rucu Pichincha and Pan de Azucar volcanoes (Ecuadorian arc): major, trace element, and boron isotope evidences from olivine-hosted melt inclusions. Geochem Geophys Geosyst 9:Q12027. https://doi.org/10.1029/2008GC002173

Le Voyer M, Rose-Koga EF, Shimizu N, Grove TL, Schiano P (2010) Two contrasting H_2O-rich components in primary melt inclusions from Mount Shasta. J Petrol 51:1571–1595

Leroux P, Shirey S, Hauri E, Perfit M, Bender J (2006) The effects of variable sources, processes and contaminants on the composition of northern EPR MORB (8–10°N and 12–14°N): evidence from volatiles (H_2O, CO_2, S) and halogens (F, Cl). Earth Planet Sci Lett 251:209–231

Médard E, Schmidt M, Schiano P, Ottolini L (2006) Melting of Amphibole-bearing wehrlites: an experimental study on the origin of ultra-calcic nepheline-normative melts. J Petrol 47:481–504

Métrich N, Wallace PJ (2008) Volatile abundances in basaltic magmas and their degassing paths tracked by melt inclusions. Rev Mineral Geochem 69:363–402

Métrich N, Clocchiatti R, Mosbah M, Chaussidon M (1993) The 1989–1990 activity of Etna magma mingling and ascent of H_2O–Cl–S-rich basaltic magma. Evidence from melt inclusions. J Volcanol Geotherm Res 59:131–144

Métrich N, Schiano P, Clocchiatti R, Maury RC (1999) Transfer of sulfur in subduction settings: an example from Batan island (Luzon volcanic arc, Philippines). Earth Planet Sci Lett 167:1–14

Métrich N, Allard P, Spilliaert N, Andronico D, Burton M (2004) 2001 flank eruption of the alkali- and volatile-rich primitive basalt responsible for Mount Etna's evolution in the last three decades. Earth Planet Sci Lett 228:1–17

Michaud F, Chabert A, Collot JY, Sallarès V, Flueh ER, Charvis P, Graindorge D, Gutscher MA, Bialas G (2005) Fields of multi-kilometer-scale sub-circular depressions in the Carnegie Ridge sedimentary blanket: effect of underwater carbonate dissolution? Mar Geol 216:205–219. https://doi.org/10.1016/j.margeo.2005.01.003

Monzier M, Robin C, Samaniego P, Hall ML, Cotten J, Mothes P, Arnaud N (1999) Sangay volcano, Ecuador: structural development, present activity and petrology. J Volcanol Geotherm Res 90:49–79

Myers ML, Geist DJ, Rowe MC, Harpp KS, Wallace PJ, Dufek J (2014) Replenishment of volatile-rich mafic magma into a degassed chamber drives mixing and eruption of Tungurahua volcano. Bull Volcanol 76:872. https://doi.org/10.1007/s00445-014-0872-0

Nandedkar RH, Ulmer P, Müntener O (2014) Fractional crystallization of primitive, hydrous arc magmas: an experimental study at 0.7 GPa. Contrib Mineral Petrol 167:1015

O'Hara MJ (1976) Data reduction and projection schemes for complex compositions. Prog Exp Petrol 6:103–126

Ordóñez J (2012) Depósitos volcánicos del Pleistoceno Tardío en la cuenca de Ambato: caracterización, distribución y origen. EPN, Quito

Peccerillo A, Taylor SR (1976) Geochemistry of Eocene calc-alkaline volcanic rocks from the Kastamonu area, northern Turkey. Contrib Mineral Petrol 58:63–81

Pilet S, Baker MB, Stolper EM (2008) Metasomatized lithosphere and the origin of alkaline lavas. Science 320:916–919. https://doi.org/10.1126/science.1156563

Plank T (2005) Constraints from thorium/lanthanum on sediment recycling at subduction zones and the evolution of the continents. J Petrol 46:921–944. https://doi.org/10.1093/petrology/egi005

Plank T (2014) The chemical composition of subducting sediments. Treatise on Geochemistry. Elsevier, Amsterdam, pp 607–629

Pratt WT, Duque P, Ponce M (2005) An autochthonous geological model for the eastern Andes of Ecuador. Tectonophysics 399:251–278. https://doi.org/10.1016/j.tecto.2004.12.025

Prevot R, Chatelain J, Guillier B, Yepes H (1996) Mapping of the P-wave velocity structure beneath the Ecuadorian Andes: evidence for continuity of the Central Andes. Comptes Rendus Acad Sci Ser II-A 323:833–840

Proust JN, Martillo C, Michaud F, Collot JY, Dauteuil O (2016) Subduction of seafloor asperities revealed by a detailed stratigraphic analysis of the active margin shelf sediments of Central Ecuador. Mar Geol 380:345–362. https://doi.org/10.1016/j.margeo.2016.03.014

Robin C, Eissen JP, Samaniego P, Martin H, Hall ML, Cotten J (2009) Evolution of the late Pleistocene Mojanda–Fuya Fuya volcanic complex (Ecuador), by progressive adakitic involvement in mantle magma sources. Bull Volcanol 71:233–258. https://doi.org/10.1007/s00445-008-0219-9

Rose-Koga EF, Koga KT, Schiano P, Le Voyer M, Shimizu N, Whitehouse MJ, Clocchiatti R (2012) Mantle source heterogeneity for South Tyrrhenian magmas revealed by Pb isotopes and halogen contents of olivine-hosted melt inclusions. Chem Geol 334:266–279

Rose-Koga EF, Koga KT, Hamada M, Hélouis T, Whitehouse MJ, Shimizu N (2014) Volatile (F and Cl) concentrations in Iwate olivine-hosted melt inclusions indicating low-temperature subduction. Earth Planets Space 66:1–12

Sallarès V, Charvis P (2003) Crustal thickness constraints on the geodynamic evolution of the Galapagos Volcanic Province. Earth Planet Sci Lett 214:545–559

Samaniego P, Martin H, Robin C, Monzier M (2002) Transition from calc-alkalic to adakitic magmatism at Cayambe volcano, Ecuador: insights into slab melts and mantle wedge interactions. Geology 30:967–970

Samaniego P, Martin H, Monzier M, Robin C, Fornari M, Eissen JP, Cotten J (2005) Temporal evolution of magmatism in the northern volcanic zone of the Andes: the geology and petrology of Cayambe Volcanic Complex (Ecuador). J Petrol 46:2225–2252. https://doi.org/10.1093/petrology/egi053

Samaniego P, Eissen JP, Le Pennec JL, Robin C, Hall ML, Mothes P, Chavrit D, Cotten J (2008) Pre-eruptive physical conditions of El Reventador volcano (Ecuador) inferred from the petrology of the 2002 and 2004–05 eruptions. J Volcanol Geotherm Res 176:82–93

Samaniego P, Robin C, Chazot G, Bourdon E, Cotten J (2010) Evolving metasomatic agent in the Northern Andean subduction zone, deduced from magma composition of the long-lived Pichincha volcanic complex (Ecuador). Contrib Mineral Petrol 160:239–260

Samaniego P, Barba D, Robin C, Fornari M, Bernard B (2012) Eruptive history of Chimborazo volcano (Ecuador): a large, ice-capped and hazardous compound volcano in the Northern Andes. J Volcanol Geotherm Res 221–222:33–51. https://doi.org/10.1016/j.jvolgeores.2012.01.014

Schiano P, Eiler JM, Hutcheon ID, Stolper EM (2000) Primitive CaO-rich, silica-undersaturated melts in island arc: evidence for the involvement of clinopyroxene-rich lithologies in the petrogenesis of arc magmas. Geochem Geophys Geosyst 1:1999GC000032

Schiano P, Clocchiatti R, Ottolini L, Sbrana A (2004) The relationship between potassic, calc-alkaline and Na-alkaline magmatism in South Italy volcanoes: a melt inclusion approach. Earth Planet Sci Lett 220:121–137

Schiano P, Monzier M, Eissen JP, Martin H, Koga KT (2010) Simple mixing as the major control of the evolution of volcanic suites in the Ecuadorian Andes. Contrib Mineral Petrol 160:297–312

Schmidt MW, Jagoutz O (2017) The global systematics of primitive arc melts. Geochem Geophys Geosyst. https://doi.org/10.1002/2016gc006699

Shaw DM (1970) Trace element fractionation during anatexis. Geochim Cosmochim Acta 34:237–243

Smith DJ (2014) Clinopyroxene precursors to amphibole sponge in arc crust. Nat Commun 5:4329

Sorbadère F, Schiano P, Métrich N, Garaebiti E (2011) Insights into the origin of primitive silica-undersaturated arc magmas of Aoba volcano (Vanuatu arc). Contrib Mineral Petrol 162:995–1009

Sorbadère F, Schiano P, Métrich N (2013a) Constraints on the origin of nepheline-normative primitive magmas in island arcs inferred from olivine-hosted melt inclusion compositions. J Petrol 54:215–233

Sorbadère F, Schiano P, Métrich N, Bertagnini A (2013b) Small-scale coexistence of island-arc- and enriched-MORB-type basalts in the central Vanuatu arc. Contrib Mineral Petrol 166:1305–1321

Spandler C, Pirard C (2013) Element recycling from subducting slabs to arc crust: a review. Lithos 170–171:208–223

Spilliaert N, Métrich N, Allard P (2006) S–Cl–F degassing pattern of water-rich alkali basalt: modelling and relationship with eruption styles on Mount Etna volcano. Earth Planet Sci Lett 248:772–786

Straub SM, Layne GD (2003) The systematics of chlorine, fluorine, and water in Izu arc front volcanic rocks: implications for volatile recycling in subduction zones. Geochim Cosmochim Acta 67:4179–4203

Sun SS, McDonough WS (1989) Chemical and isotopic systematics of oceanic basalts: implications for mantle composition and processes. Geol Soc Lond Spec Publ 42:313–345

Syracuse EM, van Keken PE, Abers GA (2010) The global range of subduction zone thermal models. Phys Earth Planet Inter 183:73–90

Toplis MJ (2005) The thermodynamics of iron and magnesium partitioning between olivine and liquid: criteria for assessing and predicting equilibrium in natural and experimental systems. Contrib Mineral Petrol 149:22–39

Vaggelli G, De Vivo B, Triglla R (1993) Silicate-melt inclusions in recent Vesuvius lavas (1631–1944): II. Analytical chemistry. J Volcanol Geotherm Res 58:367–376

van den Bleeken G, Koga KT (2015) Experimentally determined distribution of fluorine and chlorine upon hydrous slab melting, and implications for F–Cl cycling through subduction zones. Geochim Cosmochim Acta 171:353–373

Vigouroux N, Wallace PJ, Kent AJR (2008) Volatiles in high-K magmas from the Western Trans-Mexican Volcanic Belt: evidence for fluid fluxing and extreme enrichment of the mantle wedge by subduction processes. J Petrol 49:1589–1618

Wallace P, Carmichael ISE (1992) Sulfur in basaltic magmas. Geochim Cosmochim Acta 56:1863–1874

Walter MJ (1998) Melting of garnet peridotite and the origin of komatiite and depleted lithosphere. J Petrol 39:29–60

Wasylenki LE, Baker MB, Kent AJR, Stolper EM (2003) Near-solidus melting of the shallow upper mantle: partial melting experiments on depleted peridotite. J Petrol 44:1163–1191. https://doi.org/10.1093/petrology/44.7.1163

Workman RK, Hart SR (2005) Major and trace element composition of the depleted MORB mantle (DMM). Earth Planet Sci Lett 231:53–72

Yepes H, Audin L, Alvarado A, Beauval C, Aguilar J, Font Y, Cotton F (2016) A new view for the geodynamics of Ecuador: implication in seismogenic source definition and seismic hazard assessment. Tectonics 35:1249–1279. https://doi.org/10.1002/2015TC003941

Chapter V

Extended melt inclusion analysis from Ecuadorian volcanoes.

5.1 Background

After the publication of our work in 2018 and that of Le Voyer et al. (2008), the knowledge about the slab component composition and the lithologies at the origin of primitive melts in Ecuador was improved. For example, we knew that the slab material that metasomatise the subarc mantle under Pan de Azucar and Puñalica volcanoes was a hydrous siliceous melt, while the metasomatic agent under Rucu Pichincha and Sangay was an aqueous fluid. Also, by studying major elements in melt inclusions, we presumed that primitive melts were produced from peridotites in the mantle that were mixed with amphibole-bearing clinopyroxenite melts from the upper mantle or the lower crust. Despite the significant progress in knowledge about the composition of the slab component and primitive melts in Ecuador, some questions remained unanswered, especially, those related with the spatial distribution of hydrous siliceous melts added from the slab. For instance, why melt inclusions from Rucu Pichincha and Puñalica volcanoes have different signatures of the slab component, although, they are located in the Western Cordillera and north of GFZ? Or, are melt inclusions from Sangay representative of primitive magmas formed south of GFZ? Therefore, we decided to enlarge the study of primitive melt inclusions from other volcanoes located to the north and south of the inland GFZ projection.

Our work "Two types of slab components under Ecuadorian volcanoes supported by primitive olivine-hosted melt inclusion study" is under review in the journal *Geochemistry, Geophysics, Geosystems* and contribute with more than 80 new composition of melt inclusions from four new volcanoes (Cotacachi, Cubilche, Cono de la Virgen, Conos de Licto) and one new sample from Sangay. The spatial distribution of selected samples was limited by the occurrence of primitive whole-rocks containing high-forsterite olivine ($Fo_{>80}$) and the access to those samples. The main contribution of this

work is the recognition of hydrous siliceous melt signature in volcanoes located north of GFZ and 120 km (or more) above the subducting slab. In contrast, melt inclusions from volcanoes located <120 km above the subducting slab (e.g. Cubilche, Cotacachi, Rucu Pichincha) or south of GFZ (Conos de Licto and Sangay) show an aqueous fluid signature. Also, we conclude from major element analysis that the source of Cono de la Virgen is a phlogopite bearing peridotite. Finally, this work shows that the volatile signature of melt inclusions, especially their F/Cl, can change from common values (F/Cl = 0.3 to 0.9 for most melt inclusions) due to the stability of phlogopite in the source (i.e. Cono de la Virgen, Fl/Cl = 6.99) or addition of Cl-rich fluid due to the presence of GFZ (i.e. Puñalica, F/Cl = 0.14).

5.2 Two types of slab components under Ecuadorian volcanoes supported by primitive olivine-hosted melt inclusion study

Two types of slab components under Ecuadorian volcanoes supported by primitive olivine-hosted melt inclusion study

D. F. Narváez[1,2,3], P. Samaniego[1], K.T. Koga[1] , E. F. Rose-Koga[1], S. Hidalgo[3], G. Ratzov[4]

[1] Université Clermont Auvergne, CNRS, IRD, OPGC, Laboratoire Magmas et Volcans, F-63000 Clermont-Ferrand, France

[2] Departamento de Geología, Escuela Politécnica Nacional, Ladrón de Guevara E11-253, Quito, Ecuador

[3] Instituto Geofísico, Escuela Politécnica Nacional, Ladrón de Guevara E11-253, Aptdo. 2759, Quito, Ecuador

[4] Université Côte d'Azur, CNRS, IRD, Observatoire de la Côte d'Azur, Géoazur, 250 rue Albert Einstein, Sophia Antipolis 06560 Valbonne, France

Corresponding author: Diego F. Narváez (diego.narvaez@etu.uca.fr; ORCID ID: 0000-0003-1902-2472)

Key points:

- We report new data for major, trace, and volatile element concentrations in olivine-hosted melt inclusions from five Ecuadorian volcanoes
- Geochemical systematics identify two distinctive compositional components added to the mantle wedge from the slab
- The slab component dichotomy is related to a change in the thermal regime of the subduction zone

Abstract

The origin of several geochemical indices in continental arc lavas (e.g., La/Yb, Ba/Th) is controversial as to whether it is imparted by the slab or acquired in the crust. In Ecuador, where volcanoes are built over a thick crust (~50 km), this problem is grounded in the lack of primitive rocks. Here, we use melt inclusions hosted in Fo_{80-90} olivines to

decipher the slab component signatures that metasomatises the sub-arc mantle. We report major, trace and volatile elements analyzed in experimentally heated melt inclusions, which are from high-Mg rocks of Cotacachi, Cubilche, Cono de la Virgen, Conos de Licto, and Sangay volcanoes located in the north and south of Ecuador. On the basis of trace elements and supported by geochemical modelling, we recognize two types of slab components: one is indicative of aqueous fluids (e.g., high Ba/La, Pb/Ce, B/Nb), and the other is indicative of hydrous siliceous melts (e.g., high La/Nb, Th/Nb). The aqueous fluid signature is recognized in all volcanoes (except for Cono de la Virgen), and their F/Cl are distributed around 0.49±0.1, independent of the distance to the Benioff zone. We propose a model where hydrous siliceous melts result from the subduction of a young oceanic crust north of the Grijalva fracture zone. Additionally, we show that the mantle under Licto and Sangay volcanoes is already enriched prior to metasomatism by slab fluids. This study shows that melt inclusions give valuable insights into the composition of primitive melts that are rarely accessible as whole rocks.

Plain text summary

Magmas supplied to arc volcanoes are derived from melting of mantle after the addition of water-rich material (slab component) from the subducting slab. In Ecuador, the subduction of the Nazca plate beneath the south-American plate produces magmas, which then traverse a thick continental crust of ~50 km. On route to the surface, magmas can change their composition due to crustal interactions. In order to understand mechanism of magma genesis at the depth, one must find the composition of primitive magmas that are little affected by crustal interactions. Our research finds such primitive magma by studying drops of magmas trapped inside olivine crystals (melt inclusions). By studying the composition of melt inclusions, we could identify two different slab components added to the mantle, and we could also constraint the mantle composition. The two different slab components are related to a change in the temperature along the subduction zone. Hot subduction zones allow the subducting slab to melt and produce hydrous siliceous melts, while cold subduction zones promote dehydration reactions releasing aqueous fluids. We propose that the two slab components are related to a change

in the temperature along the subduction zone due to a different age of the subducting Nazca plate.

Index terms: 1009, 1031, 1037, 1065, 1043

Key words: primitive magma, subduction zone, trace element, mantle metasomatism, Northern Volcanic Zone, Andes

1 Introduction

The slab component imparts the incompatible trace element arc signature (Ulmer, 2001) and, together with the mantle and the crust, contributes to the final composition of arc magmas. Defining the geochemical slab component signature is not an easy task because magmas change their compositions during their ascent toward the surface, hindering or overprinting the slab and mantle contributions. For example, arc magma signatures acquired in the crust (i.e., high Sr/Y, La/Yb, Th/La) are similar to those imparted by the slab. This geochemical complexity has led to a long-lasting discussion focused on characterizing the role of the slab and the crust components in the chemistry of arc magmas (e.g., Davidson, 1987, 1996; Elliott et al., 1997; Plank, 2005; Rogers & Hawkesworth, 1989, 1990; Smith et al., 1997; Stern, 1990, 1991; Turner et al., 2012; van Soest et al., 2002).

When the slab component can be identified, it also gives insight into the dehydration and melting processes occurring in the subducting slab (e.g., Elliot, 2003; Gómez-Tuena et al., 2006; Straub et al., 2004; Walowski et al., 2016). The efficiency of the slab material in moving incompatible elements changes depending on its temperature and the pressure at which this transport takes place (Hermann et al., 2006; Kessel et al., 2005a). For instance, aqueous fluids transferred to the mantle wedge at lower temperature are characterized by an enrichment in large-ion fluid-mobile lithophile elements (LILE, e.g., Rb, Ba, Sr), while, at higher temperature, fluids/melts/supercritical liquids – hereinafter called hydrous siliceous melts – are enriched in so-called fluid immobile elements, such as light rare earth elements (e.g., La, Ce, Nd), high-field-strength elements (HFSE, e.g., Nb, Zr), as well as Th (Kessel et al., 2005a). Aqueous fluids are most probably related to slab dehydration, occurring principally along low-temperature subduction zones (e.g. Kogiso et al., 1997; Tatsumi, 1989), while hydrous siliceous melts

are likely related to the partial melting of the subducting slab along high-temperature subduction zones (Elliott et al., 1997; Kelemen et al., 2014; Martin et al., 2005; Rapp et al., 1999)

In the Ecuadorian segment of the Northern Volcanic Zone – "Ecuadorian Arc" – the slab contribution to basaltic andesites and andesites with low Ba/Th and high La/Yb, Th/La has been debated for several years. Some studies propose that such geochemical signatures are imprinted into the sub-arc mantle by hydrous siliceous melts coming from the slab melting, and these signatures persist until the magmas reach the surface due to low degrees of crustal contamination (e.g. Ancellin et al., 2017; Hidalgo et al., 2012; Robin et al., 2009; Samaniego et al., 2005, 2010). On the other hand, others propose that the slab component is an aqueous fluid, and therefore the high La/Yb and Th/La are acquired in the crust due to hornblende and (or) garnet crystallization and crustal assimilation (e.g. Bryant et al., 2006; Chiaradia et al., 2009, 2020; Garrison & Davidson, 2003).

In this work, we studied melt inclusions (MI) hosted in Fo_{80-90} olivines from whole rocks in which Mg# [defined as molar 100*Mg/(Mg+Fe_T)] was greater than 55. We selected those rocks in order to focus our effort on the most primitive melts – those less affected by crustal processes – from the Ecuadorian arc. The sampled rocks came from Cono de la Virgen (CLV), Cotacachi and Cubilche volcanoes that are located in the northern part of the Ecuadorian arc, and from Conos de Licto (Licto) and Sangay volcanoes, located in the southern termination of the arc (Fig. 1). We also compiled MI data from the literature from Pan de Azúcar (PDA) and Rucu Pichincha volcanoes located in the north (Le Voyer et al. 2008), and Puñalica volcano located in the south (Narváez et al., 2018, see Fig. 1). We used ratios of incompatible trace elements in MI to avoid the effect of fractional crystallization, and we demonstrated: (1) that their chemical variability was not acquired in the crust and (2) that MI compositions resulted from melting of mantle that has been metasomatised by both aqueous fluids and (or) hydrous siliceous melts. Also, we gave some insights about the composition of the sub-arc mantle beneath

Ecuador, and interpreted the geochemical MI signature, for example, F/Cl ratio, in the context of the geodynamical setting of the Ecuadorian arc.

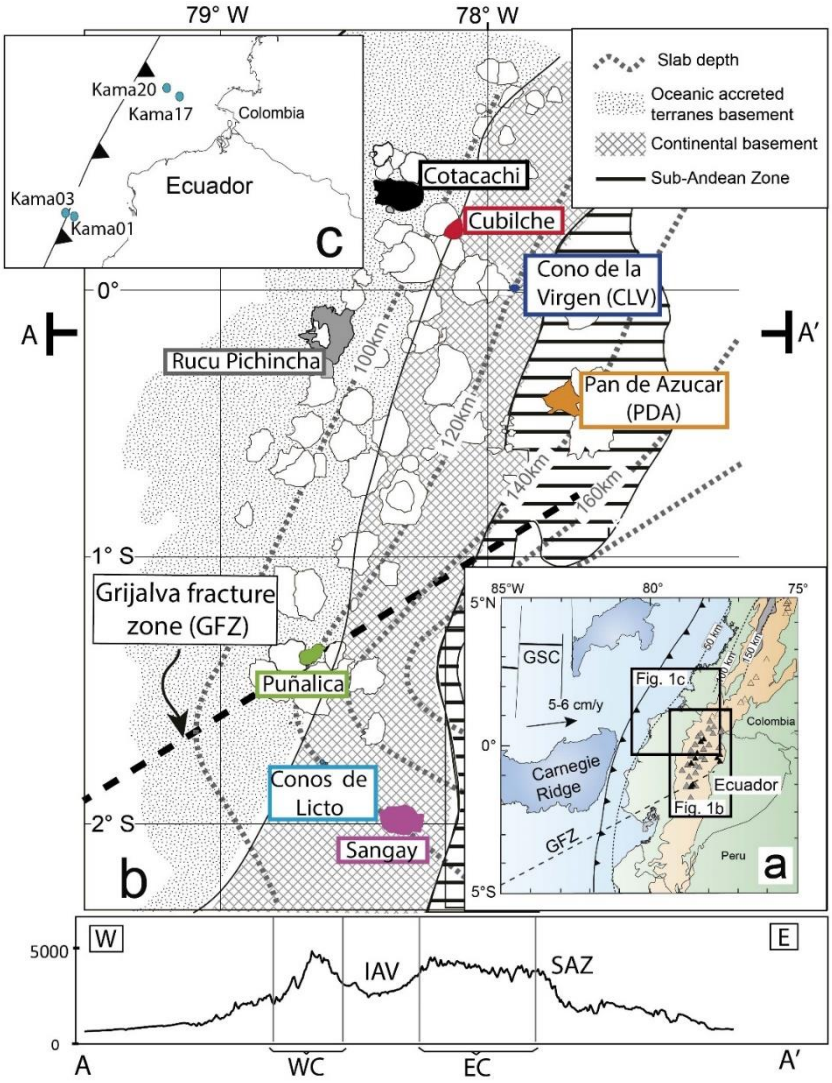

Figure 1 (a) Geodynamic setting of Ecuadorian arc. Shown in black triangles are volcanoes located along the Inter-Andean valley and Sub-Andean zone, and in grey triangles are volcanoes located on the Western and Eastern cordillera. **(b)** Schematic map of the main geological units in Ecuador [modified from Jaillard et al., (2008)] showing quaternary volcano locations. Analyses of melt inclusions were performed in rock samples from Cotacachi, Cubilche, Cono de la Virgen (CLV), Conos de Licto and Sangay. Also shown are Rucu Pichincha, Pan de Azúcar (PDA), and Puñalica volcanoes, whose melt inclusions were studied by Le Voyer et al. (2008), and Narváez et al. (2018). The dashed black line is the surface projection of the Grijalva fracture zone (GFZ). Slab depth contours are from Yepes et al. (2016). **(c)** Map of Northern Ecuador showing the location of sediments analyzed for this study. Kama 01, 03, 17, and 20 are the names of sedimentary piston cores studied by Ratsov et al. (2010). A-A' is a topographic profile across Fig. 1b. WC: Western Cordillera. IAV: Inter-Andean valley. EC: Eastern Cordillera. SAZ: Sub-Andean zone. The color codes for volcanoes shown in this figure are used in subsequent figures to show the provenance of MI.

2 General information on the Ecuadorian arc and sample descriptions

2.1 The Ecuadorian arc: geodynamic setting and geochemical summary

The Andean Northern Volcanic Zone (NVZ) spans from Northern Colombia (~6°N) to Central Ecuador (~2°S), and results from the oblique convergence of the Nazca and the South-American plates, at a rate of 5-6 cm/year (Kellogg et al., 1995; Nocquet et al., 2014; Trenkamp et al., 2002). In Colombia (6°N to 2°N), the Nazca plate subducts at a 30°- 40° dip to the east (Vargas & Mann, 2013), while in Southern Ecuador and Northern Peru (between ~3°S and 8°S), the Nazca plate subducts at a 10º dip, defining the Peruvian flat slab (Tavera & Buforn, 2001). In Northern and Central Ecuador, the subducting slab contains two significant structures. The first is the Carnegie ridge (located between 0° and 3°S), which is a 200-250 km-wide, 2 km-high submarine mountain range (Fig. 1a) originating from Galápagos hotspot activity. The Carnegie ridge is responsible for the low angle of subduction (~25° dip) of the Nazca plate at this latitude due to its higher buoyancy (Guillier et al., 2001; Yepes et al., 2016). The second structure is the N60ºE Grijalva fracture zone (GFZ, Fig. 1a), which consists of a 500 m-high escarpment separating, to the south, an older subducting slab (25-30 Ma) from a younger oceanic crust to the north (12-20 Ma; Gutscher et al., 1999; Sallarès & Charvis 2003). One important feature of Ecuadorian volcanoes is their location with respect to GFZ. Among the volcanoes studied, Licto and Sangay are the only ones located south of GFZ while the others are located just above or to the north of GFZ.

The east-west width of the Ecuadorian arc is greater (~120 km) than that of the volcanic arc in Colombia (40-50 km), and is characterized by more than 80 quaternary volcanic centers (Hall et al., 2008). Those volcanoes are distributed along four groups based on their location with respect to the two principal mountain ranges (the Western and Eastern Cordilleras, see topographic profile in Fig. 1). The frontal and the main arc groups correspond to volcanoes located above the Western and Eastern Cordilleras, respectively. Volcanoes from the frontal arc lie upon Meso-Cenozoic volcanic and sedimentary rocks of oceanic affinity (Jaillard et al., 2008; Vallejo et al., 2009), while those from the main arc are built over a continental-like crust that consists of felsic and intermediate igneous and metamorphic rocks (Aspden & Litherland, 1992; Pratt et al., 2005). The third group corresponds to the volcanoes of the Inter-Andean valley, which

are constructed above Miocene and Pliocene volcanic and sedimentary rocks (Winkler et al., 2005). Finally, a few scarce volcanoes that are further east constitute the Sub-Andean zone group, and are located in the upper Amazon basin.

The geochemical studies performed over the last two decades on Quaternary Ecuadorian volcanic rocks describe the main geochemical characteristic of this arc segment. First of all, the magma composition changes from the west to the east by an increase in incompatible trace elements, and a decrease in LILE over HFSE ratios further from the trench. This feature is conventionally interpreted as resulting from a decrease in the amount of fluids added into the sub-arc mantle from the subducting slab, and, consequently, a decrease of mantle melting (Barragan et al., 1998; Bryant et al., 2006; Hidalgo et al., 2012). More recently, significant north-south (along-arc) geochemical variations have been described, and are associated with a change in the slab component composition (Ancellin et al., 2017), or with a distinctive depth of magma-crust interactions (Chiaradia et al., 2020). In addition, Ecuadorian magmas broadly display an adakitic signature, mostly defined by high La/Yb and Sr/Y values. These compositions, mostly recognized in frontal arc volcanoes located between 0.5ºN and 1ºS, have been interpreted either in terms of partial melting of the slab and the subsequent metasomatic reactions in the mantle wedge (Bourdon et al., 2003; Hidalgo et al., 2012; Samaniego et al., 2005, 2010), or as due to lower crustal processes associated with high-pressure fractionation and (or) melting (Chiaradia et al., 2009, 2020; Garrison et al., 2011).

2.2 Sample locations

Cotacachi volcano (78.34ºW, 0.36ºN, 4944 m above sea level – asl, Fig. 1b), located in the Western Cordillera, is a Late Pleistocene stratovolcano formed by two successive edifices (Cotacachi I and II; Almeida, 2016). The oldest edifice comprises the outermost part of the present cone, and is formed by basaltic andesite and andesitic lavas. Cotacachi II includes a sequence of andesitic lavas present on the upper part of Cotacachi I and four dacitic satellite domes constructed on the lower Cotacachi I flanks. The three samples (17EQ91, MM1B, COTA02) come from Cotacachi I edifice, and are calc-alkaline basaltic andesite lavas and one tephra bomb (Table 1).

Cubilche volcano (78.13ºW, 0.23ºN, 3826 m asl) is a Late Pleistocene edifice (40-45 ka, Bablon et al., 2020), located in the Inter-Andean valley, that displays a horseshoe-shaped amphitheater opened to the north resulting from a sector collapse (Le Pennec et al., 2011). It comprises two volcanic edifices named Old and Young Cubilche (Roverato et al., 2018). Two samples come from Old Cubilche (17EQ81, 17EQ95) which are black, vesiculated, calc-alkaline andesitic lavas.

Cono de la Virgen – CLV – (77.91ºW, 0.02ºN, 3673 m asl) is a recent, Holocene satellite edifice associated with the Cayambe volcanic complex (Samaniego et al., 2005), and located on the Eastern Cordillera. This cone has a 250-300 m-thick succession of high-K calc-alkaline andesite lava flows. We selected three samples from the distal lava flows (CAY45A, CAY45B, CAY45C).

Conos de Licto – Licto – (78.62ºW, 1.78ºS) are two scoria cones with adjacent lava flows located in the southern part of the inter-Andean valley. The cones are aligned (N74°W), and are named Cerro Tulabug and Loma Bellavista. RIO10B was a lava flow sample of basaltic-andesite composition. This sample come from a lava related to Cerro Tulabug (3336 m asl) that is dated at 183 ± 9 ka (Bablon et al., 2019).

Sangay volcano (78.34ºW, 2.00º S, 5230 m asl) is the southernmost edifice of the NVZ, and is located on the Eastern Cordillera. It was constructed over the last 500 ka by three successive edifices (Sangay I, II and III; Monzier et al., 1999), which are separated by two major sector collapses. Sangay I growth extended from 500 to 250 ka, Sangay II from 100 to 50 ka, and the present cone has been active for at least 14 ka. The rock compositions span from basaltic andesites to dacites. One basalt is reported in the Sangay II sequence, and its olivine-hosted melt inclusions were previously studied by Narváez et al. (2018). The selected sample for this work, SAN21B, is from Sangay II edifice, and it is a calc-alkaline basaltic andesite lava.

Compiled MI data are from Rucu Pichincha, PDA, and Puñalica volcanoes. *Rucu Pichincha* volcano (0.85-0.1 Ma) is one of the two edifices that compose the Pichincha volcanic complex (Robin et al. 2010) and is located on the Western Cordillera. *PDA* is a poorly known stratovolcano from the Subandean zone that is hardly accessible due to its location in the Amazon jungle. One basaltic andesite from Rucu Pichincha and one

basaltic lava from PDA were studied by Le Voyer et al. (2008). *Puñalica* (18-20 ka, Bablon et al., 2019) is a 300 m-high cone-shape edifice located on the Western Cordillera. Four bombs and lavas from Puñalica volcano were studied by Narváez et al. (2018) and range from basaltic andesite to andesite in composition.

We also analyzed oceanic sediments that were sampled in sedimentary piston cores collected in the Manglares Forearc Basin (Collot et al., 2019) on the North Ecuador margin slope and subduction trench (Ratzov et al., 2010)(Fig. 1c). These sediments are related with the Esmeraldas submarine canyon, which is located immediately north of the Carnegie ridge collision zone. This submarine canyon incises the continental shelf and serves as a conduit for particle transport from the continent to the trench. The sediment contribution from the continent to the trench is probably recurrent since the beginning of the incision of this canyon (~5.3 Ma ago, Collot et al., 2019). These sediments were collected during the AMADEUS oceanographic cruise (Collot et al., 2005) at water depths ranging between 606 m below sea level – bsl – and 3797 m bsl (Table 2). These data were crucial for magma genesis discussion and geochemical modelling. The samples included either 1) hemipelagic deposits mainly composed of greenish brown-silty clay, with few fragments of wood and foraminifera, or 2) coarser silty turbidites that reflect the erosion of the arc and forearc by major rivers, or submarine slope failures of the margin sedimentary cover during earthquakes (Migeon et al., 2017; Ratzov et al, 2010).

Table 1. Major and trace element concentration of hosting rocks.

Volcano	*Cotacachi*			*Cubilche*		*Cono de la Virgen*			*Licto*	*Sangay*
Sample code	17EQ91	MM1B	COTA02	17EQ81	17EQ95	CAY45A	CAY45B	CAY45C	RIO10B	SAN21B
Rock name	Basaltic andesite	Basaltic andesite	Basaltic andesite	Andesite	Andesite	Trachy-andesite	Trachy-andesite	Trachy-andesite	Basaltic andesite	Basaltic trachy-andesite
IGSN	IEDFN0001	IEDFN0002	IEDFN0003	IEDFN0004	IEDFN0005	IEDFN0006	IEDFN0007	IEDFN0008	IEDFN0009	IEDFN000A
Deposit	lava flow	tephra bomb	lava flow	lava flow	lava flow	lava flow	lava flow	lava flow	lava flow	lava flow
Mineral assemblage	pl+cpx+opx+ol			pl+cpx+opx+ol		pl+amph+opx+cpx+ol			pl+opx+ol	pl+opx+ol
SiO_2	56.9	55.2	56.3	58.0	59.5	59.9	60.0	59.6	53.3	54.0
TiO_2	0.6	0.7	0.6	0.7	0.5	0.8	0.8	0.9	1.0	1.0
Al_2O_3	16.1	15.3	15.4	17.3	16.8	15.2	15.2	15.1	16.0	18.1
FeOt	7.4	8.2	7.8	6.6	6.2	5.7	5.6	5.7	8.2	7.5
MnO	0.1	0.2	0.1	0.1	0.1			0.1	0.1	0.1
MgO	6.8	7.9	7.8	4.8	5.3	4.6	4.6	4.8	8.3	5.1
CaO	8.0	8.8	8.2	7.1	7.0	6.6	6.4	6.6	8.1	8.3
Na_2O	3.0	2.9	2.9	3.9	3.5	3.7	3.7	3.6	3.6	4.1
K_2O	1.1	0.8	0.8	1.3	1.0	2.9	2.9	3.0	1.2	1.4
P_2O_5	0.1	0.1	0.1	0.2	0.1	0.6	0.6	0.6	0.2	0.3
Mg#	62.2	63.4	64.0	56.7	60.1	58.9	59.0	60.2	64.3	54.6
Sc	27.5	31.9	28.2	18.7	23.5			15.3	20.2	19.0
V	185.0	209.5	205.5	163.4	152.9			147	200.0	212.0
Rb	20.9	15.9	14.3	26.1	14.2			79.3	18.5	28.0
Sr	371	389	375	557	443			1427	720	920
Y	14.5	15.8	14.2	12.0	12.5			18.9	14.4	16.3
Zr	63.5	66.6	67.1	98.7	73.4			236	110.0	96.0
Nb	2.6	2.3	1.2	4.6	2.1			8.7	5.1	6.1
Ba	475	399	444	615	581			1687	526	700
La	6.5	6.1	7.2	13.2	8.1			72.7	15.0	18.5
Ce	14.0	13.2	15.9	23.4	13.3			149	30.0	38.0
Nd	8.5	8.9	9.4	14.1	8.5			69.5	18.5	21.4
Sm	2.5	2.4	2.6	3.0	1.7			11.9	4.0	
Eu	0.7	0.8	0.6	1.0	0.4			3.2	1.2	1.3
Gd	2.6	2.6	2.6	2.8	2.1			8.3	3.6	4.0
Dy	2.4	2.6	2.5	2.2	2.0			4.0	2.7	2.9
Er	1.1	1.5	1.2	0.8	0.8			1.5	1.3	1.6
Yb	1.5	1.5	1.5	1.1	1.2			1.1	1.2	1.4
Th	1.3	1.0	1.3	2.6	1.6			16.4	2.2	3.7
Reference	*A*	*B*	*A*	*A*	*A*	*C*	*C*	*C*	*B*	*D*

Note. The rock names are based on TAS classification after Le Bas et al. (1986). Mg# is calculated as 100*molar (MgO/(MgO+FeOT)). Olivine represents less than 5 vol.% in all rock samples. A, This study. B, Ancellin et al. (2017). C, Samaniego et al. (2005). D, Monzier et al. (1999).

Table 2. Major and trace element concentration of sediment samples.

Sample name	*S-K01-2*	*S-K03-2*	*S-K03-4*	*S-K17-T4*	*S-K20-3*
Core name	Kama01	Kama03	Kama03	Kama17	Kama20
Location	margin slope	trench	trench	Manglares basin	Manglares basin
Latitud	N 0°16.70'	N 0°18.89'	N 0°18.89'	N 1°43.08'	N 1°49.33'
Longitud	W 80°43.4'	W 80°49.65'	W 80°49.65	W 79°27.8'	W 79°7.8'
Water depth (m bsl)	3046.0	3797.0	3797.0	865.0	606.0
SiO_2	64.6	64.6	62.6	57.7	57.7
TiO_2	0.6	0.5	0.6	0.6	0.6
Al_2O_3	15.7	15.3	14.9	17.5	17.4
FeOt	5.2	4.9	5.6	6.3	5.8
MnO	0.0	0.1	0.0	0.0	0.1
MgO	2.7	2.6	3.1	3.1	3.0
CaO	4.4	5.3	6.0	8.5	9.7
Na_2O	4.8	5.0	5.0	4.1	4.2
K_2O	1.8	1.7	1.9	1.8	1.4
P_2O_5	0.2	0.2	0.2	0.2	0.1
Total	85.5	87.3	81.8	79.7	89.2
Rb	34.2	33.0	39.9	34.4	27.7
Sr	279.2	333.9	284.2	337.7	456.2
Ba	734.4	786.3	667.5	591.8	561.1
Sc	13.2	12.2	14.3	16.1	16.3
V	104.1	103.4	114.9	123.0	136.7
Cr	72.6	64.1	81.5	86.0	81.1
Co	9.2	9.0	8.9	11.2	14.4
Ni	35.7	30.0	42.6	46.2	31.5
Y	11.1	10.1	13.6	12.7	10.3
Zr	66.2	70.2	58.2	61.7	68.4
Nb	3.2	2.7	2.2	4.5	2.8
La	9.4	8.8	9.6	12.0	9.7
Ce	18.9	18.2	17.3	24.4	19.8
Nd	9.4	9.0	10.1	10.5	11.0
Sm	2.0	2.0	2.2	2.0	2.4
Eu	0.6	0.6	0.6	0.6	0.8
Gd	2.4	2.1	2.1	2.3	2.4
Dy	1.7	1.6	1.8	1.8	2.1
Er	1.4	1.2	1.1	0.9	1.4
Yb	0.9	0.9	1.1	1.0	1.1
Th	2.2	1.6	2.6	3.2	2.3
Th/La	0.23	0.18	0.27	0.26	0.23
Sm/La	0.21	0.23	0.23	0.17	0.25

3 Methods

3.1 Olivine-hosted melt inclusion preparation

We crushed 9 lavas and one volcanic bomb, and separated the 0.4-1.5 mm fraction. We picked olivine crystals under a binocular microscope. Then, we selected olivines with MI bigger than 25 μm. MI were typically sub-spherical to elongate, rounded, and between 25-300 μm in diameter (detailed dimensions were noted in extended Table 3 available on EarthChem library, Narváez et al., 2020). All MI were partially crystalized and presented bubbles; therefore, we performed a heating procedure using a Vernadsky-type microscope heating stage at 1-atm (Sobolev et al., 1980) following the method described by Le Voyer et al. (2010). The heating procedure observed these steps: an increase in the temperature of an olivine crystal (containing one or more MI) from a room temperature up to the temperature for melting crystals inside the MI, in order to reverse the crystallization that occurred after MI entrapment. For each experiment, the temperature was increased at a rate of 80°C/min until the heating stage reached the Au melting point (1064 °C), then at 10-30°C/min. The oxygen fugacity was kept below 10^{-10} at 1200°C to avoid oxidation of the host mineral. Once we observed the disappearance of all minerals inside the MI, we kept the temperature constant for 5 min and quenched the experiment by turning off the electric current to the heater. The whole procedure was completed in less than 30 minutes. The MI were visually monitored during the entire heating procedure with a microscope (*cf.* Schiano, 2003). Generally, one or more bubbles were present inside the MI at the beginning of the experiments. Bubbles moved and often coalesced during heating and they remained after quenching. Bubbles grew during the quench gaining up to ~12% in volume (see supplementary material for more details). After the experiment, the bubble sizes ranged from 10 to 100 μm, and on average represented 8 vol.% of MI. We polished 67 olivines with silicon carbide papers and exposed the quenched MI, and used alumina powder for the final polish.

3.2 Analytical methods

Major and trace element compositions of olivine crystals and MI were analyzed at Laboratoire Magmas et Volcans (LMV, Clermont-Ferrand, France) using a CAMECA

SX100 electron microprobe, and a Laser Ablation Inductively Coupled Plasma Mass Spectrometer (LA-ICP-MS), respectively. For major elements, the standard analytical procedure was reported in detail in Le Voyer et al. (2008). Olivine analyses were performed with a focused beam, at 15 kV accelerating voltage, and a current of 15 nA, and a 10s counting time for each element. Glasses were analyzed with a beam of 5-20 µm in diameter (depending on the diameter of the MI), a low current (8 nA) for major elements, and 80 nA for Cl, S, and F (Rose-Koga et al., 2020). No alkali loss was detected on the natural basaltic glass VG-A99 under these beam conditions, and also, alkalis of all MI (except for three MI from CLV) plotted along expected liquid lines of descent which suggest no alkali loss.

For trace elements, we used a laser ablation system (193 nm Eximer Resonetics M-50E) coupled with an inductively coupled plasma mass spectrometer (Agilent 7500 cs) following the procedure outlined in previous studies (Le Voyer et al., 2010; Rose-Koga et al., 2012, 2017). To summarize, we used a pulse energy of ~3 mJ, a spot diameter between 15 and 33 µm, and a laser pulse frequency of 2-3 Hz, depending on the inclusion size ensuring a fluence at sample surface of ~4 J/cm^{-2}. The background was measured for 40 seconds before ablation, and the analysis time was approximately 100s. Data reduction was performed using GLITTER software. We used BCR-2G and NIST SRM 612 basaltic glasses (Gao et al., 2002) as standard samples, and Ca as the reference element. Typical errors on the MI (1σ error of mean, $1/\sqrt{n}$ where n is the number of cycles) were less than 15% for all trace elements, except for Ta (<25%), and B (<40%).

We measured volatiles (H_2O, CO_2, F, S, Cl) in the melt inclusions using the CAMECA HR1280 housed at Centre de Recherches Pétrographiques et Géochimiques (CRPG, Nancy, France). Olivine crystals were pressed into high-purity indium in a 1-inch aluminum mount, which was then gold-coated. We used SIMS settings similar to those detailed in other studies (e.g., Rose-Koga et al., 2012, 2014), and summarized below. We used a Cs^+ primary ion beam with a current of 1 nA, a 10 kV secondary accelerating voltage, a -80 V offset, and a projected beam size of 10-20 µm. The instrument was operated with the contrast aperture at 400 µm, the energy aperture at 40 eV, the entrance slit at 52 µm, and the exit slit at 173 µm, for a mass resolution power of 7007, enough to separate all mass interfering signals. The standard basaltic glasses used

during SIMS analysis were KL2G, VG2, 47963-b, M35, M40, and N72 (Jochum et al., 2006, for F, Cl and S; Shishkina et al., 2010, for H_2O and CO_2).

Lava samples from Cotacachi and Cubilche volcanoes, as well as five samples of sediments from the Ecuadorian subduction trench and Manglares forearc basin were analyzed following the analytical procedure detailed in Cotten et al. (1995). Rock samples were crushed in agate grinder. Major and trace elements were measured by inductively coupled plasma-atomic emission spectrometry (ICP-AES) using a Horiba Jobin Yvon® Ultima 2 spectrometer, at the Université de Bretagne Occidentale (Brest, France). For major elements, the relative standard deviations were ≤1% for SiO_2, ≤2% for other major elements, and ≤5% for trace elements.

4 Results

The following description of major, trace and volatile elements only concern new data. MI data from Rucu Pichincha, PDA, Puñalica and Sangay (SAN20B shown in pink triangles in figures) are extensively compared with the new data, but they are not reported in this section. The details are found in Le Voyer et al. (2008) and Narváez et al. (2018).4.1 Major and trace elements

4.1. Major and trace elements

The MI are mostly silica-poor (41.6-53.9 wt.% SiO_2, Fig. 2), and range from sub-alkalic to alkalic, with K_2O ranging widely, from medium-K calc-alkaline to shoshonitic compositions. In general, for all MI compositions, MgO, FeO, CaO and TiO_2 produce a negative correlation with SiO_2, while Na_2O, K_2O and Al_2O_3 display a positive trend (Fig. 2b, d).

Table 3 Major, trace and volatile element concentrations of olivine-hosted melt inclusions from Cayambe, Cotacachi, Cubilche, Conos de Licto and Sangay volcanoes, normalized to an anhydrous basis.

	Cayambe *CAY45C*										*CAY45A*			*CAY45B*				***Cotacachi*** *17EQ91*		
	3A_1	3A_2	3A_3	5A_1	5A_2	1A	3C	4B	5C	6A	2B	3A	3B	1A	4A	5A	6A	1A_c	1A_r	1C
SiO_2	43.0	42.9	43.3	46.3	45.0	46.4	45.7	45.8	41.9		44.9	53.9	43.5	47.4	41.6	46.8	44.6	44.2	45.5	49.1
TiO_2	1.3	1.6	1.4	1.2	1.5	1.7	1.3	1.4	1.7		1.7	0.4	1.8	1.4	1.7	1.7	1.4	1.0	1.0	1.0
Al_2O_3	14.1	13.2	13.6	15.7	15.9	12.7	14.8	16.1	13.2		14.9	15.5	14.8	12.4	10.4	15.1	15.7	17.0	17.6	18.6
FeOt	9.8	9.5	9.8	7.1	7.7	5.9	6.8	6.8	10.2		7.0	7.0	6.4	6.0	12.5	8.1	7.8	8.4	7.9	5.4
MnO	0.1	0.1	0.0	0.1	0.1	0.1	0.1	0.1	0.2		0.1	0.2	0.1	0.1	0.1	0.1	0.1	0.1	0.1	0.1
MgO	8.9	8.5	9.3	8.1	7.8	9.6	9.6	8.7	8.4		7.8	9.9	9.2	8.2	8.9	8.0	9.4	9.2	8.6	9.3
CaO	12.9	13.8	13.0	10.9	11.7	14.0	11.6	11.4	13.8		13.2	7.7	13.8	13.7	15.7	8.9	11.4	16.6	16.0	12.9
Na_2O	3.1	3.1	2.5	4.0	3.6	2.2	3.3	3.6	3.1		3.4	2.3	3.3	2.0	1.2	3.7	3.1	2.8	2.6	2.6
K_2O	5.3	5.6	4.9	5.0	4.8	5.7	5.1	4.5	5.5		5.3	0.9	5.5	6.6	5.1	6.6	4.5	0.6	0.6	0.8
P_2O_5	1.4	1.9	2.0	1.6	1.8	1.8	1.9	1.6	2.0		1.7	2.2	1.6	2.3	2.8	1.1	2.0	0.0	0.2	0.2
Total	96.7	96.5	97.0	98.4	95.6	97.4	97.8	97.4	96.1		98.1		96.3	95.4	97.0	98.1	93.6	98.8	102.1	101.3
H_2O	0.57		0.52	0.33		0.52	0.45		0.78	0.42	0.25		0.21	0.60		0.51				0.05
CO_2	7828		6672	1160		775	1846				4852		5907	6078		859				194
F	2570		2489	2197		2803	2455		3038	3785	2629		2633	3137		2136				339
Cl	369		371	366		374	400		858	308	428		387	432		304				823
S	5265		5245	4239		2968	5224		6516		5448		5448	5924		3640				749
B			7.7	<12.8		10.7	11.9	<49	<10.7	16.4	<11.1	<14.6	13.2	<11.3	<16.7	28.1	<11.7	20.1	<19.4	12.1
Sc			29.3	14.7		33.6	24.9	28.0	30.9	29.9	23.0	<3.33	22.9	18.9	30.6	13.0	19.9	73.0	67.2	50.6
V			285	308		289	267	307	301	311	274	57	289	226	324	201	258	488	461	293
Rb			96	85		117	97	101	100	129	100		107	133	125	116	93	13.0	13.0	15.3
Sr			2586	2406		2558	2589	2649	2682	1914	2696	1451	2721	2899	2244	2239	2719	367	351	422
Y			26.1	21.9		31.7	25.4	25.2	26.9	34.6	28.0	25.6	26.6	27.0	41.0	17.1	22.6	23.4	23.2	18.6
Zr			374	319		477	375	407	410	365	423		402	395	638	355	339	55.5	53.8	63.7
Nb			9.7	9.9		10.7	9.7	11.4	10.3	10.6	10.6		10.3	11.1	14.7	11.9	8.9	1.1	1.1	1.9
Ba			2450	2066		2875	2475	2005	2612	3329	2645	2397	2554	3060	2848	2189	4324	329	339	381
La			141	128		166	138	128	150	162	148	152	139	163	195	86	118	3.1	3.1	5.1
Ce			282	248		348	279	249	306	363	300	313	294	331	411	145	243	8.5	8.2	12.0
Pr			34.3	30.5		40.8	32.1	33.1	35.2	44.6	36.2	38.1	35.2	38.7	49.9	24.3	28.1	1.4	1.3	1.8
Nd			142	113		174	135	132	154	195	151	155	145	151	214	100	117	7.0	6.9	8.2
Sm			24.3	18.8		30.5	23.0	24.2	25.5	33.2	24.8	24.7	25.3	26.9	39.0	18.5	21.0	2.9	2.8	2.5
Eu			6.3	5.2		7.9	6.0	3.8	6.5	8.5	6.6	5.6	6.4	6.9	9.8	6.8	5.2	0.9	1.1	0.9
Gd			15.2	10.5		18.1	13.5	14.5	16.5	21.0	16.3	15.1	14.4	15.6	23.2	10.8	12.1	2.7	3.1	2.9
Tb			1.5	1.3		1.7	1.4	2.0	1.6	2.1	1.5	1.6	1.5	1.5	2.3	1.3	1.2	0.5	0.6	0.5
Dy			6.8	6.3		8.2	6.4	3.7	7.0	8.9	6.9	6.7	6.8	6.8	10.2	4.9	6.3	3.9	4.2	3.1
Ho			0.9	0.9		1.2	1.0	1.0	1.1	1.2	1.1	0.9	0.9	1.0	1.4	0.9	0.9	1.0	0.9	0.7
Er			2.0	2.0		2.7	2.0	3.2	2.1	2.6	2.2	1.8	2.2	2.3	2.7	2.0	1.8	2.7	3.1	2.3
Tm			0.2	0.1		0.3	0.2	<0.16	0.3	0.3	0.2	0.2	0.3	0.2	0.3	0.1	0.2	0.4	0.4	0.3
Yb			1.6	0.6		1.4	1.2	1.0	1.4	1.8	1.5	1.2	1.5	1.1	2.1	1.4	1.1	3.0	3.2	1.8
Lu			0.2	0.1		0.2	0.2	0.3	0.2	0.2	0.2	0.2	0.2	0.2	0.2	0.1	0.2	0.4	0.4	0.3
Th			30.3	27.2		34.6	29.9	28.6	32.1	21.1	30.9	20.8	29.7	35.1	37.8	17.6	25.0	0.3	0.4	0.6
Pb			25.2	15.9		26.1	20.3	17.4	27.2	8.2	22.6		24.0	28.3	13.5	15.2	18.1	2.0	1.8	1.9
U			9.2	9.0		10.4	9.7	9.0	9.7	5.3	9.7	5.1	9.8	11.0	8.3	7.6	8.6	0.2	0.3	0.4
Hf			9.6	7.2		11.8	9.1	13.0	10.4	10.3	10.8	2.0	9.5	9.5	15.6	9.4	8.9	1.5	1.6	2.0
Ta			0.4	0.2		0.4	0.4	0.6	0.4	3.0	0.5	1.2	0.3	0.4	0.6	0.4	0.3	<0.12	<0.11	0.1
Fo	89.1	89.3	89.1	87.1	87.1	89.9	88.4	86.3	89.4	89.8	87.5		89.5	89.6	89.3	86.3	86.9	85.4	84.7	87.9

Note. The total given are the measured values. *Fo*=100*molar (Mg/Mg+Fe) of hosting olivines. "<" concentrations under the detection limit.

Table 3 continued

	Cotacachi *17EQ91*					*COTA02*			*MM-1B*			***Cubilche*** *17EQ81*								
	2B	2C	4C	5C	7A_b	2A_b	2A_m	2A_t	1B	5B	6A	1B	1C	1E	2A_b	2A_t	2B_c	2C	3C_b	3C_t
SiO_2	46.8	47.1	49.7	49.4	48.4	50.6	50.0	49.1	47.5	45.7	46.4	50.8	51.0	48.9	49.0	48.8		50.1	51.8	51.2
TiO_2	0.8	0.9	0.9	0.7	0.9	1.0	0.9	1.1	1.0	1.0	0.9	0.8	0.9	0.7	0.8	0.8		0.6	1.1	0.8
Al_2O_3	16.8	17.7	18.7	17.9	18.5	18.3	18.6	18.6	19.0	18.3	18.6	19.8	19.2	20.2	19.7	19.3		19.3	19.9	20.1
FeOt	6.6	9.2	5.8	6.4	5.5	5.3	5.4	4.8	7.6	7.4	8.0	4.5	4.9	5.3	4.9	5.2		5.6	4.8	5.0
MnO	0.1	0.1	0.1	0.1	0.1	0.1	0.1	0.1	0.1	0.1	0.1	0.1	0.1	0.0	0.0	0.1		0.1	0.1	0.0
MgO	9.8	8.6	8.3	9.3	9.2	8.2	8.0	8.4	9.1	10.6	10.2	6.9	7.5	7.1	7.8	8.0		7.2	6.8	6.9
CaO	15.1	12.8	11.1	11.4	12.5	12.0	12.3	13.1	11.3	12.2	11.6	12.8	9.9	13.8	13.4	13.3		12.5	9.6	11.2
Na_2O	3.2	2.6	4.1	3.7	3.7	3.3	3.6	3.7	3.6	3.9	3.4	3.4	4.8	3.2	3.3	3.4		3.5	4.3	3.5
K_2O	0.6	0.7	1.1	1.0	1.1	0.9	0.8	0.8	0.7	0.8	0.7	1.0	1.4	0.7	0.8	0.8		0.8	1.3	1.1
P_2O_5	0.3	0.2	0.1	0.1	0.1	0.2	0.2	0.3	0.2	0.1	0.1	0.0	0.3	0.1	0.1	0.2		0.2	0.2	0.2
Total	101.3	99.6	100.1	97.7	98.6	100.3	100.1	100.1	100.5	98.5	99.3	101.4	97.7	100.7	100.8	100.1		100.6	99.0	100.7
H_2O	0.06				0.23	0.05		0.04	0.06	0.25	0.16	0.20		0.18	0.24		0.27	0.36	0.19	
CO_2	1465					352		603	4058	3446	205	298		708	745					
F	287				397	457		359	319	313	327	328		331	338		453	322	380	
Cl	730				919	890		754	696	755	754	683		650	710		687	701	678	
S	1226				832	686		577	1339	1375	1295	1772		871	851			867	525	
B	<16.8	23.8			<19.7	<20	<17.8	23.2	<15.2	<16.5	<8.6	22.5	13.0	24.9	<16.3	18.1	<8.9	17.4	<16	<8.6
Sc	74.4	52.6			38.2	18.1	19.1	23.7	24.7	22.8	32.4	34.1	15.7	31.8	31.4	26.3	12.5	18.4	15.6	25.6
V	464	334			299	409	298	392	344	356	330	329	227	357	377	381	204	344	243	265
Rb	12.3	16.1			20.1	12.8	13.8	14.1	17.2	14.4	13.7	18.4	26.8	15.2	15.5	16.2	25.4	19.2	27.3	21.7
Sr	365	406			427	442	449	461	451	448	435	391	534	407	383	386	542	393	528	445
Y	21.1	19.4			17.4	15.6	16.5	16.0	15.5	18.7	17.8	17.6	13.8	17.4	17.1	17.7	12.1	17.8	13.9	15.8
Zr	52.6	65.9			66.9	55.4	68.6	67.3	62.8	65.0	66.0	58.1	89.5	50.0	52.7	54.9	71.0	52.6	89.0	74.0
Nb	1.4	1.6			2.0	2.1	2.2	2.1	2.5	2.0	2.3	1.5	3.3	1.1	1.4	1.6	2.9	1.8	3.1	2.2
Ba	323	421			435	363	369	368	384	396	392	397	534	318	342	360	522	380	516	460
La	3.4	5.3			5.3	5.7	5.4	5.5	6.5	5.4	5.1	4.4	9.1	3.8	4.1	4.2	8.8	4.6	9.0	6.9
Ce	9.5	12.5			12.4	13.5	13.8	12.8	12.5	12.6	12.5	10.9	20.1	9.6	10.8	10.5	19.0	10.1	20.0	15.3
Pr	1.5	1.8			1.7	2.0	2.0	1.8	2.2	1.9	1.8	1.5	2.6	1.3	1.5	1.4	2.3	1.5	2.2	2.1
Nd	7.6	9.4			8.2	9.1	9.7	9.9	10.0	9.7	9.6	7.9	11.7	6.9	7.4	7.0	10.8	7.7	11.5	9.7
Sm	2.3	3.4			2.7	2.9	2.9	2.7	2.5	3.1	2.9	2.3	3.2	2.7	2.1	2.6	2.6	1.8	2.8	2.4
Eu	0.8	1.1			0.9	1.0	0.7	0.8	0.9	0.8	0.9	0.6	0.9	0.8	0.8	0.8	0.8	0.7	1.0	0.9
Gd	3.2	3.7			2.6	2.1	3.7	2.8	3.0	3.1	2.9	2.4	3.0	2.9	2.2	2.3	2.6	2.8	2.1	2.6
Tb	0.5	0.6			0.4	0.5	0.5	0.3	0.5	0.5	0.5	0.4	0.5	0.4	0.4	0.4	0.4	0.4	0.4	0.4
Dy	3.9	4.0			3.1	2.8	3.4	2.5	2.9	3.1	3.1	3.0	2.6	3.1	3.4	2.9	2.4	2.7	2.4	3.0
Ho	0.8	0.7			0.6	0.6	0.7	0.6	0.7	0.8	0.6	0.5	0.5	0.7	0.6	0.7	0.5	0.5	0.5	0.6
Er	2.3	2.2			2.2	1.9	2.3	1.9	1.9	2.1	2.0	2.0	1.6	1.8	2.3	2.2	1.3	2.2	1.3	1.6
Tm	0.4	0.4			0.3	0.3	0.4	0.3	0.3	0.3	0.3	0.3	0.2	0.3	0.3	0.3	0.2	0.3	0.2	0.2
Yb	2.5	1.8			2.3	1.8	1.5	1.9	1.9	2.3	1.9	1.5	1.3	1.5	1.9	2.1	1.1	1.3	1.3	1.6
Lu	0.4	0.3			0.3	0.3	0.2	0.2	0.2	0.3	0.3	0.3	0.2	0.3	0.3	0.2	0.2	0.3	0.2	0.2
Th	0.4	1.0			0.8	0.7	0.8	0.8	0.7	0.6	0.7	0.8	1.8	0.7	0.7	0.6	1.7	0.9	1.7	1.6
Pb	1.8	3.0			3.5	2.3	2.1	2.1	4.5	3.0	2.9	2.7	3.8	2.0	2.2	2.2	4.5	3.0	5.3	7.7
U	0.2	0.4			0.5	0.5	0.5	0.5	0.4	0.4	0.4	0.5	0.8	0.4	0.5	0.4	0.7	0.6	0.7	0.7
Hf	1.5	2.0			1.8	2.2	2.0	1.7	1.9	1.9	2.0	1.6	2.4	1.2	1.6	1.3	2.2	1.9	2.0	2.0
Ta	<0.1	0.1			0.1	<0.12	0.2	0.1	0.1	<0.1	0.2	<0.12	0.2	<0.11	<0.12	<0.11	0.1	<0.13	0.3	0.1
Fo	87.2	84.3	84.8	85.6	85.9	86.2	86.2	86.7	85.2	87.1	85.7	88	86.3	87.2	88.3	87.1	80.4	85.5	85.9	85.9

Table 3 continued

	Cubilche *17EQ81*			*17EQ95*			***Conos de Licto*** *RIO10B*												
	3D	5A	5B	1B	2A	4B	1A	1B	1B_l	1B_t	1C	1D	2A	2B	2D	3A_l	3A_lc	3A_rc	3B_b	3B_c
SiO_2	49.9	49.8	51.5		49.4	48.3	51.2	50.9	50.2	50.2	49.2	50.6	50.2	50.8	49.4	50.8	49.9	50.1	53.1	51.9
TiO_2	0.9	1.1	0.7		0.8	0.7	1.1	1.1	1.1	1.0	1.2	1.3	1.0	1.3	1.2	1.4	1.4	1.3	1.1	1.0
Al_2O_3	19.1	19.5	20.0		19.3	21.1	19.6	19.1	18.6	18.0	19.3	19.5	18.4	18.7	19.0	19.2	19.3	19.6	17.9	18.5
FeOt	6.1	5.5	5.7		6.3	6.6	6.3	7.2	7.3	8.5	6.6	6.3	7.1	6.8	7.4	6.7	7.0	6.9	6.2	6.7
MnO	0.1	0.1	0.1		0.1	0.1	0.0	0.1	0.1	0.2	0.1	0.1	0.1	0.1	0.1	0.1	0.2	0.1	0.1	0.0
MgO	8.4	6.7	7.6		8.0	8.0	6.1	7.2	7.7	7.2	7.7	6.5	8.7	7.8	8.1	6.1	6.1	6.0	6.3	6.4
CaO	10.7	11.4	9.0		11.5	11.5	10.1	8.8	9.2	10.0	9.8	9.1	9.2	8.5	9.6	10.0	10.1	10.1	9.2	9.0
Na_2O	3.7	4.2	4.1		3.6	2.6	3.9	3.9	4.4	3.8	4.5	4.7	3.9	4.2	3.8	4.1	4.4	4.3	4.3	4.7
K_2O	1.0	1.3	1.2		1.0	0.8	1.3	1.3	1.3	1.0	1.2	1.5	1.2	1.4	1.2	1.3	1.2	1.3	1.5	1.4
P_2O_5	0.1	0.3	0.2		0.1	0.2	0.4	0.4	0.2	0.2	0.4	0.3	0.3	0.4	0.2	0.3	0.2	0.3	0.4	0.3
Total	99.3	98.8	101.1		99.6	101.9	100.1	100.4	98.5	100.2	99.6	101.7	100.3	99.8	100.6	98.8	99.0	100.4	99.7	99.5
H_2O	0.18			0.17	0.25		0.13		0.14		0.14		0.15	0.15	0.11	0.15				
CO_2					212		188		276		790		592		784	49				
F	319			320	304		464		475		476		474	493	413	504				
Cl	554			578	596		836		916		944		901	928	767	943				
S	657			861	1337		1934		2153		1495		1865	1402	945	1991				
B		<20.5	<22.2	14.4	<16	13.4	<12.6	<15.5	<8.5		17.5	9.1	9.7	<7.8	<17.4			21.2		<16.4
Sc		15.8	8.7	18.8	36.4	37.1	7.9	11.7	12.6		13.5	22.0	9.1	13.7	6.5			13.2		6.9
V		276	218	212	293	289	259	241	218		259	235	242	228	241			250		261
Rb		24.6	27.4	22.4	19.8	16.0	17.6	17.6	17.3		18.0	21.6	17.4	20.9	16.9			21.7		21.0
Sr		447	490	446	408	364	761	755	707		746	818	754	755	744			778		857
Y		14.4	14.0	11.7	16.3	18.5	13.7	12.2	12.7		13.4	13.2	13.2	14.0	13.6			15.2		14.0
Zr		71.0	63.4	56.0	48.4	64.1	104.3	94.2	92.6		91.1	103.6	97.4	104.5	96.3			113.5		122.4
Nb		2.4	2.4	1.8	1.8	1.8	6.1	5.2	5.0		5.7	6.2	5.4	5.6	5.7			6.4		6.8
Ba		449	505	499	480	439	526	506	505		496	560	500	542	488			543		661
La		6.8	7.0	5.6	5.1	5.4	14.7	13.7	13.8		13.9	15.6	14.1	15.2	14.6			15.5		18.0
Ce		15.5	15.2	11.7	11.2	11.9	33.6	31.4	29.9		32.8	33.8	30.7	32.2	29.8			34.1		40.1
Pr		2.0	1.9	1.5	1.5	1.6	4.3	4.0	3.8		3.9	4.3	3.9	4.3	4.0			4.3		5.4
Nd		9.1	9.7	7.0	7.0	8.4	18.8	17.4	17.0		16.6	18.3	16.9	19.0	17.6			18.0		25.6
Sm		2.7	1.7	1.6	1.8	2.3	4.9	4.1	3.8		4.0	4.5	3.9	3.9	4.1			3.9		3.5
Eu		0.9	0.8	0.6	0.7	0.9	1.4	1.0	1.3		1.1	1.2	1.2	1.3	1.4			1.3		1.6
Gd		2.3	2.6	1.8	2.2	3.0	3.4	2.9	3.0		3.5	3.0	3.6	3.3	3.4			3.5		5.2
Tb		0.4	0.5	0.3	0.3	0.4	0.5	0.5	0.4		0.5		0.5	0.5	0.4			0.5		0.6
Dy		3.2	2.8	2.1	2.5	2.9	3.3	2.6	2.7		2.5	2.6	2.6	2.8	2.7			3.0		3.7
Ho		0.6	0.5	0.4	0.7	0.6	0.6	0.4	0.4		0.6		0.5	0.5	0.5			0.6		0.7
Er		1.6	1.1	1.5	1.9	1.9	1.4	1.5	1.4		1.6		1.2	1.3	1.3			1.3		2.0
Tm		0.2	0.3	0.2	0.3	0.3	0.2	0.2	0.1		0.2		0.2	0.2	0.1			0.2		0.2
Yb		1.7	1.3	1.3	2.2	2.1	1.3	1.0	1.0		1.3	1.6	1.1	1.4	1.0			1.4		1.4
Lu		0.3	0.2	0.2	0.3	0.3	0.2	0.2	0.2		0.2	0.2	0.2	0.2	0.1			0.2		0.1
Th		1.7	1.3	1.3	1.0	1.2	1.9	2.0	1.9		1.7	2.0	2.1	2.4	1.9			2.4		2.5
Pb		5.5	4.4	4.9	5.1	3.9	6.7	7.2	6.5		6.0	6.3	6.0	7.4	5.1			7.3		7.8
U		1.1	0.7	0.6	0.5	0.4	0.7	0.6	0.7		0.6	0.7	0.7	0.8	0.7			0.9		0.7
Hf		2.1	1.8	1.5	1.8	1.7	2.8	2.8	2.3		2.3	2.4	2.5	2.8	2.5			3.0		3.0
Ta		0.3	<0.16	0.1	0.1	0.2	0.2	0.3	0.2		0.2	0.3	0.2	0.3	0.2			0.3		0.3
Fo	84.6	85.5	84	82	82	85.4	85.2	83.6	84.3	84.3	86.3	85.1	85.1	84.9	84.7	84.8	84.7	84.7	85.6	85.6

Table 3 continued

	RIO10B			***Sangay*** *SAN21B*															
	5B	5C	6B	1A_b	1A_s	1B	1C	2A	2B	2C	3B	3C	4A	4B	5A	5B_m	5B_t	6A	6B	7B
SiO_2	50.4		52.3	47.9	47.0	49.2	48.9	46.5	49.7	48.5	48.6	49.3	48.0	49.3	49.8	48.1	51.3	48.5	49.9	
TiO_2	1.3		1.1	1.4	1.5	1.1	1.3	1.2	1.2	1.3	1.2	1.4	1.3	1.1	1.2	1.3	1.0	1.1	1.0	
Al_2O_3	19.3		19.2	18.3	19.2	19.5	16.9	18.5	18.3	19.3	18.9	19.2	19.1	19.2	19.8	19.6	18.6	17.7	18.9	
FeOt	6.8		7.5	8.0	7.5	6.5	6.6	7.9	6.5	6.9	7.2	6.5	6.8	6.5	6.1	7.3	6.1	8.0	6.3	
MnO	0.1		0.1	0.1	0.1	0.1	0.1	0.1	0.1	0.1	0.1	0.1	0.1	0.1	0.1	0.1	0.1	0.1	0.1	
MgO	7.0		5.5	8.5	8.6	8.0	8.6	9.4	7.7	7.7	8.9	6.9	8.2	7.6	7.1	7.8	7.4	9.6	8.0	
CaO	9.3		8.3	10.3	10.5	8.4	12.7	12.0	11.0	10.6	9.4	10.4	10.9	9.7	9.0	10.6	9.1	9.3	7.9	
Na_2O	4.0		4.4	4.1	4.2	4.6	3.6	2.6	3.9	4.0	3.9	4.3	4.0	4.5	4.7	3.8	4.4	4.0	4.4	
K_2O	1.2		1.3	1.0	1.0	2.0	1.1	1.4	1.2	1.2	1.4	1.3	1.1	1.6	1.9	1.1	1.6	1.4	2.8	
P_2O_5	0.5		0.2	0.4	0.4	0.5	0.3	0.3	0.4	0.4	0.4	0.6	0.4	0.4	0.3	0.3	0.3	0.3	0.8	
Total	100.6		100.2	101.1	99.9	99.8	100.3	98.1	100.3	100.6	100.6	100.3	99.3	100.2	99.3	99.3	100.3	99.8	100.2	
H_2O	0.15	0.14					0.27		0.37	0.27	0.27	0.24	0.25	0.41	0.33		0.35	0.28	0.21	
CO_2	256	556					417		300	271	55	209	311	430	99		159	105	165	
F	500	549		445			411		470	468	447	477	421	481	521		444	443	548	341
Cl	949	1052		698			597		726	705	680	728	613	733	957		799	685	1638	457
S	1311	2581		1147			825		966	734	985	979	846	802	768		562	1057	728	706
B		<15.4	<20.3	5.8		10.7		<8.7		12.5		<15.6	9.8	9.7	<7.1			11.9	10.5	
Sc		5.8	13.9	24.3		12.9		25.5		18.0		19.0	20.3	17.9	16.6			20.8	14.3	
V		300	239	283		207		275		261		255	273	228	203			221	247	
Rb		19.9	22.5	17.2		25.1		25.5		19.9		24.4	15.8	27.8	34.1			22.3	11.5	
Sr		891	685	865		1441		937		846		919	788	907	1096			842	841	
Y		14.9	14.2	17.9		13.0		18.4		15.3		15.6	15.2	14.7	14.4			14.5	14.0	
Zr		109.4	109.0	98.3		87.7		100.1		83.1		87.2	85.5	91.9	103.5			86.7	85.8	
Nb		6.4	6.1	6.2		6.7		8.3		5.5		5.9	5.1	6.2	7.8			5.5	5.3	
Ba		578	499	558		1006		566		557		599	485	673	835			586	463	
La		16.6	14.0	14.8		27.2		19.4		14.6		15.7	13.0	16.4	23.7			15.2	14.7	
Ce		36.1	30.9	34.3		55.0		42.4		32.8		33.5	28.9	35.2	48.4			32.7	33.2	
Pr		4.3	3.8	4.5		6.7		5.7		4.2		4.6	4.0	4.6	6.1			4.3	4.5	
Nd		21.1	17.0	20.6		27.2		24.9		19.8		19.3	19.0	19.7	26.3			19.5	21.4	
Sm		4.5	4.0	5.2		5.1		5.7		4.0		4.2	3.9	4.1	5.6			4.3	4.6	
Eu		1.5	1.3	1.5		1.4		1.8		1.3		1.3	1.4	1.2	1.4			1.3	1.4	
Gd		3.6	3.4	4.4		3.2		4.2		3.4		4.1	3.7	3.7	4.0			3.7	3.9	
Tb		0.5	0.4	0.6		0.4		0.5		0.5		0.6	0.5	0.5	0.5			0.5	0.5	
Dy		2.9	2.9	3.7		2.5		3.8		3.2		3.1	3.1	3.2	3.0			2.8	2.9	
Ho		0.5	0.6	0.6		0.4		0.7		0.6		0.7	0.6	0.5	0.5			0.5	0.6	
Er		1.3	1.5	1.6		1.2		1.9		1.6		2.0	1.7	1.6	1.6			1.6	1.5	
Tm		0.1	0.2	0.2		0.2		0.3		0.2		0.1	0.2	0.2	0.2			0.2	0.2	
Yb		1.2	1.1	1.7		1.3		1.7		1.4		1.5	1.3	1.4	1.4			1.3	1.2	
Lu		0.2	0.2	0.2		0.2		0.3		0.2		0.2	0.2	0.2	0.2			0.2	0.2	
Th		2.1	2.2	2.7		4.3		3.6		2.2		2.5	1.9	2.8	4.8			2.8	1.9	
Pb		7.3	21.9	6.1		5.8		<0.11		3.9		4.0	3.8	5.3	6.5			6.1	2.0	
U		0.8	0.8	0.8		1.1		1.1		0.7		0.8	0.5	1.0	1.5			0.8	0.6	
Hf		3.0	2.9	2.6		2.3		2.6		2.3		2.7	2.3	2.8	3.0			2.3	2.4	
Ta		0.3	0.3	0.3		0.3		0.4		0.3		0.5	0.2	0.3	0.4			0.3	0.3	
Fo	85.4	85.2	84.1	82.9	83.4	83.2	83.4	83.7	82.6	81.9	81.2	83	83.6	81.3	82.3	82.2	82.2	81.4	82.6	

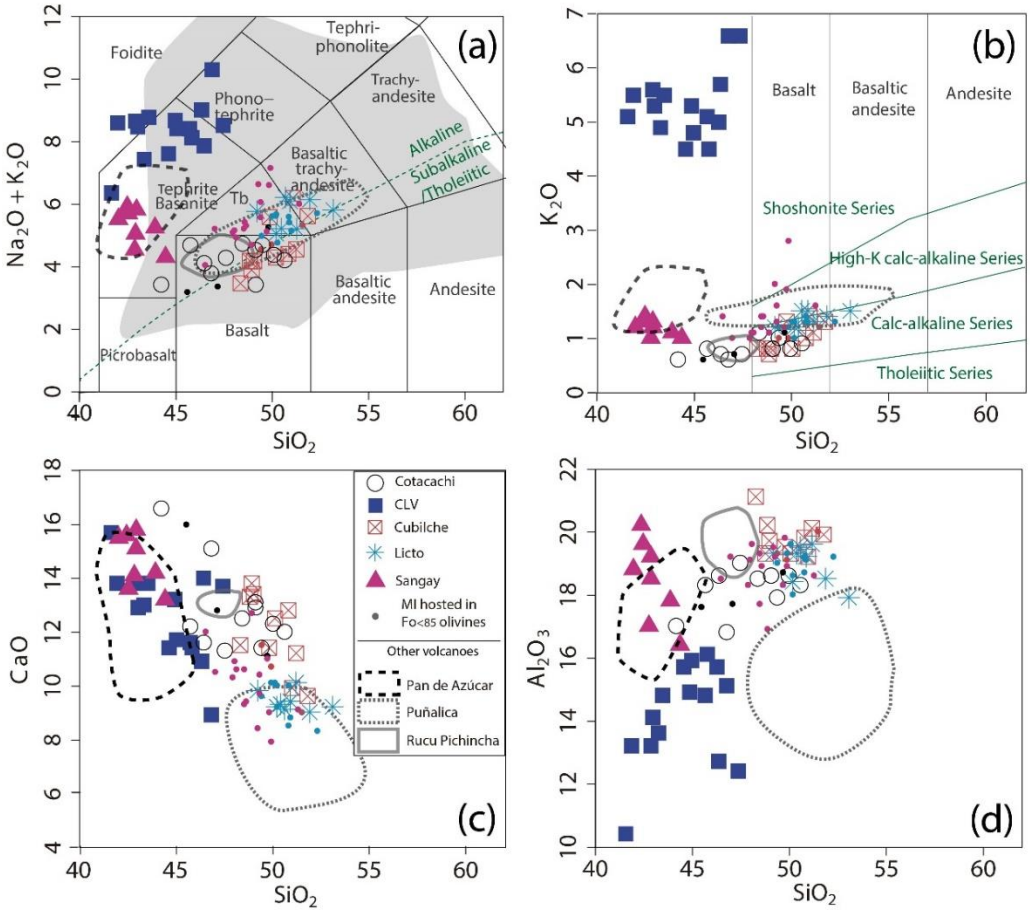

Figure 2 (**a**) SiO_2 *vs.* Na_2O + K_2O classification diagram (Le Bas et al., 1986) of olivine-hosted MI compositions from the Ecuadorian arc. MI are divided in two groups. MI hosted in Fo>85 olivines are shown with larger colored symbols, while those hosted in Fo<85 olivines are depicted with small colored filled circles to show potential compositional variations related to magma evolution. The colors are the same as the volcano color codes in Fig. 1. Sangay MI shown with pink triangles and Puñalica MI compositions from Narváez et al. (2018), PDA, and Rucu Pichincha MI from Le Voyer et al. (2008). The area labeled "Tb" corresponds to trachy-basalt field. The gray shade without a black border is the entire compositional variation of Ecuadorian quaternary volcanoes rocks (database from Ancellin et al., 2017). (**b**) SiO_2 *vs.* K_2O classification diagram from Peccerillo and Taylor (1976). (**c-d**) Harker diagram of silica versus CaO and Al_2O_3 wt.%. Plotted data are uncorrected for post-entrapment modifications, and are normalized for an anhydrous basis.

All the studied MI display a typical arc signature based on their trace element abundance spectrum (Fig. 3) and are characterized by an enrichment in large-ion-lithophile elements (LILE, e.g., Ba, Sr) relative to high-field-strength elements (HFSE, e.g., Nb, Ta). It is noteworthy that all MI have similar compositional ranges to their host-lavas, except for MI from CLV that show higher concentrations than its host lava.

The fractionation between light rare earth elements (LREE) and heavy REE (HREE) is weak in Cotacachi and Cubilche MI and display relatively flat or low-slope REE patterns when normalized to primitive mantle (Fig. 3a, b). Such a feature is represented by low values of $(La/Yb)_N$ (normalized to the primitive mantle values of McDonough & Sun (1995), Table 4). On the other hand, CLV MI show very steep REE patterns with high $(La/Yb)_N$ values (up to 140) and correspond to the highest values so far reported in olivine-hosted MI in the Ecuadorian arc (*cf.* Le Voyer et al., 2008; Narváez et al., 2018). The REE patterns of all the other MI (Licto, Puñalica, Sangay, PDA) display intermediate positions. CLV MI also show the highest concentration in trace elements (Fig. 3e) compared to other MI from this arc segment (except for Ta, Ti, Y, Yb and Lu).

Trace element compositions from Cotacachi and Cubilche MI showed several similarities. For instance, MI from both volcanoes are enriched in fluid-mobile elements compared to HFSE (e.g., B/Nb, Table 4), and LILE relative to LREE (e.g., Ba/La and Pb/Ce) and they are richer in Ti, Eu, and poorer in Th compared to whole-rock compositions of their host lavas (Fig. 3b, c).

Sangay and Licto MI display intermediate $(La/Yb)_N$ values, and their trace element composition is very similar to one another (Fig. 3g). This set of MI has lower Ba/La and Pb/Ce values than MI from Cubilche and Cotacachi, but higher than those from CLV (see Table 4). A remarkable feature of Sangay and Licto MI are their Nb-enrichment, represented by a less prominent negative Nb-anomaly (Fig. 3c, d), yielding a higher Nb/Nb* value between 0.1 and 0.17 ($\log(Nb^*) = ((\log(U)+\log(K))/2)$, normalized to NMORB), compared to Cubilche, Cotacachi, and CLV MI with Nb/Nb* ranging from 0.03 to 0.1.

Table 4 Some major, volatile and incompatible trace element ratio values for Ecuadorian olivine-hosted MI.

	Hosting olivine				Melt inclusions by groups						
Volcano	**Sample**	**Forsterite content**	**Fo>80**	**Fo>85**	**K_2O/Na_2O**	**F/Cl**	**B/Nb**	**Pb/Ce**	**Ba/La**	**Ba/Th**	**Reference**
Cotacachi	17EQ91 MM1B COTA02	84.3-87.9	15	12	0.24 (0.04) **0.24**	0.44 (0.04) **0.44**	10.4 (4.4) **9.3**	0.22 (0.06) **0.22**	79.6 (16.1) **76.7**	640 (212) **628**	*this work*
Cubilche	17EQ81 17EQ95	80.4-88.3	17	10	0.27 (0.03) **0.27**	0.53 (0.06) **0.5**	9.1 (4.9) **9.8**	0.3 (0.1) 0.28	76.5 (12.7) **75.6**	399 (103) **402**	*this work*
Conos de Licto	RIO10B	83.6-86.3	18	9	0.3 (0.02) **0.3**	0.53 (0.01) **0.53**	2.4 (0.7) **2.3**	0.24 (0.14) **0.19**	35.8 (1.0) **35.9**	256 (20) **266**	*this work*
Sangay	SAN21B	81.2-83.7	17	0	0.35 (0.1)	0.62 (0.1)	1.7 (0.6)	0.12 (0.05)	36.3 (3.6)	222 (34)	*this work*
	SAN20B	86.8-89.0	8	8	0.29 (0.01) **0.29**	0.42 (0.05) **0.42**	1.1 (0.5) **1.1**	0.15 (0.01) **0.15**	29.3 (1.6) **29.3**	261 (17) **261**	Narváez et al. (2018)
Rucu Pichincha		86.2-89.1	38	38	0.25 (0.01) **0.25**	0.42 (0.06) **0.42**	7.9 (2.5) **7.9**		66.9 (17.1) **66.9**		Le Voyer et al. (2008)
Cono de la virgen	CAY45A CAY45B CAY45C	86.3-89.9	18	18	1.94 (0.8) **1.94**	6.99 (2.08) **6.99**	1.5 (0.9) **1.5**	0.07 (0.02) **0.07**	19.6 (5.8) **19.6**	98 (32) **98**	*this work*
Puñalica		82.4-85.8	42	5	0.41 (0.04) **0.41**	0.19 (0.08) **0.14**	2.0 (0.7) **0.73**	0.13 (0.05) **0.15**	23.6 (20.8) **22.5**	108 (102) **104**	Narváez et al. (2018)
PDA		78-88.2	17	7	0.4 (0.03) **0.39**	0.72 (0.24) **0.83**	0.4 (0.1)		26.1 (2.3)		Le Voyer et al. (2008)

Note. Forsterite content is calculated as 100*molar (MgO/(MgO+FeOt)). The Fo>80 column represents the number of MI hosted in olivines with a forsterite content greater than 80. Values in parentheses are 1σ (standard deviation) of mean values. Bold type values are mean values calculated for MI hosted in Fo>85 olivines. Nb/Nb* is Nb content of MI normalized to NMORB (Sun & McDonough, 1989) divided by Nb* where log(Nb*) = ((log(U)+log(K))/2).

Table 4 continued

	Melt inclusions by groups								
Volcano	**Sample**	**$(La/Yb)_N$**	**Th/Nb**	**Th/La**	**La/Nb**	**Nb/Nb***	**Hf/Nb**	**Zr/Nb**	**Reference**
Cotacachi	17EQ91 MM1B COTA02	1.7 (0.6) **1.7**	0.35 (0.1) **0.33**	0.13 (0.02) **0.13**	2.7 (0.3) **2.6**	0.08 (0.01) **0.08**	1.0 (0.2) **0.97**	35 (7.7) **33.2**	*this work*
Cubilche	17EQ81 17EQ95	2.8 (1.3) **2.6**	0.57 (0.1) **0.56**	0.2 (0.03) **0.19**	2.9 (0.2) **2.9**	0.06 (0.01) **0.08**	0.89 (0.14) **0.91**	31.9 (5.4) **33.7**	*this work*
Conos de Licto	RIO10B	8.4 (1.0) **8.4**	0.36 (0.03) **0.36**	0.14 (0.01) **0.14**	2.6 (0.1) **2.6**	0.14 (0.01) **0.15**	0.46 (0.04) **0.44**	17.5 (0.7) **17.2**	*this work*
Sangay	SAN21B	8.6 (2.5)	0.46 (0.1)	0.17 (0.02)	2.8 (0.5)	0.12 (0.02)	0.41 (0.05)	14.8 (1.5)	*this work*
	SAN20B*	10.7 (2.6) **10.7**	0.19 (0.01) **0.19**	0.11 (0.00) **0.11**	1.7 (0.1) **1.7**	0.35 (0.14) **0.35**	0.2 (0.02) **0.2**	7.2 (0.8) **7.2**	Narváez et al. (2018)
Rucu Pichincha		2.7 (0.7) **2.7**			3.3 (1.6) **3.3**			47.7 (21.2) **47.7**	Le Voyer et al. (2008)
Cono de la virgen	CAY45A CAY45B CAY45C	75.8 (24.1) **75.8**	2.7 (0.5) **2.7**	0.2 (0.03) **0.2**	13.4 (2.2) **13.4**	0.04 (0.01) **0.04**	0.96 (0.12) **0.96**	37.7 (4.1) **37.7**	*this work*
Puñalica		19.3 (9.2) **13.3**	2.1 (0.7) **1.56**	0.22 (0.02) **0.22**	9.7 (1.6) **7.3**	0.04 (0.01) **0.05**	0.63 (0.1) **0.58**	24.5 (2.7) **22.8**	Narváez et al. (2018)
PDA		13.1 (2.6)			2.2 (0.6)			7 (2.5)	Le Voyer et al. (2008)

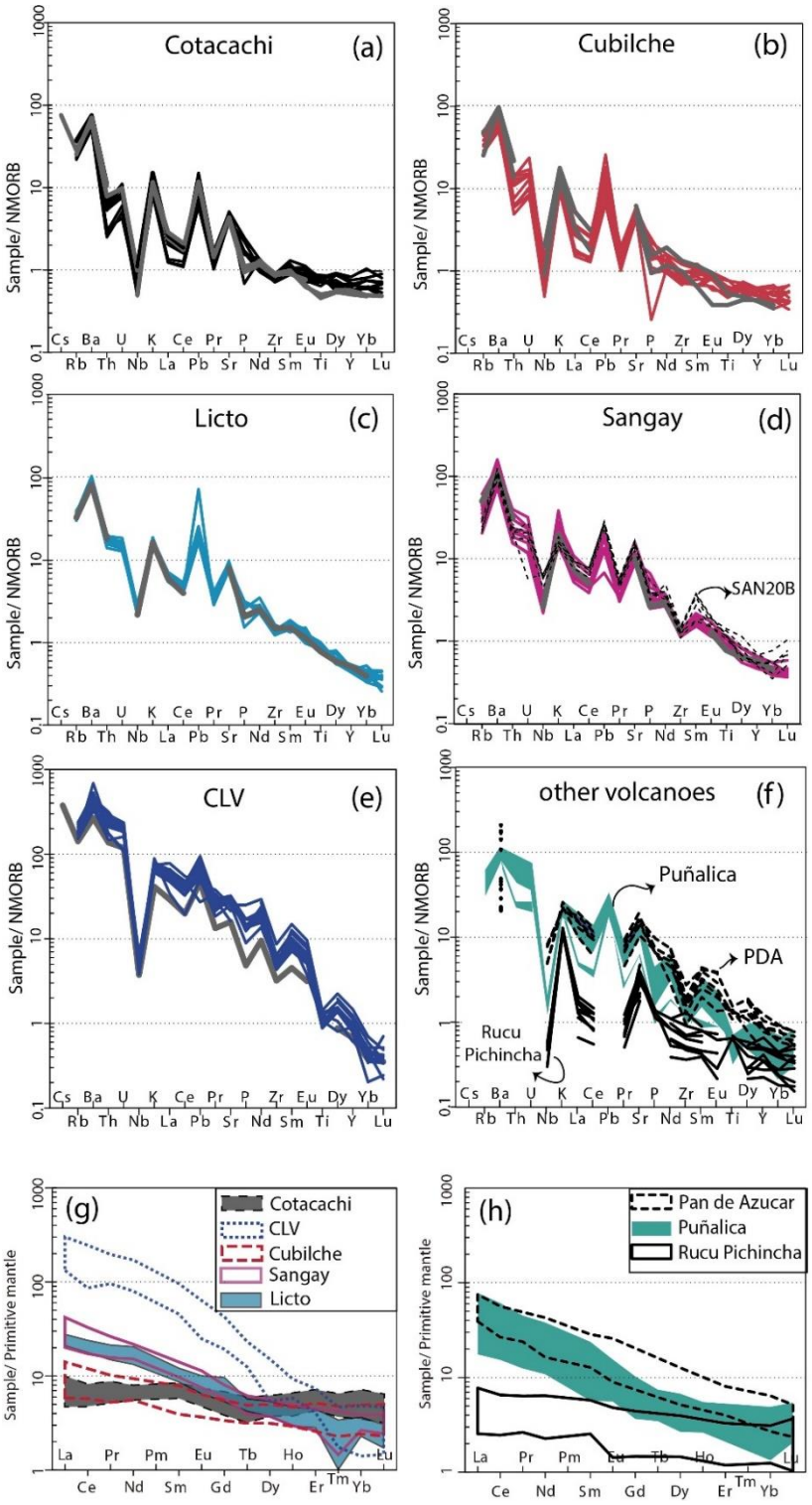

Figure 3 (a-e) Spidergram plot of MI (black and colored lines) and hosted-lava (gray and thick solid lines) compositions from Cotacachi, Cubilche, Licto, Sangay and CLV volcanoes, normalized to N-MORB (Sun & McDonough, 1989). MI labelled SAN20B in (d) from Narváez et al. (2018). **(f)** Spidergram plot similar to (a-e) of MI from Puñalica, PDA, and Rucu Pichincha studied by Le Voyer et al. (2008) and Narváez et al. (2018). **(g)** REE diagram – showing subset of elements used in panels (a)-(f) – for MI compositions of this study normalized to primitive mantle (Sun & McDonough, 1989). **(h)** REE diagram similar to (g) for MI from Puñalica, PDA, and Rucu Pichincha.

4.2. Volatile elements

MI from all volcanoes, except for CLV, have similar Cl (503-1991 ppm) and F contents (283-491 ppm). MI from CLV have lower Cl (305-1018 ppm) and display the highest F contents (1703-2969 ppm) reported so far in Ecuadorian MI (Fig. 4).

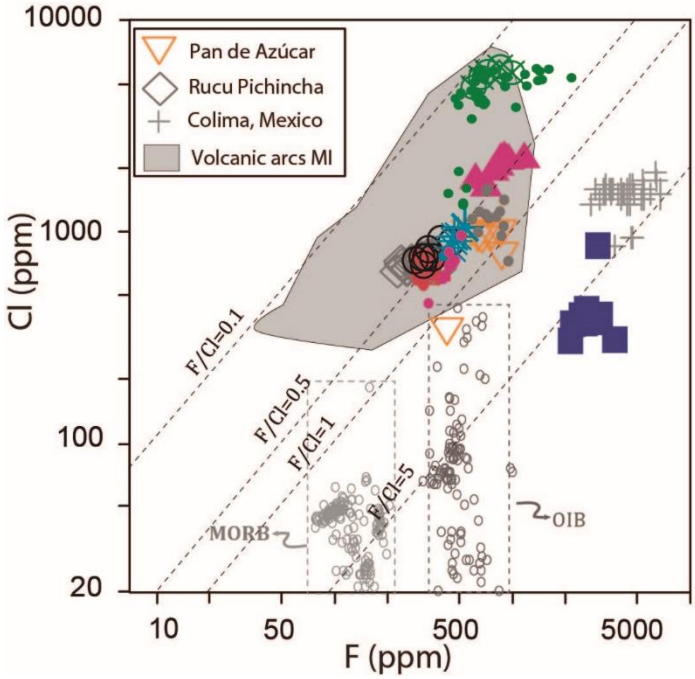

Figure 4 (a) F *vs.* Cl for Ecuadorian MI. Sangay MI shown with pink triangles and Puñalica MI compositions from Narváez et al. (2018), PDA, and Rucu Pichincha MI from Le Voyer et al. (2008) and Le Voyer (2009). The volcanic arc MI field is taken from Rose-Koga et al. (2014). Melt inclusion compositions from Colima, Mexico are from Vigouroux et al. (2008). MORB olivine-hosted MI samples from Gakkel Ridge (Shaw et al., 2010), Juan de Fuca Ridge (Wanless & Shaw, 2012) and East Pacific Rise (Wanless & Shaw, 2012). OIB olivine-hosted MI are from Hawaiian volcanoes (Hauri et al, 2002). The colors are the same as the volcano color codes in Fig. 1.

Similar to Cl and F, MI from Cotacachi, Cubilche, Licto, and Sangay span similar ranges of H_2O and S contents, from almost no H_2O to 0.41 wt.%, and from 0.052 to 0.26 wt.% of S. These MI differ in CO_2 concentrations because MI from Cotacachi have slightly higher CO_2 of up to 0.4 wt.%, compared to the other MI ($CO_2 < 0.1$ wt.%). As for F, MI from CLV show the highest concentrations of H_2O (0.2 to 0.8 wt.%), CO_2 (0.08 to 0.78 wt.%), and S (0.3 to 0.65 wt.%). Although all the precautions were taken (working on the same heating stage as Chen et al.'s 2011 study), H^+ diffusion could still have occurred during the experimental heating, during ascent of melt inclusions (Lloyd et al.,

2013; Rasmussen et al., 2017), and during cooling of volcanic products (Chen et al., 2011; Gaetani et al., 2012). In general, H_2O, CO_2, and to a lesser extent S, in MI are partitioned in the fluid phase (bubble, e.g., Bucholz et al., 2013; Lesne et al. 2011; Moore et al., 2015; Scaillet & Pichavant, 2005; Tucker et al., 2019). Therefore, the reported MI concentrations of these volatile elements are different from those present in the melt at the time of entrapment and must be considered as minimum values. On the contrary, F and Cl concentrations in MI are better preserved than H_2O, CO_2, and S, at the time of entrapment, because they are less affected by diffusion (Bucholz et al., 2013), because they have low degassing pressure (100 and 10 MPa, respectively, Lesne et al., 2011; Spilliaert et al., 2006), and because few weight percent of fluid exsolution from melt (degassing) is not effective changing F and Cl concentration in melt (e.g. SolEx model, Witham et al, 2012), making them less prone to be exsolved from the melt to the bubble.

5 Discussion

5.1 Assessment of post-entrapment modifications and entrapment pressure

Major and volatile element concentrations measured in MI rarely represent the composition of the melt at the time of entrapment because they change during cooling of host lavas and during experimental heating. The heating stage homogenization is considered to bring the MI closer to the composition of entrapment (Schiano, 2003) by reversing crystallization. However, there are other processes that modify MI composition after its entrapment. For example, Fe and Mg can be modified due to re-equilibration with the host olivine via diffusion of Fe out of and Mg into the MI (Danyushevsky et al., 2000, 2002). Also, Si depletion in MI can be caused by incorporation of silica and H^+ in the olivine structure through crystallization of metal-defect olivine (Portnyagin et al., 2019). Such MI-olivine interactions are potentially significant during magma cooling in the crust over a time period that is several orders of magnitude longer than the laboratory heating procedure. After careful examination of proposed corrections of these Fe, Mg, and Si modifications, it was not possible to reconstruct the major element composition of our MI accounting for post-entrapment modifications (PEM) without making assumptions on the initial FeO and SiO_2 concentrations. We concluded that the data presentation would be

less biased using the measured MI data as is, without any correction for PEM. Furthermore, we consider such data presentations to negligibly affect the following discussions of geochemical systematics of trace elements ratios, as incompatible trace elements have lower diffusion coefficients (i.e., REE) compared to Mg, Fe, and water (Cherniak, 2010).

Concentrations of volatile elements in MI, especially those of H_2O and CO_2, potentially record the pressure (i.e., depth) of entrapment, assuming that the magma was at the H_2O-CO_2 saturation. We used Ghiorso and Gualda (2015) H_2O-CO_2 mixed saturation model to calculate the pressure of 29 MI for which we had major and volatile data. Mean pressures range from 35 MPa for Sangay to 215 MPa for Cotacachi MI (Table S1). The pressure determined is in fact a minimum value, because (1) the entrapment can potentially occur under volatile undersaturated conditions, and (2) MI can lose water by H^+ proton diffusion (e.g. Gaetani et al., 2012, Portnyagin et al., 2019). In addition, some H_2O and most of the CO_2 is contained in the bubble instead of MI glass, even after homogenization (e.g., Moore et al., 2015, 2018; Tucker et al., 2019). This process can be reversed by calculation, and several approaches, including experimental procedures, have been described in the literature (e.g. Mironov et al., 2015; Moore et al., 2015; Shaw et al., 2008; Steele-Macinnis et al., 2011; Tucker et al., 2019). We assessed the mass of C in the bubble by using MELTS software (RhyoliteMELTS 1.2.0, Gualda et al., 2012) and measured the bubble and MI volumes. We assumed that the bubble and MI reached equilibrium during experimental heating, and that there was negligible exchange of CO_2 between the melt and the bubble during the quench because the timescales are too short (e.g. Aster et al., 2016; Wallace et al., 2015). We used MELTS software to calculate the weight percentage of H_2O and CO_2 in the fluid of each MI at their melting temperatures (1237-1327 °C), from the measured composition in the homogenized glass. Once the weight percentage of H_2O and CO_2 is calculated, MELTS estimate the density of the fluid based on the equation of state of the H_2O-CO_2 system given by Duan and Zhang (2006). Based on those parameters and the bubble size we could add the CO_2 and H_2O present in the bubble back into the melt to reconstruct the total volatile composition of MI and calculate the entrapment pressure (see Table S1 for calculation details).

The volume of each MI was approximated as an ellipsoid. The major and minor axis of the 29 MI were measured under a microscope after quench. The third axis was calculated as (a+b)/2 where "a" is the major and "b" is the minor axis length. The volume of the bubble was considered to be that of a sphere. The bubbles inside Ecuadorian MI represented 1-25% of the MI volumes (avg. 8%), and contained 45-99% of the carbon budget of MI. The entrapment pressures were calculated for these MI with the bubble component added. The obtained pressures ranged between 50-1675 MPa, and the highest average pressure was obtained for Cotacachi and Cubiche (1200 MPa), while it was around 600 MPa for the other volcanoes. The calculated pressures correspond to the middle and lower crust of the Ecuadorian arc, which is ~50 km thick (Feininger & Seguin, 1983; Vaca et al., 2019). Such pressures should be considered maximum values because we calculated the volume of bubbles from images taken after the heating experiments when the bubbles were bigger (~12%, bubble expansion calculations in supplementary material) compared to bubbles at magmatic temperature during heating.

5.2 Composition of Ecuadorian primitive magmas

5.2.1 Melt inclusions represent the most primitive magmas beneath Ecuador

Quaternary rocks from the Ecuadorian arc typically display silica contents higher than 52 wt.% (*cf.* database from Ancellin et al., 2017 and Hidalgo et al., 2012). Among these large database (~1500 rock analyses), few primitive rocks (Mg#>55) bearing high-forsterite olivines ($Fo_{>80}$) have been reported. The most common minerals are plagioclase, orthopyroxene, clinopyroxene, and amphibole, with biotite and some rare quartz present in more evolved rocks (Hall et al., 2008). Rocks from the sub-Andean zone are mainly basanites and tephrites showing Na-pyroxene and hauyne (Bourdon, et al., 2003; Garrison et al., 2018; Hoffer et al., 2008). Here, we stress that, for this study, we selected rare high-forsterite olivines (Fo_{80-90}) hosted in rocks with Mg#>55 from the frontal arc, the inter-Andean valley, and the main arc. They are therefore a small subset representing the most mafic olivine-bearing lavas found in Ecuador, and thus the MI sample in such mafic lavas allowed us to study the most primitive magmas of the Ecuadorian arc that are not otherwise accessible.

We calculated the olivine compositions in equilibrium with their host-rocks using olivine-melt equilibrium model of Ford et al. (1983), and compared them to natural olivine compositions. Thus, we confirmed that olivine phenocrysts from Cotacachi (Fo_{84-88}) and Sangay (Fo_{81-84}) are in equilibrium with their host-rock (forsterite content of equilibrium-olivine is 85.9 and 82.8, respectively). On the contrary, olivine phenocrysts from Cubilche, CLV and Licto are not. Olivines from Cubilche and CLV have higher forsterite content (84-88 and 86-90, respectively) than the expected equilibrium-olivines (83.4 for Cubilche and 86.0 for CLV) which means that such olivines crystalized from a different and more primitive magma. On the other hand, olivine phenocrysts from Licto show lower forsterite content (83-86) than expected olivine (87-89) meaning that their host lava composition is the result of olivine accumulation. We consider that olivines from Cubilche, CLV and Licto come from the same magmatic system because their MI showed similar patterns and similar trace element concentrations to their host lavas (Fig. 3). Those olivines must be considered antecrysts (*cf.* Streck, 2008). Thus, although MI come from the same magmatic system one key question remained: are the chemical compositions of MI the result of fractional crystallization or crustal assimilation?

Igneous processes such as fractional crystallization, assimilation, and magma mixing could affect trace element composition of magmas after their formation in the mantle prior to entrapment in olivine crystals. To identify the main process affecting trace elements, and to assess the presence or absence of primary character, we used a graphical approach similar to Allègre and Minster (1978) to distinguish between fractional crystallization from partial melting and mixing. For this, we plotted MI in a diagram of C_H/C_M versus C_H, where C_H and C_M are the concentrations of a highly incompatible (e.g., Rb, Th, U, Ta), and moderately incompatible (e.g., Nd, Zr) element, respectively. Compositions that plot along a straight line with a slope greater than zero (Fig. 5a, b) are consistent with a partial melting process, while those that plot along a horizontal line are consistent with fractional crystallization. Partial melting is a more effective process for fractionating C_H/C_M than fractional crystallization. In such a graph, mixing produces a hyperbole tendency, almost indistinguishable from partial melting. Ecuadorian MI plot along straight lines suggesting a partial melting process of the sub-arc mantle. It is impossible to distinguish mixing from partial melting for arc magmas, as typical arc magmas are generated by adding a slab flux to the sub-arc mantle, thus mixing and partial

melting occurs simultaneously (Grove et al., 2002). So although we show that partial melting is the most likely process, we cannot rule out that MI resulted from the mixing of magmas that have similar compositions coming from the mantle.

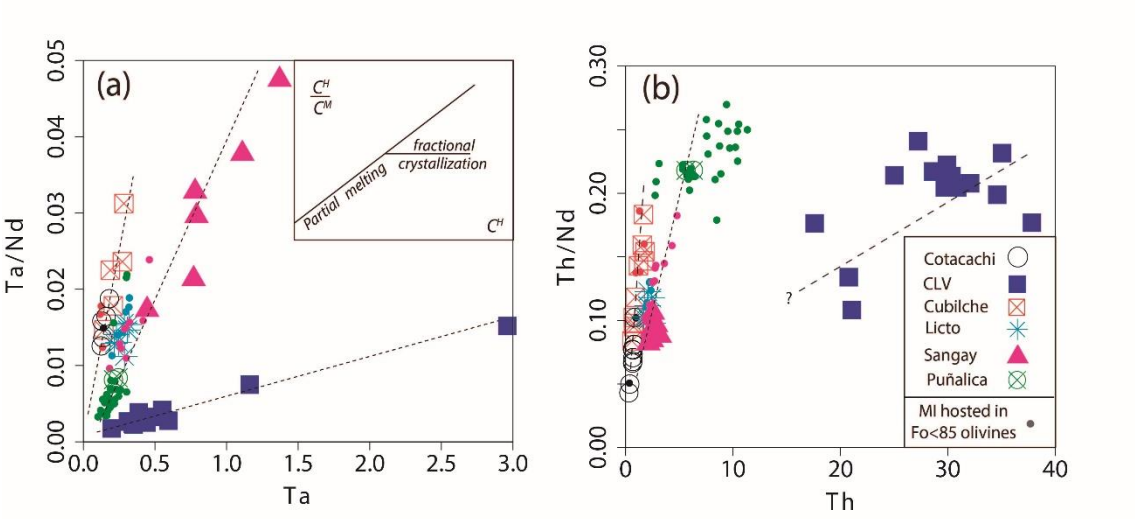

Figure 5 (a-b) C_H *vs.* C_H/C_M diagram where C_H (e.g., Th and Ta) is a highly incompatible element and C_M a moderately incompatible (e.g., Nd) element following the method of Allègre and Minster (1978) to discriminate partial melting or mixing from fractional crystallization. Sangay MI shown with pink triangles and Puñalica MI compositions from Narváez et al. (2018). Th and Ta compositions are not available for PDA and Rucu Pichincha MI.

Additionally, assimilation of crust can be viewed as both mixing of crustal component simultaneously occurring with crystallization (e.g. DePaolo, 1981). Because of trace element trends not supporting fractional crystallization, we argue that these MI compositions have been negligibly modified by crustal assimilation. As for the mixing contribution, Ancellin et al. (2017), using Sr-Nd-Pb isotope signatures of andesitic and dacitic rocks from volcanoes of our study, modeled the assimilation from the lower crust to range between 5 and 15 vol.%. Ancellin et al. (2017) data also shows that crustal contamination signatures are positively correlated with silica content, therefore we expect the assimilation in basaltic compositions to be lower than 5%.

5.2.2 Clues for CLV melt inclusion source given by alkali and volatile elements

Compositions of CLV MI are distinctively different from other Ecuadorian MI. We consider most MI to be classified as high-alumina basalts (HAB, Sisson & Grove, 1993) broadly within the calk-alkaline series because of their low K_2O, high Al_2O_3, and

intermediate composition of CaO (Fig. 2b-d). Potential modifications of Fe, Mg, Si, and H concentrations would not alter this classification, as corrections are expected to be minor based on our test calculation. However, CLV MI were clearly richer in K_2O, and lower in Al_2O_3 (Fig. 2b-d). This dichotomy of Ecuadorian MI suggests that different magma genesis mechanisms are present in the arc system.

CLV MI, which are hosted in Fo_{88-90} olivines, were not (petrologically) related to HAB. In addition to lower Al_2O_3 and high K_2O concentrations, they were distinctively high in K_2O/Na_2O values (~1.9 while other MI ~0.3; Table 4), which indicate a different source for CLV MI. In fact, K-rich lavas are not unusual in the Ecuadorian arc, and have been reported in volcanoes belonging to sub-Andean group (i.e., Sumaco volcano, Puyo cones and Mera lava flows), located to the south-east of CLV (Barragan et al., 1998; Bourdon et al., 2003; Garrison et al., 2018; Hoffer et al., 2008). On the basis of the two following arguments, we concluded that a phlogopite (phl) lherzolite is the source of CLV. (1) The high K_2O/Na_2O values of CLV MI were comparable to those measured in small-degree (less than 5%) experimental melts of a phl-lherzolite in the garnet stability field (3 GPa) reported by Condamine et al. (2016; K_2O ~6.4 wt.% and $(K_2O/Na_2O)<2$). (2) The high F (0.17-0.3 wt.%) measured in the MI indicated the presence of a mineral rich in F in the source. In fact, experimentally derived-melts of phl-bearing rocks can have F concentrations of between 0.3 to 0.5 wt.% (with phl and foiditic melts in equilibrium; Condamine et al., 2015). Fluorine concentration is controlled by the presence of phlogopite during mantle melting, similar to K_2O ($D_F^{(phl/m)}$~2, LaTourrette et al., 1995). Olivine-hosted MI from a phl-bearing mantle source show high F/Cl values of up to 5.1 (lava cones from Western Trans-Mexican Volcanic Belt, Vigouroux et al., 2008), while typical MI from continental arcs have F/Cl between values of 0.1-1 (Fig. 4). MI from CLV were the highest F/Cl (~6.99, Table 4) values reported so far in MI for the Ecuadorian arc, and even higher than those reported by Vigouroux et al. (2008).

5.3. Mantle and slab contributions, the constraints from trace elements systematics

5.3.1. Mantle end-members and continental sediment contribution

Plank et al. (2005) showed that volcanic arc primitive basalts form linear mixing arrays between mantle and sediment compositions in a diagram of Sm/La *vs.* Th/La. Due to a lack of chemical composition data from oceanic sediments, and the low Th/La values of sediments along the subduction trench of Colombia and Peru (Th/La<0.15, Plank et al. 2014), the high Th/La of some Ecuadorian lavas was interpreted as a crustal signature (Chiaradia et al., 2011). In this study, we used the newly analyzed compositions of sediments sampled along the Ecuadorian subduction trench and Manglares forearc basin related to the presence of the Esmeraldas submarine canyon nearby. These new data allowed us to reproduce Plank et al. (2005) diagram (Fig. 6a, b) and decipher mixing curves best representing the MI compositions. MI from the Ecuadorian arc plot between two mixing lines, where the Ecuadorian sediments constitute one end-member, and the other is the mantle (represented by two compositions). The Th/La values of the subducting sediments (up to 0.27) are higher than those of MI, suggesting that subducting sediments alone can be responsible for the high Th/La of MI. This rules out the need for the crust contribution to explain the variation of Th/La.

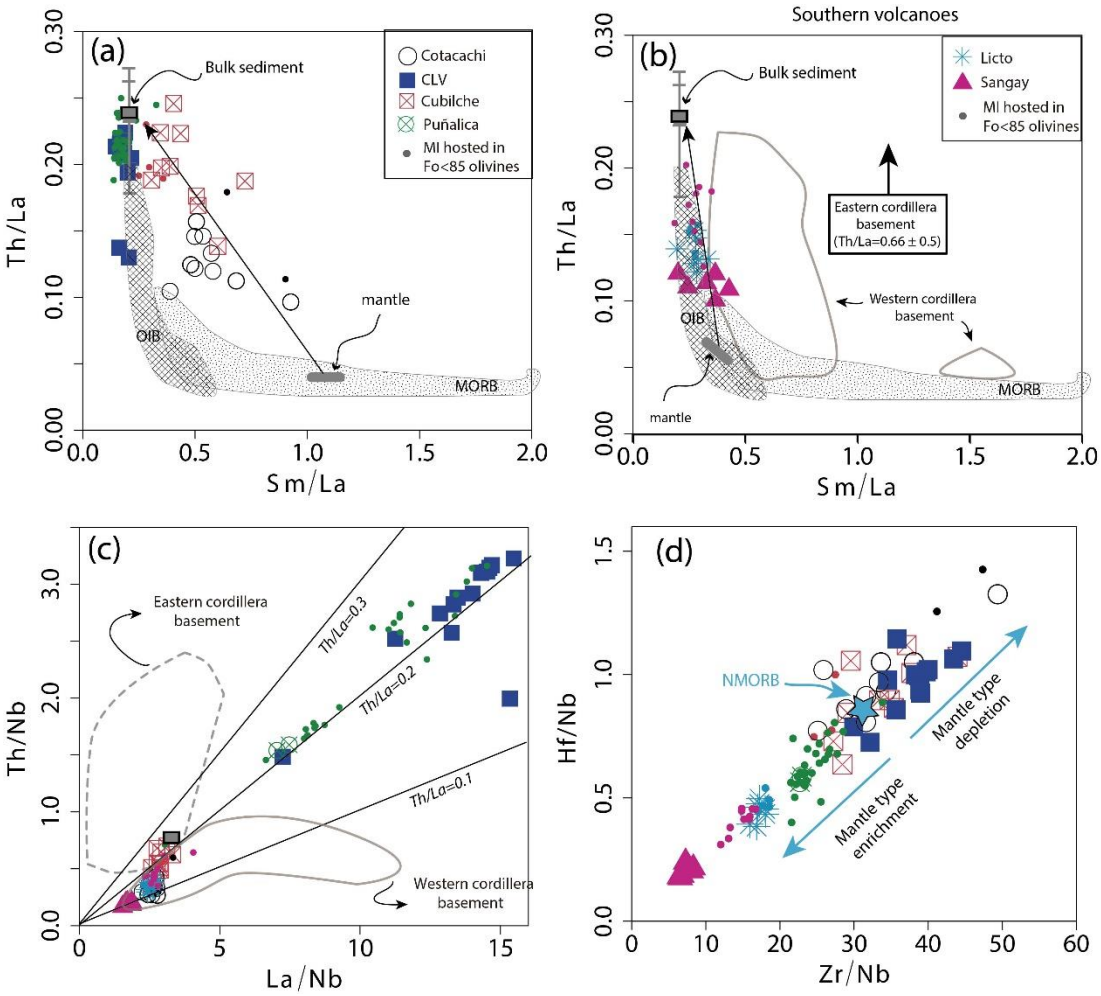

Figure 6 Sm/La vs. Th/La diagram for MI from **(a)** Puñalica and volcanoes located in the northern part of Ecuador, and **(b)** for MI from southern volcanoes. MORB and OIB fields are from Plank et al. (2005). Hf and Th concentrations are not available for PDA and Rucu Pichincha MI. The Western Cordillera basement field is from Allibon et al. (2008), Kerr et al. (2002), and Mamberti et al. (2003). Eastern cordillera basement field is from Litherland et al. (1994). **(c)** La/Nb *vs.* Th/Nb for Ecuadorian MI and Western and Eastern Cordillera basements. **(d)** Zr/Nb *vs.* Hf/Nb similarly to Sorbadère et al. (2013) to discriminate between enriched or depleted mantle liquid derived compositions. Sangay MI shown with pink triangles and Puñalica MI compositions from Narváez et al. (2018). Th compositions are not available for PDA and Rucu Pichincha MI.

The end-member mantle for the CLV, Cotacachi, Cubilche and Puñalica MI array (Fig. 6a) intersects with the MORB region at a mid-point of Sm/La variation, indicating that the source mantle is depleted (i.e., MORB-like), whereas the end-member mantle for the Sangay and Licto (Fig. 6b) array is placed at a lower Sm/La, indicating an enriched mantle with Sm/La values more similar to those of ocean island basalts (OIB). This dual-mantle composition of the Ecuadorian arc, north of Puñalica compared to the south, was also found with other trace elements. For instance, Nb/Nb* for Licto and Sangay MI varies from 0.1 to 0.62, while in other MI, it varies from 0.03 to 0.1. Furthermore, Zr/Nb

and Hf/Nb, which are low in OIB compared to MORB (Davidson, 1996; Dupuy et al., 1992), are also low in Sangay and Licto MI (Fig. 6d). Therefore, we concluded that the mantle end-member for Licto and Sangay MI was more enriched, compared to the mantle end-member of MI from northern volcanoes and Puñalica.

5.3.2. Two types of slab components

The addition of incompatible elements via slab components to the mantle wedge gives arc magmas their archetypical trace element signature. The slab-related elements that enrich the mantle are referred to as non-conservative (Pearce & Peate, 1995). On the contrary, elements with no detectable slab contribution are referred to as conservative. Nb, for instance, can be considered analogous of conservative elements in Ecuadorian MI because they show the Nb negative anomaly when normalized to N-MORB with respect to La and Th (Fig. 3a-e). In Fig. 7a, MI are shown in a diagram of Nb/Yb *vs*. Th/Yb, and all MI plot above the MORB and OIB array, indicating that Th behaves as a non-conservative element (Pearce, 2008). The main characteristic that stands out in Fig. 7a, is the two trends parallel to the MORB-OIB array, one with high Th/Nb values (between 1.5 and 3) represented by MI from Puñalica and CLV, and the other with low Th/Nb (between 0.15 to 0.72) represented by MI from Cotacachi, Cubilche, Licto, and Sangay volcanoes (no data for Rucu Pichincha and PDA). Three Puñalica MI from one evolved lava (CAR83A, *cf*. Narváez et al. 2018) plot in the low Th/Nb trend unlike most MI from this volcano. The two trends of Fig. 7a, are also observed with other elements (e.g., with Ce, Nd as a numerator in the y-axis, Fig. S4). It should be noted that Fig. 7 is advantageous for deciphering the non-conservative slab inputs of non-conservative elements in a volcanic arc with different geochemical signals of mantle enrichment (or depletion), because both MORB (depleted mantle derived melt) and OIB (enriched mantle derived melt) plot along almost the same Th/Nb trend.

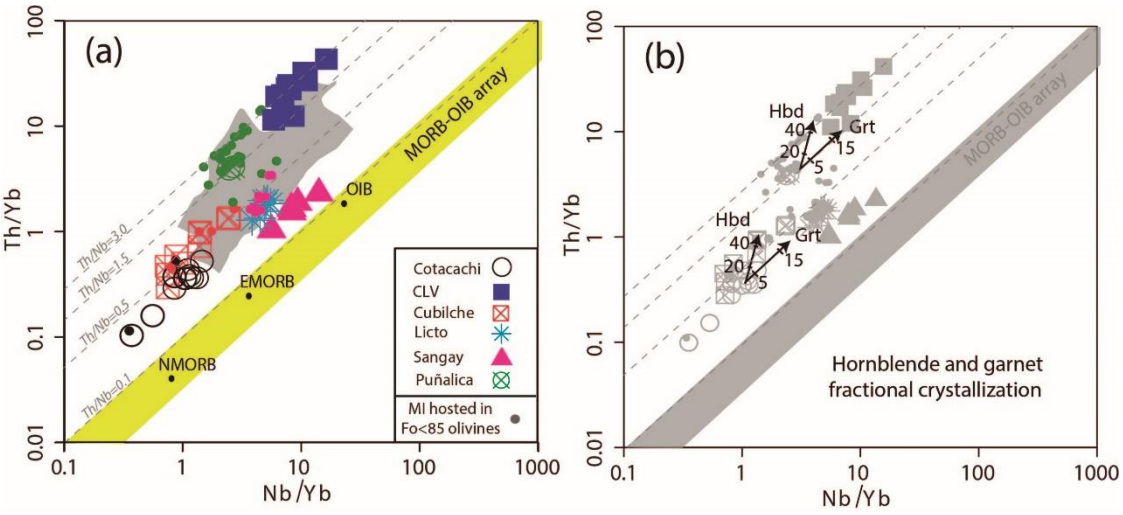

Figure 7 (a-b) Nb/Yb *vs.* Th,/Yb of Ecuadorian MI compared to MORB-OIB compositions used to discriminate between conservative and non-conservative elements (Pearce et al., 2008). Th compositions are not available for PDA and Rucu Pichincha MI. The gray shade in (a) is the entire compositional variation of Ecuadorian quaternary volcanic rocks (data from Ancellin et al., 2017). The black black arrow in (b) is the result of 45 and 20% fractional crystallization of a mono-mineral cumulate composed of hornblende and garnet, respectively, using $D^{mineral/melt}$ for individual minerals in contact with basaltic melts given by Green et al. (2000). The corresponding arrows for other typical minerals (plagioclase, pyroxenes) are smaller than the size of the symbols. Sangay MI shown with pink triangles and Puñalica MI compositions from Narváez et al. (2018). Th compositions are not available for PDA and Rucu Pichincha MI.

Fig. 7b shows that the fractional crystallization of two mineral phases able to fractionate Yb (hornblende and garnet) do not modify the Th/Nb value significantly and are unable to change the value from the low to the high Th/Nb trend. The assimilation-fractional crystallization (AFC) process was also unable to increase the Th/Nb from Cotacachi to CLV MI values. The assimilation of metamorphic rocks from the Eastern Cordillera (Th/Nb = 1.1, Litherland et al., 1994) using the DePaolo (1981) equation with a value of r=0.2, increases Th/Nb from 0.33 (mean value for Cotacachi MI) to 0.7 after 50% crystallization (bulk $D^{rock/magma}$ used for Th and Nb was 0.1 and 0.3, respectively, based on mineral partition coefficients from Green, 1994). Th/Nb values for Puñalica and CLV are even higher than 1.5; therefore, intracrustal processes (AFC or FC) cannot be the main responsible for the high Th/Nb trend (Fig. 7). With these quantitative evaluations, we concluded that these two trends were due to a change in the metasomatic agent, one with low Th/Nb, and the other with high Th/Nb, added to the mantle wedge.

To identify the slab components, we compared trace element ratios that characterize the amount of material from the slab (Sr/Nb) to ratios indicative of its nature (B/Nb, La/Nb; either it is an aqueous fluid or a hydrous siliceous melt), to identify the slab components. Thus, two different trends were observed in a plot Sr/Nb *vs.* B/Nb (Fig. 8), in accordance with Th/Nb systematics. Because B is highly soluble in aqueous fluids (Leeman & Sisson, 1996), one trend rich in B/Nb (up to 22) corresponding to MI from Cotacachi, Cubilche (and to a lesser extent, Sangay and Licto) was considered to have a stronger "fluid" signature than those poor in B/Nb from CLV, Puñalica and PDA (B/Nb: up to 4.4). Contrarily, in Fig. 8b, and given that La is an element preferentially partitioned into melts (Elliott et al., 1997), MI from CLV and Puñalica are considered to have a hydrous siliceous melt signature. PDAs MI (orange filled circles) belong to the hydrous siliceous melt trend because of their lower B/Nb and higher La/Nb than the MI of the aqueous fluid trend and because Le Voyer et al. (2008) concluded that their B isotopes signatures were correlated with this metasomatic agent. MI from Licto and Sangay clearly belong to the aqueous fluid trend in Fig. 8b, but plot at low values of B/Nb in Fig. 8a, because these MI have higher Nb than the MI of northern volcanoes (Nb/Nb*, Table 4) and Puñalica. The two trends observed in Fig. 8a, b are also seen when other fluid-immobile elements were used (i.e., Ce and Th; see Fig. S5).

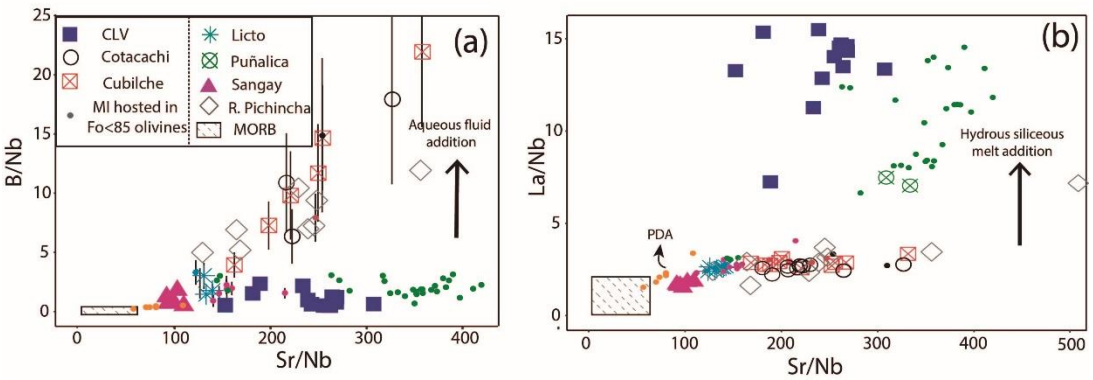

Figure 8 (a) Sr/Nb *vs.* B/Nb and **(b)** Sr/Nb *vs.*La/Nb for Ecuadorian MI. Propagated standard error bars (±1σ) of new data are shown in vertical lines in (a). The hatched boxes in (a) and (b) are MORB fields based on data from Leroux et al. (2006) and Chaussidon and Marty (1995). Sangay MI shown with pink triangles and Puñalica MI compositions from Narváez et al. (2018), PDA, and Rucu Pichincha MI from Le Voyer et al. (2008).

This contrasting behavior of trace elements is illustrated by Fig. 9 with $(La/Sm)_N$ *vs.* (Ba/Th) (Elliot, 2003), where magmas in which the source was enriched by the altered oceanic crust and/or sediment melts plotted at low Ba/Th and high $(La/Sm)_N$. On the contrary, magmas in which the source was metasomatised by aqueous fluids had high Ba/Th and low $(La/Sm)_N$. The newly reported MI compositions plotted as end-members in this diagram: those from Cotacachi in the Ba/Th-rich pole, and those from CLV in the high $(La/Sm)_N$ pole. Therefore, the Ecuadorian primitive MI demonstrate that the Ecuadorian sub-arc mantle was metasomatised by aqueous fluids or hydrous siliceous melts. This change of the nature of the slab flux implies a variation of physical conditions at the surface of the slab, as dehydration reactions occur at lower temperature conditions than melting reactions, as a general rule.

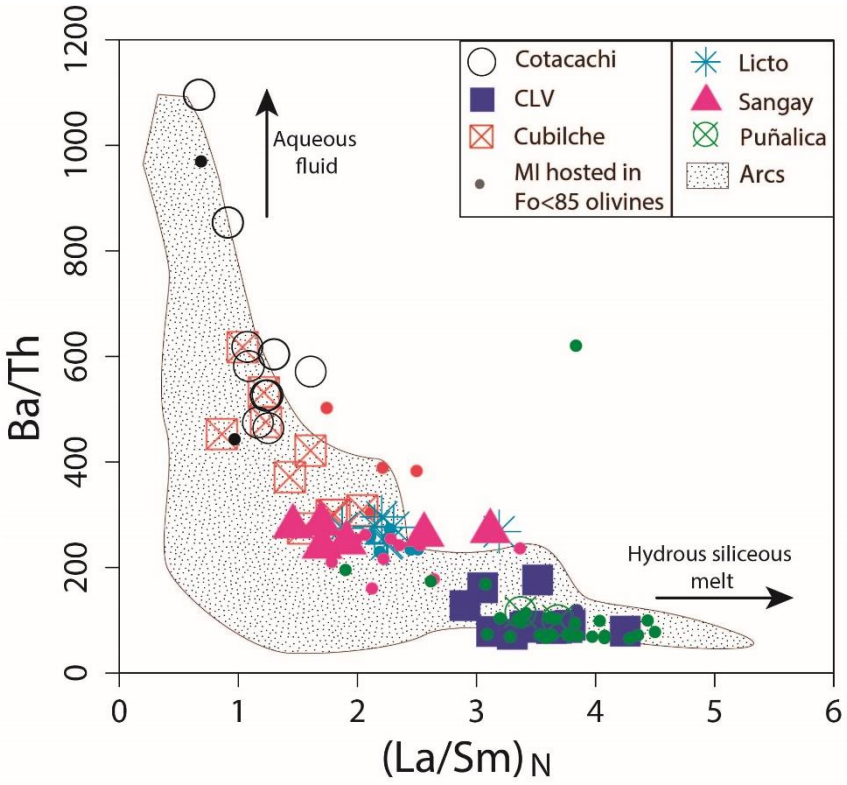

Figure 9 $(La/Sm)_N$ *vs.* Ba/Th for Ecuadorian MI. The arc basalt field is from Elliot (2003). Sangay MI shown with pink triangles and Puñalica MI compositions from Narváez et al. (2018). Th compositions are not available for PDA and Rucu Pichincha MI.

5.3.3 Geochemical modelling of primitive melt inclusions

We modelled the magma genesis of Ecuadorian arc with representative MI from each volcano in three-steps. First, we calculated the composition of the slab component using Arc Basalt Simulator 3 spreadsheet (ABS; Kimura et al., 2010). Second, we mixed the slab component with the peridotite composition, and lastly we melted the metasomatised source using the batch melting equation (Shaw, 1970). We considered the following geochemical constraints established in previous sections. First, the slab component for CLV, Puñalica, and PDA was set as a hydrous siliceous melt, while, for the others, it was an aqueous fluid (sec 5.3.2). Second, the mantle composition was determined as enriched for Puñalica and Sangay volcanoes compared to other volcanoes (sec 5.3.1).

ABS tracks the residual mineral proportion during mantle melting and the mineral proportion during dehydration or melting of altered oceanic crust and sediment, following the information determined by pMELTS and Perple_X simulations for different mantle, basaltic, and terrigenous sediment (SED) compositions. The equilibrium mineral assemblages for the altered oceanic crust and SED were calculated at 3.6 GPa (~120 km) for CLV, Puñalica, Licto, and Sangay, and 2.5 GPa (~80 km) for Cotacachi, and Cubilche, corresponding roughly to the pressure at the surface of the subducted slab under each volcano (Fig. 1). The temperature of the slab surface was taken from the P-T trajectories determined by Syracuse et al. (2010) model for the Colombia/Ecuador subduction zone (911°C at 3.6 GPa, and 780 °C at 2.5 GPa). Under such P-T conditions, ABS calculated that the subducting slab dehydrates at depths of the Cotacachi and Cubilche locations, and melts beneath CLV and Puñalica. The depth of the slab beneath Licto and Sangay volcanoes is similar to that beneath CLV (Fig. 1). Such conditions modelled the presence of a hydrous siliceous melt component with the temperature of Syracuse et al. (2010) model for the Colombia/Ecuador slab. This was in contradiction with the conclusion that the slab component under these two volcanoes was geochemically identified as an aqueous fluid (sec 5.3.3). To account for this disparity, and due to the lack of a P-T geodynamic simulation for the subduction zone in Southern Ecuador, we concluded that the slab surface temperature should be lower than Northern Ecuador, and we ran the ABS

calculation with temperature lower by 40°C for these two volcanoes, thus fullfilling the subsolidus condition of altered oceanic crust and SED.

Having defined the degree of melting or dehydration and the mineral proportion of the residue for every reservoir (i.e., altered oceanic crust, SED), ABS calculates the partition coefficient ($D_a^{mineral/(melt,fluid)}$) between fluid (or melt) and mineral, accounting for their temperature dependence (Kessel et al., 2005a). For the partition coefficients for mantle melting, ABS uses the fixed values of Green et al. (2000). For altered oceanic crust and SED, we used the mean basalt composition from the Carnegie ridge (Harpp et al., 2005), and that of the sediments on the Ecuadorian subduction system (Table 2), respectively. For Licto and Sangay, we used a primitive mantle composition (Sun & McDonough, 1989) –with an extraction of 1% of MORB– and that of a depleted mantle composition (Workman & Hart, 2005) for all the other volcanoes. These compositions, therefore, accounted for the heterogeneity of the subarc mantle (Fig. 6a, b). Finally, we used the batch melting equation (Shaw, 1970) for mantle melting, considering an arbitrary melting degree of 5% (or 10%), and an initial composition, resulting from mixing between the slab component and the mantle. For each simulation, we added an amount of slab component until we obtained a good fit between the natural and the modelled compositions (Fig. 10a for CLV and Cotacachi and Fig. S6 for other volcanoes, see Table 5 for modeling details).

Table 5 Geochemical model parameters used to reproduce Cotacachi, Sangay, Cubilche, and CLV MI compositions.

Volcano/sample	Aqueous fluid (A)-Siliceous melt (M)	Slab addition (mass %)	Degree of mantle melting (%)	Garnet (vol. %)	P (GPa) mantle melting	Slab fluid/melt fraction			% fusion	
						Fliq (SED)	Fliq (AOC)	Fliq (DMM)	SED	AOC
Cotacachi-MM1B_1B	A	1	5	0.6	2	0	1	0		
Sangay-SAN21B_4B, Licto-RIO10B 2A	A	2.5	5	4.1	2.5	0.3	0.7	0		
Cubilche-17EQ81_3C_b	A	1	5	1.4	2.2	0.1	0.9	0		
CLV-CAY45C_5A	M	15	5	2.7	1.8	0.25	0.75	0	15	10
CLV-CAY45C_5A	M and phlogopite (7%)	15	5	6.1	2.2	0.16	0.64	0.2	15	10
Puñalica	M	5	5	2.4	2.2	0.25	0.75	0	15	10

Note. The model parameters for Licto are similar to those shown for Sangay. MI from CLV is modelled with a hydrous siliceous melt, unlike all the other MI that are modelled with an aqueous fluid-like component. The parameter for CLV MI using phlogopite in the residue is also shown. The slab liquid fraction refers to either aqueous fluid or siliceous melt coming from sediments (SED), altered oceanic crust (AOC), or depleted mantle (DMM) making up the subducted slab.

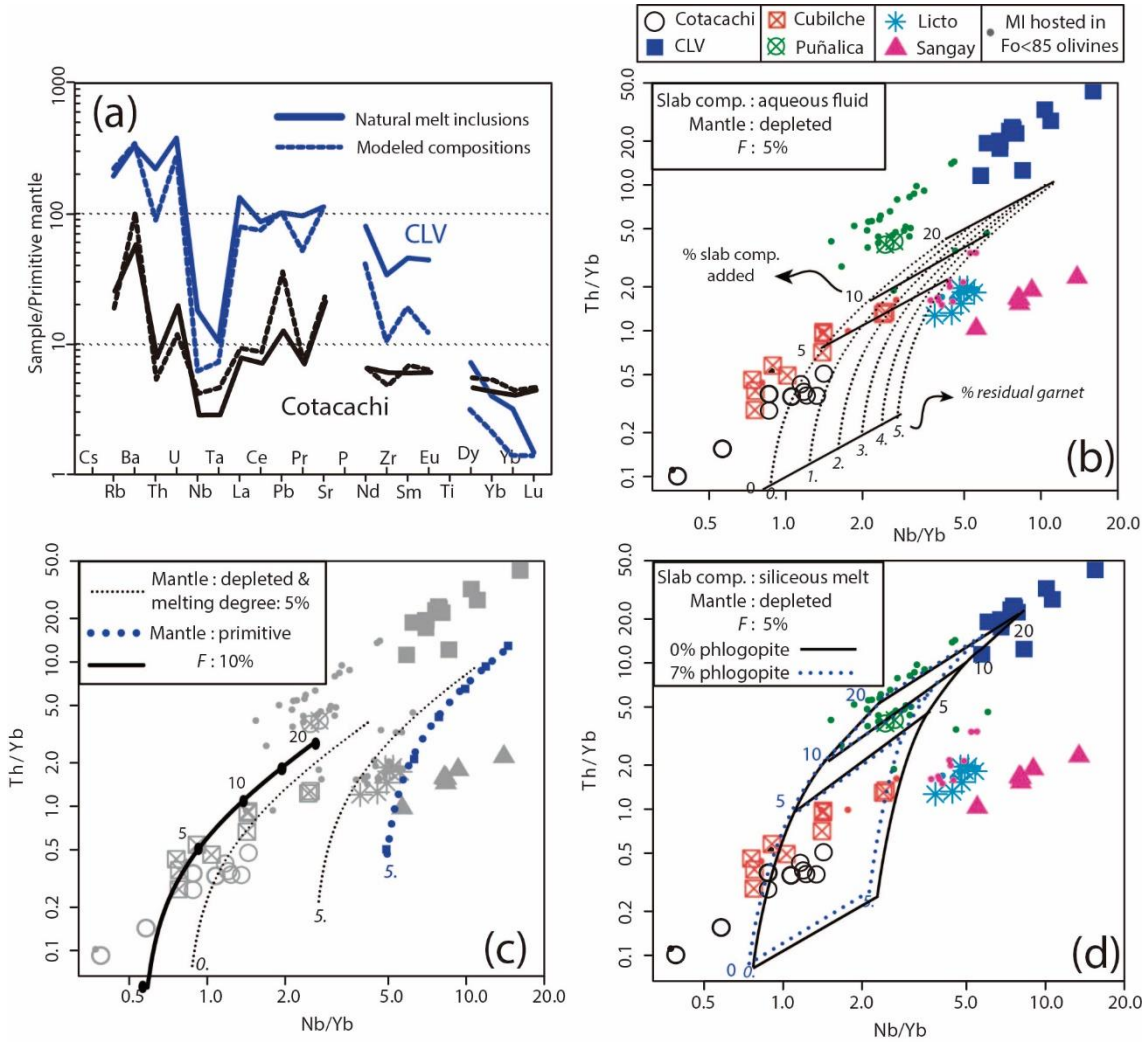

Figure 10 (a) Selected trace element composition of natural MI (colored solid lines), compared to modelled compositions (colored dashed lines). MI compositions were reproduced using a modified version of ABS to apply the batch melting formula. The degree of mantle melting is set to 5%. The slab component for CLV is a hydrous siliceous melt, while, for Cotacachi, it is an aqueous fluid. Detailed parameters are given in Table 5 and in the text. **(b-d)** Nb/Yb *vs.* Th/Yb, similar to Fig. 7a, but showing the results of geochemical modelling. **(b)** Results of an aqueous fluid-like component added to a depleted mantle (Workman & Hart, 2005). The grid formed by dotted and solid lines are results obtained at different garnet % left in the residue from mantle melting (dotted lines representing contours), and slab component percentage (solid lines, up to 20%) added to the mantle wedge. The degree of mantle melting is 5%, and the residue mineralogy is ol-opx-cpx in a proportion of 58:26:16. **(c)** Influence of mantle composition and degree of melting compared to the field shown in (b). Solid line is the results for 10% of mantle melting while keeping all parameters constant (note residual garnet is 0%), and dotted blue line shows the result for primitive mantle composition (note residual garnet is 5%). Model with primitive mantle reproduces MI composition with higher Nb/Yb. The gray symbols are those in (b). SAN20B MI (pink triangles outside the modeled grid) are reproducible when we consider them to contain amphibole-bearing clinopyroxenite derived melts (*cf.* Narváez et al., 2018). **(d)** Results obtained under the same condition as (b), but with a hydrous siliceous melt-like component added to the mantle wedge. The solid line grid represents the results calculated with a residual source without phlogopite, and the dotted line grid with 7% phlogopite. CLV MI that plot off the grid can be reproduced with a lower degree of mantle melting or higher garnet % left in the residue. Phlogopite partition coefficients are from Halliday et al. (1995), and that for thorium from LaTourrette et al. (1995).

Fig. 10b shows the composition of the aqueous fluid component calculated by ABS for Cotacachi to illustrate the effect of adding different proportions of this component into the mantle wedge in the Nb/Yb *vs.* Th/Yb space. Also, the figure shows the effect of the abundance of garnet in the mantle residue. Fig. 10c displays the model results of varying degrees of mantle melting and mantle compositions, in the Nb/Yb *vs.* Th/Yb diagram. From Fig. 10b-c, we concluded that the magma compositions of the low Th/Nb array were reproducible with combinations of the following parameters with an aqueous fluid input from the slab: vol.% of garnet left in the residue (dotted lines in Fig. 10b, causing large variation of Th/Nb), percentage of slab component added (solid lines in Fig. 10b, causing variation along a constant Th/Nb), degree of mantle melting (Fig. 10c, variation to low Th and Nb with constant Th/Nb), and mantle composition (Fig. 10c, variation to high Th and Nb with mantle enrichment, constant Th/Nb).

The change in Th/Nb due to melting of an aqueous fluid-metasomatised mantle is insufficient to reproduce the magma compositions of CLV and Puñalica (Fig. 10b, c). No combination of parameters resulted in an observed Th increase over Nb. An obvious alternative explanation was the change in the nature of the slab component to a silicate melt instead of aqueous fluid. In fact, the presence of the slab melt beneath CLV and Puñalica was expected from the PT condition (Syracuse et al., 2010), and trace element systematics (sec 5.3.2). ABS simulation therefore provides a test that examines the full spectrum of trace elements with this scenario. According to Kimura et al. (2010), ABS calculates the slab melt with a set of D_a that are different from those of aqueous fluid by a factor of 2 to 10, similar to the values reported by Moyen and Stevens (2006) for amphibolite melting. The results of this calculation are shown in Fig. 10d (solid line), where CLV and Puñalica magmas are reproduced with 5% mantle melting after the addition of 5 to 20 wt.% of a hydrous siliceous melt. Also shown in Fig. 10d are the results of the phlogopite-lherzolite melting model. For this, we took phlogopite partition coefficients from Halliday et al. (1995), and assigned 7% residual phlogopite to the mantle, which is similar to the values reported by Condamine et al. (2016) for phlogopite-lherzolite melting experiments at 3 GPa. In summary, the high Th/Nb array is only attainable by adding a hydrous siliceous melt to the mantle wedge given that a siliceous melt component is enriched in most trace elements compared to an aqueous fluid component.

5.4 Geochemical signatures of melt inclusions in the geodynamic context of Ecuadorian continental arc

The across-arc geochemical variations are conventionally explained by compositional changes of slab component due to continuous devolatilization during slab subduction, which in turn controls the extent of partial melting of the mantle (e.g., Arculus & Powell, 1986; Gill, 1981; Stolper & Newman, 1994; Tatsumi, 1986). In their pioneering work on the Ecuadorian arc, Barragan et al. (1998) interpreted that the amount of fluids added to the mantle wedge decreases from west to east, resulting in a high LILE over HFSE or LREE ratios (e.g., Ba/La, Ba/Nb, Pb/Ce) in volcanoes of the frontal arc (i.e., Atacazo volcano), and low ratios in those from the sub-Andean group in the east (i.e. Sumaco volcano). In general, MI show similar tendency to whole-rocks (Fig. 11a-c): Cotacachi and Rucu Pichincha being among the volcanoes with the highest LILE over HFSE or LREE ratios, and PDA showing the lowest values. The results of this study confirms the variations of slab component across the arc.

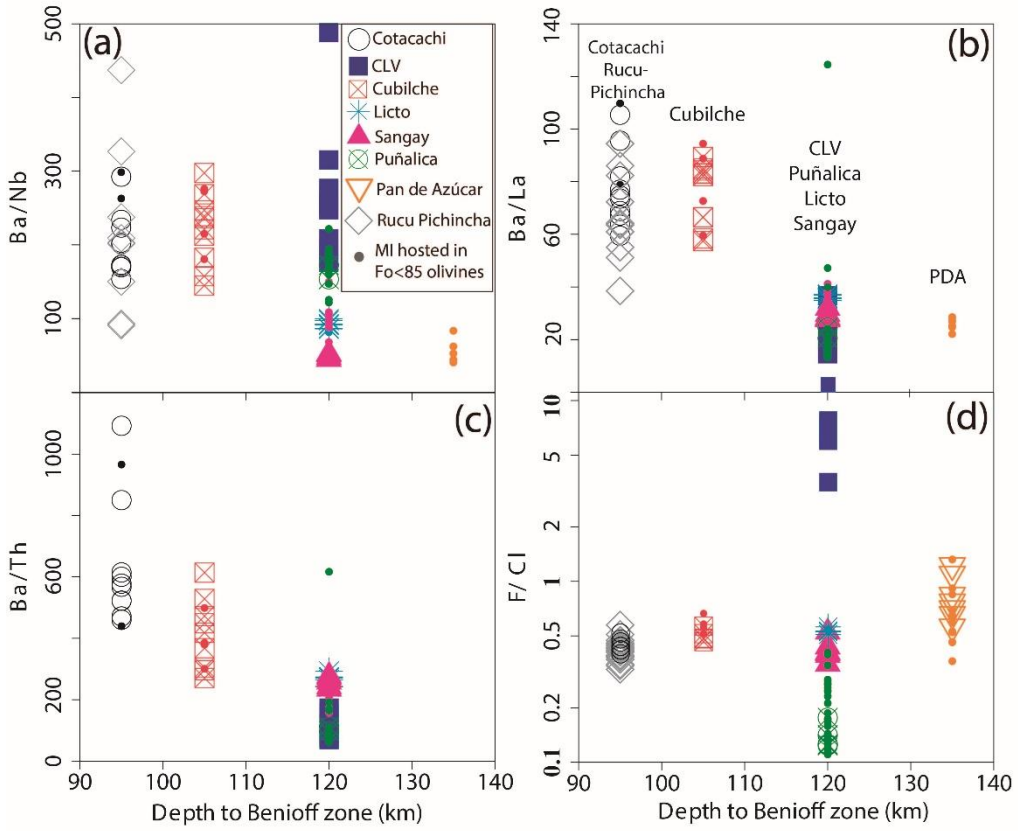

Figure 11 (a-c) Ba/Nb, Ba/La, Ba/Th plotted against the depth to the Benioff zone under each volcano. The numerator (Ba) is an element that is abundant in the slab component, and the denominators are substantially less mobile elements. **(d)** Log (F/Cl) *vs.* depth to the Benioff zone. Sangay MI shown with pink triangles and Puñalica MI compositions from Narváez et al. (2018), PDA, and Rucu Pichincha MI from Le Voyer et al. (2008) and Le Voyer (2009).

More recently, Ancellin et al. (2017), and Chiaradia et al. (2020) recognized a north-south (along-arc) geochemical zonation among the lavas from the frontal arc. Both studies show that Ba/Th was maximum around the equator, and decreases towards the north and south. Ancellin et al. (2017) proposed that such geochemical zonation is due to a change in the slab component composition, while Chiaradia et al. (2020), who also reported a north-south variation of other elements (i.e., Nd, Sm, Nb), argue that it is due to magma-crust interactions at a distinctive depth. Our data are unable to confirm the origin of this geochemical zonation reported in volcanoes from the frontal arc, as Cotacachi and Rucu Pichincha volcanoes are the only frontal arc volcanoes in this study, and Th concentration data is not available for Rucu Pichincha MI. However, we found an along-arc variability of trace elements in MI from volcanoes that are located at approximately 120 km above the subducting slab (i.e., CLV, Puñalica, Licto, and Sangay). CLV and Puñalica MI are relatively enriched in fluid-immobile elements (high

La/Nb, Th/Nb), while Licto and Sangay MI show a preference for fluid-mobile elements (high Ba/La, Pb/Ce, and B/Nb). We concluded that such variation was due to a change in the slab component composition. Such systematics are therefore consistent with the interpretation of Ancellin et al. (2017). We stress again that these previous studies reported whole-rock geochemical data, and it would have been difficult to separate geochemical signals from crustal or slab components.

To account for the change in the slab component along the Ecuadorian arc, we propose that the thermal regime along the subduction zone is hotter to the north of GFZ compared to the south. Thus, a higher temperature at a given pressure would allow the slab to melt and produce the hydrous siliceous melt component under CLV, Puñalica, and PDA volcanoes. We consider that the age difference of the oceanic crust in the north and south of the GFZ is the main cause that controls the thermal regime. North of the GFZ, the oceanic crust is younger (12-20 Ma, Lonsdale, 2005; Sallarès & Charvis, 2003) than to the south (25-30 Ma). In this model, the location of the GFZ under the Ecuadorian arc is a crucial dividing line of the arc thermal regime, and thus slab geochemical component. It should be noted that the prolongation of GFZ into the volcanic arc was identified under Puñalica volcano based on an anomalous chlorine enrichment of Puñalica MI (Fig. 4; Narváez et al., 2018). Greater interaction between the oceanic water and the oceanic crust along the fracture zone was attributed as the cause of Cl enrichment and imparts its signature to Puñalica MI. In conclusion, we interpret that the subducting slab to the north of Puñalica introduces greater thermal energy into the sub-arc zone than the south, and this produces the along-arc geochemical variations.

The high Cl content and low F/Cl (0.14 ± 0.02) of Puñalica MI are indicative of the GFZ location under Puñalica volcano. On the contrary, other Ecuadorian MI with aqueous fluid signatures have a F/Cl value of around ~0.49±0.1 that is independent of the depth to the Benioff zone (i.e., Cotacachi, Cubilche, Licto, Sangay, and Rucu Pichincha, Fig. 11d), making it a contrasting geochemical signature from Ba/Nb and Ba/La, which negatively correlated with the Benioff zone depth, probably related to the amount of fluid. We speculate that the almost constant F/Cl value represents the composition of the aqueous fluids released during metamorphic dehydration reactions occurring in the subducting slab, and provides a reference value to identify the involvement of fluid in its

source. A constant F/Cl value is possible if the fluid composition is buffered by the mineral assemblage during dehydration reactions. Finally, we consider that the F/Cl of CLV (6.99±2.08), PDA (0.83±0.24), and Sangay-SAN20B (0.42±0.05) do not represent that of the fluids or melts coming from the subducting slab, as the mantle source of these MI was in equilibrium either with phlogopite (CLV) or hornblende (PDA, Le Voyer et al., 2018; SAN20B, Narváez et al., 2018) capable of fractionating F/Cl.

In a previous section, we argued that the low Zr/Nb and Hf/Nb in Sangay and Licto MI (Fig. 6d) were indicative of a mantle enrichment under those volcanoes. The southern location of Sangay and Licto volcanoes led us to think that there was an along-arc variation of composition of the sub-arc mantle. However, the presence of geochemical heterogeneity of the Ecuadorian sub-arc mantle is less clear when whole-rock data are examined. For example, primitive whole rocks (Mg#>55, using Ancellin et al. 2017 database), from volcanoes located in the north and some from the sub-Andean zone, also show low Zr/Nb values (Hf is not available for whole-rocks). Therefore, we conclude that low Zr/Nb (and most probably low Hf/Nb) is not only a feature of southern volcanoes, and that local heterogeneities of the sub-arc mantle may occur all along the Ecuadorian arc. We note that Chiaradia et al. (2020) proposed that the variability of Nb in volcanoes from the frontal arc was related to variable rutile fractionation in the crust. This explanation can be applied to silicic hydrous magma in which rutile can be saturated at several hundred ppm of TiO_2 (Gaetani et al., 2008). However, it would not apply to the primitive basalt study presented here. Rutile saturation in basalt requires several wt.% of TiO_2 (Ryerson & Watson, 1987). Based on these studies, the Nb variations in our primitive MI cannot be derived from rutile crystallization or from dissolution in the crust, but rather represent the variable composition of the parental magmas.

6 Conclusions

In order to decipher the slab components that metasomatise the sub-arc mantle, we studied 83 olivine-hosted MI that represent the most primitive melts from the Ecuadorian arc. Together with the dataset published by Le Voyer et al. (2008), and Narváez et al. (2018) from other Ecuadorian volcanoes, we identified two types of slab components. On the basis of a systematic trace element analysis, we identified a slab component that is rich in fluid-mobile elements (Ba/La: 30-110 and Pb/Ce: 0.1-0.5, B/Nb:

up to 22), and poor in fluid-immobile elements (La/Nb: 2.2-4, Th/Nb: up to 0.7), indicating an aqueous fluid. The second slab component that is relatively enriched in fluid-immobile elements (La/Nb:7.2-15.5, Th/Nb: up to 3.2), and has low contents of fluid-mobile elements (Ba/La: 15-36, Pb/Ce: 0.02-0.1, B/Nb: up to 4.4) is indicative of a hydrous siliceous melt. We distinguished the aqueous fluid signature in most MI, except for those coming from CLV, Puñalica, and PDA volcanoes. In addition to these systematics, all MI with an aqueous fluid-like signature show a similar F/Cl value of around 0.49 ± 0.1 potentially indicating the aqueous fluid component in the Ecuadorian arc.

The geographical limit separating the production of aqueous fluids and hydrous siliceous melt at the surface of the slab depends on the location of the GFZ, which is below Puñalica volcano. This oceanic structure separates a young and probably hotter oceanic crust to the north from an older and likely colder oceanic crust to the south. Thus, the hotter thermal regime to the north of the GFZ would allow the subducting slab to melt.

We also showed that Ecuadorian MI compositions are indicative of the mantle composition and phlogopite stability in the sub-arc mantle. For instance, we correlated the high Nb/Nb* and low Zr/Nb, Hf/Nb, Sm/La of Conos de Licto and Sangay MI with the melting of an enriched mantle. Such enrichment is not correlated with the slab component addition, and shows that the sub-arc mantle is heterogeneous under the Ecuadorian arc. Finally, we consider that the high K_2O/Na_2O (~1.9) and F/Cl (6.99±2.08) are indicative of the phlogopite stability in the mantle source of CLV MI.

This MI study of Ecuadorian volcanoes achieved the identifications of primitive magmas in each of the studied volcanoes. With minimum influence from crustal modifications, these data illustrated the thermal variations below the arc, and identified the location of the geographical divide between hot and cold regimes. In addition, we reported potential indications of mantle heterogeneity below the arc. Presence of slab melting was geochemically identified, as well as the involvement of phlogopite as a residual phase during mantle melting.

Chapter VI

General conclusions and perspectives

6.1 General conclusions

The geodynamic setting of the subduction zone in Ecuador is unique. The subduction of the young oceanic crust containing the Carnegie ridge results in a high thermal regime along the subduction zone in the Northern Ecuador that is among the hottest in the world (*cf.* Syracuse et al., 2010). The thermal regime at the southern termination of the Ecuadorian arc is probably colder (at least compared with the northern segment of the same arc), because south of GFZ an older oceanic crust subducts. It is known that the capacity for transporting trace elements by the subducted slab component increase with the temperature at which this process occur (i.e. Kessel et al., 2005a; Klimm et al., 2008; Hermann and Rubatto, 2009). Therefore, hydrous siliceous melts, which resulted from the melting of the oceanic crust and/or the subducted sediments, can mobilize more easily some trace elements (i.e. Th, La, etc.) than aqueous fluids which are transported at lower temperature. In Ecuador, the influence of the slab component in the chemistry of magmas is difficult to disentangle because the primary signature of magmas is obscured by crustal processes associated with the thick Ecuadorian arc crust.

I studied melt inclusions hosted in high-forsterite (80-89) olivines to constrain the participation of the slab component into the composition of Ecuadorian magmas. Ecuadorian melt inclusions were silica-poor and cannot be related through a liquid-line of descent to their hosted whole-rocks. Instead, they represent a small subset of melts resulting from (1) the mixing between melts derived from amphibole-bearing clinopyroxenites and peridotites or (2) melts coming from phlogopite-peridotites.

A detailed analysis of melt inclusions trace compositions indicated that these compositions cannot be reproduced by intracrustal processes (assimilation and fractional crystallization). The composition of melt inclusions are reproduced by the addition of at least two distinctive slab components, which change from north to south depending on its

thermal regime. A higher thermal regime along the subduction zone north of GFZ allows the slab component to be enriched in fluid-immobile elements (e.g., high La/Nb, Th/Nb) while south of GFZ is enriched in fluid-mobile elements (e.g., high Ba/La, Pb/Ce, B/Nb) probably because the thermal regime is colder. The main outcome to retain from this work is that the composition of the slab component under Ecuador is not homogeneous (and thus, that the primitive mantle-derived magmas should be heterogeneous) and this has to be taken into consideration for future studies of magma genesis in this arc.

6.2 Perspectives

1. The study of melt inclusions has given access to melts that are considered the most primitive magmas in the arc. However, they may have suffer some small extend of crustal contamination that can be resolved by analysis of radiogenic isotopes (i.e. $^{87}Sr/^{86}Sr$ and $^{143}Nd/^{144}Nd$) of individual melt inclusions (*cf.* Koornneef et al., 2015; Reinhard et al., 2018). This type of analysis is limited by the size and the concentration of Sr of the melt inclusions (Koornneef et al., 2015). Thus, considering the size and Sr content of melt inclusions reported in this study, only melt inclusions bigger than 100µm are good candidates for radiogenic isotope analysis, specifically melt inclusions from Sangay and Puñalica volcanoes (i.e. SAN21B and RIO17 samples). Once this is done, I expect it would confirm that melt inclusions represent melts the least affected by crustal contamination from the Ecuadorian volcanic arc.

2. In this work we concluded that whole rocks and melt inclusions are not related through a liquid-line-of-descent but they represent different batches of magma mixed during their ascent to the surface. The relationship between melt inclusions and whole rocks can be better constrained from the study of melt inclusions hosted in clinopyroxene and more evolved olivines (Fo<80) from one single volcano (i.e. Puñalica). The study of such melt inclusions may show intermediate compositions between the whole rocks and the primitive melt inclusions that allow us to complete the mixing array sequence and maybe define the primitive pole for whole rocks.

3. One important conclusion of this work is that the trace element signature of melt inclusions is not acquired in the crust and that most of their trace element geochemical variability is due to the slab components. If these results are extrapolated to whole rocks, previous geochemical models that considered the slab component to be an aqueous fluid might need to be revised. This can be done by changing the composition of the starting magma in previous geochemical models for one enriched in trace elements (specifically fluid-immobile elements). This would result in lower and probably more appropriate values of crustal contaminations of Ecuadorian lavas.

4. If someone is interested in finding more evidence for the hydrous siliceous melt addition from the slab to the mantle wedge, the analysis of Ni in primitive olivines could be appropriate. Primitive magmas coming from a mantle peridotite metasomatised by hydrous siliceous melts usually contain Ni-rich olivines (Sobolev et al., 2005; Straub et al., 2011). The enrichment of Ni in olivines occurs because the addition of melts to the mantle wedge transforms olivine into orthopyroxene. The subsequent melting of these pyroxenites produce a liquid enriched in Ni because of olivine absence. Finally, the crystallization of olivine from this melt is, therefore, enriched in Ni.

References

A

Allègre, C. J., & Minster, J. F. (1978). Quantitative models of trace element behavior in magmatic processes. Earth and Planetary Science Letters, 38(1), 1–25. https://doi.org/10.1016/0012-821X(78)90123-1

Allibon, J., Monjoie, P., Lapierre, H., Jaillard, E., Bussy, F., Bosch, D., & Senebier, F. (2008). The contribution of the young Cretaceous Caribbean Oceanic Plateau to the genesis of late Cretaceous arc magmatism in the Cordillera Occidental of Ecuador. Journal of South American Earth Sciences, 26(4), 355–368. https://doi.org/10.1016/j.jsames.2008.06.003

Almeida, M. (2016). Estudio petrográfico y geoquímico del volcán Cotacachi – provincia de Imbabura (Ingeniero Geólogo). Escuela Politécnica Nacional, Ecuador.

Alonso-Perez, R., Ulmer, P., Muntener, O., & Thompson, A. B. (2004). Experimental phase equilibria and trace element partitioning in differentiated hydrous calc-alkaline melts at high pressures. AGU Fall Meeting Abstracts, 13, V13B-1473.

Ancellin, M.-A., Samaniego, P., Vlastélic, I., Nauret, F., Gannoun, A., & Hidalgo, S. (2017). Across-arc versus along-arc Sr-Nd-Pb isotope variations in the Ecuadorian volcanic arc. Geochemistry, Geophysics, Geosystems. https://doi.org/10.1002/2016GC006679

Andersen, C. A., & Hinthorne, J. R. (1972). Ion microprobe mass analyzer. Science, 175(4024), 853–860. https://doi.org/10.1126/science.175.4024.853

Anderson, A. T., & Wright, T. L. (1972). Phenocrysts and glass inclusions and their bearing on oxidation and mixing of basaltic magmas, Kilauea volcano, Hawaii. American Mineralogist, 57(1–2), 188–216.

Annen, C. (2006). The genesis of intermediate and silicic magmas in deep crustal hot zones. Journal of Petrology, 47(3), 505–539. https://doi.org/10.1093/petrology/egi084

Arculus, R. J., & Powell, R. (1986). Source component mixing in the regions of arc magma generation. Journal of Geophysical Research: Solid Earth, 91(B6), 5913–5926. https://doi.org/10.1029/JB091iB06p05913

Aspden, J. A., & Litherland, M. (1992). The geology and Mesozoic collisional history of the Cordillera Real, Ecuador. Tectonophysics, 205(1), 187–204. https://doi.org/10.1016/0040-1951(92)90426-7

Aster, E. M., Wallace, P. J., Moore, L. R., Watkins, J., Gazel, E., & Bodnar, R. J. (2016). Reconstructing CO2 concentrations in basaltic melt inclusions using Raman analysis of vapor bubbles. Journal of Volcanology and Geothermal Research. https://doi.org/10.1016/j.jvolgeores.2016.04.028

Atherton, M. P., & Petford, N. (1993). Generation of sodium-rich magmas from newly underplated basaltic crust. Nature, 362, 144–146. https://doi.org/10.1038/362144a0

B

Bablon, M., Quidelleur, X., Samaniego, P., Le Pennec, J.-L., Audin, L., Jomard, H., et al. (2019). Interactions between volcanism and geodynamics in the southern termination of the Ecuadorian arc. Tectonophysics, 751, 54–72. https://doi.org/10.1016/j.tecto.2018.12.010

Bablon, M., Quidelleur, X., Samaniego, P., Le Pennec, J.-L., Santamaría, S., Liorzou, C., et al. (2020). Volcanic history reconstruction in northern Ecuador: insights for eruptive and erosion rates on the whole Ecuadorian arc. Bulletin of Volcanology, 82(1), 11. https://doi.org/10.1007/s00445-019-1346-1

Baker, M. B., & Stolper, E. M. (1994). Determining the composition of high-pressure mantle melts using diamond aggregates. Geochimica et Cosmochimica Acta, 58(13), 2811–2827. https://doi.org/10.1016/0016-7037(94)90116-3

Barragan, R., Geist, D., Hall, M., Larson, P., & Kurz, M. (1998). Subduction controls on the compositions of lavas from the Ecuadorian Andes. Earth and Planetary Science Letters, 154(1–4), 153–166. https://doi.org/10.1016/S0012-821X(97)00141-6

Béguelin, P., Chiaradia, M., Beate, B., & Spikings, R. (2015). The Yanaurcu volcano (Western Cordillera, Ecuador): A field, petrographic, geochemical, isotopic and geochronological study. Lithos, 218–219, 37–53. https://doi.org/10.1016/j.lithos.2015.01.014

Bell, D. R., Rossman, G. R., Maldener, J., Endisch, D., & Rauch, F. (2003). Hydroxide in olivine: A quantitative determination of the absolute amount and calibration of the IR spectrum. Journal of Geophysical Research: Solid Earth, 108(B2). https://doi.org/10.1029/2001JB000679

Bellver-Baca, M. T., Chiaradia, M., Beate, B., Beguelin, P., Deriaz, B., Mendez-Chazarra, N., & Villagómez, D. (2019). Geochemical evolution of the Quaternary Chachimbiro Volcanic Complex (frontal volcanic arc of Ecuador). Lithos, 105237. https://doi.org/10.1016/j.lithos.2019.105237

van den Bleeken, G., & Koga, K. T. (2015). Experimentally determined distribution of fluorine and chlorine upon hydrous slab melting, and implications for F–Cl cycling through subduction zones. Geochimica et Cosmochimica Acta, 171, 353–373.

Bourdon, E., Eissen, J.-P., Cotten, J., Monzier, M., Robin, C., & Hall, M. L. (1999). Les laves calco-alcalines et à caractère adakitique du volcan Antisana (Equateur): hypothèse pétrogénétique. Comptes Rendus de l'Académie des Sciences - Series IIA - Earth and Planetary Science, 328(7), 443–449. https://doi.org/10.1016/S1251-8050(99)80144-X

Bourdon, E., Eissen, J.-P., Monzier, M., Robin, C., Martin, H., Cotten, J., & Hall, M. L. (2002). Adakite-like lavas from Antisana Volcano (Ecuador): evidence for slab melt metasomatism beneath Andean Northern Volcanic Zone. Journal of Petrology, 43(2), 199–217.

Bourdon, E., Eissen, J.-P., Gutscher, M.-A., Monzier, M., Hall, M. L., & Cotten, J. (2003). Magmatic response to early aseismic ridge subduction: The Ecuadorian margin case

(South America). Earth and Planetary Science Letters, 205(3–4), 123–138. https://doi.org/10.1016/S0012-821X(02)01024-5

Bouvier, A.-S., Deloule, E., & Métrich, N. (2010). Fluid Inputs to Magma Sources of St. Vincent and Grenada (Lesser Antilles): New Insights from Trace Elements in Olivine-hosted Melt Inclusions. Journal of Petrology, 51(8), 1597–1615. https://doi.org/10.1093/petrology/egq031

Brandt, F. E., Holm, P. M., & Søager, N. (2017a). South-to-north pyroxenite–peridotite source variation correlated with an OIB-type to arc-type enrichment of magmas from the Payenia backarc of the Andean Southern Volcanic Zone (SVZ). Contributions to Mineralogy and Petrology, 172(1). https://doi.org/10.1007/s00410-016-1318-9

Brandt, F. E., Holm, P. M., & Hansteen, T. H. (2017b). Volatile (Cl, F and S) and major element constraints on subduction-related mantle metasomatism along the alkaline basaltic backarc, Payenia, Argentina. Contributions to Mineralogy and Petrology, 172(48). https://doi.org/10.1007/s00410-017-1359-8

Bryant, J. A., Yogodzinski, G. M., Hall, M. L., Lewicki, J. L., & Bailey, D. G. (2006). Geochemical constraints on the origin of volcanic rocks from the Andean northern volcanic zone, Ecuador. Journal of Petrology, 47(6), 1147–1175. https://doi.org/10.1093/petrology/egl006

Bucholz, C. E., Gaetani, G. A., Behn, M. D., & Shimizu, N. (2013). Post-entrapment modification of volatiles and oxygen fugacity in olivine-hosted melt inclusions. Earth and Planetary Science Letters, 374, 145–155. https://doi.org/10.1016/j.epsl.2013.05.033

Burgess, K. D., & Cooper, R. F. (2013). Extended planar defects and the rapid incorporation of Ti+4 into olivine. Contributions to Mineralogy and Petrology, 166(4), 1223–1233. https://doi.org/10.1007/s00410-013-0918-x

C

de Capitani, C., & Brown, T. H. (1987). The computation of chemical equilibrium in complex systems containing non-ideal solutions. Geochimica et Cosmochimica Acta, 51(10), 2639–2652. https://doi.org/10.1016/0016-7037(87)90145-1

Carter, L. B., Skora, S., Blundy, J. D., De Hoog, J. C. M., & Elliott, T. (2015). An experimental study of trace element fluxes from subducted oceanic crust. Journal of Petrology, 56(8), 1585–1606. https://doi.org/10.1093/petrology/egv046

Chakraborty, S. (1997). Rates and mechanisms of Fe-Mg interdiffusion in olivine at 980°–1300°C. Journal of Geophysical Research: Solid Earth, 102(B6), 12317–12331. https://doi.org/10.1029/97JB00208

Chaussidon, M., & Marty, B. (1995). Primitive boron isotope composition of the mantle. Science, 269(5222), 383–386. https://doi.org/10.1126/science.269.5222.383

Chen, Y., Provost, A., Schiano, P., & Cluzel, N. (2011). The rate of water loss from olivine-hosted melt inclusions. Contributions to Mineralogy and Petrology, 162(3), 625–636. https://doi.org/10.1007/s00410-011-0616-5

Cherniak, D. J. (2010). REE diffusion in olivine. American Mineralogist, 95(2–3), 362–368. https://doi.org/10.2138/am.2010.3345

Chiaradia, M., Müntener, O., Beate, B., & Fontignie, D. (2009). Adakite-like volcanism of Ecuador: Lower crust magmatic evolution and recycling. Contributions to Mineralogy and Petrology, 158(5), 563–588. https://doi.org/10.1007/s00410-009-0397-2

Chiaradia, M., Müntener, O., & Beate, B. (2011). Enriched basaltic andesites from mid-crustal fractional crystallization, recharge, and assimilation (Pilavo volcano, western cordillera of Ecuador). Journal of Petrology, 52(6), 1107–1141. https://doi.org/10.1093/petrology/egr020

Chiaradia, M., Barnes, J. D., & Cadet-Voisin, S. (2014). Chlorine stable isotope variations across the Quaternary volcanic arc of Ecuador. Earth and Planetary Science Letters, 396, 22–33. https://doi.org/10.1016/j.epsl.2014.03.062

Chiaradia, M., Müntener, O., & Beate, B. (2020). Effects of aseismic ridge subduction on the geochemistry of frontal arc magmas. Earth and Planetary Science Letters, 531, 115984. https://doi.org/10.1016/j.epsl.2019.115984

Clapperton, C. M. (1990). Glacial and volcanic geomorphology of the Chimborazo-Carihuairazo massif, Ecuadorian Andes. Transactions of the Royal Society of Edinburgh: Earth Sciences, 81(02), 91–116.

Class, C., Miller, D. M., Goldstein, S. L., & Langmuir, C. H. (2000). Distinguishing melt and fluid subduction components in Umnak Volcanics, Aleutian Arc. Geochemistry, Geophysics, Geosystems, 1(6). https://doi.org/10.1029/1999GC000010

Clocchiatti, R., Gioncada, A., Mosbah, M., & Sbrana, A. (1994). Possible deep origin of sulfur output at Vulcano (Southern Italy) in the light of melt inclusion studies. Acta Vulcanologica, 5, 49–53.

Collot, J. -Y., Migeon, S., Spence, G., Legonidec, Y., Marcaillou, B., Schneider, J.-L., et al. (2005). Seafloor margin map helps in understanding subduction earthquakes. Eos, Transactions American Geophysical Union, 86(46), 463–465. https://doi.org/10.1029/2005EO460003

Collot, J.-Y., Ratzov, G., Silva, P., Proust, J. -N., Migeon, S., Hernandez, M. -J., et al. (2019). The Esmeraldas canyon: A helpful marker of the Pliocene-Pleistocene tectonic deformation of the north Ecuador-southwest Colombia convergent margin. Tectonics, 2019TC005501. https://doi.org/10.1029/2019TC005501

Condamine, P. (2015). Rôle du phlogopite sur la genèse de magmas riches en potassium : Approche expérimentale (Doctoral Thesis). Université Blaise Pascal - Clermont-Ferrand II, France.

Condamine, P., & Médard, E. (2014). Experimental melting of phlogopite-bearing mantle at 1 GPa: Implications for potassic magmatism. Earth and Planetary Science Letters, 397, 80–92. https://doi.org/10.1016/j.epsl.2014.04.027

Condamine, P., Médard, E., & Devidal, J.-L. (2016). Experimental melting of phlogopite-peridotite in the garnet stability field. Contributions to Mineralogy and Petrology, 171(11), 95. https://doi.org/10.1007/s00410-016-1306-0

Cotten, J., Le Dez, A., Bau, M., Caroff, M., Maury, R. C., Dulski, P., et al. (1995). Origin of anomalous rare-earth element and yttrium enrichments in subaerially exposed basalts: Evidence from French Polynesia. Chemical Geology, 119(1), 115–138. https://doi.org/10.1016/0009-2541(94)00102-E

Cottrell, E., Spiegelman, M., & Langmuir, C. H. (2002). Consequences of diffusive reequilibration for the interpretation of melt inclusions. Geochemistry, Geophysics, Geosystems, 3(4), 1–26. https://doi.org/10.1029/2001GC000205

Cottrell, E., Kelley, K. A., Lanzirotti, A., & Fischer, R. A. (2009). High-precision determination of iron oxidation state in silicate glasses using XANES. Chemical Geology, 268(3), 167–179. https://doi.org/10.1016/j.chemgeo.2009.08.008

D

Danyushevsky, L. V., & Plechov, P. (2011). Petrolog3: Integrated software for modeling crystallization processes. Geochemistry, Geophysics, Geosystems, 12(7), 32. https://doi.org/10.1029/2011GC003516

Danyushevsky, L. V., Della-Pasqua, F. N., & Sokolov, S. (2000). Re-equilibration of melt inclusions trapped by magnesian olivine phenocrysts from subduction-related magmas: petrological implications. Contributions to Mineralogy and Petrology, 138(1), 68–83. https://doi.org/10.1007/PL00007664

Danyushevsky, L. V., Sokolov, S., & Falloon, T. J. (2002). Melt inclusions in olivine phenocrysts: using diffusive re-equilibration to determine the cooling history of a crystal, with implications for the origin of olivine-phyric volcanic rocks. Journal of Petrology, 43(9), 1651–1671. https://doi.org/10.1093/petrology/43.9.1651

Danyushevsky, L. V., Leslie, R. A., Crawford, A. J., & Durance, P. (2004). Melt inclusions in primitive olivine phenocrysts: the role of localized reaction processes in the origin of anomalous compositions. Journal of Petrology, 45(12), 2531–2553. https://doi.org/10.1093/petrology/egh080

Davidson, J., Turner, S., Handley, H., Macpherson, C., & Dosseto, A. (2007). Amphibole “sponge” in arc crust? Geology, 35(9), 787–790.

Davidson, J. P. (1987). Crustal contamination versus subduction zone enrichment: Examples from the Lesser Antilles and implications for mantle source compositions of island arc volcanic rocks. Geochimica et Cosmochimica Acta, 51(8), 2185–2198. https://doi.org/10.1016/0016-7037(87)90268-7

Davidson, J. P. (1996). Deciphering mantle and crustal signatures in subduction zone magmatism. In Subduction: top to bottom (pp. 251–262). American Geophysical Union (AGU). https://doi.org/10.1029/GM096p0251

Defant, M. J., & Drummond, M. (1990). Derivation of some modern arc magmas by melting of young subducted lithosphere. Nature, 347, 4.

DePaolo, D. J. (1981). Trace element and isotopic effects of combined wallrock assimilation and fractional crystallization. Earth and Planetary Science Letters, 53(2), 189–202. https://doi.org/10.1016/0012-821X(81)90153-9

Dohmen, R., Chakraborty, S., & Becker, H.-W. (2002). Si and O diffusion in olivine and implications for characterizing plastic flow in the mantle. Geophysical Research Letters, 29(21), 26-1-26–4. https://doi.org/10.1029/2002GL015480

Duan, Z., & Zhang, Z. (2006). Equation of state of the H2O, CO2, and H2O–CO2 systems up to 10 GPa and 2573.15K: Molecular dynamics simulations with ab initio potential surface. Geochimica et Cosmochimica Acta, 70(9), 2311–2324. https://doi.org/10.1016/j.gca.2006.02.009

Dupuy, C., Liotard, J. M., & Dostal, J. (1992). Zr/Hf fractionation in intraplate basaltic rocks: carbonate metasomatism in the mantle source. Geochimica et Cosmochimica Acta, 56(6), 2417–2423. https://doi.org/10.1016/0016-7037(92)90198-R

Dutkiewicz, A., Müller, R. D., O'Callaghan, S., & Jónasson, H. (2015). Census of seafloor sediments in the world's ocean. Geology, 43(9), 795–798. https://doi.org/10.1130/G36883.1

E

Elburg, M. A., Kamenetsky, V. S., Foden, J. D., & Sobolev, A. (2007). The origin of medium-K ankaramitic arc magmas from Lombok (Sunda arc, Indonesia): Mineral and melt inclusion evidence. Chemical Geology, 240(3–4), 260–279. https://doi.org/10.1016/j.chemgeo.2007.02.015

Elliot, T., Plank, T., Zindler, A., White, W., & Bourdon, B. (1997). Element transport from slab to volcanic front at the Mariana arc. Journal of Geophysical Research: Solid Earth, 102(B7), 14991–15019. https://doi.org/10.1029/97JB00788

Elliott, T. (2003). Tracers of the slab. In J. Eiler (Ed.), Geophysical Monograph Series (Vol. 138, pp. 23–45). Washington, D. C.: American Geophysical Union.

Esposito, R., Bodnar, R. J., Danyushevsky, L. V., De Vivo, B., Fedele, L., Hunter, J., et al. (2011). Volatile evolution of magma associated with the Solchiaro eruption in the phlegrean volcanic district (Italy). Journal of Petrology, 52(12), 2431–2460. https://doi.org/10.1093/petrology/egr051

F

Falloon, T. J., Danyushevsky, L. V., & Green, D. H. (2001). Peridotite melting at 1 GPa: reversal experiments on partial melt compositions produced by peridotite–basalt sandwich experiments. Journal of Petrology, 42(12), 2363–2390. https://doi.org/10.1093/petrology/42.12.2363

Feininger, T., & Seguin, M. K. (1983). Simple Bouguer gravity anomaly field and the inferred crustal structure of continental Ecuador. Geology, 11(1), 40–44. https://doi.org/10.1130/0091-7613(1983)11<40:SBGAFA>2.0.CO;2

Férot, A., & Bolfan-Casanova, N. (2012). Water storage capacity in olivine and pyroxene to 14GPa: Implications for the water content of the Earth's upper mantle and nature of seismic discontinuities. Earth and Planetary Science Letters, 349–350, 218–230. https://doi.org/10.1016/j.epsl.2012.06.022

Foley, S. (1992). Vein-plus-wall-rock melting mechanisms in the lithosphere and the origin of potassic alkaline magmas. Lithos, 28(3–6), 435–453. https://doi.org/10.1016/0024-4937(92)90018-T

Ford, C. E., Russell, D. G., Craven, J. A., & Fisk, M. R. (1983). Olivine-liquid equilibria: Temperature, pressure and composition dependence of the crystal/liquid cation partition coefficients for Mg, Fe 2+, Ca and Mn. Journal of Petrology, 24(3), 256–266. https://doi.org/10.1093/petrology/24.3.256

Frezzotti, M.-L. (2001). Silicate-melt inclusions in magmatic rocks: applications to petrology. Lithos, 55(1), 273–299.

G

Gaetani, G. A., & Grove, T. L. (1998). The influence of water on melting of mantle peridotite. Contributions to Mineralogy and Petrology, 131(4), 323–346.

Gaetani, G. A., & Watson, E. B. (2000). Open system behavior of olivine-hosted melt inclusions. Earth and Planetary Science Letters, 183(1–2), 27–41. https://doi.org/10.1016/S0012-821X(00)00260-0

Gaetani, G. A., Asimow, P. D., & Stolper, E. M. (2008). A model for rutile saturation in silicate melts with applications to eclogite partial melting in subduction zones and mantle plumes. Earth and Planetary Science Letters, 272(3–4), 720–729. https://doi.org/10.1016/j.epsl.2008.06.002

Gaetani, G. A., O'Leary, J. A., Shimizu, N., Bucholz, C. E., & Newville, M. (2012). Rapid reequilibration of H2O and oxygen fugacity in olivine-hosted melt inclusions. Geology, 40(10), 915–918. https://doi.org/10.1130/G32992.1

Gaetani, G. A., O'Leary, J. A., Koga, K. T., Hauri, E. H., Rose-Koga, E. F., & Monteleone, B. D. (2014). Hydration of mantle olivine under variable water and oxygen fugacity conditions. Contributions to Mineralogy and Petrology, 167(2). https://doi.org/10.1007/s00410-014-0965-y

Gao, S., Liu, X., Yuan, H., Hattendorf, B., Günther, D., Chen, L., & Hu, S. (2002). Determination of forty two major and trace elements in USGS and NIST SRM glasses by laser ablation-inductively coupled plasma-mass spectrometry. Geostandards and Geoanalytical Research, 26(2), 181–196. https://doi.org/10.1111/j.1751-908X.2002.tb00886.x

Garrison, J. M., & Davidson, J. P. (2003). Dubious case for slab melting in the Northern volcanic zone of the Andes. Geology, 31(6), 565–568.

Garrison, J. M., Davidson, J., Reid, M., & Turner, S. (2006). Source versus differentiation controls on U-series disequilibria: Insights from Cotopaxi Volcano, Ecuador. Earth and Planetary Science Letters, 244(3), 548–565. https://doi.org/10.1016/j.epsl.2006.02.013

Garrison, J. M., Davidson, J. P., Hall, M. L., & Mothes, P. (2011). Geochemistry and petrology of the most recent deposits from Cotopaxi volcano, Northern volcanic zone, Ecuador. Journal of Petrology, 52(9), 1641–1678. https://doi.org/10.1093/petrology/egr023

Garrison, J. M., Sims, K. W. W., Yogodzinski, G. M., Escobar, R. D., Scott, S., Mothes, P., et al. (2018). Shallow-level differentiation of phonolitic lavas from Sumaco volcano, Ecuador. Contributions to Mineralogy and Petrology, 173(1). https://doi.org/10.1007/s00410-017-1431-4

Gavrilenko, M., Krawczynski, M., Ruprecht, P., Li, W., & Catalano, J. G. (2019). The quench control of water estimates in convergent margin magmas. American Mineralogist, 104(7), 936–948. https://doi.org/10.2138/am-2019-6735

Ghiorso, M. S., & Gualda, G. A. R. (2015). An H2O–CO2 mixed fluid saturation model compatible with rhyolite-MELTS. Contributions to Mineralogy and Petrology, 169(6). https://doi.org/10.1007/s00410-015-1141-8

Ghiorso, M. S., Hirschmann, M. M., Reiners, P. W., & Kress, V. C. (2002). The pMELTS: A revision of MELTS for improved calculation of phase relations and major element partitioning related to partial melting of the mantle to 3 GPa. Geochemistry, Geophysics, Geosystems, 3, 1–35. https://doi.org/10.1029/2001gc000217

Gill, J. B. (1981). Orogenic Andesites and Plate Tectonics (First edition, Vol. 16). Springer-Verlag Berlin Heidelberg.

Gioncada, A., Clocchiatti, R., Sbrana, A., Bottazzi, P., Massare, D., & Ottolini, L. (1998). A study of melt inclusions at Vulcano (Aeolian Islands, Italy): insights on the primitive magmas and on the volcanic feeding system. Bulletin of Volcanology, 60(4), 286–306. https://doi.org/10.1007/s004450050233

Gómez-Tuena, A., Langmuir, C. H., Goldstein, S. L., Straub, S. M., & Ortega-Gutierrez, F. (2006). Geochemical evidence for slab melting in the Trans-Mexican volcanic belt. Journal of Petrology, 48(3), 537–562. https://doi.org/10.1093/petrology/egl071

Green, T. H. (1994). Experimental studies of trace-element partitioning applicable to igneous petrogenesis—Sedona 16 years later. Chemical Geology, 117(1–4), 1–36.

Green, T. H., Blundy, J. D., Adam, J., & Yaxley, G. M. (2000). SIMS determination of trace element partition coefficients between garnet, clinopyroxene and hydrous basaltic liquids at 2–7.5 GPa and 1080–1200°C. Lithos, 53(3–4), 165–187. https://doi.org/10.1016/S0024-4937(00)00023-2

Greene, A. R. (2006). A detailed geochemical study of island arc crust: the Talkeetna arc section, south-central Alaska. Journal of Petrology, 47(6), 1051–1093. https://doi.org/10.1093/petrology/egl002

Grove, T. L., Parman, S., Bowring, S., Price, R., & Baker, M. (2002). The role of an H2O-rich fluid component in the generation of primitive basaltic andesites and andesites from the Mt. Shasta region, N California. Contributions to Mineralogy and Petrology, 142(4), 375–396. https://doi.org/10.1007/s004100100299

Gualda, G. A. R., Ghiorso, M. S., Lemons, R. V., & Carley, T. L. (2012). Rhyolite-MELTS: a modified calibration of MELTS optimized for silica-rich, fluid-bearing magmatic systems. Journal of Petrology, 53(5), 875–890. https://doi.org/10.1093/petrology/egr080

Guillier, B., Chatelain, J.-L., Jaillard, É., Yepes, H., Poupinet, G., & Fels, J.-F. (2001). Seismological evidence on the geometry of the orogenic system in Central-Northern

Ecuador (South America). Geophysical Research Letters, 28(19), 3749–3752. https://doi.org/10.1029/2001GL013257

Gutscher, M.-A., Malavieille, J., Lallemand, S., & Collot, J.-Y. (1999). Tectonic segmentation of the North Andean margin: impact of the Carnegie Ridge collision. Earth and Planetary Science Letters, 168(3–4), 255–270. https://doi.org/10.1016/S0012-821X(99)00060-6

Gutscher, M.-A., Maury, R., Eissen, J.-P., & Bourdon, E. (2000). Can slab melting be caused by flat subduction? Geology, 28(6), 535–538.

H

Hall, M. L., Samaniego, P., Le Pennec, J. L., & Johnson, J. B. (2008). Ecuadorian Andes volcanism: A review of Late Pliocene to present activity. Journal of Volcanology and Geothermal Research, 176(1), 1–6. https://doi.org/10.1016/j.jvolgeores.2008.06.012

Halliday, A. N., Lee, D.-C., Tommasini, S., Davies, G. R., Paslick, C. R., Godfrey Fitton, J., & James, D. E. (1995). Incompatible trace elements in OIB and MORB and source enrichment in the sub-oceanic mantle. Earth and Planetary Science Letters, 133(3), 379–395. https://doi.org/10.1016/0012-821X(95)00097-V

Harpp, K. S., Wanless, V. D., Otto, R. H., Hoernle, K., & Werner, R. (2005). The Cocos and Carnegie aseismic ridges: a trace element record of long-term plume–spreading center interaction. Journal of Petrology, 46(1), 109–133. https://doi.org/10.1093/petrology/egh064

Hauri, E. (2002). SIMS analysis of volatiles in silicate glasses, 2: isotopes and abundances in Hawaiian melt inclusions. Chemical Geology, 183(1), 115–141. https://doi.org/10.1016/S0009-2541(01)00374-6

Hermann, J., & Korsakov, A. (2006). Aqueous fluids and hydrous melts in high-pressure and ultra-high pressure rocks: implications for element transfer in subduction zones. Lithos, 92(3–4), 399–417. https://doi.org/10.1016/j.lithos.2006.03.055

Hermann, J., & Rubatto, D. (2009). Accessory phase control on the trace element signature of sediment melts in subduction zones. Chemical Geology, 265(3–4), 512–526. https://doi.org/10.1016/j.chemgeo.2009.05.018

Hermann, J., & Spandler, C. J. (2008). Sediment melts at sub-arc depths: an experimental study. Journal of Petrology, 49(4), 717–740. https://doi.org/10.1093/petrology/egm073

Hernández-Uribe, D., & Palin, R. M. (2019). A revised petrological model for subducted oceanic crust: Insights from phase equilibrium modelling. Journal of Metamorphic Geology, 37(6), 745–768. https://doi.org/10.1111/jmg.12483

Hernández-Uribe, D., Hernández-Montenegro, J. D., Cone, K. A., & Palin, R. M. (2019). Oceanic slab-top melting during subduction: Implications for trace-element recycling and adakite petrogenesis. Geology. https://doi.org/10.1130/G46835.1

Hidalgo, S. (2006). Les intéractions entre magmas calco-alcalins “‘classiques’” et adakitiques: exemple du complexe volcanique Atacazo-Ninahuilca (Equateur)

(Doctoral Thesis). Université Blaise Pascal - Clermont-Ferrand II, Clermont-Ferrand, France.

Hidalgo, S., Monzier, M., Martin, H., Chazot, G., Eissen, J.-P., & Cotten, J. (2007). Adakitic magmas in the Ecuadorian volcanic front: petrogenesis of the Iliniza volcanic complex (Ecuador). Journal of Volcanology and Geothermal Research, 159(4), 366–392. https://doi.org/10.1016/j.jvolgeores.2006.07.007

Hidalgo, S., Gerbe, M. C., Martin, H., Samaniego, P., & Bourdon, E. (2012). Role of crustal and slab components in the Northern Volcanic Zone of the Andes (Ecuador) constrained by Sr–Nd–O isotopes. Lithos, 132–133, 180–192. https://doi.org/10.1016/j.lithos.2011.11.019

Hildreth, W., & Moorbath, S. (1988). Crustal contributions to arc magmatism in the Andes of central Chile. Contributions to Mineralogy and Petrology, 98(4), 455–489. https://doi.org/10.1007/BF00372365

Hirose, K., & Kawamoto, T. (1995). Hydrous partial melting of lherzolite at 1 GPa: The effect of H2O on the genesis of basaltic magmas. Earth and Planetary Science Letters, 133(3), 463–473. https://doi.org/10.1016/0012-821X(95)00096-U

Hirose, K., & Kushiro, I. (1993). Partial melting of dry peridotites at high pressures: determination of compositions of melts segregated from peridotite using aggregates of diamond. Earth and Planetary Science Letters, 114(4), 477–489. https://doi.org/10.1016/0012-821X(93)90077-M

Hirschmann, M. M., & Stolper, E. M. (1996). A possible role for garnet pyroxenite in the origin of the "garnet signature" in MORB. Contributions to Mineralogy and Petrology, 124(2), 185–208.

Hirschmann, M. M., Aubaud, C., & Withers, A. C. (2005). Storage capacity of H2O in nominally anhydrous minerals in the upper mantle. Earth and Planetary Science Letters, 236(1), 167–181. https://doi.org/10.1016/j.epsl.2005.04.022

Hoffer, G., Eissen, J.-P., Beate, B., Bourdon, E., Fornari, M., & Cotten, J. (2008). Geochemical and petrological constraints on rear-arc magma genesis processes in Ecuador: The Puyo cones and Mera lavas volcanic formations. Journal of Volcanology and Geothermal Research, 176(1), 107–118. https://doi.org/10.1016/j.jvolgeores.2008.05.023

Hofmann, A. W. (1988). Chemical differentiation of the Earth: the relationship between mantle, continental crust, and oceanic crust. Earth and Planetary Science Letters, 90(3), 297–314. https://doi.org/10.1016/0012-821X(88)90132-X

Honda, S., Gerya, T., & Zhu, G. (2010). A simple three-dimensional model of thermo–chemical convection in the mantle wedge. Earth and Planetary Science Letters, 290(3–4), 311–318. https://doi.org/10.1016/j.epsl.2009.12.027

J

Jackson, S. E. (2008). Calibration strategies for elemental analysis by LA-ICP-MS. In Laser Ablation–ICP–MS in the Earth Sciences: current practices and outstanding issues (Paul Sylvester, Vol. 40, p. 21). Canada: Mineral association of Canada.

Jagoutz, O., & Kelemen, P. B. (2015). Role of arc processes in the formation of continental crust. Annual Review of Earth and Planetary Sciences, 43(1), 363–404. https://doi.org/10.1146/annurev-earth-040809-152345

Jagoutz, O. E. (2010). Construction of the granitoid crust of an island arc. Part II: a quantitative petrogenetic model. Contributions to Mineralogy and Petrology, 160(3), 359–381. https://doi.org/10.1007/s00410-009-0482-6

Jaillard, E., Bengtson, P., Ordoñez, M., Vaca, W., Dhondt, A., Suárez, J., & Toro, J. (2008). Sedimentary record of terminal cretaceous accretions in Ecuador: The Yunguilla group in the Cuenca area. Journal of South American Earth Sciences, 25(2), 133–144. https://doi.org/10.1016/j.jsames.2007.08.002

Jochum, K. P., Stoll, B., Herwig, K., Willbold, M., Hofmann, A. W., Amini, M., et al. (2006). MPI-DING reference glasses for in situ microanalysis: new reference values for element concentrations and isotope ratios. Geochemistry, Geophysics, Geosystems, 7(2). https://doi.org/10.1029/2005GC001060

Johnston, S. T., & Thorkelson, D. J. (1997). Cocos-Nazca slab window beneath Central America. Earth and Planetary Science Letters, 146(3–4), 465–474. https://doi.org/10.1016/S0012-821X(96)00242-7

Jugo, P. J., Luth, R. W., & Richards, J. P. (2005). Experimental data on the speciation of sulfur as a function of oxygen fugacity in basaltic melts. Geochimica et Cosmochimica Acta, 69(2), 497–503. https://doi.org/10.1016/j.gca.2004.07.011

K

Kamenetsky, V. S., & Maas, R. (2002). Mantle-melt evolution (dynamic source) in the origin of a single MORB suite: a perspective from magnesian glasses of Macquarie Island. Journal of Petrology, 43(10), 1909–1922. https://doi.org/10.1093/petrology/43.10.1909

Kamenetsky, V. S., Everard, J. L., Crawford, A. J., Varne, R., Eggins, S. M., & Lanyon, R. (2000). Enriched end-member of primitive MORB melts: petrology and geochemistry of glasses from Macquarie Island (SW Pacific). Journal of Petrology, 41(3), 411–430. https://doi.org/10.1093/petrology/41.3.411

Karato, S., & Wu, P. (1993). Rheology of the upper mantle: A synthesis. Science, 260(5109), 771–778.

Kawakami, Y., Yamamoto, J., & Kagi, H. (2003). Micro-Raman Densimeter for CO2 Inclusions in Mantle-Derived Minerals. Applied Spectroscopy, 57(11), 1333–1339.

van Keken, P. E., Hacker, B. R., Syracuse, E. M., & Abers, G. A. (2011). Subduction factory: 4. Depth-dependent flux of H2O from subducting slabs worldwide. Journal of Geophysical Research, 116, 15.

van Keken, P. E., Wada, I., Sime, N., & Abers, G. A. (2019). Thermal structure of the forearc in subduction zones: a comparison of methodologies. Geochemistry, Geophysics, Geosystems, 20(7), 3268–3288. https://doi.org/10.1029/2019GC008334

Kelemen, P. B. (1995). Genesis of high Mg# andesites and the continental crust. Contributions to Mineralogy and Petrology, 120(1), 1–19. https://doi.org/10.1007/BF00311004

Kelemen, P. B., Yogodzinski, G. M., & Scholl, D. W. (2004). Along-Strike Variation in the Aleutian Island Arc: Genesis of High Mg# Andesite and Implications for Continental Crust. In J. Eiler (Ed.), Inside the Subduction Factory (pp. 223–276). American Geophysical Union. Retrieved from http://onlinelibrary.wiley.com/doi/10.1029/138GM11/summary

Kelemen, P. B., Hanghøj, K., & Greene, A. R. (2014). One view of the geochemistry of subduction-related magmatic arcs, with an emphasis on primitive andesite and lower crust. In Treatise on Geochemistry (pp. 749–806). Elsevier.

Kellogg, J. N., Vega, V., Stailings, T. C., & Aiken, C. L. (1995). Tectonic development of Panama, Costa Rica, and the Colombian Andes: constraints from global positioning system geodetic studies and gravity. Geological Society of America Special Papers, 295, 75–90.

Kendrick, M. A., Kamenetsky, V. S., Phillips, D., & Honda, M. (2012). Halogen systematics (Cl, Br, I) in mid-ocean ridge basalts: a Macquarie Island case study. Geochimica et Cosmochimica Acta, 81, 82–93. https://doi.org/10.1016/j.gca.2011.12.004

Kerr, A. C., Aspden, J. A., Tarney, J., & Pilatasig, L. F. (2002). The nature and provenance of accreted oceanic terranes in western Ecuador: geochemical and tectonic constraints. Journal of the Geological Society, 159(5), 577–594.

Kessel, R., Ulmer, P., Pettke, T., Schmidt, M. W., & Thompson, A. B. (2004). A novel approach to determine high-pressure high-temperature fluid and melt compositions using diamond-trap experiments. American Mineralogist, 89(7), 1078–1086. https://doi.org/10.2138/am-2004-0720

Kessel, R., Schmidt, M. W., Ulmer, P., & Pettke, T. (2005a). Trace element signature of subduction-zone fluids, melts and supercritical liquids at 120–180 km depth. Nature, 437(7059), 724–727. https://doi.org/10.1038/nature03971

Kessel, R., Ulmer, P., Pettke, T., Schmidt, M. W., & Thompson, A. B. (2005b). The water–basalt system at 4 to 6 GPa: Phase relations and second critical endpoint in a K-free eclogite at 700 to 1400 °C. Earth and Planetary Science Letters, 237(3), 873–892. https://doi.org/10.1016/j.epsl.2005.06.018

Kimura, J.-I., Kent, A. J. R., Rowe, M. C., Katakuse, M., Nakano, F., Hacker, B. R., et al. (2010). Origin of cross-chain geochemical variation in Quaternary lavas from the northern Izu arc: using a quantitative mass balance approach to identify mantle sources and mantle wedge processes. Geochemistry, Geophysics, Geosystems, 11(10), 24. https://doi.org/10.1029/2010GC003050

Klimm, K., Blundy, J. D., & Green, T. H. (2008). Trace element partitioning and accessory phase saturation during H2O-saturated melting of basalt with implications for subduction zone chemical fluxes. Journal of Petrology, 49(3), 523–553. https://doi.org/10.1093/petrology/egn001

Kogiso, T., & Hirschmann, M. M. (2001). Experimental study of clinopyroxenite partial melting and the origin of ultra-calcic melt inclusions. Contributions to Mineralogy and Petrology, 142(3), 347–360. https://doi.org/10.1007/s004100100295

Kogiso, T., Tatsumi, Y., & Nakano, S. (1997). Trace element transport during dehydration processes in the subducted oceanic crust: 1. Experiments and implications for the origin of ocean island basalts. Earth and Planetary Science Letters, 148(1), 193–205. https://doi.org/10.1016/S0012-821X(97)00018-6

Koornneef, J. M., Nikogosian, I., van Bergen, M. J., Smeets, R., Bouman, C., & Davies, G. R. (2015). TIMS analysis of Sr and Nd isotopes in melt inclusions from Italian potassium-rich lavas using prototype 1013Ω amplifiers. Chemical Geology, 397, 14–23. https://doi.org/10.1016/j.chemgeo.2015.01.005

Krawczynski, M. J., Grove, T. L., & Behrens, H. (2012). Amphibole stability in primitive arc magmas: effects of temperature, H2O content, and oxygen fugacity. Contributions to Mineralogy and Petrology, 164(2), 317–339. https://doi.org/10.1007/s00410-012-0740-x

Kushiro, I. (1996). Partial melting of a fertile mantle peridotite at high pressures: an experimental study using aggregates of diamond. In A. Basu & S. Hart (Eds.), Earth Processes: Reading the Isotopic Code (pp. 109–122). American Geophysical Union.

Kusserow, A. (2019). Dynamic secondary ion mass spectrometry (First edition). UK: John Wiley & Sons.

L

Labanieh, S., Chauvel, C., Germa, A., & Quidelleur, X. (2012). Martinique: a clear case for sediment melting and slab dehydration as a function of distance to the trench. Journal of Petrology, 53(12), 2441–2464. https://doi.org/10.1093/petrology/egs055

Laporte, D., Toplis, M. J., Seyler, M., & Devidal, J.-L. (2004). A new experimental technique for extracting liquids from peridotite at very low degrees of melting: application to partial melting of depleted peridotite. Contributions to Mineralogy and Petrology, 146(4), 463–484. https://doi.org/10.1007/s00410-003-0509-3

LaTourrette, T., Hervig, R. L., & Holloway, J. R. (1995). Trace element partitioning between amphibole, phlogopite, and basanite melt. Earth and Planetary Science Letters, 135(1), 13–30. https://doi.org/10.1016/0012-821X(95)00146-4

Laubier, M., Schiano, P., Doucelance, R., Ottolini, L., & Laporte, D. (2007). Olivine-hosted melt inclusions and melting processes beneath the FAMOUS zone (Mid-Atlantic Ridge). Chemical Geology, 240(1–2), 129–150. https://doi.org/10.1016/j.chemgeo.2007.02.002

Le Bas, M. J., Le Maitre, R. W., Streckeisen, A., Zanettin, B., & others. (1986). A chemical classification of volcanic rocks based on the total alkali-silica diagram. Journal of Petrology, 27(3), 745–750.

Le Pennec, J. L., Ruiz, A. G., Eissen, J. P., Hall, M. L., & Fornari, M. (2011). Identifying potentially active volcanoes in the Andes: radiometric evidence for late Pleistocene-early Holocene eruptions at Volcán Imbabura, Ecuador. Journal of Volcanology and

Geothermal Research, 206(3–4), 121–135. https://doi.org/10.1016/j.jvolgeores.2011.06.002

Le Voyer, M. (2009). Rôle des fluides dans la genèse des magmas d'arcs : analyses in situ des éléments volatils et des isotopes du bore dans les inclusions magmatiques des olivines primitives (Doctoral Thesis). Université Blaise Pascal - Clermont-Ferrand II, France.

Le Voyer, M., Rose-Koga, E. F., Laubier, M., & Schiano, P. (2008). Petrogenesis of arc lavas from the Rucu Pichincha and Pan de Azúcar volcanoes (Ecuadorian arc): major, trace element, and boron isotope evidences from olivine-hosted melt inclusions. Geochemistry, Geophysics, Geosystems, 9(12), 27. https://doi.org/10.1029/2008GC002173

Le Voyer, M., Rose-Koga, E. F., Shimizu, N., Grove, T. L., & Schiano, P. (2010). Two Contrasting H2O-rich Components in Primary Melt Inclusions from Mount Shasta. Journal of Petrology, 51(7), 1571–1595. https://doi.org/10.1093/petrology/egq030

Leeman, W. P., & Sisson, V. B. (1996). Geochemistry of boron and its implications for crustal and mantle processes. Reviews in Mineralogy and Geochemistry, 33(1), 645–707.

Leroux, P., Shirey, S., Hauri, E., Perfit, M., & Bender, J. (2006). The effects of variable sources, processes and contaminants on the composition of northern EPR MORB (8–10°N and 12–14°N): evidence from volatiles (H2O, CO2, S) and halogens (F, Cl). Earth and Planetary Science Letters, 251(3–4), 209–231. https://doi.org/10.1016/j.epsl.2006.09.012

Lesne, P., Kohn, S. C., Blundy, J., Witham, F., Botcharnikov, R. E., & Behrens, H. (2011). Experimental Simulation of Closed-System Degassing in the System Basalt–H2O–CO2–S–Cl. Journal of Petrology, 52(9), 1737–1762. https://doi.org/10.1093/petrology/egr027

Lin, J., Liu, Y., Yang, Y., & Hu, Z. (2016). Calibration and correction of LA-ICP-MS and LA-MC-ICP-MS analyses for element contents and isotopic ratios. Solid Earth Sciences, 1(1), 5–27. https://doi.org/10.1016/j.sesci.2016.04.002

Lister, J. R., & Kerr, R. C. (1991). Fluid-mechanical models of crack propagation and their application to magma transport in dykes. Journal of Geophysical Research: Solid Earth, 96(B6), 10049–10077. https://doi.org/10.1029/91JB00600

Litherland, M., Aspen, J. A., & Jemielita, R. A. (1994). The metamorphic belts of Ecuador. British Geological Survey.

Lloyd, A. S., Plank, T., Ruprecht, P., Hauri, E. H., & Rose, W. (2013). Volatile loss from melt inclusions in pyroclasts of differing sizes. Contributions to Mineralogy and Petrology, 165, 25. https://doi.org/10.1007/s00410-012-0800-2

Longerich, H. (2008). Laser ablation-Inductively coupled plasma-mass spectrometer spectrometry (LA–ICP–MS): an introduction. In Laser Ablation–ICP–MS in the Earth Sciences: current practices and outstanding issues (Paul Sylvester, Vol. 40, p. 21). Canada: Mineral association of Canada.

Lonsdale, P. (2005). Creation of the Cocos and Nazca plates by fission of the Farallon plate. Tectonophysics, 404(3–4), 237–264. https://doi.org/10.1016/j.tecto.2005.05.011

Lowenstern, J. B. (1995). Applications of silicate melt inclusions to the study of magmatic volatiles. In Magmas, Fluids and Ore Deposits (J.F.H. Thompson, Vol. 23, pp. 71–99). Mineralogical Association of Canada.

Luhr, J. F. (1997). Extensional tectonics and the diverse primitive volcanic rocks in the western Mexican volcanic belt. The Canadian Mineralogist, 35(2), 473–500.

M

Mamberti, M., Lapierre, H., Bosch, D., Jaillard, E., Ethien, R., Hernandez, J., & Polvé, M. (2003). Accreted fragments of the late cretaceous Caribbean–Colombian plateau in Ecuador. Lithos, 66(3), 173–199.

Martin, H. (1999). Adakitic magmas: modern analogues of Archaean granitoids. Lithos, 46(3), 411–429.

Martin, H., Smithies, R. H., Rapp, R., Moyen, J.-F., & Champion, D. (2005). An overview of adakite, tonalite–trondhjemite–granodiorite (TTG), and sanukitoid: relationships and some implications for crustal evolution. Lithos, 79(1–2), 1–24. https://doi.org/10.1016/j.lithos.2004.04.048

Martin, L. A. J., & Hermann, J. (2018). Experimental phase relations in altered oceanic crust: implications for carbon recycling at subduction zones. Journal of Petrology, 59(2), 299–320. https://doi.org/10.1093/petrology/egy031

McDonough, W. F., & Sun, S. S. (1995). The composition of the Earth. Chemical Geology, 120(3), 223–253. https://doi.org/10.1016/0009-2541(94)00140-4

Médard, E., Schmidt, M., & Schiano, P. (2006). Melting of amphibole-bearing wehrlites: an experimental study on the origin of ultra-calcic nepheline-normative melts. Journal of Petrology, 47(3), 481–504. https://doi.org/10.1093/petrology/egi083

Métrich, N., & Wallace, P. J. (2008). Volatile abundances in basaltic magmas and their degassing paths tracked by melt inclusions. Reviews in Mineralogy and Geochemistry, 69(1), 363–402. https://doi.org/10.2138/rmg.2008.69.10

Métrich, N., Clocchiatti, R., Mosbah, M., & Chaussidon, M. (1993). The 1989–1990 activity of Etna magma mingling and ascent of H2O, Cl, S rich basaltic magma. Evidence from melt inclusions. Journal of Volcanology and Geothermal Research, 59(1), 131–144. https://doi.org/10.1016/0377-0273(93)90082-3

Métrich, N., Schiano, P., Clocchiatti, R., & Maury, R. C. (1999). Transfer of sulfur in subduction settings: an example from Batan Island (Luzon volcanic arc, Philippines). Earth and Planetary Science Letters, 167(1), 1–14. https://doi.org/10.1016/S0012-821X(99)00009-6

Métrich, N., Allard, P., Spilliaert, N., Andronico, D., & Burton, M. (2004). 2001 flank eruption of the alkali- and volatile-rich primitive basalt responsible for Mount Etna's

evolution in the last three decades. Earth and Planetary Science Letters, 228(1–2), 1–17. https://doi.org/10.1016/j.epsl.2004.09.036

Mibe, K., Kawamoto, T., Matsukage, K. N., Fei, Y., & Ono, S. (2011). Slab melting versus slab dehydration in subduction-zone magmatism. Proceedings of the National Academy of Sciences, 108(20), 8177–8182. https://doi.org/10.1073/pnas.1010968108

Michaud, F., Chabert, A., Collot, J.-Y., Sallarès, V., Flueh, E. R., Charvis, P., et al. (2005). Fields of multi-kilometer scale sub-circular depressions in the Carnegie Ridge sedimentary blanket: Effect of underwater carbonate dissolution? Marine Geology, 216(4), 205–219. https://doi.org/10.1016/j.margeo.2005.01.003

Michaud, F., Witt, C., & Royer, J.-Y. (2009). Influence of the subduction of the Carnegie volcanic ridge on Ecuadorian geology: Reality and fiction. Geological Society of America Memoirs, 204(0), 217–228. https://doi.org/10.1130/2009.1204(10)

Migeon, S., Garibaldi, C., Ratzov, G., Schmidt, S., Collot, J.-Y., Zaragosi, S., & Texier, L. (2017). Earthquake-triggered deposits in the subduction trench of the north Ecuador/south Colombia margin and their implication for paleoseismology. Marine Geology, 384, 47–62. https://doi.org/10.1016/j.margeo.2016.09.008

Mironov, N., Portnyagin, M., Botcharnikov, R., Gurenko, A., Hoernle, K., & Holtz, F. (2015). Quantification of the CO2 budget and H2O–CO2 systematics in subduction-zone magmas through the experimental hydration of melt inclusions in olivine at high H2O pressure. Earth and Planetary Science Letters, 425, 1–11. https://doi.org/10.1016/j.epsl.2015.05.043

Monzier, M., Robin, C., Samaniego, P., Hall, M. L., Cotten, J., Mothes, P., & Arnaud, N. (1999). Sangay volcano, Ecuador: structural development, present activity and petrology. Journal of Volcanology and Geothermal Research, 90(1–2), 49–79. https://doi.org/10.1016/S0377-0273(99)00021-9

Moore, L. R., Gazel, E., Tuohy, R., Lloyd, A. S., Esposito, R., Steele-MacInnis, M., et al. (2015). Bubbles matter: An assessment of the contribution of vapor bubbles to melt inclusion volatile budgets. American Mineralogist, 100(4), 806–823. https://doi.org/10.2138/am-2015-5036

Moore, L. R., Mironov, N., Portnyagin, M., Gazel, E., & Bodnar, R. J. (2018). Volatile contents of primitive bubble-bearing melt inclusions from Klyuchevskoy volcano, Kamchatka: Comparison of volatile contents determined by mass-balance versus experimental homogenization. Journal of Volcanology and Geothermal Research, 358, 124–131. https://doi.org/10.1016/j.jvolgeores.2018.03.007

Moussallam, Y., Oppenheimer, C., Scaillet, B., Gaillard, F., Kyle, P., Peters, N., et al. (2014). Tracking the changing oxidation state of Erebus magmas, from mantle to surface, driven by magma ascent and degassing. Earth and Planetary Science Letters, 393, 200–209. https://doi.org/10.1016/j.epsl.2014.02.055

Moussallam, Y., Edmonds, M., Scaillet, B., Peters, N., Gennaro, E., Sides, I., & Oppenheimer, C. (2016). The impact of degassing on the oxidation state of basaltic magmas: A case study of Kīlauea volcano. Earth and Planetary Science Letters, 450, 317–325. https://doi.org/10.1016/j.epsl.2016.06.031

Moyen, J.-F., & Stevens, G. (2006). Experimental constraints on TTG petrogenesis: implications for Archean geodynamics. In K. Benn, J.-C. Mareschal, & K. C. Condie (Eds.), Geophysical Monograph Series (Vol. 164, pp. 149–175). Washington, D. C.: American Geophysical Union. https://doi.org/10.1029/164GM11

Müntener, O., & Ulmer, P. (2006). Experimentally derived high-pressure cumulates from hydrous arc magmas and consequences for the seismic velocity structure of lower arc crust. Geophysical Research Letters, 33(21). https://doi.org/10.1029/2006GL027629

Myers, M. L., Geist, D. J., Rowe, M. C., Harpp, K. S., Wallace, P. J., & Dufek, J. (2014). Replenishment of volatile-rich mafic magma into a degassed chamber drives mixing and eruption of Tungurahua volcano. Bulletin of Volcanology, 76(11). https://doi.org/10.1007/s00445-014-0872-0

N

Nandedkar, R. H., Ulmer, P., & Müntener, O. (2014). Fractional crystallization of primitive, hydrous arc magmas: an experimental study at 0.7 GPa. Contributions to Mineralogy and Petrology, 167(6), 1015. https://doi.org/10.1007/s00410-014-1015-5

Narváez, D. F., Rose-Koga, E. F., Samaniego, P., Koga, K. T., & Hidalgo, S. (2018). Constraining magma sources using primitive olivine-hosted melt inclusions from Puñalica and Sangay volcanoes (Ecuador). Contributions to Mineralogy and Petrology, 173(10), 80. https://doi.org/10.1007/s00410-018-1508-8

Narváez, D. F., Samaniego, P., Rose-Koga, E., Koga, K. T., Hidalgo, S., & Ratzov, G. (2020). Olivine-hosted re-heated melt inclusion composition from Ecuadorian volcanoes, Version 1.0. Interdisciplinary Earth Data Alliance (IEDA). Retrieved from https://doi.org/10.26022/IEDA/111625

Nichols, G. T., Wyllie, P. J., & Stern, C. R. (1994). Subduction zone melting of pelagic sediments constrained by melting experiments. Nature, 371, 4.

Nocquet, J.-M., Villegas-Lanza, J. C., Chlieh, M., Mothes, P. A., Rolandone, F., Jarrin, P., et al. (2014). Motion of continental slivers and creeping subduction in the northern Andes. Nat. Geosci, 7(4), 287–291.

O

O'Hara, M. J. (1976). Data reduction and projection schemes for complex compositions. Progress in Experimental Petrology, 6, 103–126.

Ordóñez, J. (2012). Depósitos volcánicos del pleistoceno tardío en la cuenca de Ambato: caracterización, distribución y origen. EPN, Quito (Ecuador).

P

Peacock, S. M., & Wang, K. (1999). Seismic Consequences of Warm Versus Cool Subduction Metamorphism: Examples from Southwest and Northeast Japan. Science, 286(5441), 937–939. https://doi.org/10.1126/science.286.5441.937

Pearce, J. A. (1982). Trace element characteristics of lavas from destructive plate boundaries. In R. S. Thorpe (Ed.), Orogenic andesites and related rocks (pp. 528–548). Chichester, England: John Wiley and Sons. Retrieved from http://orca.cf.ac.uk/8625/

Pearce, J. A. (2008). Geochemical fingerprinting of oceanic basalts with applications to ophiolite classification and the search for Archean oceanic crust. Lithos, 100(1–4), 14–48. https://doi.org/10.1016/j.lithos.2007.06.016

Pearce, J. A., & Peate, D. W. (1995). Tectonic implications of the composition of volcanic arc magmas. Annual Review of Earth and Planetary Sciences, 23(1), 251–285.

Peccerillo, A., & Taylor, S. R. (1976). Geochemistry of Eocene calc-alkaline volcanic rocks from the Kastamonu area, northern Turkey. Contributions to Mineralogy and Petrology, 58(1), 63–81.

Pilet, S., Baker, M. B., & Stolper, E. M. (2008). Metasomatized Lithosphere and the Origin of Alkaline Lavas. Science, 320(5878), 916–919. https://doi.org/10.1126/science.1156563

Plank, T. (2005). Constraints from thorium/lanthanum on sediment recycling at subduction zones and the evolution of the continents. Journal of Petrology, 46(5), 921–944. https://doi.org/10.1093/petrology/egi005

Plank, T. (2014). The Chemical Composition of Subducting Sediments. In Treatise on Geochemistry (pp. 607–629). Elsevier.

Plank, T., & Langmuir, C. H. (1998). The chemical composition of subducting sediment and its consequences for the crust and mantle. Chemical Geology, 145(3), 325–394. https://doi.org/10.1016/S0009-2541(97)00150-2

Plank, T., Kelley, K. A., Zimmer, M. M., Hauri, E. H., & Wallace, P. J. (2013). Why do mafic arc magmas contain ~4wt% water on average? Earth and Planetary Science Letters, 364, 168–179. https://doi.org/10.1016/j.epsl.2012.11.044

Poli, S., & Schmidt, M. W. (1998). The high-pressure stability of zoisite and phase relationships of zoisite-bearing assemblages. Contributions to Mineralogy and Petrology, 130, 162–175.

Portnyagin, M., Almeev, R., Matveev, S., & Holtz, F. (2008). Experimental evidence for rapid water exchange between melt inclusions in olivine and host magma. Earth and Planetary Science Letters, 272(3–4), 541–552. https://doi.org/10.1016/j.epsl.2008.05.020

Portnyagin, M., Mironov, N., Botcharnikov, R., Gurenko, A., Almeev, R. R., Luft, C., & Holtz, F. (2019). Dehydration of melt inclusions in olivine and implications for the origin of silica-undersaturated island-arc melts. Earth and Planetary Science Letters, 517, 95–105. https://doi.org/10.1016/j.epsl.2019.04.021

Pratt, W. T., Duque, P., & Ponce, M. (2005). An autochthonous geological model for the eastern Andes of Ecuador. Tectonophysics, 399(1–4), 251–278. https://doi.org/10.1016/j.tecto.2004.12.025

Prevot, R., Chatelain, J., Guillier, B., & Yepes, H. (1996). Mapping of the P-wave velocity structure beneath the Ecuadorian Andes: evidence for continuity of the

Central Andes. Presented at the 3rd International Symposium on Andean Geodynamics (ISAG), France.

Proust, J. N., Martillo, C., Michaud, F., Collot, J. Y., & Dauteuil, O. (2016). Subduction of seafloor asperities revealed by a detailed stratigraphic analysis of the active margin shelf sediments of Central Ecuador. Marine Geology, 380, 345–362. https://doi.org/10.1016/j.margeo.2016.03.014

Putirka, K. D. (2017). Down the crater: where magmas are stored and why they erupt. Elements, 13(1), 11–16. https://doi.org/10.2113/gselements.13.1.11

Putirka, K. D., Perfit, M., Ryerson, F. J., & Jackson, M. G. (2007). Ambient and excess mantle temperatures, olivine thermometry, and active vs. passive upwelling. Chemical Geology, 241(3–4), 177–206. https://doi.org/10.1016/j.chemgeo.2007.01.014

R

Rapp, R. P., Shimizu, N., Norman, M. D., & Applegate, G. S. (1999). Reaction between slab-derived melts and peridotite in the mantle wedge: experimental constraints at 3.8 GPa. Chemical Geology, 160(4), 335–356. https://doi.org/10.1016/S0009-2541(99)00106-0

Rasmussen, D. J., Kyle, P. R., Wallace, P. J., Sims, K. W. W., Gaetani, G. A., & Phillips, E. H. (2017). Understanding degassing and transport of CO2-rich alkalic magmas at Ross Island, Antarctica using olivine-hosted melt inclusions. Journal of Petrology. https://doi.org/10.1093/petrology/egx036

Ratzov, G., Collot, J.-Y., Sosson, M., & Migeon, S. (2010). Mass-transport deposits in the Northern Ecuador subduction trench: Result of frontal erosion over multiple seismic cycles. Earth and Planetary Science Letters, 296(1–2), 89–102. https://doi.org/10.1016/j.epsl.2010.04.048

Reed, S. J. B. (2005). Electron microprobe analysis and scanning electron microscopy in geology. Cambridge University Press.

Reinhard, A. A., Jackson, M. G., Koornneef, J. M., Rose-Koga, E. F., Blusztajn, J., Konter, J. G., et al. (2018). Sr and Nd isotopic compositions of individual olivine-hosted melt inclusions from Hawai'i and Samoa: Implications for the origin of isotopic heterogeneity in melt inclusions from OIB lavas. Chemical Geology, 495, 36–49. https://doi.org/10.1016/j.chemgeo.2018.07.034

Remmert, P., Dohmen, R., & Chakraborty, S. (2008). Diffusion of REE, Hf and Sr in Olivine. AGU Fall Meeting Abstracts, 33, MR33A-1844.

Ringwood, A. E. (1974). The petrological evolution of island arc systems. Journal of the Geological Society, 130(3), 183–204. https://doi.org/10.1144/gsjgs.130.3.0183

Robin, C., Eissen, J.-P., Samaniego, P., Martin, H., Hall, M., & Cotten, J. (2009). Evolution of the late Pleistocene Mojanda–Fuya Fuya volcanic complex (Ecuador), by progressive adakitic involvement in mantle magma sources. Bulletin of Volcanology, 71(3), 233–258.

Robin, C., Samaniego, P., Pennec, J.-L. L., Fornari, M., & Mothes, P. (2010). New radiometric and petrological constraints on the evolution of the Pichincha volcanic complex (Ecuador). Bulletin of Volcanology, 72, 21. https://doi.org/10.1007/s00445-010-0389-0

Roedder, E. (1979). Origin and significance of magmatic inclusions. Bulletin de Minéralogie, 102(5), 487–510. https://doi.org/10.3406/bulmi.1979.7299

Roedder, E., & Ribbe, P. H. (1984). Fluid inclusions (Vol. 12). Mineralogical Society of America Washington, DC. Retrieved from http://www.sidalc.net/cgi-bin/wxis.exe/?IsisScript=LIBRO.xis&method=post&formato=2&cantidad=1&expression=mfn=031279

Roeder, P. L., & Emslie, R. F. (1970). Olivine-liquid equilibrium. Contributions to Mineralogy and Petrology, 29(4), 275–289. https://doi.org/10.1007/BF00371276

Rogers, G., & Hawkesworth, C. J. (1989). A geochemical traverse across the North Chilean Andes: evidence for crust generation from the mantle wedge. Earth and Planetary Science Letters, 91(3), 271–285. https://doi.org/10.1016/0012-821X(89)90003-4

Rogers, G., & Hawkesworth, C. J. (1990). Reply to comment of C.R. Stern on "A geochemical traverse across the North Chilean Andes: Evidence for crust generation from the mantle wedge." Earth and Planetary Science Letters, 101(1), 134–137. https://doi.org/10.1016/0012-821X(90)90135-K

Rollinson, H. R. (1993). Using Geochemical Data: Evaluation, Presentation, Interpretation. England: Pearson/ Prentice Hall.

Rose-Koga, E. F., Koga, K. T., Schiano, P., Le Voyer, M., Shimizu, N., Whitehouse, M. J., & Clocchiatti, R. (2012). Mantle source heterogeneity for South Tyrrhenian magmas revealed by Pb isotopes and halogen contents of olivine-hosted melt inclusions. Chemical Geology, 334, 266–279. https://doi.org/10.1016/j.chemgeo.2012.10.033

Rose-Koga, E. F., Koga, K. T., Hamada, M., Hélouis, T., Whitehouse, M. J., & Shimizu, N. (2014). Volatile (F and Cl) concentrations in Iwate olivine-hosted melt inclusions indicating low-temperature subduction. Earth, Planets and Space, 66(1), 1–12.

Rose-Koga, E. F., Koga, K. T., Moreira, M., Vlastelic, I., Jackson, M. G., Whitehouse, M. J., et al. (2017). Geochemical systematics of Pb isotopes, fluorine, and sulfur in melt inclusions from São Miguel, Azores. Chemical Geology, 458, 22–37. https://doi.org/10.1016/j.chemgeo.2017.03.024

Rose-Koga, E. F., Koga, K. T., Devidal, J.-L., Shimizu, N., Le Voyer, M., Dalou, C., & Döbeli, M. (2020). In-situ measurements of magmatic volatile elements, F, S, and Cl, by electron microprobe, secondary ion mass spectrometry, and heavy ion elastic recoil detection analysis. American Mineralogist, 105, 11.

Rosenbaum, G., Sandiford, M., Caulfield, J., & Garrison, J. M. (2018). A trapdoor mechanism for slab tearing and melt generation in the northern Andes. Geology, 47(1), 23–26. https://doi.org/10.1130/G45429.1

Roverato, M., Larrea, P., Casado, I., Mulas, M., Béjar, G., & Bowman, L. (2018). Characterization of the Cubilche debris avalanche deposit, a controversial case from the northern Andes, Ecuador. Journal of Volcanology and Geothermal Research, 360, 22–35. https://doi.org/10.1016/j.jvolgeores.2018.07.006

Rowe, M. C., Nielsen, R. L., & Kent, A. J. R. (2006). Anomalously high Fe contents in rehomogenized olivine-hosted melt inclusions from oxidized magmas. American Mineralogist, 91(1), 82–91. https://doi.org/10.2138/am.2006.1818

Ryerson, F. J., & Watson, E. B. (1987). Rutile saturation in magmas: implications for Ti-Nb-Ta depletion in island-arc basalts. Earth and Planetary Science Letters, 86(2), 225–239. https://doi.org/10.1016/0012-821X(87)90223-8

S

Sallarès, V., & Charvis, P. (2003). Crustal thickness constraints on the geodynamic evolution of the Galapagos volcanic province. Earth and Planetary Science Letters, 214(3–4), 545–559. https://doi.org/10.1016/S0012-821X(03)00373-X

Samaniego, P., Martin, H., Robin, C., & Monzier, M. (2002). Transition from calc-alkalic to adakitic magmatism at Cayambe volcano, Ecuador: Insights into slab melts and mantle wedge interactions. Geology, 30(11), 967–970.

Samaniego, P., Martin, H., Monzier, M., Robin, C., Fornari, M., Eissen, J.-P., & Cotten, J. (2005). Temporal evolution of magmatism in the northern volcanic zone of the Andes: the geology and petrology of Cayambe Volcanic Complex (Ecuador). Journal of Petrology, 46(11), 2225–2252. https://doi.org/10.1093/petrology/egi053

Samaniego, P., Robin, C., Chazot, G., Bourdon, E., & Cotten, J. (2010). Evolving metasomatic agent in the Northern Andean subduction zone, deduced from magma composition of the long-lived Pichincha volcanic complex (Ecuador). Contributions to Mineralogy and Petrology, 160(2), 239–260. https://doi.org/10.1007/s00410-009-0475-5

Samaniego, P., Barba, D., Robin, C., Fornari, M., & Bernard, B. (2012). Eruptive history of Chimborazo volcano (Ecuador): A large, ice-capped and hazardous compound volcano in the Northern Andes. Journal of Volcanology and Geothermal Research, 221–222, 33–51. https://doi.org/10.1016/j.jvolgeores.2012.01.014

Scaillet, B., & Pichavant, M. (2005). A model of sulphur solubility for hydrous mafic melts: application to the determination of magmatic fluid compositions of Italian volcanoes. Annals of Geophysics, 48(4–5). https://doi.org/10.4401/ag-3226

Schiano, P. (2003). Primitive mantle magmas recorded as silicate melt inclusions in igneous minerals. Earth-Science Reviews, 63(1–2), 121–144. https://doi.org/10.1016/S0012-8252(03)00034-5

Schiano, P., Eiler, J. M., Hutcheon, I. D., & Stolper, E. M. (2000). Primitive CaO-rich, silica-undersaturated melts in island arcs: Evidence for the involvement of clinopyroxene-rich lithologies in the petrogenesis of arc magmas. Geochemistry, Geophysics, Geosystems, 1(5), n/a-n/a. https://doi.org/10.1029/1999GC000032

Schiano, P., Clocchiatti, R., Ottolini, L., & Sbrana, A. (2004). The relationship between potassic, calc-alkaline and Na-alkaline magmatism in South Italy volcanoes: A melt inclusion approach. Earth and Planetary Science Letters, 220(1), 121–137. https://doi.org/10.1016/S0012-821X(04)00048-2

Schiano, P., Monzier, M., Eissen, J.-P., Martin, H., & Koga, K. T. (2010). Simple mixing as the major control of the evolution of volcanic suites in the Ecuadorian Andes. Contributions to Mineralogy and Petrology, 160(2), 297–312. https://doi.org/10.1007/s00410-009-0478-2

Schiavi, F., Bolfan-Casanova, N., Buso, R., Laumonier, M., Laporte, D., Medjoubi, K., et al. (2020). Quantifying magmatic volatiles by Raman microtomography of glass inclusion-hosted bubbles. Geochemical Perspectives Letters, 16, 17–24. https://doi.org/10.7185/geochemlet.2038

Schmidt, M. W., & Jagoutz, O. (2017). The global systematics of primitive arc melts. Geochemistry, Geophysics, Geosystems, 18(8), 2817–2854. https://doi.org/10.1002/2016GC006699

Schmidt, M. W., & Poli, S. (1998). Experimentally based water budgets for dehydrating slabs and consequences for arc magma generation. Earth and Planetary Science Letters, 163(1–4), 361–379. https://doi.org/10.1016/S0012-821X(98)00142-3

Schmidt, M. W., & Poli, S. (2014). Devolatilization During Subduction. In Treatise on Geochemistry (pp. 669–701). Elsevier. Retrieved from http://linkinghub.elsevier.com/retrieve/pii/B9780080959757003211

Schmidt, M. W., Vielzeuf, D., & Auzanneau, E. (2004). Melting and dissolution of subducting crust at high pressures: the key role of white mica. Earth and Planetary Science Letters, 228(1–2), 65–84. https://doi.org/10.1016/j.epsl.2004.09.020

Sen, C., & Dunn, T. (1994). Dehydration melting of a basaltic composition amphibolite at 1.5 and 2.0 GPa: implications for the origin of adakites. Contributions to Mineralogy and Petrology, 117(4), 394–409. https://doi.org/10.1007/BF00307273

Shaw, A. M., Hauri, E. H., Fischer, T. P., Hilton, D. R., & Kelley, K. A. (2008). Hydrogen isotopes in Mariana arc melt inclusions: Implications for subduction dehydration and the deep-Earth water cycle. Earth and Planetary Science Letters, 275(1–2), 138–145. https://doi.org/10.1016/j.epsl.2008.08.015

Shaw, A. M., Behn, M. D., Humphris, S. E., Sohn, R. A., & Gregg, P. M. (2010). Deep pooling of low degree melts and volatile fluxes at the 85°E segment of the Gakkel Ridge: Evidence from olivine-hosted melt inclusions and glasses. Earth and Planetary Science Letters, 289(3–4), 311–322. https://doi.org/10.1016/j.epsl.2009.11.018

Shaw, D. M. (1970). Trace element fractionation during anatexis. Geochimica et Cosmochimica Acta, 34(2), 237–243. https://doi.org/10.1016/0016-7037(70)90009-8

Shimizu, N., & Hart, S. R. (1982). Applications of the Ion Microprobe to Geochemistry and Cosmochemistry. Annual Review of Earth and Planetary Sciences, 10(1), 483–526. https://doi.org/10.1146/annurev.ea.10.050182.002411

Shishkina, T. A., Botcharnikov, R. E., Holtz, F., Almeev, R. R., & Portnyagin, M. V. (2010). Solubility of H2O- and CO2-bearing fluids in tholeiitic basalts at pressures up

to 500MPa. Chemical Geology, 277(1–2), 115–125. https://doi.org/10.1016/j.chemgeo.2010.07.014

Sisson, T. W., & Grove, T. L. (1993). Experimental investigations of the role of H2O in calc-alkaline differentiation and subduction zone magmatism. Contributions to Mineralogy and Petrology, 113(2), 143–166. https://doi.org/10.1007/BF00283225

Skora, S., & Blundy, J. (2010). High-pressure Hydrous Phase Relations of Radiolarian Clay and Implications for the Involvement of Subducted Sediment in Arc Magmatism. Journal of Petrology, 51(11), 33.

Smith, D. J. (2014). Clinopyroxene precursors to amphibole sponge in arc crust. Nature Communications, 5. https://doi.org/10.1038/ncomms5329

Smith, H. J., Leeman, W. P., Davidson, J., & Spivack, A. J. (1997). The B isotopic composition of arc lavas from Martinique, Lesser Antilles. Earth and Planetary Science Letters, 146(1), 303–314. https://doi.org/10.1016/S0012-821X(96)00209-9

Sobolev, A. V. (1996). Melt inclusions in minerals as a source of principle petrological information. Petrology, 4(3), 209-220.

Sobolev, A. V., Dmitriev, L. V., Barsukov, V. L., Nevsorov, V. N., & Slutskii, A. B. (1980). The formation conditions of the high-magnesium olivines from the monomineralic fraction of Luna 24 regolith. In Lunar and Planetary Science Conference Proceedings (Vol. 11, pp. 105–116).

Sobolev, A. V., Hofmann, A. W., Sobolev, S. V., & Nikogosian, I. K. (2005). An olivine-free mantle source of Hawaiian shield basalts. Nature, 434(7033), 590–597. https://doi.org/10.1038/nature03411

Sobolev, A. V., Hofmann, A. W., Kuzmin, D. V., Yaxley, G. M., Arndt, N. T., Chung, S.-L., et al. (2007). The amount of recycled crust in sources of mantle-derived melts. Science, 316(5823), 412–417.

Sorbadere, F., Schiano, P., Métrich, N., & Garaebiti, E. (2011). Insights into the origin of primitive silica-undersaturated arc magmas of Aoba volcano (Vanuatu arc). Contributions to Mineralogy and Petrology, 162(5), 995–1009. https://doi.org/10.1007/s00410-011-0636-1

Sorbadere, F., Schiano, P., & Metrich, N. (2013a). Constraints on the origin of nepheline-normative primitive magmas in island arcs Inferred from olivine-hosted melt inclusion compositions. Journal of Petrology, 54(2), 215–233. https://doi.org/10.1093/petrology/egs063

Sorbadere, F., Schiano, P., Métrich, N., & Bertagnini, A. (2013b). Small-scale coexistence of island-arc- and enriched-MORB-type basalts in the central Vanuatu arc. Contributions to Mineralogy and Petrology, 166(5), 1305–1321. https://doi.org/10.1007/s00410-013-0928-8

Sorbadere, F., Médard, E., Laporte, D., & Schiano, P. (2013c). Experimental melting of hydrous peridotite–pyroxenite mixed sources: Constraints on the genesis of silica-undersaturated magmas beneath volcanic arcs. Earth and Planetary Science Letters, 384, 42–56. https://doi.org/10.1016/j.epsl.2013.09.026

Spandler, C., & Pirard, C. (2013). Element recycling from subducting slabs to arc crust: A review. Lithos, 170–171, 208–223. https://doi.org/10.1016/j.lithos.2013.02.016

Spilliaert, N., Metrich, N., & Allard, P. (2006). S–Cl–F degassing pattern of water-rich alkali basalt: Modelling and relationship with eruption styles on Mount Etna volcano. Earth and Planetary Science Letters, 248(3–4), 772–786. https://doi.org/10.1016/j.epsl.2006.06.031

Steele-Macinnis, M., Esposito, R., & Bodnar, R. J. (2011). Thermodynamic model for the effect of post-entrapment crystallization on the H2O–CO2 systematics of vapor-saturated, silicate melt inclusions. Journal of Petrology, 52(12), 2461–2482. https://doi.org/10.1093/petrology/egr052

Stern, C. R. (1990). Comment on "A geochemical traverse across the North Chilean Andes: Evidence for crust generation from the mantle wedge" by G. Rogers and C.J. Hawkesworth. Earth and Planetary Science Letters, 101(1), 129–133. https://doi.org/10.1016/0012-821X(90)90134-J

Stern, C. R. (1991). Comment on "Crustal contributions to arc magmatism in the Andes of Central Chile" by W. Hildreth and S. Moorbath. Contributions to Mineralogy and Petrology, 108(1), 241–246. https://doi.org/10.1007/BF00307341

Stolper, E., & Newman, S. (1994). The role of water in the petrogenesis of Mariana trough magmas. Earth and Planetary Science Letters, 121(3–4), 293–325. https://doi.org/10.1016/0012-821X(94)90074-4

Straub, S. M., & Layne, G. D. (2003). Decoupling of fluids and fluid-mobile elements during shallow subduction: Evidence from halogen-rich andesite melt inclusions from the Izu arc volcanic front: DECOUPLING OF FLUIDS AND FLUID-MOBILE ELEMENTS. Geochemistry, Geophysics, Geosystems, 4(7). https://doi.org/10.1029/2002GC000349

Straub, S. M., Layne, G. D., Schmidt, A., & Langmuir, C. H. (2004). Volcanic glasses at the Izu arc volcanic front: New perspectives on fluid and sediment melt recycling in subduction zones. Geochemistry, Geophysics, Geosystems, 5(1). https://doi.org/10.1029/2002GC000408

Straub, S. M., LaGatta, A. B., Martin-Del Pozzo, A. L., & Langmuir, C. H. (2008). Evidence from high-Ni olivines for a hybridized peridotite/pyroxenite source for orogenic andesites from the central Mexican Volcanic Belt: ANDESITE PETROGENESIS IN CENTRAL MVB. Geochemistry, Geophysics, Geosystems, 9(3), n/a-n/a. https://doi.org/10.1029/2007GC001583

Straub, S. M., Gomez-Tuena, A., Stuart, F. M., Zellmer, G. F., Espinasa-Perena, R., Cai, Y., & Iizuka, Y. (2011). Formation of hybrid arc andesites beneath thick continental crust. Earth and Planetary Science Letters, 303(3–4), 337–347. https://doi.org/10.1016/j.epsl.2011.01.013

Straub, S. M., Gómez-Tuena, A., Zellmer, G. F., Espinasa-Perena, R., Stuart, F. M., Cai, Y., et al. (2013). The processes of melt differentiation in arc volcanic rocks: insights from OIB-type arc magmas in the central Mexican volcanic belt. Journal of Petrology, 54(4), 665–701. https://doi.org/10.1093/petrology/egs081

Streck, M. J. (2008). Mineral textures and zoning as evidence for open system processes. Reviews in Mineralogy and Geochemistry, 69(1), 595–622. https://doi.org/10.2138/rmg.2008.69.15

Sun, S. S., & McDonough, W. S. (1989). Chemical and isotopic systematics of oceanic basalts: implications for mantle composition and processes. Geological Society, London, Special Publications, 42(1), 313–345. https://doi.org/10.1144/GSL.SP.1989.042.01.19

Syracuse, E. M., van Keken, P. E., & Abers, G. A. (2010). The global range of subduction zone thermal models. Physics of the Earth and Planetary Interiors, 183(1–2), 73–90. https://doi.org/10.1016/j.pepi.2010.02.004

T

Tatsumi, Y. (1986). Formation of the volcanic front in subduction zones. Geophysical Research Letters, 13(8), 717–720. https://doi.org/10.1029/GL013i008p00717

Tatsumi, Y. (1989). Migration of fluid phases and genesis of basalt magmas in subduction zones. Journal of Geophysical Research: Solid Earth, 94(B4), 4697–4707. https://doi.org/10.1029/JB094iB04p04697

Tavera, H., & Buforn, E. (2001). Source mechanism of earthquakes in Peru. Journal of Seismology, 5(4), 519–540. https://doi.org/10.1023/A:1012027430555

Thornber, C. R., Sherrod, D. R., Siems, D. F., Heliker, C. C., Meeker, G. P., Oscarson, R. L., & Kauahikaua, J. P. (2002). Whole-rock and glass major-element geochemistry of Kilauea Volcano, Hawaii, near-vent eruptive products: September 1994 through September 2001 (Open-File Report No. 02–17). U.S. Geological Survey.

Toplis, M. J. (2005). The thermodynamics of iron and magnesium partitioning between olivine and liquid: criteria for assessing and predicting equilibrium in natural and experimental systems. Contributions to Mineralogy and Petrology, 149(1), 22–39. https://doi.org/10.1007/s00410-004-0629-4

Trenkamp, R., Kellogg, J. N., Freymueller, J. T., & Mora, H. P. (2002). Wide plate margin deformation, southern Central America and northwestern South America, CASA GPS observations. Journal of South American Earth Sciences, 15(2), 157–171. https://doi.org/10.1016/S0895-9811(02)00018-4

Tucker, J. M., Hauri, E. H., Pietruszka, A. J., Garcia, M. O., Marske, J. P., & Trusdell, F. A. (2019). A high carbon content of the Hawaiian mantle from olivine-hosted melt inclusions. Geochimica et Cosmochimica Acta, 254, 156–172. https://doi.org/10.1016/j.gca.2019.04.001

Turner, S., Caulfield, J., Turner, M., van Keken, P., Maury, R., Sandiford, M., & Prouteau, G. (2012). Recent contribution of sediments and fluids to the mantle's volatile budget. Nature Geoscience, 5(1), 50–54. https://doi.org/10.1038/ngeo1325

U

Ulmer, P. (2001). Partial melting in the mantle wedge — the role of H2O in the genesis of mantle-derived 'arc-related' magmas. Physics of the Earth and Planetary Interiors, 127(1), 215–232. https://doi.org/10.1016/S0031-9201(01)00229-1

Ulmer, P., Kaegi, R., & Müntener, O. (2018). Experimentally Derived Intermediate to Silica-rich Arc Magmas by Fractional and Equilibrium Crystallization at 1•0 GPa: an Evaluation of Phase Relationships, Compositions, Liquid Lines of Descent and Oxygen Fugacity. Journal of Petrology, 59(1), 11–58. https://doi.org/10.1093/petrology/egy017

V

Vaca, S., Vallée, M., Nocquet, J.-M., & Alvarado, A. (2019). Active deformation in Ecuador enlightened by a new waveform-based catalog of earthquake focal mechanisms. Journal of South American Earth Sciences, 93, 449–461. https://doi.org/10.1016/j.jsames.2019.05.017

Vaggelli, G., De Vivo, B., & Trigila, R. (1993). Silicate-melt inclusions in recent Vesuvius lavas (1631–1944): II. Analytical chemistry. Journal of Volcanology and Geothermal Research, 58(1), 367–376. https://doi.org/10.1016/0377-0273(93)90118-B

Vallejo, C., Winkler, W., Spikings, R. A., Luzieux, L., Heller, F., & Bussy, F. (2009). Mode and timing of terrane accretion in the forearc of the Andes in Ecuador. Geological Society of America Memoirs, 204(0), 197–216. https://doi.org/10.1130/2009.1204(09)

Van Soest, M. C., Hilton, D. R., Macpherson, C. G., & Mattey, D. P. (2002). Resolving sediment subduction and crustal contamination in the Lesser Antilles island arc: a combined He–O–Sr isotope approach. Journal of Petrology, 43(1), 143–170. https://doi.org/10.1093/petrology/43.1.143

Vargas, C. A., & Mann, P. (2013). Tearing and breaking off of subducted slabs as the result of collision of the Panama Arc-indenter with northwestern South America. Bulletin of the Seismological Society of America, 103(3), 2025–2046. https://doi.org/10.1785/0120120328

Venugopal, S., Schiavi, F., Moune, S., Bolfan-Casanova, N., Druitt, T., & Williams-Jones, G. (2020). Melt inclusion vapour bubbles: the hidden reservoir for major and volatile elements. Scientific Reports, 10(1), 9034. https://doi.org/10.1038/s41598-020-65226-3

Vielzeuf, D., & Schmidt, M. W. (2001). Melting relations in hydrous systems revisited: application to metapelites, metagreywackes and metabasalts. Contributions to Mineralogy and Petrology, 141, 17.

Vigouroux, N., Wallace, P. J., & Kent, A. J. R. (2008). Volatiles in high-K magmas from the Western Trans-Mexican Volcanic Belt: evidence for fluid fluxing and extreme enrichment of the mantle wedge by subduction processes. Journal of Petrology, 49(9), 1589–1618. https://doi.org/10.1093/petrology/egn039

W

Wada, I., He, J., Hasegawa, A., & Nakajima, J. (2015). Mantle wedge flow pattern and thermal structure in Northeast Japan: Effects of oblique subduction and 3-D slab geometry. Earth and Planetary Science Letters, 426, 76–88. https://doi.org/10.1016/j.epsl.2015.06.021

Wallace, P. J. (2005). Volatiles in subduction zone magmas: concentrations and fluxes based on melt inclusion and volcanic gas data. Journal of Volcanology and Geothermal Research, 140(1–3), 217–240. https://doi.org/10.1016/j.jvolgeores.2004.07.023

Wallace, P. J., & Carmichael, I. S. E. (1992). Sulfur in basaltic magmas. Geochimica et Cosmochimica Acta, 56(5), 1863–1874. https://doi.org/10.1016/0016-7037(92)90316-B

Wallace, P. J., Kamenetsky, V. S., & Cervantes, P. (2015). Melt inclusion CO2 contents, pressures of olivine crystallization, and the problem of shrinkage bubbles. American Mineralogist, 100(4), 787–794. https://doi.org/10.2138/am-2015-5029

Walowski, K. J., Wallace, P. J., Hauri, E. H., Wada, I., & Clynne, M. A. (2015). Slab melting beneath the Cascade Arc driven by dehydration of altered oceanic peridotite. Nature Geoscience, 8(5), 404–408. https://doi.org/10.1038/ngeo2417

Walowski, K. J., Wallace, P. J., Clynne, M. A., Rasmussen, D. J., & Weis, D. (2016). Slab melting and magma formation beneath the southern Cascade arc. Earth and Planetary Science Letters, 446, 100–112. https://doi.org/10.1016/j.epsl.2016.03.044

Walter, M. J. (1998). Melting of garnet peridotite and the origin of komatiite and depleted lithosphere. Journal of Petrology, 39(1), 29–60.

Wanless, V. D., & Shaw, A. M. (2012). Lower crustal crystallization and melt evolution at mid-ocean ridges. Nature Geoscience, 5(9), 651–655. https://doi.org/10.1038/ngeo1552

Wasylenki, L. E., Baker, M. B., Kent, A. J. R., & Stolper, E. M. (2003). Near-solidus melting of the shallow upper mantle: partial melting experiments on depleted peridotite. Journal of Petrology, 44(7), 1163–1191. https://doi.org/10.1093/petrology/44.7.1163

Winkler, W., Villagómez, D., Spikings, R., Abegglen, P., Tobler, St., & Egüez, A. (2005). The Chota basin and its significance for the inception and tectonic setting of the inter-Andean depression in Ecuador. Journal of South American Earth Sciences, 19(1), 5–19. https://doi.org/10.1016/j.jsames.2004.06.006

Witham, F., Blundy, J., Kohn, S. C., Lesne, P., Dixon, J., Churakov, S. V., & Botcharnikov, R. (2012). SolEx: A model for mixed COHSCl-volatile solubilities and exsolved gas compositions in basalt. Computers & Geosciences, 45, 87–97. https://doi.org/10.1016/j.cageo.2011.09.021

Workman, R. K., & Hart, S. R. (2005). Major and trace element composition of the depleted MORB mantle (DMM). Earth and Planetary Science Letters, 231(1), 53–72.

Y

Yepes, H., Audin, L., Alvarado, A., Beauval, C., Aguilar, J., Font, Y., & Cotton, F. (2016). A new view for the geodynamics of Ecuador: implication in seismogenic sources definition and seismic hazard assessment. Tectonics. https://doi.org/10.1002/2015TC003941

Z

Zhang, Y. (1998). Mechanical and phase equilibria in inclusion–host systems. Earth and Planetary Science Letters, 157(3–4), 209–222. https://doi.org/10.1016/S0012-821X(98)00036-3

Annex A

Electronic Supplementary material of the paper published on *Contribution to Mineralogy and Petrology*

Constraining magma sources using primitive olivine-hosted melt inclusions from Puñalica and Sangay volcanoes (Ecuador)

Contributions to Mineralogy and Petrology

Diego F. Narvaez[1,2], Estelle F. Rose-Koga[1], Pablo Samaniego[1], Kenneth T. Koga[1], Silvana Hidalgo[3]

[1] Université Clermont Auvergne, CNRS, IRD, OPGC, Laboratoire Magmas et Volcans, F-63000 Clermont-Ferrand, France

[2] Departamento de Geología, Escuela Politécnica Nacional, Ladrón de Guevara E11-253, Quito, Ecuador

[3] Instituto Geofísico, Escuela Politécnica Nacional, Ladrón de Guevara E11-253, Aptdo. 2759, Quito, Ecuador

Corresponding author: Diego F. Narvaez (diego.narvaez@etu.uca.fr; ORCID ID: 0000-0003-1902-2472)

Sample selection, olivine preparation and heating experiments

The chosen rocks (CAR83A, CAR 96A, CAR 113B, RIO 17A from Puñalica and SAN20B from Sangay volcano) were crushed and the fraction 0.4-1.5 mm was separated. We picked about 500 olivine crystals under a binocular microscope. We used crystal-bound to attach crystals on glass slides in order to polish and select olivines in which melt inclusions were observed (about 100 olivines). We sorted about 50 crystals with melt inclusions bigger than 30 µm. All melt inclusions were crystallized and presented bubbles. Thus, we performed homogenization using Vernadsky-type microscope heating stage following Le Voyer et al., 2010.

Vernadsky-type microscope heating stage allows visual observation during the entire heating procedure. Heating experiments aim to reverse the post-entrapment processes that occurred inside the melt inclusions during cooling. After homogenization and upon quenching just a mixture of melt and gas is present in the melt inclusion (i.e. no more crystals). Vernadsky-type heating stage uses a 1 atm furnace gas-tight sealed, cooled by water. The experiment lasted less than 30 minutes and throughout an oxygen fugacity less than 10^{-10} atm was kept so that no oxidation of olivine occurs. This highly reduced conditions are maintained by the circulation inside the furnace of purified Helium. The latter is obtained by passing regular Helium gas on Zirconium at 700 °C. The high thermal conductivity of He improves the cooling rate at the moment of quenching. The homogenization temperatures determined for the melt inclusions in this study varied from 1143 to 1309 ± 3 °C. We measured the temperature inside the furnace using a Pt-Pt_{90}-Rh_{10} thermocouple welded to the sample holder and calibrated using Au (melting temperature equal to 1064 °C).

The increasing temperature rate was between 80 °C/min in the first stage until reach the Au fusion temperature, then 10-30 °C/min until the last crystal disappear. The bubble inside the melt inclusions remained after homogenization. The prevalence of bubbles likely reflects the dropping of the internal pressure inside the melt inclusion and changing of volume after entrapment. The internal pressure variation probably changes due to the H^+ diffusion through olivine host crystal (e.g. Bucholz et al., 2013; Chen et al., 2011). In order to avoid H^+ diffusion during homogenization we follow the procedure described by Chen et al.(2011). Once homogenizeed, the 50 olivine crystals were polished on silicon carbide paper to expose melt inclusions. Final polishing were done using ¼ µm alumina paste to get a smooth surface.

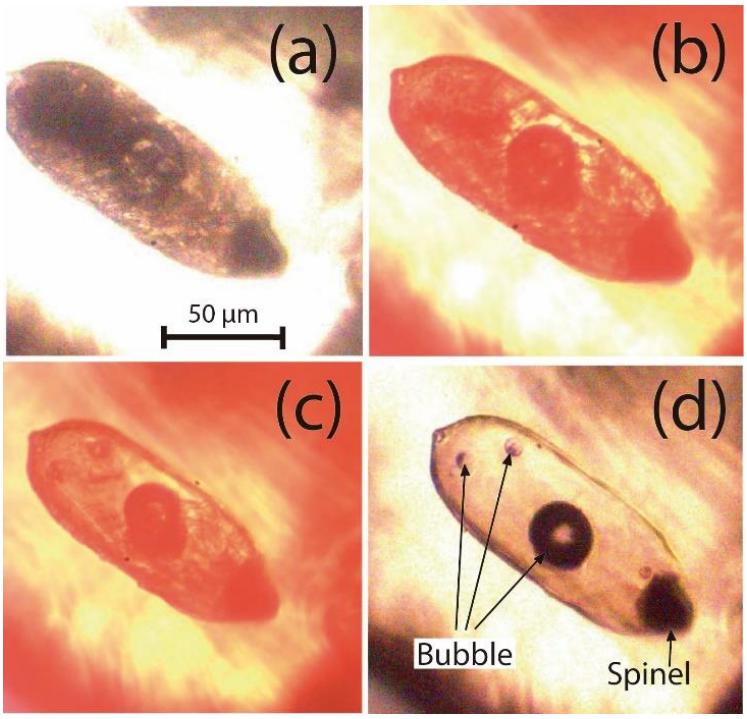

Fig. SM1. Photograph sequence taken under Vernadsky-type microscope during heating stage of melt inclusion #T belonging to RIO17A rock sample. T_H (temperature of homogenization) =1112 °C. **a)** Crystallized melt inclusion before heating. **b)** and **c)** show the homogenization process as observed under the microscope. We increase temperature until the last crystal disappears. **d)** Melt inclusion after homogenization. Some of the isolated bubbles coalesced. The spinel crystal did not melt because it is likely a pre-entrapment crystal.

Electron microprobe (EMP)

Major element compositions of olivine crystals and melt inclusions (50) were determined using a CAMECA SX100 electron microprobe at the Laboratoire Magmas et Volcans (Clermont-Ferrand). The standard analytical procedure is reported in details elsewhere (Le Voyer et al., 2008). In brief, olivine analysis were performed with a focused beam, a 15 kV accelerating voltage, a current of 15 nA and 10s counting time. Glasses were analyzed with a focused beam of 5-20 µm in diameter (depending in the

diameter of the inclusions), a low current (8 nA) for major elements, and 80 nA for Cl, S, and F. The counting time for major elements were 40 s for Fe; 30 s for Mn; 20 s for Ca, Ti, Al, K, Mg and 10 s for Na, Si. Relative analytical uncertainties obtained from replicate measurements on VG-A99 standard (Jarosewich et al., 1979) were less than 2% for SiO_2, MgO, and Al_2O_3; 3.5% for FeO and CaO; 5% for K_2O, TiO_2, and Na_2O; 10% for P_2O_5; and 30% for MnO. Relative standard deviation (1σ) of MI are less than 1% for SiO_2 and <2% for the other major elements except for Mn that display concentrations less than detection limit (0.2 wt. %). Cl and S were measured 4 times during 40 s/cycle and F for 3 times during 60s/cycle. The standard deviation (1σ) for Cl and S are less than 170 and 145 ppm, respectively.

Secondary Ion Mass Spectrometry (SIMS)

We measured volatile elements (H_2O, CO2, F, S, Cl) in the melt inclusions with the CAMECA HR1280 housed at Centre de Recherches Pétrographiques et Géochimiques (CRPG, Nancy). Olivine crystals were pressed in a high purity indium in a 1 inch aluminum mount which was then gold-coated. We use a classical SIMS settings (e.g. Hauri et al., 2002; Rose-Koga et al., 2014) summarized here after. We use a Cs^+ primary ion beam with a current of 1 nA, a 10 kV secondary accelerating voltage, a -80 V offset and a projected beam size of 20 µm. The instrument was operated with the contrast aperture at 400 µm, the energy aperture at 40 eV, the entrance slit at 52 µm and the exit slit at 173 µm, for a mass resolution power of 7007. After 3 min of pre-sputtering, we collected signals for ^{12}C (8 seconds), ^{17}O (3 seconds), $^{16}O^1H$ (6 seconds), ^{18}O (3 seconds), ^{19}F (4 seconds), ^{27}Al (3 seconds), ^{30}Si (3 seconds), ^{32}S (4 seconds) and ^{35}Cl (6 seconds) (counting times in parenthesis), with 2 seconds waiting time after each switch of the magnet. This cycle was repeated 10 times during one analysis. One measurement lasted 12 min per spot. The concentrations were determined using calibration curves obtained by measuring a set of natural basaltic glasses during the same session and under the same analytical conditions (KL2G, M40, KE12, M48, KL2Gest, Tlg, ML3BG, alv-2746, alv-2390; e.g. Helo et al., 2011) with a large range of concentrations of volatile elements overlapping most of our samples concentrations (H_2O, 0.05-3.07 wt.%; CO_2, 5.2-2182 ppm, F, 70-4200 ppm, S, 1.2-144 ppm and Cl, 7.5-3280 ppm). The maximum errors, taking into account the reproducibility over the 10 cycles of analyses and the errors on the regression of the calibration line, were less than 15% for CO_2, 3% for Cl, 4% for S, and 5% for F and H_2O. MI with low concentrations of H_2O (<0.3 wt. % H_2O) show H_2O errors less than 30%.

Because the photograph quality under SIMS is poor and the melt inclusions are small, the ion beam was sometimes misplaced inside melt inclusions and in some case touched the host crystal provoking a "dilution" of the concentration of the desired elements (Cl, F, etc.). We corrected this "dilution" considering the Al_2O_3 wt. % value obtained by EMP, since Al is not an element that is in the olivine composition. In addition, if Al given by SIMS showed a notably decrease (>15%) compared to EMP, data was discarded.

LA-ICP-MS analysis of trace elements

Trace elements were analyzed in 37 melt inclusions using a Laser Ablation Induced Coupled Plasma Mass Spectrometer (LA-ICP-MS) at the Laboratoire Magmas et Volcans (Clermont-Ferrand). Analysis were performed using a 193ArF excimer laser following classical procedures outlined in previous studies (Le Voyer et al., 2010; Rose-Koga et al., 2012. To summarize, we used a pulse energy of about 3 mJ, a spot diameter between 15 and 33 µm and a laser pulse frequency of 2-3Hz depending in the inclusion size ensuring a fluence at sample surface around 4 J/cm^{-2}. The background was measured for 40 seconds before ablation and analysis time was approximately 100s. Data reduction was performed by the GLITTER software (www.es.mq.edu.au/GEMOC). This technique uses CaO (measured by EMP) as an internal standard. Reproducibility and accuracy of the analysis were constrained by systematic analysis BCR2-G and 612 standard samples each 8 analysis. Typical errors on the samples (1σ error of mean, $1/\sqrt{n}$ where n is the number of cycles) is less than 10 % for all trace elements, except for Cr, Lu (<20%) and B (<40%).

Oxidation state of melt inclusions

We measured the S^{2-} and S^{6+} peak positions by EMP to estimate the speciation of sulfur in melt inclusions. The sulfur speciation is consider as a function of oxygen fugacity and was calculated by measuring the peak shift of the sulfur Kα radiation relative to a sulfide standard (Jugo et al., 2005). We used *f*O2, bulk composition of MI, temperature of homogenization to calculate the redox state of iron following the process explained in Wallace and Carmichael (1992). The used $Fe^{+3}/\sum Fe$ ratio for Puñalica and Sangay MI are shown in table ESM 1.

The Mg# of Puñalica and Sangay melt inclusions after post-entrapment crystallization correction is shown in Fig. SM2b. Fosterite contents of olivine crystals that contain the studied melt inclusions are shown in Fig. SM2a.

Table ESM 1. Sulfur speciation measured by EMP for each inclusion group. n: number of inclusion. $X(S^{6+})$: fraction of S^{6+} using peak positions in EMP. σ: standard deviation of $X(S^{6+})$ for the n inclusions. $Fe^{+3}/\sum Fe$: measured following process explained by Wallace and Carmichael, (1992).

Sample	n	$X(S^{6+})$	σ	$Fe^{+3}/\sum Fe$
CAR83A	4	0.09	0.11	0.16
CAR96A	12	0.29	0.15	0.2
CAR113B	12	0.49	0.13	0.23
RIO17A	14	0.37	0.16	0.23
SAN20B	8	0.46	0.13	0.28

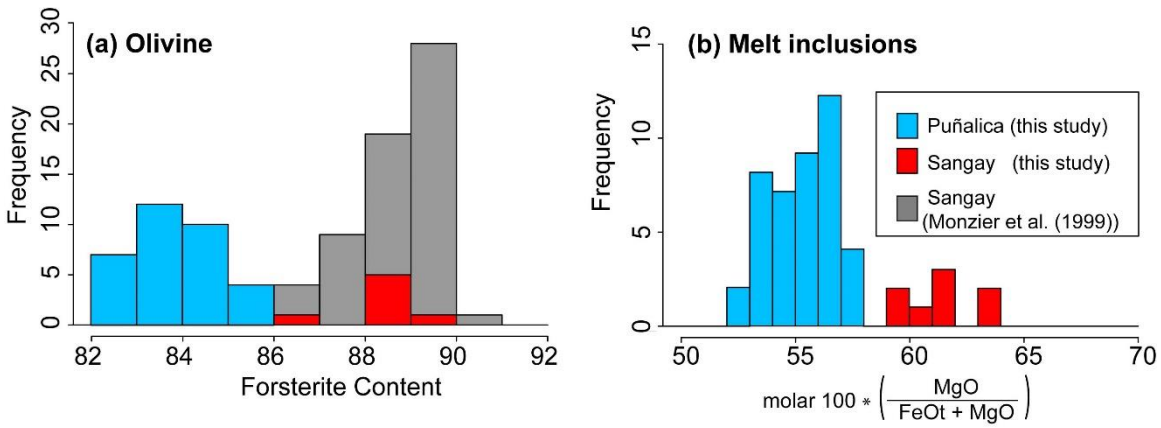

Fig. SM2 Frequency histogram of the forsterite content of the olivine phenocrysts (a) and of melt inclusions (b) from Puñalica and Sangay volcanoes. Diagram (a) shows data from this study and that of Monzier et al. (1999). Forsterite contents for melt inclusions are plotted using homogenization-corrected values and Fe2+/∑Fe obtained using sulfur speciation. We did not differentiate the Puñalica groups

References:

Bucholz, C.E., Gaetani, G.A., Behn, M.D., Shimizu, N., 2013. Post-entrapment modification of volatiles and oxygen fugacity in olivine-hosted melt inclusions. Earth Planet. Sci. Lett. 374: 145–155. doi:10.1016/j.epsl.2013.05.033

Chen, Y., Provost, A., Schiano, P., Cluzel, N., 2011. The rate of water loss from olivine-hosted melt inclusions. Contrib. Mineral. Petrol. 162: 625–636. doi:10.1007/s00410-011-0616-5

Hauri, E., Wang, J., Dixon, J. E., King, P. L., Mandeville, C., & Newman, S. (2002). SIMS analysis of volatiles in silicate glasses: 1. Calibration, matrix effects and comparisons with FTIR. Chem Geol, 183: 99-114. https://doi.org/10.1016/S0009-2541(01)00375-8

Helo, C., Longpré, M.-A., Shimizu, N., Clague, D.A., Stix, J., 2011. Explosive eruptions at mid-ocean ridges driven by CO2-rich magmas. Nat. Geosci. 4: 260–263. doi:10.1038/ngeo1104

Jarosewich, E., Parkes, A. S., & Wiggins, L. B. (1979). Microprobe analyses of four natural glasses and one mineral: an interlaboratory study of precision and accuracy. Smithson Contrib Earth, 22: 53–67

Jugo PJ, Luth RW, Richards JP (2005) Experimental data on the speciation of sulfur as a function of oxygen fugacity in basaltic melts. Geochim Cosmochim Acta 69:497–503

Le Voyer M, Rose-Koga EF, Shimizu N, Grove TL Schiano P (2010) Two contrasting H2O-rich components in primary melt inclusions from Mount Shasta. J. Petrol. 51: 1571–1595

Le Voyer M, Rose-Koga EF, Laubier M, Schiano P (2008) Petrogenesis of arc lavas from the Rucu Pichincha and Pan de Azucar volcanoes (Ecuadorian arc): Major, trace element, and boron isotope evidences from olivine-hosted melt inclusions. Geochem Geophys Geosyst 9:Q12027. https://doi:10.1029/2008GC002173

Monzier M, Robin C, Samaniego P, Hall ML, Cotten J, Mothes P, Arnaud N (1999) Sangay volcano, Ecuador: structural development, present activity and petrology. J Volcanol Geotherm Res 90:49–79

Rose-Koga EF, Koga KT, Hamada M, Hélouis T, Whitehouse MJ, Shimizu N (2014) Volatile (F and Cl) concentrations in Iwate olivine-hosted melt inclusions indicating low-temperature subduction. Earth Planets Space 66:1–12

Rose-Koga EF, Koga KT, Schiano P, Le Voyer M, Shimizu N, Whitehouse MJ, Clocchiatti R (2012) Mantle source heterogeneity for South Tyrrhenian magmas revealed by Pb isotopes and halogen contents of olivine-hosted melt inclusions. Chem Geol 334:266–279

Wallace, P., Carmichael, I.S.E., 1992. Sulfur in basaltic magmas. Geochim. Cosmochim. 56: 1863–1874. doi:10.1016/0016-7037(92)90316-B

Annex B

Supplementary material of the manuscript submitted to *Geochemistry, Geophysics, Geosystems*

Geochemistry, Geophysics, Geosystems

Supporting Information for

Two types of slab components under Ecuadorian volcanoes supported by primitive olivine-hosted melt inclusion study

D. F. Narváez[1,2,3], P. Samaniego[1], K. T. Koga[1], E. F. Rose-Koga[1], S. Hidalgo[3], G. Ratzov[4]

[1] Université Clermont Auvergne, CNRS, IRD, OPGC, Laboratoire Magmas et Volcans, F-63000 Clermont-Ferrand, France
[2] Departamento de Geología, Escuela Politécnica Nacional, Ladrón de Guevara E11-253, Quito, Ecuador
[3] Instituto Geofísico, Escuela Politécnica Nacional, Ladrón de Guevara E11-253, Aptdo. 2759, Quito, Ecuador
[4] Université Côte d'Azur, CNRS, IRD, Observatoire de la Côte d'Azur, Géoazur, 250 rue Albert Einstein, Sophia Antipolis 06560 Valbonne, France

Contents of this file

Text S1
Figures S1 to S6
Table S1to S3

Additional Supporting Information (Files uploaded separately)

Captions for Table S3

Introduction

Text S1 is an extended description of CO_2 correction calculation for bubble presence.

Figures S4 to S6 are figures that we consider are not as important as those selected for the manuscript. Table S3 is data compilation of Ecuadorian melt inclusions hosted in primitive olivines.

Text S1.

Further details about bubbles correction in experimentally-heated melt inclusions

The main goal of the heating experiments was to melt the minerals inside the melt inclusions to obtain a homogeneous melt phase (glass after rapid quench). These minerals

were formed after the entrapment of melt in a host crystal, and the procedure was to recover the melt composition close to the time of entrapment. Heating was stopped as soon as the inclusion dissolved secondary minerals and became transparent liquid state, which was confirmed by free movements of the bubble inside the inclusion. From the experience homogenizing different melt inclusions, we were aware that it is sometimes possible to dissolve bubbles completely back into the inclusion. Dissolving the bubble into the melt would have had required to run the experiments for longer time and usually at higher temperature than the procedure applied here. Such heating process would have resulted in the loss of water (i.e. hydrogen) in melt inclusion, and dissolution of olivine from the walls to the melt inclusion (Danyushevsky et al. 2000). Clearly, melt inclusion composition would be further away from what we suppose as the composition at the time of entrapment.

During the heating experiment, we had visual observation of the changes occurring inside the melt inclusions. We took photos during the experiments (Fig. S1) when the melt inclusions were ideally distinguished under the microscope. In general, one or more bubbles were present inside the melt inclusions at the beginning of the experiments and they often merged/coalesced and a bubble remained after quenching. We consider those bubbles to be a "gas bubble" formed by volatile components (i.e. H_2O, CO_2) exsolved from the melt phase when pressure inside the melt inclusions decrease due to H^+ diffusion out of the inclusion (Bucholz et al., 2013) or olivine inelastic relaxation decreasing internal pressure of the inclusion.

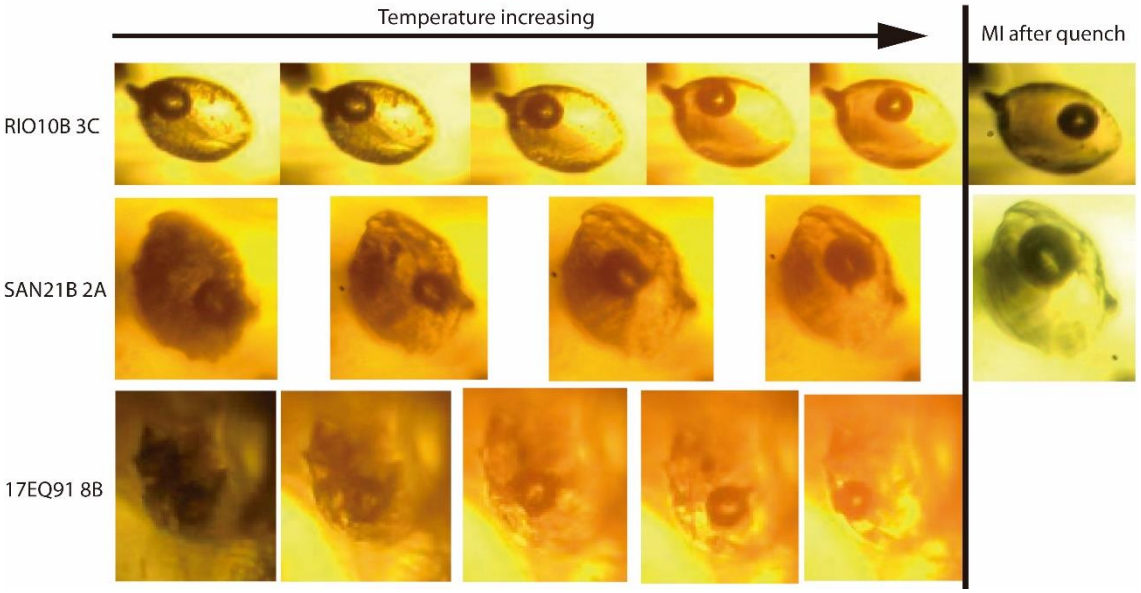

Figure S1. Microscope image sequence taken during heating experiment of RIO10B 3, SAN21B 2A and 17EQ91 8B melt inclusions. To the left are crystalized melt inclusions that became a homogeneous melt after increasing the temperature of the experiment. Melt inclusions were kept at the highest temperature for 5 min before quenching. Photos taken after quenching are shown in the extreme right.

The volume increase of the bubble observed during quenching would result in an overestimation of calculated CO_2 in the melt because bubble parameters given in Table S1 were calculated at high temperature when the volume of the bubbles were smaller. We used the images obtained during the heating experiment (the bubble size at the last heating step compare to the bubble size after the quench) to assess the volume increase of the bubble during the quench. We analyze 15 image sequences which do not necessary correspond to those for which we calculated the entrapment pressure. However, this

analysis gave us a range of the volume change experimented by Ecuadorian MI during quenching. Bubbles increased their volumes up to 29% with a median value of 12% (Table S2). Therefore, the values (i.e. CO_2 concentrations and corresponding saturation pressure) obtained by bubble correction must be considered overestimated because the bubble where in general 12% smaller at the highest temperature before quenching. The effect in the calculated pressure of the bubble correction is opposite to H^+ loss during natural cooling, but H^+ loss effect on pressure is less important than overestimation of bubble volume.

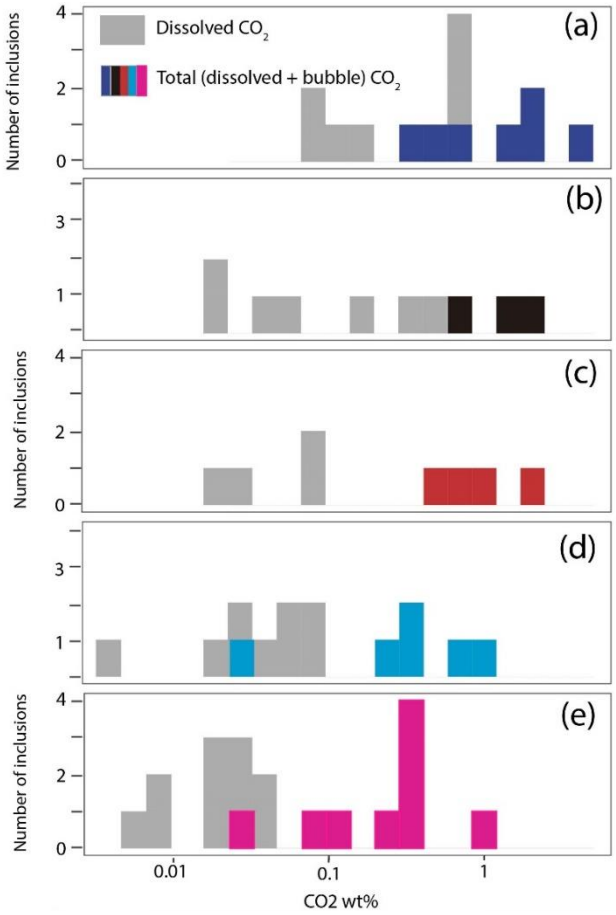

Figure S2 (a-e) Histograms of dissolved (grey) and total (dissolved + bubble, colored) CO_2 concentrations in olivine hosted melt inclusions from Ecuadorian volcanoes.

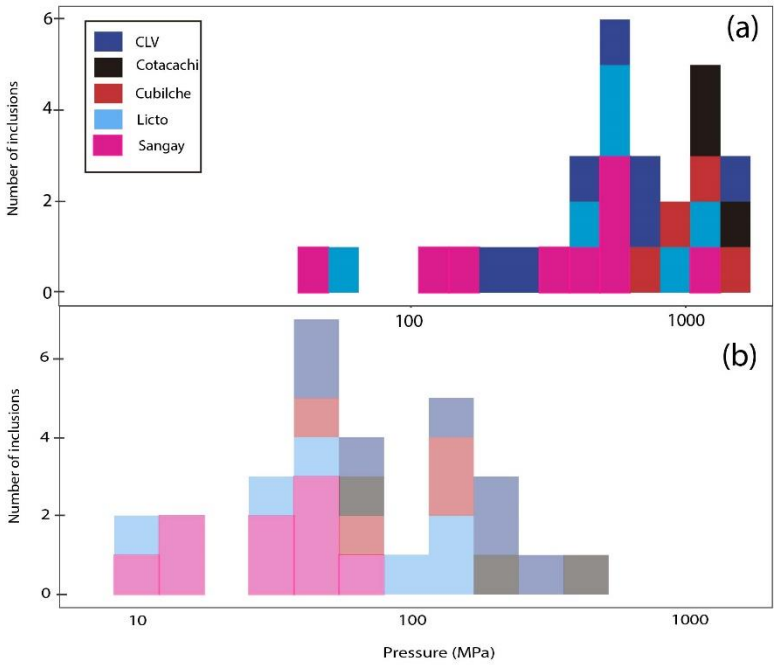

Figure S3 (a) Histogram of pressure (log scale) obtained with total CO_2 (dissolve + bubble). **(b)** Histogram of pressure obtained before bubble correction.

Table S1 CO_2 and H_2O correction calculation for bubble presence

		Melt inclusion (MI)				Bubble (B)		Bubble/MI volume	Fluid properties in equilibrium with melt			
	Code number	a (µm)	b (µm)	c=(a+b)/2 (µm)	Volume (µm^3)	Diameter (µm)	Volume (µm^3)		H_2O wt%	CO_2 wt%	Density (g.cm^{-3})	Mass (g)
1	17EQ81 1B	56	42	49	60344	19	3591	6.0%	0.52	99.48	0.180	0.01072
2	17EQ81 1E	62	38	50	61680	20	4189	6.8%	0.20	99.80	0.361	0.02453
3	17EQ81 2A_b	53	35	44	42736	22	5575	13.0%	0.36	99.64	0.361	0.04711
4	17EQ91 2B	50	29	39.5	29989	17	2572	8.6%	0.02	99.98	0.5	0.03945
5	17EQ95 2A	75	51	63	126175	30	14137	11.2%	1.27	98.73	0.1205	0.01350
6	CAY45A 2B	36	16	26	7841	10	524	6.7%	0.24	99.76	0.482	0.03218
7	CAY45A 3B	37	25	31	15014	14	1437	9.6%	0.19	99.81	0.4345	0.04158
8	CAY45B 5A	190	50	120	596904	103	572152	11.0%	3.72	96.28	0.1449	0.13889
9	CAY45C 1A	126	65	95.5	409531	52	73622	18.0%	3.97	96.03	0.1454	0.02614
10	CAY45C 3A_3	80	61	70.5	180139	37	26522	14.7%	0.84	99.16	0.5956	0.08769
11	CAY45C 3C	102	34	68	123477	15	1767	1.4%	1.38	98.62	0.303	0.00434
12	CAY45C 5A_1	36	26	31	15193	10	524	3.4%	1.08	98.92	0.2163	0.00745
13	COTA02 2A_b	40	27	33.5	18944	15	1767	9.3%	0.03	99.97	0.1944	0.01813
14	MM1B 5B	55	44	49.5	62722	21	4849	7.7%	0.19	99.81	0.6525	0.05044
15	RIO10B 1A	62	48	55	85703	20	4189	4.9%	0.37	99.63	0.114	0.00557
16	RIO10B 1C	30	21	25.5	8412	9	382	4.5%	0.14	99.86	0.3408	0.01546
17	RIO10B 2A	66	55	60.5	114990	19	3591	3.1%	0.20	99.80	0.2693	0.00841
18	RIO10B 2D	25	25	25	8181	10	524	6.4%	0.08	99.92	0.3497	0.02238
19	RIO10B 3A_l	60	26	43	35123	11	697	2.0%	1.81	98.19	0.0302	0.00060
20	RIO10B 5B	49	31	40	31814	15	1767	5.6%	0.40	99.60	0.1449	0.00805
21	SAN21B 2B	64	51	57.5	98269	21	4849	4.9%	2.09	97.91	0.155	0.00765
22	SAN21B 2C	104	53	78.5	226558	29	12770	5.6%	1.30	98.70	0.1415	0.00798
23	SAN21B 3B	233	37	135	609384	31	15599	2.6%	6.35	93.65	0.0275	0.00070
24	SAN21B 3C	133	56	94.5	368529	31	15599	4.2%	1.25	98.75	0.1132	0.00479
25	SAN21B 4A	73	65	69	171429	26	9203	5.4%	1.03	98.97	0.1554	0.00834
26	SAN21B 4B	123	51	87	285755	29	12770	4.5%	1.92	98.08	0.2004	0.00896
27	SAN21B 5A	117	110	113.5	764846	40	33510	4.4%	4.57	95.43	0.0541	0.00237
28	SAN21B 5B_t	80	37	58.5	90667	35	22449	24.8%	3.18	96.82	0.0869	0.02152
29	SAN21B 6A	281	46	163.5	1106577	44	44602	4.0%	3.85	96.15	0.0495	0.00200

Table S1. continued

	Melt properties					Melt + bubble					P sat (Mpa) before correction	P sat (Mpa) corrected for bubble
	Vol. Melt	H_2O wt%	CO_2 ppm	Density ($g.cm^{-3}$)	Mass (g)	Mass (g)	mass H_2O (g)	mass CO_2 (g)	**H_2O wt%**	**CO_2 wt%**		
17EQ81 1B	94.0%	0.20	298	2.588	2.434	2.445	0.0048	0.011	0.20	0.47	60	766
17EQ81 1E	93.2%	0.18	708	2.625	2.447	2.472	0.0046	0.026	0.18	1.06	143	1254
17EQ81 2A_b	87.0%	0.24	745	2.618	2.277	2.324	0.0057	0.049	0.25	2.09	142	1675
17EQ91 2B	91.4%	0.06	1465	2.7	2.458	2.497	0.0016	0.043	0.06	1.72	207	1257
17EQ95 2A	88.8%	0.25	212	2.6087	2.316	2.330	0.0059	0.014	0.26	0.59	38	822
CAY45A 2B	93.3%	0.25	4852	2.6385	2.462	2.495	0.0062	0.044	0.25	1.77	220	675
CAY45A 3B	90.4%	0.21	5907	2.6443	2.391	2.433	0.0052	0.056	0.21	2.29	188	677
CAY45B 5A	89.0%	0.51	859	2.5586	2.278	2.294	0.0121	0.017	0.53	0.75	51	381
CAY45C 1A	82.0%	0.52	775	2.5872	2.122	2.148	0.0120	0.027	0.56	1.25	50	594
CAY45C 3A_3	85.3%	0.52	6672	2.6795	2.285	2.373	0.0126	0.102	0.53	4.31	320	1502
CAY45C 3C	98.6%	0.45	1846	2.5962	2.559	2.563	0.0115	0.009	0.45	0.35	118	217
CAY45C 5A_1	96.6%	0.33	1160	2.591	2.502	2.509	0.0083	0.010	0.33	0.41	76	247
COTA02 2A_b	90.7%	0.05	352	2.6125	2.369	2.387	0.0011	0.019	0.05	0.79	65	1083
MM1B 5B	92.3%	0.25	3446	2.7012	2.492	2.543	0.0063	0.059	0.25	2.32	372	1384
RIO10B 1A	95.1%	0.13	188	2.5865	2.460	2.466	0.0033	0.006	0.13	0.24	35,5	448
RIO10B 1C	95.5%	0.14	790	2.6207	2.502	2.517	0.0035	0.017	0.14	0.69	129	839
RIO10B 2A	96.9%	0.15	592	2.6149	2.533	2.542	0.0037	0.010	0.15	0.39	97	592
RIO10B 2D	93.6%	0.11	784	2.6376	2.469	2.491	0.0027	0.024	0.11	0.98	134	1147
RIO10B 3A_l	98.0%	0.15	49	2.5907	2.539	2.540	0.0038	0.001	0.15	0.03	9	51
RIO10B 5B	94.4%	0.15	256	2.6012	2.457	2.465	0.0036	0.009	0.15	0.35	46	583
SAN21B 2B	95.1%	0.37	300	2.5982	2.470	2.478	0.0094	0.008	0.38	0.33	51	484
SAN21B 2C	94.4%	0.27	271	2.6147	2.467	2.475	0.0067	0.009	0.27	0.35	45	499
SAN21B 3B	97.4%	0.27	55	2.6087	2.542	2.543	0.0068	0.001	0.27	0.03	9	49
SAN21B 3C	95.8%	0.24	209	2.5989	2.489	2.494	0.0059	0.005	0.24	0.21	35	332
SAN21B 4A	94.6%	0.25	311	2.6226	2.482	2.490	0.0062	0.009	0.25	0.36	50	501
SAN21B 4B	95.5%	0.41	430	2.5877	2.472	2.481	0.0104	0.010	0.42	0.40	68	520
SAN21B 5A	95.6%	0.33	99	2.5707	2.458	2.460	0.0081	0.003	0.33	0.10	17	160
SAN21B 5B_t	75.2%	0.35	159	2.5658	1.930	1.952	0.0074	0.021	0.38	1.08	27	1166
SAN21B 6A	96.0%	0.28	105	2.614	2.509	2.511	0.0070	0.002	0.28	0.09	16	124

Table S2. Calculation of bubble expansion during experimental quenching

	From photos taken during heating			From photos taken after heating			Bubble diameter increase	Volume increase
	Long axis (pixels)	Bubble diameter (pixels)	Bubble diameter / long axis	Long axis (µm)	Bubble diameter (µm)	Bubble diameter / long axis		
17EQ81_1B	58.7	15.4	0.26	55.76	19.5	0.35	8.7%	28.6%
17EQ81_1C	45.5	18.3	0.40	51.66	19.8	0.38	-1.9%	-5.6%
17EQ81_5A	60.4	21.6	0.36	52.08	20.85	0.40	4.3%	13.4%
17EQ91_1C	50.7	17	0.34	38.55	13.19	0.34	0.7%	2.1%
CAY45B_6A	74.5	17.4	0.23	39.08	12.2	0.31	7.9%	25.5%
RIO10B_2_bis	93.9	23.3	0.25	*94.9*	*23.5*	0.25	-0.1%	-0.2%
RIO10B_2B	87.5	19.6	0.22	118.55	32.28	0.27	4.8%	15.2%
RIO10B_3A_c	32.2	10.2	0.32	*53.4*	*19*	0.36	3.9%	12.2%
RIO10B_3A_r	73.7	12.8	0.17	*106.2*	*22.4*	0.21	3.7%	11.6%
RIO10B_3C	76	21.4	0.28	58.64	19.42	0.33	5.0%	15.6%
RIO10B_6C	73.14	19.5	0.27	85.5	25.3	0.30	2.9%	9.0%
SAN21_2A	102	35.4	0.35	*120.5*	*43.8*	0.36	1.6%	5.0%
SAN21_2C	92.3	21.5	0.23	103.4	28.7	0.28	4.5%	14.0%
SAN21_3C	115.7	21.8	0.19	133.2	30.7	0.23	4.2%	13.2%
SAN21_4B	135.6	29.6	0.22	123.4	28.6	0.23	1.3%	4.1%

Note. Italic values are given in pixel units

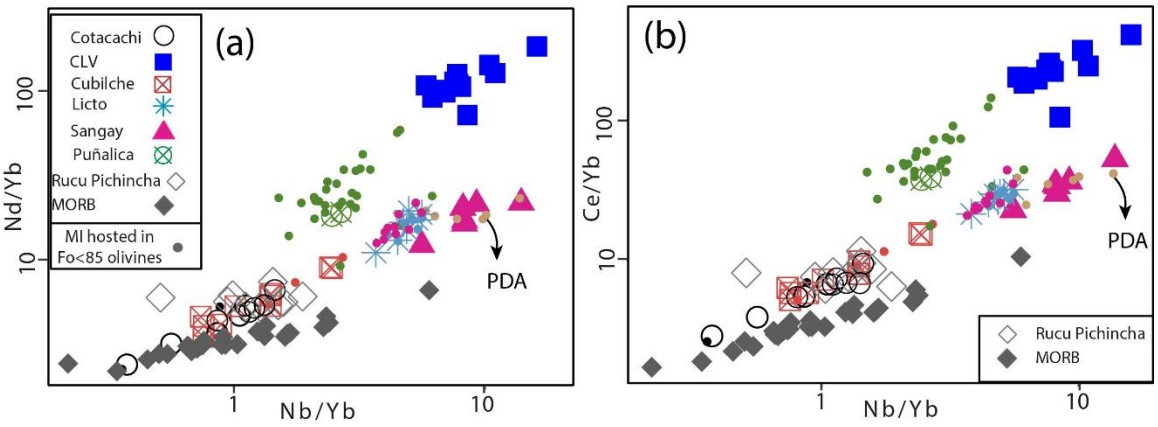

Figure S4 (a-d) Nb/Yb *vs.* (Nd, Ce),/Yb of Ecuadorian MI compared to MORB-OIB compositions used to discriminate between conservative and non-conservative elements (Pearce et al., 2008). MORB compositions from Leroux et al. (2006).

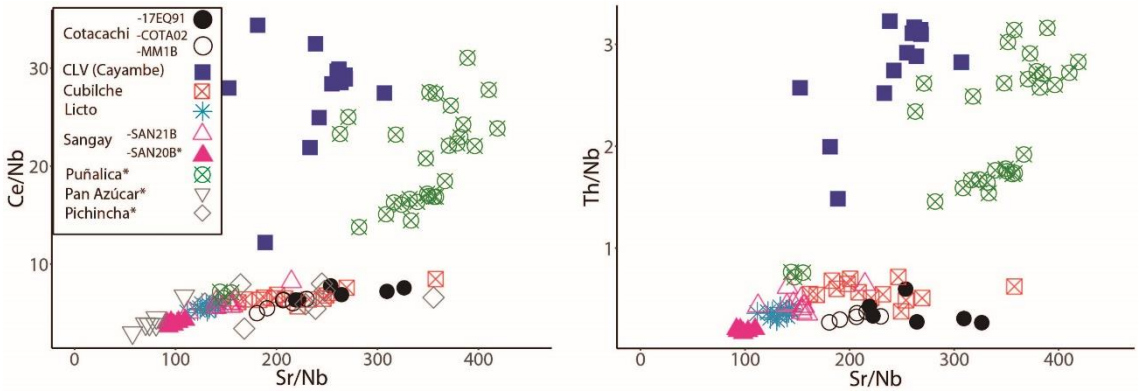

Figure S5. Sr/Nb vs. (Ce, Th)/ Nb of Ecuadorian MI

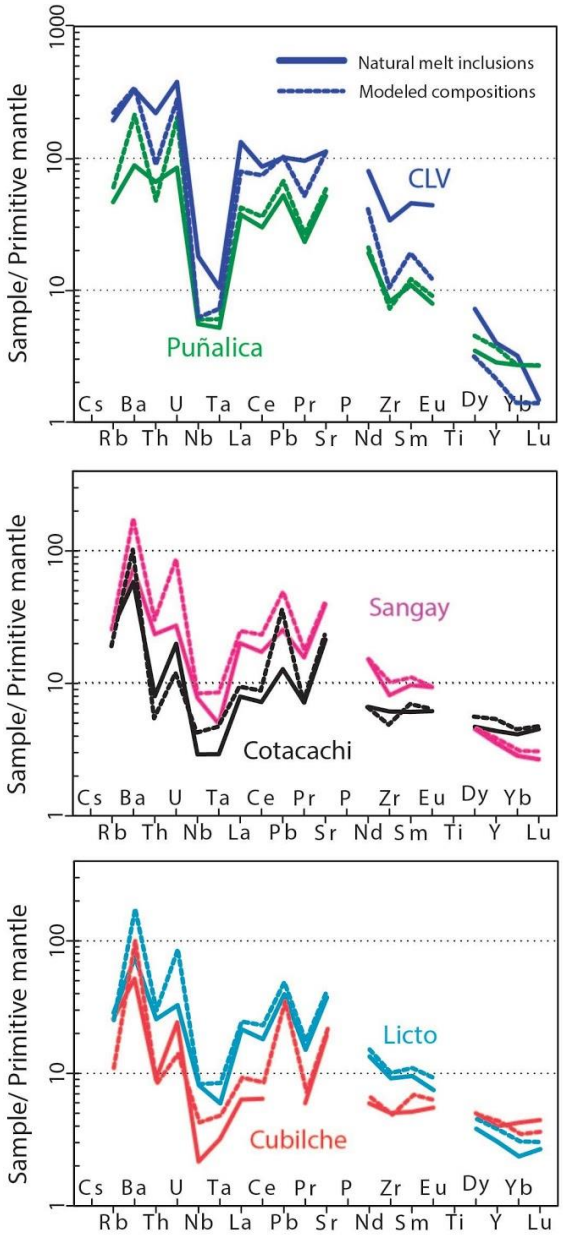

Figure S6. Trace element composition of natural MI (colored solid lines) compared to modelled composition (colored dashed lines). MI compositions were reproduced using a modified version of ABS3 to apply batch melting formulation. Degree of mantle melting is fixed to 5%. Slab component for Puñalica and CLV is a hydrous siliceous melt while for the others is an aqueous fluid. Detailed parameter for modeling are given in Table 5 and in subsection 5.3.3

Table S3. Major, trace and volatiles elements of olivine-hosted melt inclusions from Ecuadorian volcanoes. Data are from Le Voyer et al. (2008, 2009), Narváez et al. (2018) and this study. Major oxide values are raw data.

References

Bucholz, C. E., Gaetani, G. A., Behn, M. D., & Shimizu, N. (2013). Post-entrapment modification of volatiles and oxygen fugacity in olivine-hosted melt inclusions. *Earth and Planetary Science Letters, 374,* 145–155. https://doi.org/10.1016/j.epsl.2013.05.033

Danyushevsky, L. V., Della-Pasqua, F. N., & Sokolov, S. (2000). Re-equilibration of melt inclusions trapped by magnesian olivine phenocrysts from subduction-related magmas: petrological implications. *Contributions to Mineralogy and Petrology*, *138*(1), 68–83. https://doi.org/10.1007/PL00007664

Leroux, P., Shirey, S., Hauri, E., Perfit, M., & Bender, J. (2006). The effects of variable sources, processes and contaminants on the composition of northern EPR MORB (8–10°N and 12–14°N): evidence from volatiles (H_2O, CO_2, S) and halogens (F, Cl). *Earth and Planetary Science Letters*, *251*(3–4), 209–231. https://doi.org/10.1016/j.epsl.2006.09.012

Le Voyer, M., Rose-Koga, E. F., Laubier, M., & Schiano, P. (2008). Petrogenesis of arc lavas from the Rucu Pichincha and Pan de Azúcar volcanoes (Ecuadorian arc): major, trace element, and boron isotope evidences from olivine-hosted melt inclusions. *Geochemistry, Geophysics, Geosystems*, *9*(12), 27. https://doi.org/10.1029/2008GC002173

Le Voyer, M. (2009). *Rôle des fluides dans la genèse des magmas d'arcs : analyses in situ des éléments volatils et des isotopes du bore dans les inclusions magmatiques des olivines primitives* (Doctoral Thesis). Université Blaise Pascal - Clermont-Ferrand II, France.

Narváez, D. F., Rose-Koga, E. F., Samaniego, P., Koga, K. T., & Hidalgo, S. (2018). Constraining magma sources using primitive olivine-hosted melt inclusions from Puñalica and Sangay volcanoes (Ecuador). *Contributions to Mineralogy and Petrology*, *173*(10), 80. https://doi.org/10.1007/s00410-018-1508-8

Pearce, J. A. (2008). Geochemical fingerprinting of oceanic basalts with applications to ophiolite classification and the search for Archean oceanic crust. *Lithos*, *100*(1–4), 14–48. https://doi.org/10.1016/j.lithos.2007.06.016

Annex C

Size of Ecuadorian melt inclusions measured petrographically

Table A3 Size of Ecuadorian melt inclusions measured petrographically

	Metl inclusion	Sample	Volcano	Melt inclusion size (leght/width/bubble)
1	17EQ81 1B	17EQ81	Cubilche	56 µm/42 µm/19 µm
2	17EQ81 1C	17EQ81	Cubilche	52 µm/38 µm/20 µm
3	17EQ81 1E	17EQ81	Cubilche	62 µm/38 µm/20 µm
4	17EQ81 2A_b	17EQ81	Cubilche	53 µm/35 µm/22 µm
5	17EQ81 2A_t	17EQ81	Cubilche	47 µm/29 µm/18 µm
6	17EQ81 2B_c	17EQ81	Cubilche	48 µm/32 µm/14 µm
7	17EQ81 2B_t	17EQ81	Cubilche	50 µm
8	17EQ81 2C	17EQ81	Cubilche	57 µm/47 µm/23 µm
9	17EQ81 3C_b	17EQ81	Cubilche	64 µm/54 µm/28 µm
10	17EQ81 3C_t	17EQ81	Cubilche	70 µm/ /28 µm
11	17EQ81 3D	17EQ81	Cubilche	70 µm/52 µm/29 µm
12	17EQ81 4D	17EQ81	Cubilche	39 µm/36 µm/19 µm
13	17EQ81 5A	17EQ81	Cubilche	52 µm/50 µm/21 µm
14	17EQ81 5B	17EQ81	Cubilche	40 µm/28 µm/17 µm
15	17EQ91 1A_c	17EQ91	Cotacachi	52 µm/34 µm/20 µm
16	17EQ91 1A_r	17EQ91	Cotacachi	43 µm
17	17EQ91 1C	17EQ91	Cotacachi	39 µm/34 µm13 µm
18	17EQ91 2B	17EQ91	Cotacachi	50 µm/29 µm/17 µm
19	17EQ91 2C	17EQ91	Cotacachi	47 µm/37 µm/30 µm
20	17EQ91 4C	17EQ91	Cotacachi	36 µm/28 µm/12 µm
21	17EQ91 5C	17EQ91	Cotacachi	33 µm/17 µm/10 µm
22	17EQ91 7A_b	17EQ91	Cotacachi	74 µm/55 µm/25 µm
23	17EQ91 7A_s	17EQ91	Cotacachi	31 µm
24	17EQ95 1B	17EQ95	Cubilche	114 µm/78 µm/40 µm
25	17EQ95 2A	17EQ95	Cubilche	75 µm/51 µm/30 µm
26	17EQ95 4B	17EQ95	Cubilche	166 µm/30 µm/89 µm
27	CAY45A 2B	CAY45A	CLV	36 µm/16 µm/10 µm
28	CAY45A 3A	CAY45A	CLV	35 µm/22 µm/12 µm
29	CAY45A 3B	CAY45A	CLV	37 µm/25 µm/14 µm
30	CAY45B 4A	CAY45B	CLV	70 µm/52 µm/35 µm
31	CAY45B 5A	CAY45B	CLV	190 µm/50 µm/103 µm
32	CAY45B 6A	CAY45B	CLV	40 µm/28 µm/12 µm
33	CAY45C 1A	CAY45C	CLV	126 µm/65 µm/52 µm
34	CAY45C 3A_1	CAY45C	CLV	48 µm/ /23 µm
35	CAY45C 3A_2	CAY45C	CLV	32 µm
36	CAY45C 3A_3	CAY45C	CLV	80 µm/61 µm/37 µm
37	CAY45C 3C	CAY45C	CLV	102 µm/34 µm/15 µm
38	CAY45C 4B	CAY45C	CLV	38 µm/28 µm/10 µm
39	CAY45C 5A_1	CAY45C	CLV	36 µm/26 µm/10µm
40	CAY45C 5A_2	CAY45C	CLV	25 µm
41	CAY45C 5C	CAY45C	CLV	56 µm/30 µm/16 µm
42	CAY45C 6A	CAY45C	CLV	122 µm/82 µm/57 µm
43	COTA02 2A_b	COTA02	Cotacachi	40 µm/27 µm/15 µm
44	COTA02 2A_m	COTA02	Cotacachi	40 µm
45	COTA02 2A_t	COTA02	Cotacachi	40 µm
46	MM1B 1B	MM1B	Cotacachi	28 µm/21 µm/13 µm
47	MM1B 5B	MM1B	Cotacachi	55 µm/44 µm/21 µm
48	MM1B 6A	MM1B	Cotacachi	71 µm/37 µm/37 µm
49	RIO10B 1A	RIO10B	Licto	62 µm/48 µm/20 µm
50	RIO10B 1B	RIO10B	Licto	66 µm/31 µm/16 µm
51	RIO10B 1B_l	RIO10B	Licto	90 µm
52	RIO10B 1B_t	RIO10B	Licto	60 µm
53	RIO10B 1C	RIO10B	Licto	30 µm/21 µm/9 µm
54	RIO10B 1D	RIO10B	Licto	80 µm/35 µm
55	RIO10B 2A	RIO10B	Licto	66 µm/55 µm/19 µm
56	RIO10B 2B	RIO10B	Licto	119 µm/52 µm/32 µm
57	RIO10B 2D	RIO10B	Licto	25 µm/25 µm/10 µm
58	RIO10B 3A_l	RIO10B	Licto	60 µm/26 µm/11 µm
59	RIO10B 3A_lc	RIO10B	Licto	30 µm/23 µm/10 µm
60	RIO10B 3A_rc	RIO10B	Licto	35 µm/24 µm/11 µm
61	RIO10B 3B_b	RIO10B	Licto	25 µm/25 µm/9 µm
62	RIO10B 3B_c	RIO10B	Licto	20 µm

Table A3 continued

63	RIO10B 3B_t	RIO10B	Licto	25 µm
64	RIO10B 5B	RIO10B	Licto	49 µm/31 µm/15 µm
65	RIO10B 5C	RIO10B	Licto	30 µm/18 µm/9 µm
66	RIO10B 6B	RIO10B	Licto	35 µm/19 µm/17 µm
67	SAN21B 1A_b	SAN21B	Sangay	300 µm/200 µm/81 µm
68	SAN21B 1A_s	SAN21B	Sangay	30 µm
69	SAN21B 1B	SAN21B	Sangay	62 µm/46 µm/22 µm
70	SAN21B 1C	SAN21B	Sangay	35 µm
71	SAN21B 2B	SAN21B	Sangay	64 µm/51 µm/21 µm
72	SAN21B 2C	SAN21B	Sangay	104 µm/53 µm/29 µm
73	SAN21B 3B	SAN21B	Sangay	233 µm/ 37 µm/31 µm
74	SAN21B 3C	SAN21B	Sangay	133 µm/56 µm/31µm
75	SAN21B 4A	SAN21B	Sangay	73 µm/65 µm/26 µm
76	SAN21B 4B	SAN21B	Sangay	123 µm/51 µm/29 µm
77	SAN21B 5A	SAN21B	Sangay	117 µm/110 µm/40 µm
78	SAN21B 5B_m	SAN21B	Sangay	35 µm
79	SAN21B 5B_t	SAN21B	Sangay	80 µm/37 µm/35 µm
80	SAN21B 6A	SAN21B	Sangay	281 µm/46 µm/44 µm
81	SAN21B 6B	SAN21B	Sangay	187 µm
82	SAN21B 7B	SAN21B	Sangay	249 µm/47 µm/95 µm
83	A	SAN20B	Sangay	38 µm/35 µm/13 µm
84	B	SAN20B	Sangay	25 µm/15 µm/11 µm
85	C	SAN20B	Sangay	46 µm/33 µm/13 µm
86	D	SAN20B	Sangay	47 µm/28 µm/15 µm
87	E	SAN20B	Sangay	25 µm/17 µm/9 µm
88	F	SAN20B	Sangay	48 µm/31 µm/13 µm
89	AA	CAR96A	Puñalica	45 µm/27 µm/17 µm
90	AB	CAR96A	Puñalica	33 µm/20 µm/10 µm
91	AC	CAR96A	Puñalica	49 µm/37 µm/19 µm
92	AE	CAR96A	Puñalica	74 µm/59 µm/22 µm
93	AF	CAR96A	Puñalica	41 µm/27 µm/15 µm
94	AG	CAR96A	Puñalica	96 µm/56 µm/36 µm
95	AH	CAR96A	Puñalica	56 µm/39 µm/21 µm
96	AI	CAR96A	Puñalica	46 µm/39 µm/25 µm
97	AJ	CAR96A	Puñalica	69 µm/59 µm/28 µm
98	AK	CAR96A	Puñalica	82 µm/61 µm/33 µm
99	BA	CAR83A	Puñalica	48 µm/48 µm/28 µm
100	BC	CAR83A	Puñalica	56 µm/42 µm/21 µm
101	BD1	CAR83A	Puñalica	32 µm/25 µm/9 µm
102	H	CAR113B	Puñalica	35 µm/19 µm/6 µm
103	I	CAR113B	Puñalica	171 µm/57 µm/31 µm
104	J	CAR113B	Puñalica	85 µm/46 µm/23 µm
105	K	CAR113B	Puñalica	92 µm/44 µm/20 µm
106	L	CAR113B	Puñalica	48 µm/34 µm/17 µm
107	M	CAR113B	Puñalica	62 µm/41 µm/18 µm
108	N	CAR113B	Puñalica	44 µm/29 µm/13 µm
109	O	CAR113B	Puñalica	64 µm/23 µm/12 µm
110	Q	RIO17	Puñalica	51 µm/48 µm/19 µm
111	S	RIO17	Puñalica	109 µm/73 µm/40 µm
112	T	RIO17	Puñalica	112 µm/47 µm/26 µm
113	U	RIO17	Puñalica	44 µm/36 µm/15 µm
114	V	RIO17	Puñalica	35 µm/27 µm/12 µm
115	W	RIO17	Puñalica	34 µm/24 µm/11 µm
116	X	RIO17	Puñalica	108 µm/92 µm/51 µm